ALMA MATER STUDIORUM
UNIVERSITÀ DI BOLOGNA

DOTTORATO DI RICERCA IN

SCIENZE E TECNOLOGIE DELLA SALUTE

Ciclo XXXVIII

Settore Concorsuale: 09/G2 - BIOINGEGNERIA

Settore Scientifico Disciplinare: ING-IND/34 – BIOINGEGNERIA INDUSTRIALE

OPTIMISATION OF IMAGING METHODS FOR AN ENHANCED STRUCTURAL ASSESSMENT OF THE TISSUES OF THE OSTEOCHONDRAL UNIT

Presentata da: Simone Fantoni

Coordinatore Dottorato

Prof. Igor Diemberger

Supervisore

Prof. Marco Viceconti

Co-supervisori

Ing. Massimiliano Baleani

Dott. Fabio Baruffaldi

Esame finale anno 2026

A Dina e Vittoria

Summary

Imaging is critical for investigating heterogenous tissues such as articular cartilage. The depiction of its hierarchical structure provides the basis for relating to its unique mechanical properties, which are crucial for a proper joint functionality. Such aspect acquires paramount significance when the aetiology of degenerative conditions such as osteoarthritis is deepened. Techniques combining mechanical testing and high-resolution imaging, particularly time-resolved protocols, are sought to advance the field. To this end, X-ray imaging is preferred thanks to unsurpassed spatial resolution and short acquisition times. Nevertheless, the intrinsic radiotransparency of cartilage to X-rays advocates alternative approaches. The present PhD thesis investigated several advanced X-ray imaging techniques for characterization of articular cartilage, aiming to enhance several features. Techniques such as contrast-enhanced imaging, spectral microCT, and synchrotron-based phase contrast X-ray imaging were explored for their potential to depict tissue structures typically undetected to conventional approaches, and to enable the study of cartilage mechanical behaviour under stress.

The first part of this work introduces the application of advanced X-ray techniques to imaging of articular cartilage. These methods include absorption-based, refraction-based, and scattering-based approaches. While absorption-based methods, such as contrast agents, enhance imaging by improving the visibility of inner structures, they may compromise tissue integrity. Refraction-based methods avoid this by enhancing tissue interfaces without the need for contrast agents, though they require specialized equipment. Scattering-based methods provide valuable mesoscale information but face similar limitations to refraction-based methods. According to the presented review of existing literature, propagation-based phase-contrast imaging was found to offer the most promising results, particularly for rheology-oriented studies, due to its simple setup and short acquisition times.

The second part of the work focused on the use of the iodine-based cationic contrast agent, CA4+, for imaging of articular cartilage. This molecule enhances the visibility of proteoglycan content in articular cartilage, allowing for its quantitative analysis. The impact of CA4+ on mechanical properties of cartilage was explored first, through indentation testing. Results showed that CA4+exposure leads to a significant modification of tissue's mechanical response to localised compressions. Nonetheless, preliminary results highlighted an effective resorption of CA4+ from the tissue, following the immersion in a bath of saline solution. The returning of the tissue's mechanical

properties to baseline suggested the potential for reversal of effects related to the use of CA4+. Further analysis using high-resolution peripheral quantitative computed tomography demonstrated that CA4+-enhanced imaging can predict the tissue's mechanical behaviour based on imaging data, correlating with proteoglycan content in the articular cartilage.

In the wake of such promising results, the CA4+-enhancement was implemented to detector-based spectral imaging. This novel approach uses photon energy discrimination to produce density maps of both articular cartilage and bone tissues. The technique was particularly effective at resolving structural features, such as the calcified cartilage layer, whose modification is recognised as a hallmark of degenerative conditions such as osteoarthritis, offering potential applications in preclinical research.

The third part of this work applied synchrotron-based propagation-based phase-contrast imaging to visualize articular cartilage under mechanical compression at the SYRMEP beamline, in Elettra synchrotron facility. The effects of synchrotron radiation on cartilage mechanical properties were investigated, highlighting a significant stiffening related to the exposure to synchrotron radiation. While previous studies have shown inconsistent effects of synchrotron radiation on articular cartilage, this work provides insight into the underlying causes, suggesting that the design of the imaging protocol, including the choice on X-ray spectrum and exposure time, may influence the results.

In conclusion, this PhD thesis demonstrates the potential of advanced X-ray imaging techniques for the preclinical investigation of articular cartilage. While these approaches show promising results, particularly in the context of rheological studies, their application remains primarily limited to research settings. Nonetheless, propagation-based phase-contrast imaging emerges as a valuable tool for high-resolution, non-invasive imaging of articular cartilage with minimal tissue alteration, offering significant advantages for future studies of joint diseases.

List of Abbreviations

ABI	Analyzer-Based Imaging
AC	Articular Cartilage
CA	Contrast Agent
CT	Computed Tomography
CE	Contrast-Enhanced
DE	Duale-Energy
DF	Dark-Field
DVC	Digital Volume Correlation
ECM	Extracellular Matrix
EI	Edge-Illumination
EID	Energy-Integrating Detector
FCD	Fixed-Charged Density
FTIR	Fourier-Transform Infrared
GAG	Glycosaminoglycan
GI	Gratings Interferometry
HA	Hydroxyapatite
HR-pQCT	High-Resolution peripheral Quantitative Computed Tomography
microCT	micro-Computed Tomography
MIR	Multiple-Image Radiography
MRI	Magnetic Resonance Imaging
NP	Nanoparticle
OA	Osteoarthritis
OC	Osteochondral
PBPC	Propagation-Based Phase-Contrast
PBS	Phosphate-Buffered Saline
PC	Phase-Contrast
PCD	Photon-Counting Detector
PG	Proteoglycan
PMA	Phosphomolybdic Acid
PTA	Phosphotungstic Acid
SB	Subchondral Bone
SR	Synchrotron Radiation
USAXS	Ultra Small-Angle X-ray Scattering

Table of Contents

CHAPTER 1

Introduction

1.1. The Problem

Despite its seemingly subordinate relevance compared to other organs and tissues, articular cartilage (AC) plays a crucial role in granting smooth motion and proper distribution of loads. As a matter of fact, diarthrodial joints (i.e., joints with a synovial capsule) fulfil tasks related to several assignments, ranging from locomotion to load-bearing tasks and shock-absorbing events.

The elusive function of AC persists even at the onset of its early alterations, attributable to traumas, autoimmune diseases or tissue overuse. Due to the lack of innervation in the AC, the degeneration advances undetected until the joint functionality is compromised. As a result, the individual's mobility is severely hindered. This is the case of osteoarthritis (OA), a widespread joint-affecting disease with considerable socio-economic impact [1]. At its late stages, treatments for severe degeneration of the osteochondral unit may include invasive procedures such as partial or total knee arthroplasty. The economic burden related to such a treatment increases with the prosthesis revision, implying further complications for the patient [2,3].

In this context, early detection of AC degeneration is crucial. Recent approaches to regenerative medicine emphasise the need to preserve as much of the native AC as possible, given the tissue's minimal intrinsic ability to regenerate [4]. The prescription of any pharmacological treatment depends on the timely assessment of the AC condition.

To this end, non-invasive imaging approaches are privileged in the clinical framework. X-ray imaging and magnetic resonance imaging (MRI) are broadly employed for the three-dimensional evaluation of osteoarticular tissues. Conventional X-ray imaging delivers optimal contrast of mineralised tissues at unparalleled spatial resolution. On the other hand, soft tissues are indistinguishable as they are X-ray transparent. Such a limitation is easily overcome by MRI, thanks to its superior sensitivity to either hydrated or lipidic soft tissues. Still, clinical MRI delivers images at low spatial resolution, incapable of resolving the most subtle alterations of thin tissues such as AC. On the other hand, research-oriented MRI scanners could reach voxel size (e.g., 100 μm downwards) comparable to X-ray microcomputed tomography (microCT) systems [5,6]. Notably, contrast of tailored AC

components, based on the collection of different signals, allows for their quantitative evaluation. Nevertheless, acceptable signal-to-noise ratios demand exceedingly long acquisition times (i.e., tens of hours) [7].

Besides the detection of alterations in pre-clinical and clinical frames, imaging approaches find applications in the research field, aiming for the characterisation of the tissue. The investigation of AC mechanical competence could contribute in shedding light on the aetiology of OA [8]. To this end, specific methods based on rheology rely upon the simultaneous mechanical perturbation of the investigated tissue and high-resolution imaging. In this context, time-resolved imaging protocols that can support complementary techniques (e.g., mechanical testing of AC) are highly desirable. The high spatial resolution offered by X-ray imaging methods, combined with short acquisition times enabled by advanced radiation sources, represents a critical requirement.

1.2. Articular Cartilage

Articular cartilage is an aneural and avascular connective tissue directly implicated in diarthroses and located at the extremities of the involved bones. Articular cartilage is anchored to the subchondral bone (SB) with a thin layer of calcified tissue. The tidemark marks the separation between soft AC and the underlying calcified cartilage. Articular cartilage features a solid phase, a cellular phase and a fluid phase [9]:

1. The solid phase includes the extracellular matrix (ECM), mainly composed of a fibril component and a non-fibril component:
    a. The fibril component mainly consists of collagen II (90% to 95%) and collagen X in minor percentages [10]. The fibril component is arranged in bundles of fibres that are disposed differently, depending on the relative depth in AC. For instance, they originate from the tidemark orthogonally to its surface, and assume the characteristic arcade-like configuration towards the superficial layer of AC. The arrangement of collagen bundles determines the subdivision of AC into tangential (superficial), transition (intermediate) and radial (deep) zones [11].
    b. The non-fibril component includes proteoglycans (PGs) and other aggrecans in fewer fractions. The PGs are complex chains of glycosaminoglycans (GAGs), smaller polar molecules displaying a residual net negative charge [12]. Proteoglycans originate from the pericellular environment and distribute depth-wise in the ECM, reflecting a gradient increasing towards the deep zone of AC.

2. The cellular phase is composed of chondrocytes, which distribute inside the tissue in cavities (i.e., lacunae) and synthesise the main components of the ECM. [13]. The concentration of the number of chondrocytes varies along the depth of the tissue, being maximum in the deep zone and decreasing towards the superficial layer. The size and shape of chondrocytes differ depending on the specific layer.
3. The fluid phase is the interstitial fluid permeating the ECM. It is composed of water with dissolved cations (i.e., mainly mono-cations Na+) [14] .

The interplay of those components confers unique mechanical properties to AC. Upon the application of a localised pressure to the surface of AC, its response could be distinguished into an instantaneous flow-independent and a viscoelastic flow-dependent contribution [15].

The piling up of residual charges of GAGs sums up as the fixed charge density (FCD) observed in PGs. Owing to the intricate arrangement of PGs entwined with collagen bundles, the mutual electrostatic repulsion between GAGs leads to the spatial outstretch of the ECM. This effect is associated with the mechanical pre-tensioning of cartilage tissue [16]. Another crucial function of FCD is related to the hydration of the tissue. The negative charges attract cations, increasing their concentration within the tissue. As a result, an imbalance of solutes with respect to the outer environment is generated. Further hydration compensates for the greater solute concentration in the cartilage environment, as a result of the so-called Donnan osmotic pressure. The packed arrangement of collagen bundles and aggrecans is reflected in the porosity of the ECM, which regulates the flow of interstitial fluid, following any mechanical perturbation. The latter, added to the tissue pre-tensioning and the increased hydration, confers the characteristic viscoelastic flow-dependent response of AC to any localised pressure [17].

Besides the described phenomena, AC displays unique features attributable to the solid phase. In particular, the hierarchical configuration of collagen bundles confers shear tensile resistance to shear stimuli [18]. Eventually, the fluid phase contributes to the lubrication, thanks to its pressurisation upon the application of a load [19].

The degeneration of AC leads to a modification of both the composition and structure of the tissue [20]. For instance, the fibrillation of collagen bundles is associated with an increased porosity of the ECM and diminished resistance to shear stimuli [1]. The depletion of PG content implies a reduced outstretch of the ECM and a decreased stiffness to compressive pressures [21]. The aforementioned effects reflect in an augmented content of interstitial fluid [22]. These are renowned as hallmarks of progressive diseases such as osteoarthritis (OA), which develop with ageing or following traumatic events [23]. In response to the tissue degeneration, regenerative mechanisms are heavily hindered by the aneural and avascular nature of the tissue and the loss of chondrocytes. Modifications of the deep

layer include duplication of the tidemark (i.e., advance of the calcified cartilage) and increased roughness of the cement line [24]. The frame becomes more intricate if the whole osteochondral unit is considered. The debate is still open on whether the trigger for AC degeneration dwells in either AC itself or SB [25]. Thus, any attempt to evaluate simultaneously AC and SB is highly desired. To this end, imaging techniques sensitive to both tissues with high spatial resolution are sought after.

1.3. X-ray Imaging

Since the discovery of Wilhelm Conrad Röntgen in 1895, the applications of X-rays have been manifold [26]. In the field of biomedical research, X-rays marked significant progress for the diagnosis and treatment of human diseases. As for the first historical radiograph, depicting the hand of Röntgen's wife, mineralised tissues and metal objects could be easily detected, avoiding any invasive surgical procedure. X-rays unveiled their potential in distinguishing different materials, depending on their composition. The electron density of the elements (namely, their atomic number Z) governs the absorption of X-rays, and in turn their discernibility. Later, the advent of computed tomography enabled the three-dimensional assessment, ensuring volumetric reconstructions in relatively short acquisition times [27]. Eventually, the development of X-ray sources and radiation detectors has pushed towards the evaluation of tissues to progressively higher spatial resolutions [28].

1.3.1. X-ray Sources

X-rays are electromagnetic radiation in an energy spectrum ranging between 10 keV and 100 keV. Besides the natural emission from radioactive elements, X-rays for imaging purposes can be provided typically by two sources, namely X-ray tubes and synchrotron accelerators.

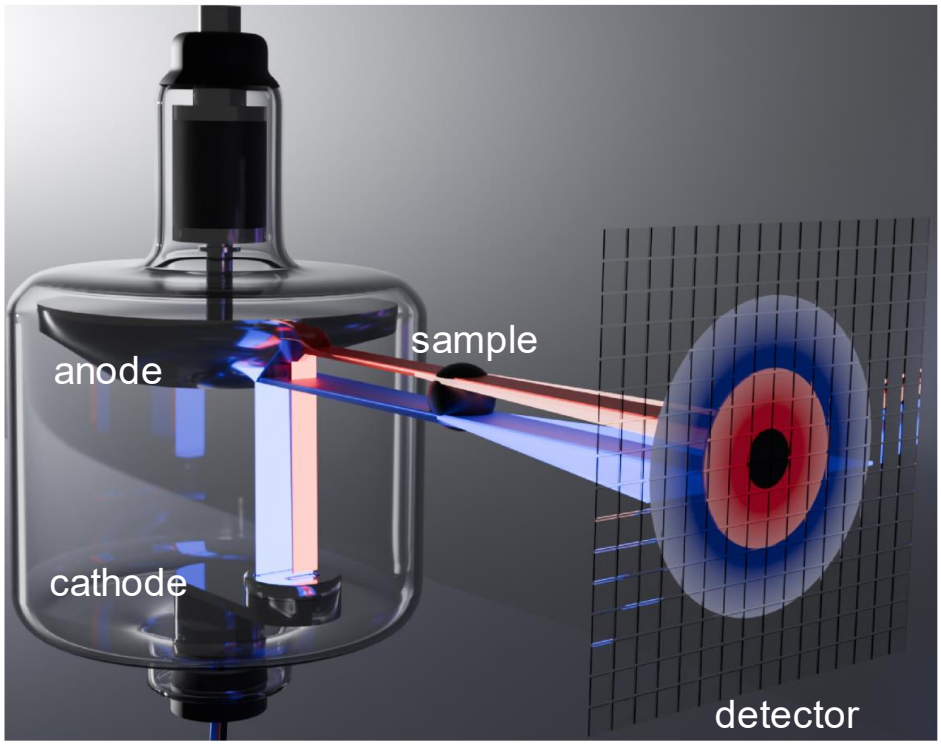

Figure 1.1. Scheme of an X-ray tube. Electrons are emitted from the cathode via thermionic emission and are subsequently accelerated towards the rotating anode by a voltage difference. The rapid deceleration of these electrons results in the emission of photons from a localized region on the anode, referred to as the focal spot. As will be discussed in the following subsections, key features of the X-ray tube, including the focal spot, play a critical role in determining image quality.

1.3.1.1. X-ray tubes

X-ray tubes are the most spread radiation sources, thanks to their small footprint and low costs. A scheme of an X-ray tube is reported in Figure 1.1. They generate X-rays via bremsstrahlung, namely the emission following the acceleration (or deceleration) of light charged particles (i.e., electrons). Ideally, the photon yield is maximised for high electron counts and high-Z elements that stop the electrons. The typical scheme of an X-ray tube includes a cathode (i.e., one or more thin filaments) and a rotating anode. Upon the application of a high electrostatic potential, electrons emitted by the cathode via the thermionic effect are accelerated towards the anode. The rotation of the latter avoids overheating and its subsequent disruption. The incoming electrons impinge on the rotating anode. The abrupt deceleration of electrons on the anode generates X-rays, which are reflected from the anode surface, in a focused region called the focal spot. The composition of both cathode and anode, selected to withstand high temperatures, determines the shape of the emerging X-ray spectrum and is optimised to yield a profitable photon flux. For these reasons, the most frequent combination of cathode-anode contemplates elements featuring a high melting point (i.e., W-W or Mo-W). The accelerating voltage marks the maximum energy of the spectrum, whilst the filament current determines the flux of the X-ray beam. The design of the imaging protocol should carefully consider

the influence of both X-ray tube current and voltage. For instance, increased current corresponds to extended focal spot sizes, with significant effects on image quality [29].

1.3.1.2. Synchrotron radiation sources

The synchrotron emission process foresees the generation of X-rays from the bending of light charged particles (i.e., electrons) upon the application of an external magnetic field. Electrons experience a relativistic boost with subsequent emission of X-rays, depending on the magnitude of the applied magnetic field. Extraction devices such as undulators and wigglers increase the radiation output, conferring the synchrotron emission unsurpassed characteristics when compared to table-top X-ray tubes [30]. For instance, high fluence, high spatial coherence, and, on purpose, monochromaticity (i.e., X-ray spectrum including a restricted range of wavelengths) are essential in accessing imaging techniques alternative to the conventional absorption-based modality [31]. Their role in determining the image quality will be presented in Subsection 1.3.3.

Owing to their significant footprint, synchrotron accelerators are hosted in dedicated facilities. Despite the possibility of extracting multiple SR beams from a single storage ring, synchrotron facilities face limited accessibility due to their restricted diffusion and high operational costs.

1.3.2. X-ray Detectors

With the advent of digital radiography, X-ray detectors replaced radiographic films. With respect to the latter, detectors allow the sequential acquisition of multiple images, a crucial aspect for tomography. Rather than a suspension of chemical compounds, detectors are solid-state devices responsible for the detection and conversion of photons to electric signals. Depending on the detection process, detectors can be categorised into energy-integrating detectors (EIDs) and photon-counting detectors (PCDs).

1.3.2.1. Energy-integrating detectors

This category mainly bases its functioning on spatially continuous scintillator screens, converting the incoming X-ray photons to visible light pulses. The latter are conveyed to a photoconductive structured device and converted into electric signals. This design accounts for the indirect inversion process [32]. Otherwise, the design of EIDs foresees the collection of X-ray photons via continuous photoconductive phosphors (i.e. amorphous Si) trapping photons. Each event in the phosphor screen triggers a cascade of electron-hole pairs, which results in an amplified electric signal. In this case, the direct inversion process occurs [33]. Regardless of the design, EIDs yield output signals locating each

incoming photon with an amplitude proportional to the number of collected photons (i.e., the intensity of the collected X-rays). Though fabrication processes are accessing progressively smaller pixels (i.e., the smallest sensitive elements of the detector surface), potentially bringing about higher spatial resolutions, EIDs are not sensitive to the energy of the collected photons. This limitation reflects a limitation in evaluating heterogeneous samples, including materials sharing similar attenuation features.

1.3.2.2. Photon-counting detectors

Photon-counting detectors share construction schemes similar to direct conversion-based EIDs. For instance, two layers build up the sensitive region of PCDs. The top layer, consisting of a semiconductor material, and the bottom layer, hosting the structured integrated circuit for the read-out of the signal, are coupled via bump-bonds. Upon the arrival of X-ray photons, energy is deposited in the semiconductor top layer of PCD and generates electron-hole pairs via ionisation. An external electric field separates electrons from holes, which are collected by the respective pixel electrode in the bottom layer. The corresponding electric signal is proportional to the energy deposited from the incoming photons (i.e., the number of electron-hole pairs generated in the semiconductor). Compared to EIDs, PCDs discriminate among photon energies, with the setting of thresholds, paving the way to spectral imaging, as it will be discussed in the following sections. Nonetheless, deleterious effects such as charge sharing constrain the downscaling of the pixel size, with a significant impact on PCDs manufacturing and the resulting spatial resolution [34]. As will emerge throughout the present thesis, decent spatial resolutions are reached if specific geometrical conditions are met (see Chapter 4).

1.3.3. Principles of Image Formation and Image Quality

In conventional X-ray imaging, the image formation is based on the projection of the photon beam onto a detector, following its interaction with the object. In the imaging domain, the interaction between X-rays and matter accounts mainly for:

- Rayleigh, or coherent, scattering. Its cross section, associated with the probability of occurrence, depends on the atomic number Z as $\sigma_R \propto Z^{2.5}/E_\gamma^2$. Owing to the elastic nature of the interaction, no energy is exchanged between the photon and the target electron. Nevertheless, the photon deviates from its original pathway, with consequences in terms of contrast reduction and blurring of details.
- Compton, inelastic, scattering, with cross section $\sigma_C \propto Z/E_\gamma$. It is the secondary channel of radiation-matter interaction, and it gains more weight at higher X-ray energies. Compton

scattering implies the deviation of an incoming photon from its original trajectory, and it translates into a decrease in photon energy. As a result, the scattered photon reaches a detector pixel differing from the projected site of interaction. Compton scattering leads to the blurring of details, lowering the overall quality of the acquired image.

- Photoelectric effect with cross section $\sigma_p \propto Z^4/E_\gamma^{-3.5}$ with discontinuities, called absorption edges, characteristic for each atomic species. It is the predominant channel at lower X-ray energies. The photoelectric effect consists of the complete absorption of a photon by an electron hosted by the interacting atom. Therefore, atoms displaying high Z are more prone to interact with the incoming photon.

X-rays impinging on the detector, following the interaction with the sample, can be quantified according to the Lambert-Beer law:

$$I = I_0 e^{-\frac{\mu}{\rho}t}$$

where I is the final X-ray intensity, I_0 the initial X-ray intensity, E the energy of the X-ray spectrum, μ is the linear attenuation coefficient of the object, ρ is the mass density of the object and t is its thickness. The linear attenuation coefficient is the macroscopic characteristic of a material associated with its absorption power towards X-rays.

Depending on energy, discrepancies between μ from different materials allow for the discrimination of details. To enhance the latter, lower energies are advocated.

The detection, identification, and quantification of such features of interest determine the image quality delivered by an X-ray system. Owing to the composite nature of an X-ray system, image quality results from the concatenation of effects related to each component. The physical phenomena underlying the image quality can be categorised into X-ray source physical and spectral characteristics, and the detector's specifications. Furthermore, features strictly related to the imaging protocol should be discussed, namely, the geometrical configuration. Eventually, aspects such as the reconstruction algorithms and environmental factors gain more weight for high-resolution imaging purposes.

1.3.3.1. X-ray source

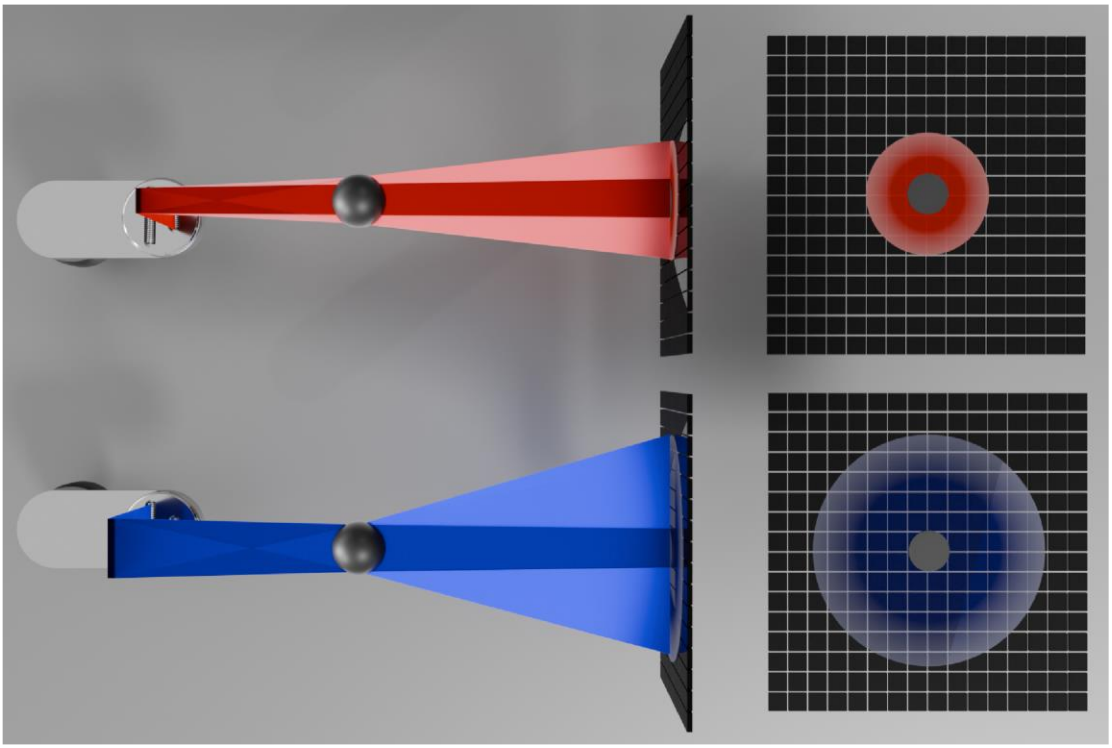

Figure 1.2. The influence of focal spot size on image quality is illustrated. Specifically, the penumbra is shown to vary with the extent of the focal spot. In the top figure, the projected image of the object exhibits a less pronounced penumbra compared to the bottom figure. An enlarged penumbra leads to increased blurring and degradation of the object's edges..

Knowing the composition of the sample a priori, X-ray spectral features should be carefully selected to optimise the discernibility of structures in the sample.

Regardless of the spectrum, general considerations hold considering low- and high-peak energies (i.e., long and short X-ray wavelengths, respectively):

- Low X-ray energies lead to increased absorption (i.e., contrast) of soft tissues. On the other hand, the radiation dose significantly increases, with implications at microscopic and macroscopic (i.e., heating) of the sample. Furthermore, the number of photons surviving the interaction with the samples significantly decreases, at the expense of statistics reaching the detector (i.e., the penetration depth is reduced).
- High X-ray energies are associated with increased penetration depths. Nevertheless, high energy spectra imply enlarged focal spot sizes, with limitations discussed in the following points.

One primary categorisation distinguishes between polychromatic and monochromatic spectra, whether they comprise a wide or restricted range of wavelengths, respectively. Due to the nature of bremsstrahlung emission, polychromatic spectra are mainly generated by X-ray tubes. The latter generate monochromatic emission as well, provided the insertion of optical elements designed to

selectively extract the desired energy component, or the inclusion of materials presenting unique X-ray signatures (i.e., K-line emissions).

Nevertheless, such implementations lead to severe beam fluence (i.e., the number of photons emitted per unit of time, area and solid angle). It determines the X-ray intensity traversing the sample and, together with the exposure time, the statistics collected by the detector. For rheological purposes, time-resolved protocols are preferred to catch transient phenomena in the sample investigated. Nevertheless, radiation absorptions in very short times could imply issues over heat dissipation, and consequent alteration of biological tissues [35].

Besides spectral features, the intrinsic characteristics of the X-ray source impact image quality. Overall, the focal spot identifies the region on the anode from which X-rays originate, following the interaction of accelerated electrons with the atoms of the anode. The size of the focal spot corresponds to the extension of the cathode projected on the anode. Extended focal spot sizes are responsible for the penumbra effect (see Figure 1.2) , which determines the geometric unsharpness, hindering the depiction of subtle details and limiting the spatial resolution of X-ray systems [36]. This limitation is circumvented by the use of SR, renowned for its negligible source size.

Additional source characteristics are crucial for the retrieval of the refraction signal, as discussed in Chapter 2. Spatial coherence is the ability of electromagnetic radiation to generate interference when different wavefronts overlap. The interferometric phenomena arising from the transit of the wavefront through the interfaces in the sample determine the contrast increment. High spatial coherence is typically featured by SR and nanofocus X-ray tubes.

1.3.3.2. Detector

The characteristics of the detector, such as the pixel size and the device configuration, influence the imaging outcome:

- pixel size. Defined as the smallest detecting element, the pixel size contributes to the spatial resolution. Smaller pixel sizes imply higher spatial resolutions [37]. Nevertheless, the reduced detecting surface tends to provide noise-dominated signals;
- scintillator thickness. In EIDs, the scintillator is the component sensitive to X-rays. Thicker scintillators grant increased sensitivity to radiation. On the other hand, the collected photon suffers from smearing, therefore its actual localisation results in an inaccurate [38].

Specific metrics translate the physical role of single components into more interpretable quantities. The resulting spatial resolution, defined as the ability to distinguish small details, can be experimentally quantified. For example, the modulation transfer function points out the preservation

of contrast at several spatial frequencies for a given imaging system. The contrast resolution, namely the ability to differentiate between regions sharing similar X-ray attenuations, is quantified by the contrast-to-noise ratio. The noise determines the fluctuations, biasing the collected signal, and can either originate from the intrinsic Poisson statistics or the electronic noise. The noise contribution is typically compensated with longer exposure times of higher X-ray beam fluences. These compensations come with larger radiation doses.

1.4. Mechanical testing

To understand the complex behaviour of AC and identify its key characteristics, a wide range of methods allows for a deeper understanding of its structure and the alterations that occur at the onset and progression of pathological conditions. Together with diagnostic imaging, mechanical testing provides complementary knowledge towards a multidisciplinary framework, essential for advanced approaches such as rheology.

To accurately investigate the mechanical behaviour of hierarchical and biphasic tissues such as AC, it is crucial to carefully define the testing conditions. One key requirement is the adoption of a humid environment, aimed at preventing the dehydration of the AC and mimicking the pristine physiological state of the tissue (i.e., the synovial capsule). For this purpose, saline solutions or phosphate-buffered saline (PBS) are commonly used [39].

Besides a consistent environmental condition, the most suitable protocol should be selected to address the manifold nature of AC mechanical response (i.e., elastic and viscous). In the study of elastic behaviour, the monotonic test constitutes the simplest investigation method. It consists of a constant compressive strain (or stress), applied until a specified level is reached. The experimental output is the tissue's instantaneous response—i.e., the instantaneous modulus, E_0—which depends on the strain level reached and the rate at which the tissue is deformed or loaded [40–43].

In the case that the viscoelastic behaviour is examined, protocols such as creep and stress-relaxation tests are employed [44]. In the creep test, a constant load is applied to the sample up to a defined level and then maintained. The resulting displacement, and thus the strain, is recorded over time. This protocol aims to mimic the behaviour of load-bearing joints, where articular tissues deform progressively in response to sustained external load.

Stress-relaxation testing consists of the application of a controlled displacement and the subsequent monitoring of the resulting force over time. In this scenario, both fluid-dependent and fluid-independent mechanisms in AC are triggered. In order, the reorganisation of the collagen network

mainly rules the initial response, the interstitial fluid flow governs the time-dependent creep or stress-relaxation behaviour, and, lastly, the properties of the ECM determine the equilibrium response.
Both creep and stress-relaxation tests, implemented with multi-step loading protocols, enable the evaluation of instantaneous, equilibrium, and rate-dependent mechanical behaviours of AC.
Although tensile and shear loads also act on the articular joint [45], AC primarily withstands compressive loads. Therefore, the compression-oriented approaches are embraced. Depending on the experimental configuration, methods for assessing compressive behaviour are generally classified into:

- confined compression. It involves the compression of a cylindrical sample of tissue by means of two rigid metal platens – one impermeable and the other porous. The sample is constrained in an impermeable chamber, matching the diameter of the sample. Upon the application of a compressive load (or displacement), the ECM responds first, together with the frictional drag opposed to fluid reconfiguration within the tissue. The presence of the porous platen underneath the sample allows the complete exudation of interstitial fluid until equilibrium is reached [44].
- Unconfined compression. It involves the compression of a cylindrical sample placed between two impermeable platens, according to a stress-relaxation or creep protocol. To ensure uniform compression across the entire sample surface, the diameter of the platens must be larger than that of the cartilage cylinder. This technique is commonly used to evaluate both the instantaneous and equilibrium responses of the tissue, yielding parameters such as the Instantaneous Modulus (E_0) and the Equilibrium Modulus (E_{eq}) [39].
- Indentation. It allows the retrieval of mechanical parameters, maintaining the continuity of AC with surrounding tissues [46]. Either a spherical or flat-ended indenter, with a radius smaller than the area of the investigated sample, induces localised tissue deformation [46–49]. Similar to confined compression and unconfined compression, stress-relaxation and creep protocols can be applied in indentation tests.

As no destructive procedure potentially altering the properties of the tissue (i.e. embedding or fixation) is required, the aforementioned approaches probe the mechanical behaviour of AC in its pristine condition. Therefore, they can be easily implemented in multidisciplinary pipelines, including complementary methods addressing the structure and the composition of the investigated tissue [50–52]. In the present work, indentation testing served as a grounded reference method, along with the advanced X-ray techniques presented throughout the proposed experiments.

1.5. Aim and outline of the thesis

The aim of this thesis is to investigate the outcome of advanced X-ray techniques on the imaging of AC, along with complementary approaches (i.e., mechanical testing) to validate the proposed methods and highlight possible drawbacks. The manuscript can be roughly divided into three main parts.

The introductory part presents notions on AC structure and composition, and the issues related to its hierarchical characterisation via X-ray imaging (Chapter 1). Therefore, an in-depth review of existing literature explores the application of advanced X-ray techniques to the imaging of AC. Lastly, a brief excursus of in-situ rheologic studies of AC is presented (Chapter 2). The main objective of the first two Chapters is to contextualise the X-ray imaging within the frame of AC assessment, highlighting the benefits and limitations of the single advanced techniques.

The second part pivoted around absorption-based X-ray methods. Several experiments involving the use of a cationic contrast agent (i.e., CA4+) aims at the X-ray visualisation of AC. The main tasks include:

- The investigation of the impact of CA4+ on the mechanical response of AC. This preliminary step has determined the suitability of the CA4+-based contrast-enhanced protocol for rheological applications (Chapter 3, Section 1).
- The reversibility study of effects induced by CA4+ on AC mechanical behaviour. Results support the viability of CA4+ for research-oriented purposes. For instance, the complete desorption and restoration of AC properties allows complementary studies following CA4+-based contrast-enhanced protocols (Chapter 3, Section 2).
- The test of reliability of contrast-enhanced X-ray imaging of AC, performed with high-resolution peripheral quantitative computed tomography (HR-pQCT). The objective of this activity is to seek correlations between imaging-driven data and the mechanical response of AC. The resulting outcome could potentially be used to predict the mechanical quality of the tissue based on contrast-enhanced imaging (Chapter 3, Section 3).
- The feasibility of detector-based spectral imaging, performed on osteochondral tissues exposed to CA4+. The experiment, performed at the multimodal imaging laboratory-based microCT PEPILab, aims at evaluating the potential of a photon-counting detector in the wake of research-oriented experiments based on such spreading technology. In this context, preliminary results are presented, aimed at simultaneously evaluating articular cartilage, bone tissue and their interface in a quantitative way (Chapter 4).

The third part focuses on refraction-based imaging of AC. Results from Section 1 of Chapter 2, discouraging the use of CA4+ for rheologic purposes, shifts the attention to phase-contrast imaging, ideal for retrieving contrast of soft tissues by avoiding the use of any CA. Nevertheless, the positive outcome of phase-contrast approaches strictly depends on the high spatial coherence of the X-ray source, typically satisfied by SR. The experiment, performed at Elettra synchrotron, has involved X-ray imaging of osteochondral samples in a propagation-based phase-contrast configuration. The primary aim is to characterise the cellular pattern through high-resolution volumetric reconstructions, with imaging data still under analysis. In this thesis, results regarding the macroscopic effects of SR on AC mechanical properties are presented (Chapter 5).

CHAPTER 2

Advanced X-rays techniques for research-oriented high-resolution imaging of articular cartilage: a scoping review

This chapter was reproduced from the manuscript:
"Advanced X-rays techniques for research-oriented high-resolution imaging of articular cartilage: a scoping review" by S. Fantoni, l. Brombal, P. Cardarelli, F. Baruffaldi. Submitted to *Proceedings of the Royal Society A: Mathematical, Physical and Engineering Sciences*.

The preprint version of the manuscript has already been published on the ArXiv repository: https://arxiv.org/abs/2507.13854v2

Abstract

Articular cartilage is a musculoskeletal soft tissue renowned for its unique mechanical properties. Understanding both its hierarchical structure and the interplay between its constituents could shed light on the mechanical competence of the tissue. Therefore, rheologic approaches based on high-resolution non- destructive imaging techniques are desired. In this context, X-ray imaging could ideally accomplish this task.

Nevertheless, the nature of articular cartilage translates into poor contrast using conventional absorption modality. To overcome this limitation, several approaches can be embraced. X-ray visibility of articular cartilage can be increased with the use of radiopaque contrast agents. Therefore, further discrimination of structures could be provided by spectral techniques, pivoting on either multi-energy acquisitions or photon-counting technology.

Alternatively, phase-contrast techniques unveil details typically undetected with conventional approaches. Phase-contrast imaging, based on the intrinsic decrement in the refractive index of the tissue, can be achieved with different configurations and implementations, including distinct X-ray sources and optical elements.

Additionally, some phase-contrast techniques retrieve the small-angle scattering-based dark- field signal, relatable to sub-pixel structures. This scoping review aims to catalogue the application of these advanced X-ray techniques to articular cartilage imaging, following PRISMA guidelines. It discusses their advantages, limitations, and includes an overview of rheologic applications to articular cartilage.

2.1. Introduction

Many biomedical imaging techniques allow for non-invasive evaluation of heterogeneous tissues. The osteoarticular tissue represents an excellent case of study, as it features different compositions and structures. Besides its crucial role in clinical routine, imaging of osteoarticular tissues has been extensively investigated in the research frame. In the latter context, the retrieved information is associated with the functional properties of osteochondral tissues. Their degradation, related to pathologies affecting the articulating joints, can be easily depicted with computed tomography (CT) and magnetic resonance imaging (MRI). The role of CT and MRI has been extensively discussed in the context of clinical diagnostics. However, such discussions are limited to conventional techniques, as diagnostic imaging performed on patients prioritizes minimizing the acquisition times, the possible hazards and the costs. Conversely, biomedical research places more emphasis on different aspects, such as spatial resolution and quantitative accuracy. In this frame, the high-resolution counterpart of CT, the microcomputed tomography (microCT), is preferred.

MicroCT can provide detailed information on microstructures of biological tissues [53], even down to the cellular level, with results comparable to histology [54]. On the other hand, nearly no contrast of soft tissues such as articular cartilage (AC) is achieved, due to their associated low atomic numbers Z. Consequently, limited information is extracted with conventional X-ray techniques, reducing their potential in assessing AC status. The need for accurate examination of AC and soft tissues, crucial for early disease detection and biomedical analysis, has driven the exploration of alternative X-ray imaging techniques, based on the implementation of non- conventional X-ray sources, detectors, contrast agents (CAs), or their combination.

The aim of the present review is to report on developments achieved in the frame of high- resolution X-ray imaging of AC in recent years, drawing attention to innovative techniques, implemented with different imaging systems.

2.1.1. Articular cartilage

Articular cartilage is a connective tissue covering joint surfaces, mainly composed of collagen fibrils (predominantly type II), proteoglycans (PGs), and interstitial fluid. Originating from the deeper zone of the tissue, the collagen fibrils arrange into bundles surging aligned to AC tissue surface, acquiring the characteristic arcade-like structure. The PGs (i.e., the non-fibrillar component of the ECM) are complex proteins bound with multiple glycosaminoglycans chains, and mainly originate from the pericellular environment of chondrocytes. Their concentration follows a peculiar depth-wise gradient,

increasing towards the deep zone of AC. The chondrocytes distribute inside the tissue in specific sites (i.e. lacunae) and synthetize the main components of ECM. The structure of AC is schematized in Figure 2.1.

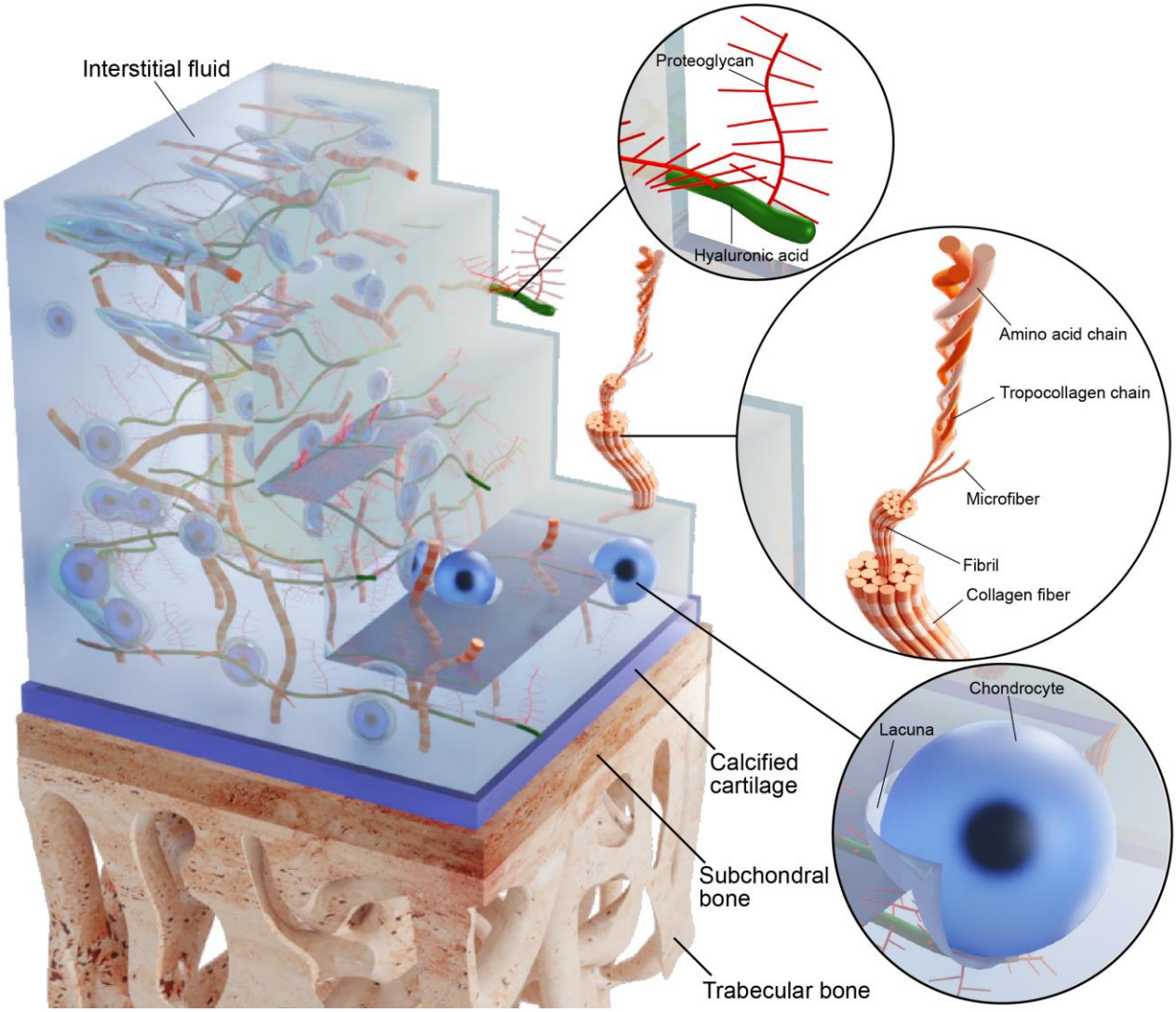

Figure 2.1. Scheme of AC

The residual negative charge density displayed by glycosaminoglycan chains confers unique properties to the tissue. For instance, the entwined arrangement of PGs in between the collagen bundles generates a spatial outstretch of the ECM, owing to the mutual repulsion of negative charge densities. This effect gives rise to the mechanical pre-tensioning of the AC. Moreover, the charge imbalance draws cations dissolved in the interstitial fluid. The latter results in Donnan osmotic pressure and induces a significant hydration and swelling of the tissue. This phenomenon, together with tissue pre-tensioning and the fibril solid component of ECM, accounts for the characteristic instantaneous response of AC to any rapid mechanical solicitation. The porosity associated with the packed ECM organization regulates the transient reconfiguration of interstitial fluid following any

mechanical stimulus, until equilibrium is reached [55,56]. In summary, the hierarchical structure and composition of AC translate into near-frictionless and smooth joint motion, provided the integrity of the tissue [55].

The degeneration of ECM, typically occurring with ageing, after traumas or associated with pathologies (i.e. osteoarthritis), alters both the composition and structure of AC [1]. More in detail, the fibrillation of collagen bundles, the depletion of PGs, and the augmented content of interstitial fluid in ECM are recognized as hallmarks of AC diseases, along with modifications of underlying subchondral bone as well [57]. The reduced mechanical performance of AC induces the progressive impairment of joint motion, with severe compromission of an individual's mobility.

In the clinical frame, the early detection of subtle changes in AC could improve the prevention of related musculoskeletal diseases. X-ray imaging methods allow for a detailed depiction of both soft and mineralized tissues at high spatial resolution in restrained acquisition times. For instance, the link between the tissue microstructure and its mechanical response has been investigated to relate the different degradation stages of AC with the tissue functionality. In- situ testing enables the study of geometrical, morphological, and densitometric properties of biological tissues in conjunction with their mechanical properties. In this context, digital volume correlation (DVC) can track down these subtle interrelationships by measuring the full three- dimensional displacement and strain maps under prescribed loading conditions. Nonetheless, the accuracy and precision of the DVC in measuring displacements strongly depend on the quality of the input images (i.e., signal-to-noise ratio and spatial resolution) [58].

As it will be discussed in the review, different mechanisms of image formation yield quantitative information of AC properties, including tissue morphology and composition. The multiple nature of signals (namely absorption, refraction, and scattering of radiation) that can be extracted with advanced X-ray techniques provides meaningful results, as supported by independent methods in the selected literature, and lay the foundations for their use in AC imaging, as introduced hereafter.

2.1.2. Advanced X-ray imaging techniques

In general X-ray imaging techniques can give access to three signals, namely absorption, refraction or scattering phenomena. Absorption-based X-ray methods are easily performed with conventional systems, but result in low contrast of soft tissues due to their low electron density. The use of high-Z CAs significantly enhances the visibility of inner structures of AC. In this context, to further enhance the discrimination of tissues sharing comparable radiopacity, spectral imaging techniques make use of the specific energy dependence of CA attenuation coefficients. Owing to their spectroscopic

capabilities, photon-counting detectors (PCDs) are a crucial implementation for spectral imaging [59]. Refraction-based methods exploit the optical phenomena originating from the shift in the phase of X-ray waves accumulated while traversing the sample. This, in combination with specific geometrical configurations or the insertion of optical elements, allows for the detection of a signal from soft tissue features, generally undetectable with absorption-based approaches. Additionally, valuable information on tissues' substructures can be retrieved by assessing the scattering of X-rays in the sample, which can be modelled as a multiple-refraction process at a scale smaller than the system's spatial resolution. Advanced X-ray imaging techniques, allowing for the collection of the different signals previously introduced, can be implemented with laboratory or synchrotron systems. The first category, including conventional microCT scanners, is widely spread thanks to the high availability of commercial systems. Nevertheless, laboratory scanners are mainly devoted to absorption-based modalities, owing to low spatial coherence and limited fluxes. Existing literature reports only a few experiences exploiting microfocus X-ray tubes for phase-contrast (PC) imaging of AC [60]. Synchrotron radiation (SR)-based systems, featuring high fluxes, monochromaticity and high spatial coherence, find applications in retrieving refraction and scattering signals. On the other hand, the limited accessibility to synchrotron facilities hinders their translation to routine practice.

2.1.2.1. Contrast-enhanced computed tomography

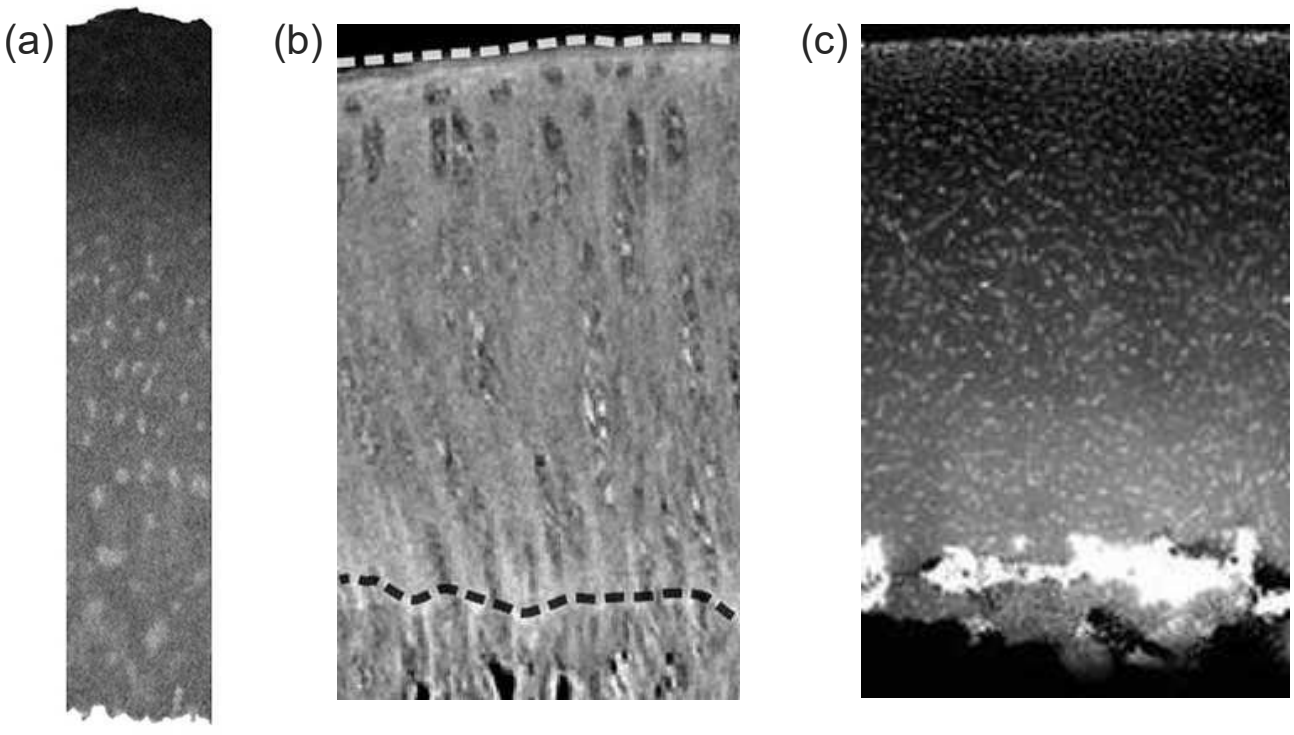

Figure 2.2. (a) Section from contrast-enhanced microCT of human AC, following the immersion in CA4+ solution (3.2 µm-pixel size, commercial microCT scanner). Along with the characteristic gradient of radiopacity increasing towards

the deep layer of AC, spots with augmented signal are recognizable as chondrocytes' lacunae. Image adapted from the work of Karhula et al. [61], published under Creative Commons license (CC BY 4.0). (b) Section from contrast-enhanced microCT of rabbit AC, following the immersion in solution of hexaammineruthenium(III) chloride and cacodylic acid (0.65 µm-pixel size, commercial microCT scanner). The proposed protocol aimed to investigate the collagen fiber orientation in a osteoarthritic AC model (dashed white line and dashed black line mark tissue surface and tidemark, respectively). Image adapted from the work of Ojanen et al. [62], published under Creative Commons license (CC BY 4.0). (c) Section from contrast-enhanced microCT of human AC, following the immersion in propidium iodide (2.6 µm-pixel size, SR- microCT). The direct binding of the selected CA to DNA in chondrocytes allowed the punctual depiction of the cellular pattern, enabling the quantification of chondrocytes' distribution even inside each lacuna. Image adapted from the work of Danalache et al. [63], published under Creative Commons license (CC BY 4.0).

Contrast-enhanced computed tomography (CECT) is an absorption-based technique that uses exogenous radiopaque contrast agents (CAs). Contrast agents are compounds including high-Z elements, which increase the attenuation coefficient and enhance the contrast of the investigated soft tissue.

First, the selection of CAs depends on the imaging purpose. In-vivo purposes require non- toxic, FDA-approved CAs [64], whereas the use of heavy metal-based stains [65] and experimental compounds is limited to ex-vivo and in-vitro studies, due to their high toxicity. Among the available CAs, iodine-based formulations have been extensively used to visualize AC (i.e., ioxaglate, iothalame, iohexol, ioversol), as denoted in Table 1. For research purposes, CA stains generally employed in histology and transmission electron microscopy have also been translated to X-ray imaging protocols.

Second, the effectiveness in enhancing AC X-ray visibility relies upon the properties of the CA molecule, namely its size, the modality of interaction, and more importantly, its net electric charge. These properties account for the steric hindrance, the reversibility of the contrast enhancement process and the affinity of CA molecule to the AC, respectively. The molecule size should be tailored to the tissue porosity, to facilitate the permeation in the tissue [66].

The net electronic charge governs the affinity of the CA to components of AC showcasing a charge imbalance. Recalling the composition and structure of AC, only PGs naturally show a net negative fixed charge density.

Table 2.1. Summary of research papers including X-ray imaging of AC with CECT protocols, ordered from the most to the least recent. For each paper, the corresponding reference is reported, along with the CA used, its net electric charge q, the model for the AC tissue, the size of the specimen S, the voltage V of the X-ray beam, the acquisition time T and the voxel size of the reconstructed volume p. † SR

ref.	contrast agent	q (e)	model	S (mm)	V	T (min)	p (µm)
[67]	$Na_{0.2}TiO_2$ NPs	NA	bovine	NA	25 keV	NA	9
	NPs	NA			17.5 keV		
[68]	CA4+	+4	equine	Ø 7	70 kVp	NA	36
[69]	Ta2O5 NPs	+1	equine	Ø 8.5	150 kVp	NA	40
[70]	PTA	-3	bovine	Ø 4-10	40 kVp	160	3
	Hf-WD POM	-16					

[71]	CA4+	+4	rat	NA	70 kVp	NA	6
[62]	cacodylic acid $Cl_3H_{18}N_6Ru$	NA NA	rabbit	Ø 2	40 kVp	240	0.65
[72]	ioxaglate	-1	rat	NA	45 kVp	26	16
[73]	iopamidol	-1	murine	NA	55 kVp	20	10.4
[74]	iohexol	0	rabbit	Ø 3.5	40 kVp	NA	18.22
[75]	ioxaglate bismuth NPs	-1 0	equine	NA	90 kVp	2	80
[76]	ioxaglate	-1	rat	NA	55 kVp	NA	8; 12
[77]	CA4+	+4	murine chicken	NA	70 kVp	2.9, 3.5	10
[78]	PTA	-3	guinea pig	NA	60 kVp	NA	10.85
[79]	CA4+	+4	murine chicken	NA	45kVp	NA	2
[80]	Bi-DOTA Gd-DOTA	+1 +1	porcine	NA	70 kVp	NA	10.06
[81]	ioxaglate	-1	rat	NA	45kVp	27	16
[82]	3,5-diiodo-L-tyrosine	NA	human murine	Ø 5	70 kVp	3	10
[83]	CA4+	+4	bovine	NA	50 kVp	NA	11.52
[84]	PTA	-3	bovine	3-5	80kVp	52/181	4.6; 3.4
[85]	ioxaglate	-1	primate	NA	80 kVp	15	90
[86]	CA4+	+4	equine	Ø 7	70 kVp	NA	36
[87]	CA4+	+4	equine	Ø 7	70 kVp	NA	36
[88]	Ta_2O_5 NPs	+13/0	human	NA	70 kVp	NA	36
[89]	CA4+	+4	rabbit	NA	70 kVp	NA	38
[90]	iothalamate	-1	bovine	NA	80 kVp	18	45
[91]	PMA	NA	rat	NA	70 kVp	NA	15
[92]	iodixanol	0	primate	NA	NA	NA	NA
[63]	propidium iodide	NA	human	NA	† 12 keV m.	5	2.6
[93]	PTA	-3	human	Ø 3	50 kVp	NA	1.8
[94]	CA4+	+4	bovine	Ø 5	70 kVp	27.9	4
[95]	ioxaglate	-1	goat	75	70 kVp	NA	18
[96]	SiO_2 ioxaglate	NA -1	rat	NA	70 kVp	NA	10
[97]	ioversol iomeron	0 0	mice bovine	Ø 5	55 kVp	NA	57
[98]	iopimadol	0	rat	NA	47 kVp	NA	21
[99]	ioxaglate	-1	murine	NA	45 kVp	NA	16
[100]	iohexol	0	human	Ø 16.3	84 kVp	17	45
[101]	gadopentetate Gd(DTPA)Lys2 ioxaglate CA4+	-2 +4 -1 +4	human	NA	70 kVp	13	18
[102]	ioxaglate	-1	murine	NA	70 kVp	NA	6
[103]	CA4+	+4	human	NA	NA	NA	100
[104]	PTA	-3	human	Ø 4	80 kVp 45 kVp	120	3.0 3.2
[105]	ioxaglate	-1	rat	NA	45 kVp	NA	14.8
[106]	iopimadol	0	bovine porcine	Ø 10	70 kVp	NA	16
[107]	CA4+	+4	equine	Ø 7	70 kVp	NA	36
[108]	iohexol	0	human	NA	68 kVp	18	61
[109]	ioxaglate	-1	rat	NA	45 kVp	27	16
[110]	PTA	-3	murine	NA	90 kVp	NA	2.5
[111]	ioxaglate	-1	human	NA	70 kVp	40	36
[112]	CA4+	+4	human	NA	120 kVp	NA	41

[113]	ioxaglate	-1	rat	NA	45 kVp	26	16
[114]	CA4+	+4	human	NA	120 kVp	NA	41
[115]	ioxaglate iodixanol	-1 0	equine	Ø 6	66 kVp	NA	10
[116]	CA4+ ioxaglate iodixanol	+4 -1 0	bovine rat	Ø 7	70 kVp	NA	36
[117]	Bi_2O_3 ioxaglate	NA -1	bovine	Ø 7	100 kVp	NA	15.98
[118]	meglumine diatrizoate	-1	rat	NA	45 kVp	NA	16
[119]	PTA	-3	human	Ø 4	80 kVp	100	3
[120]	CA4+ ioxaglate	+4 -1	murine	NA	45 kVp	NA	3
[121]	uranyl acetate lanthanide solution IKI PTA iopamidol	NA NA NA -3 0	human rat	NA	70 kVp	NA	13; 2.94
[122]	PTA ioxaglate	-3 -1	bovine	Ø 4.8	40 kVp	8	17.4
[61]	CA4+	+4	human	Ø 2	45 kVp	122	3.2
[123]	ioxaglate	-1	rat	NA	90 kVp	3	21
[124]	ioxaglate	-1	rat	NA	45 kVp	24.7	16
[125]	ioxaglate	-1	human	NA	95 kVp	30-90	35
[126]	SiO_2 ioxaglate	NA -1	rabbit	NA	70 kVp	NA	18
[127]	ioxaglate	-1	canine	NA	40 kVp	NA	13.4
[128]	CA4+	+4	murine	NA	70 kVp	NA	2; 6
[129]	CA2+	+2	bovine	Ø 6	100 kVp	NA	25
[130]	ioxaglate	-1	rabbit	NA	45 kVp	NA	20
[131]	PTA PMA	-3 NA	equine human	Ø 6 Ø 4.6	80 kVp 80 kVp	32 135	8.7 3.2
[132]	meglumine diatrizoate	-1	human	Ø 12	50 kVp	11	18
[133]	CA4+ ioxaglate	+4 -1	human	NA	70 kVp	NA	36
[134]	meglumine diatrizoate	-1	bovine	4	50 kVp	NA	18
[135]	ioxaglate	-1	rat	NA	55 kVp	42	10
[136]	ioxaglate	-1	rat	NA	55 kVp	42	10
[137]	ioxaglate	-1	rat	NA	65 kVp	NA	18
[138]	ioxaglate	-1	rat	NA	65 kVp	NA	18
[139]	ioxaglate	-1	human murine	NA	70 kVp	36	18
[140]	ioxaglate	-1	murine	NA	60 kVp	20	2
[141]	ioxaglate	-1	rat	NA	60 kVp	NA	20
[142]	Ta_2O_5 NPs ioxaglate	NA -1	human rat	NA	50 kVp	NA	6; 36; 100
[143]	iothalamate	-1	bovine	NA	58 kVp	NA	70; 100
[144]	PTA	-3	murine	NA	50 kVp	NA	5
[145]	ioxaglate	-1	rat	NA	45 kVp	NA	16
[146]	CA4+ ioxaglate	+4 -1	bovine rabbit	Ø 7	70 kVp 50 kVp	NA	36 100
[147]	CA4+	+4	bovine	Ø 7	70 kVp	NA	36
[148]	meglumine diatrizoate	-1	rat	NA	70 kVp	NA	18
[149]	ioxaglate	-1	human	NA	55 kVp	360-600	35
[150]	ioxaglate	-1	murine	NA	45 kVp	NA	6
[151]	ioxaglate	-1	murine	NA	60 kVp	20	2

[152]	ioxaglate	-1	rat	NA	55 kVp	NA	35
[153]	ioxaglate	-1	human	NA	55 kVp	360-600	35
[154]	CA4+ ioxaglate gadopentetate	+4 -1 -2	bovine	Ø 7	70 kVp	NA	36
[155]	CA4+ CA1+ iothalamate	+4 +1 -1	bovine rabbit	Ø 7	NA	NA	70; 36
[156]	ioxaglate	-1	rat	NA	45 kVp	NA	12; 16
[157]	iothalamate	-1	bovine	Ø 7	NA	NA	70; 100
[158]	ioxaglate	-1	rat	NA	45 kVp	NA	12
[159]	gadopentetate	-2	human	NA	60 kVp	NA	41
[160]	CA1+ CA2+ CA4+ iothalamate ioxaglate	+1 +2 +4 -1 -1	rabbit	NA	45 kVp	NA	30
[161]	ioxaglate	-1	rat	NA	55 kVp	15	35
[162]	ioxaglate	-1	bovine rabbit	Ø 4	45 kVp	NA	21

Otherwise, external alterations in the physiological environment of ECM (i.e., cleaving of negative charges in acid environment) make collagen fibrils a valuable target for the CA molecules [163]. Clinical CAs are water-soluble small molecules that can be categorized into ionic and non-ionic. The former are preferred to the aims of PG quantitation, thanks to non-covalent electrostatic Coulomb repulsion exerted from negative fixed charge density of PGs. The efficacy of anionic CAs has been demonstrated in various AC models, particularly those involving pathological degeneration. The stronger inverse correlation with PG content justifies the broad adoption of anionic CAs compared to non-ionic CAs [74,92,97,98,100,106,108,118]. On the contrary, non-ionic CAs are limited to reveal AC morphology, as their molecules permeate the ECM according to the interstitial fluid distribution, and occasionally with the collagen content [115,134]. The commercial availability of clinical CAs allows their prompt adoption in CECT protocols, aside from adjustments in concentration and osmolality. As a result, numerous works based on clinical ionic CAs extracted quantitative information from AC of different models, including large animals, rodents and human [76,85,90,95,96,105,111,113,116,117,120,122,123,125–127,130,132,135,139–141,143,145,148–153,156–158,161,162]. Furthermore, anionic CA-enhanced protocols served as a useful tool in monitoring the progression of osteoarthritis in several preclinical studies, as confirmed by reference methods such as histology [72,73,75,81,99,102,109,124,136–138,164]. Despite the readiness of clinical CAs, the anti-correlation to PG content is biased by factors in addition to CA accumulation [159]. Moreover, anionic CAs reasonably enhance the tissue discernability at cost of conspicuous CA concentrations, with further concerns related to beam-hardening effects [108].

In the realm of experimental CAs, the formulation of novel molecules focused on more advantageous mechanisms of interactions with AC components. The first experimental cationic CAs [160] offered higher iodine content per molecule and electrostatic attraction to PGs, yielding superior discrimination of AC. Further correlations with AC composition were confirmed with reference methods (i.e., histology and biochemical assay), at significantly lower concentrations compared to clinical anionic molecules [61,71,77,79,83,107,128,129,133,146,154,155] (see Figure 2.2a). Furthermore, mechanical tests confirmed the intertwined relationship between the attenuation of cationic CA and the mechanical behavior of AC, considering the tissue's elastic, frictional, and equilibrium properties [68,86,87,89,94,101,103,112,114,116,133,147].

Besides iodine, other radiopaque candidates have been selected for AC visualization. Gadolinium is a chemical element of lanthanide series, and enters the composition of MRI CAs, owing to its paramagnetic properties. In the clinical formulations, gadolinium-based CAs are predominantly non-ionic or anionic, and are employed as well as the iodine-based CAs, to signal the water content and PG distribution [101,159]. Due to its different K-edge energy (50.2 keV) with respect to iodine (33.2 keV), gadolinium-based CAs can be used simultaneously along with iodine-based CAs in DE and multi-energy protocols[165–171]. In the wake of novel formulations, a cationic molecule containing bismuth yielded greater correlations to reference methods for assessing PGs, compared to analogous molecules [80].

Laboratory stains, usually employed in histology and transmission electron microscopy, offer a valid alternative to clinical CAs. For instance, polyoxometalates such as phosphotungstic acid (PTA) e phosphomolybdic acid (PMA) considerably increase the X-ray visibility of the exposed soft tissue [65]. Nevertheless, different binding mechanisms oblige fixation and dehydration of the tissue, leading ot irreversible alterations of its properties. While effective for collagen quantification [62,84,91,93,104,110,121,131,144] (see Figure 2.2b), imaging protocols based on polyoxometalates imply alterations of the AC incompatible to mechanical testing [70]. Only in recent times, the adoption of physiological environments has limited the forthcoming modifications of AC properties, following the exposure to such stains [78].

Further efforts to enhance the imaging outcome of existing CAs include functionalizing ioxaglate to specifically bind to PG [164] or tyrosine (an amino acid naturally containing iodine) to type-II collagen of ECM [82]. In recent years, increasing attention has been addressed to nanoparticles (NPs) due to their small size (1–1000 nm) and tunable physicochemical properties, including shape, hindrance, and composition [142,172]. For instance, tantalum-based NPs enable the quantitation of PG [69,88] or ensure the detection of defects in the tissue [67].

In existing literature, only few studies addressed CECT on chondrocyte imaging, owing to the demanding spatial resolution. Rather than the cells themselves, the imaging of lacunae (namely, the cavities in ECM enclosing one or more chondrocytes, with typical size of 10 µm [173]) allows for more relaxed imaging protocols, carried out with nano-focus X-ray tubes. Following the contrast enhancement, lacunae were reportedly depicted as focalized sites featuring a radiopacity different from the surrounding ECM [61,119]. Nevertheless, laboratory-based systems equipped with X-ray tubes require long acquisition times, raising concerns about the stability of the sample over time. Such issue can be overcome with SR. For instance, the high monochromatic flux significantly lowers the scan time and ensures spatial resolution down the cellular level [63] (see Figure 2.2c).

2.1.2.2. Dual-energy imaging

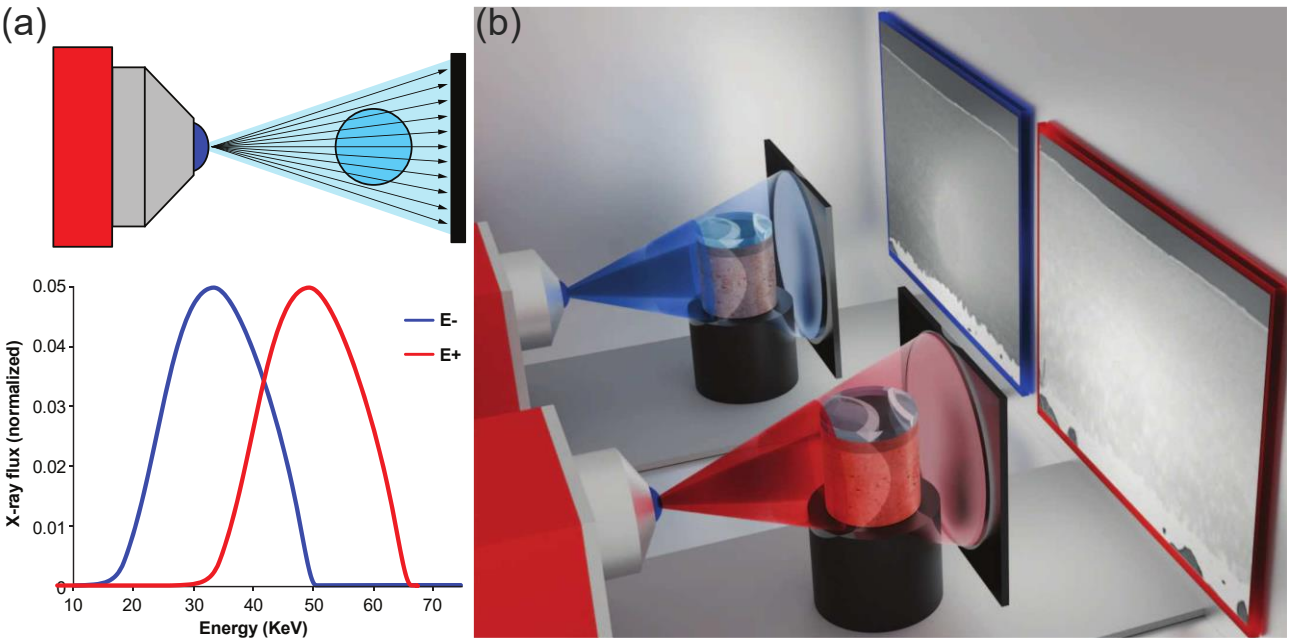

Figure 2.3. (a) Scheme of DE technique. The procedure includes two distinct X-ray exposures, each at a different beam energy. The low-energy and high-energy components serve as input for decomposition algorithms, to deliver two material maps. (b) Reconstructed section from low-energy E- and high-energy E+ binned photons is reported on blue and red screen, respectively. In the low-energy and high-energy screens are reported sections from reconstructed volume of AC, following the immersion in a gadoteridol/CA4+ mixture. In particular, the contrast in low- and high- energy sections is due mainly to gadoteridol and CA4+, respectively. Images on screens of panel (b) adapted from the work of Honkanen et al. [169], published under Creative Commons license (CC BY 4.0).

Table 2.2. Summary of research papers including X-ray imaging of AC with DE protocols, ordered from the most to the least recent. For each paper, the corresponding reference is reported, along with the CA used, its net electric charge q, the model for the AC tissue, the size of the specimen, the source type, the voltage V or associated energy E of the X-ray beam (m. monochromatic), the acquisition time T and the voxel size of the reconstructed volume p.

ref.	contrast agent	q (e)	model	S (mm)	source	V /E	T (min)	p (µm)
[171]	CA4+ gadoteridol	+4 0	equine	NA	X-ray tube	50/90 kVp	2.6	59
[170]	CA4+	+4	human	Ø 8	X-ray tube	50/90 kVp	NA	40

	gadoteridol	0		Ø 8				
[168]	CA4+ gadoteridol Bi-NPs	+4 0 0	bovine	Ø 7	synchrotron	32/34 keV m.	2.15	6.5
[169]	CA4+ gadoteridol	+4 0	human	Ø 8	synchrotron	32/34 keV m.	2.15	6.5
[167]	CA4+ gadoteridol	+4 0	human	Ø 8	X-ray tube	50/90 kVp	NA	40
[166]	CA4+ gadoteridol	+4 +4	bovine	Ø 4	synchrotron	25/37 keV	2.1	6.5
[165]	CA4+ gadoteridol	+4 0	human	Ø 8	X-ray tube	50/100 kVp	18/10	25

Dual-energy (DE) and, more in general, multi-energy imaging is based on several acquisitions taken at different X-ray beam energies. This method can provide information on sample composition, if unknown, or conversely, allows reconstructing the density distribution of certain elements, provided that the composition is known a-priori [174]. Dual-energy imaging is particularly useful when CAs or naturally occurring high-Z materials are present within the sample. By making use of attenuation properties specific to the material of interest, such as the K-edge, it is possible to discriminate structures containing the high-Z element, even though they have an overall attenuation similar to the surrounding features [175]. This is achieved through dedicated material decomposition algorithms, which, having as input two (or more) attenuation images at different energies, provide density maps of two (or more) materials. A scheme of DE technique is reported in Figure 3. The ideal conditions for DE imaging are obtained using monochromatic beams, as in the case of SR [176,177] or laser-driven radiation sources [178]. In this case, the material decomposition problem can be solved exactly, due to the absence of beam-hardening, which is commonly encountered when polychromatic spectra are used.

In the context of AC X-ray imaging, DE technique offers its potential in discerning two or more CAs, when used simultaneously. In particular, radiopaque CAs with different attenuation signatures (i.e., K-edge energies) are selected to track single AC components (see Table 2.2). The X-ray energies are carefully chosen to enclose the attenuation discontinuities of the selected CAs separately. By applying material decomposition algorithms to DE dataset, the density maps of the elements of interest are obtained [175]. Such protocols were applied to understand the various factors influencing CA diffusion in AC [165,167,170,171]. Specifically, iodine accounted for the PG content, owing to the electrostatic repulsion between the anionic CA and negative fixed charge density of glycosaminoglycans. In contrast, gadolinium CA tracked the water content.

The concurrent determination of ionic and non-ionic partitions improved the correlation between the PG-related iodine distribution and AC mechanical properties [165,166,168,170,179,180]. Dual-energy methods can be further implemented with SR. The monochromaticity and high fluxes of the

generated beam ensure improved image quality and reduced scan times [166,168,169]. Nevertheless, the material decomposition comes with the increase of radiation dose deposited to the sample, proportional to the number of X-ray exposures (i.e., number of X-ray energies) and the exposure time. On the other hand, the development of novel detectors has enabled the simultaneous measurement of transmitted X-ray photons in multiple energy windows, by using one single polychromatic X-ray exposure.

2.1.2.3. Detector-based spectral imaging

Photon-counting detectors discriminate the incoming photons, depending on their energy and recently have found applications in several imaging fields [181]. Photon-counting technology is based on the direct conversion of incoming photons by semiconductors sensors and the following discrimination of the signal at the pixel level. Unlike scintillator elements in energy-integrating detectors, which achieve X-ray conversion into visible light, semiconductors enable the direct conversion of incoming photons into electric signal, with an intensity proportional to the energy deposited by each interacting photon to the sensitive region of the detector [34]. Within each pixel of a PCD, this signal is discriminated based on one (or more) energy-calibrated threshold. If multiple energy thresholds are available, photons can be detected and grouped over multiple energy intervals (or bins). In this way, a single X-ray exposure yields multiple attenuation maps, as many as the energy bins defined by the thresholds. The application of decomposition algorithms selectively enhances or eliminates structures in the sample, similarly to the DE imaging [182]. The principles of spectral imaging are summarized schematically in Figure 2.4. Unlike DE methods, polychromatic X-ray beams are employed, and no specific constraints on X-ray spectrum are required. Therefore, the implementation of PCDs is suitable for clinical [183] and laboratory [184] X-ray systems.

Detector-based spectral imaging yielded promising results in terms of AC discernability, although the spatial resolution of clinical scanners remains limited [185,186]. This issue is partially solved by laboratory-based spectral systems equipped with small pixel (<100 μm) PCDs, where the spatial resolution has been significantly improved. Previous experiments verified the suitability of spectral imaging ex-vivo and in-vitro on human specimens, exposed to several CAs [180,187,188]. Alternatively, other works exploited a single CA but aimed to distinguish between the contrast-enhanced AC and the underlying bone tissue [189–191] (see Figures 2.4c and 2.4d), even down to the smallest pixel size reported for a spectral imaging system, namely 34 μm (see Table 3).

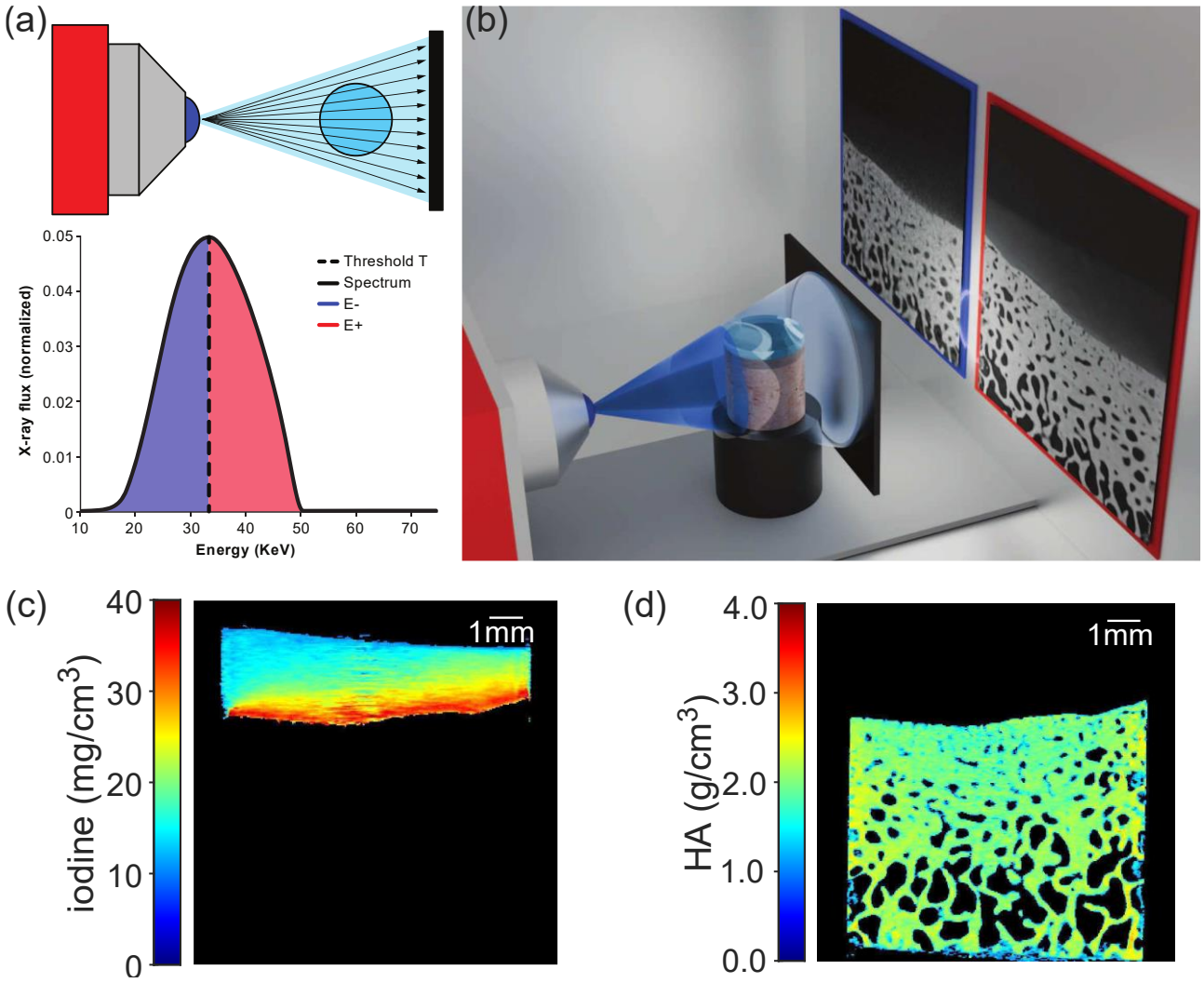

Figure 2.4. (a) Scheme of spectral imaging technique. The procedure includes a single X-ray exposure. The discrimination occurs on-chip, following the selection of an energy threshold. According to the latter, photons are binned in low-energy and high-energy components. Analogously to DE technique, both components are required for decomposition algorithms to provide two material maps. (b) Reconstructed section from low-energy E- and high-energy E+ binned photons of a bovine osteochondral sample is reported on blue and red screen, respectively. (c, d) Section of density maps, as a result of the decomposition algorithm. (c) Iodine density map accounting for iodine-based CA4+ diffused in AC. (d) Hydroxyapatite (HA) density, accounting for calcium-rich bone tissue. Images in panels (b), (c) and (d) adapted from the work of Fantoni et al. [191], published under Creative Commons license (CC BY 4.0).

Table 2.3. Summary of research papers including X-ray imaging of AC with PCD-based spectral protocols, ordered from the most to the least recent. For each paper, the corresponding reference is reported, along with the CA used, its net electric charge q, the model for the AC tissue, the size of the specimen, the PCD model, the voltage V of the X-ray beam, the acquisition time T and the voxel size of the reconstructed volume p.

ref.	contrast agent	q (e)	model	S (mm)	PCD	V	T (min)	p (μm)
[188]	Ta_2O_5 NPs	+4	equine	Ø 8.5	Xcounter	150 kVp	NA	68
	iodixanol	0			XC-Flite FX15	120 kVp		
[191]	CA4+	+4	bovine	Ø 10	Pixirad1-PixieIII	50 kVp	120	34
[180]	CA4+	+4	human	Ø 8	0.75mm CdTe	100 kVp	NA	87
	gadoteridol	0			100um pixel size			
[190]	ioxaglate	-1	bovine	Ø 8	2-mm CdTe	80/120 kVp	NA	110
	gadobenate	-3	human		Medipix3RX			
[189]	ioxaglate	-1	human	25	2-mm CdTe	80 kVp	NA	73
					Medipix3RX			

2.1.3.Refraction-based X-ray Imaging Techniques: Phase-Contrast

Phase-contrast imaging exploits the phase shift of X-rays interacting with the sample. Phase- contrast rises from interference phenomena involving the wavefront distorted by the sample [192]. The modulation of the wavefront can be described by the phase shift accumulated by the incoming X-ray wave while traversing the sample, which is proportional to the decrement from unity of the real part δ of the complex refractive index. Conversely, it can be demonstrated that X-ray attenuation, which is used in conventional X-ray imaging, is proportional to the imaginary part β of the complex refractive index ($n = 1 - i\beta - \delta$). In the case of soft tissues and energies used in conventional radiology (10 – 100 keV), PC is advantageous as δ is two to three orders of magnitude larger than β, allowing to highlight internal structures related to subtle fluctuations of density or interfaces without using exogenous CAs [193]. The sample-induced phase-shift can be related to refraction effects where local modifications to the wave vector can be described, in a simplified ray-tracing model, as small-angle deviations (order of microradians) of the impinging X-rays [194]. As the X-ray wave phase cannot be directly measured with imaging detectors, several PC techniques have been developed to transform the phase shift into detectable intensity modulations. Some of these techniques pose strict requirements on the X-ray beam coherence (namely monochromaticity and small focal spot size), and are therefore primarily implemented within SR facilities [195–197]. More recently, also alternative PC setups with relaxed coherence requirements have been introduced, therefore making PC imaging accessible within laboratory settings [198,199]. In the following subsections the image formation principles of the most widely used PC techniques will be illustrated.

2.1.3.1. Propagation-based phase-contrast

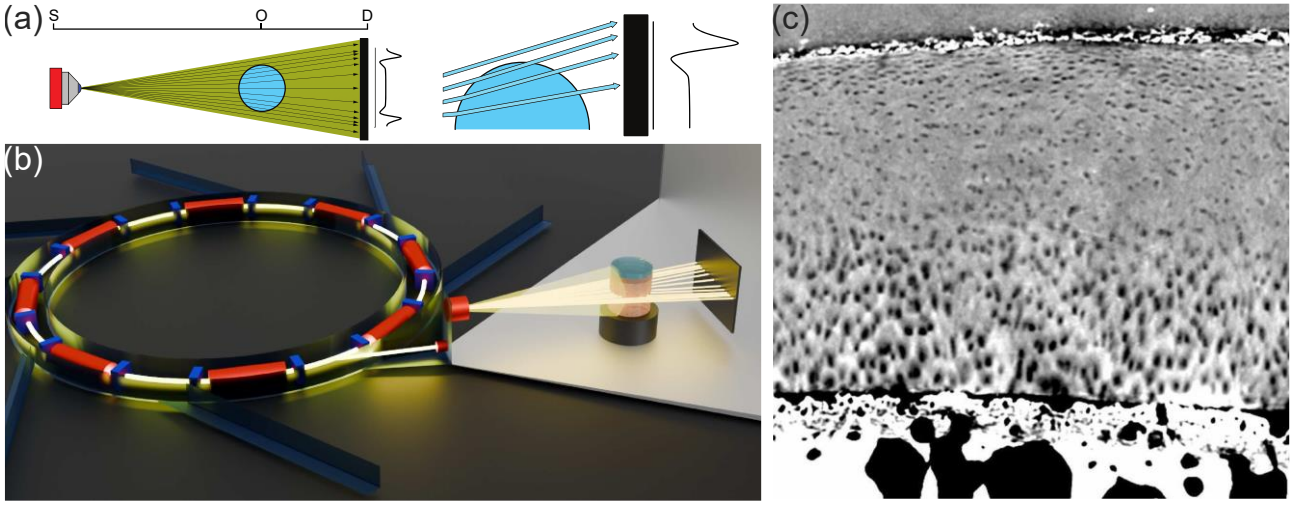

Figure 2.5. (a) Scheme of PBPC. Unlike absorption modalities, PBPC bases its mechanism on the distance between the sample and the detector. In particular, such distance is selected to produce the edge-enhancement, originating from interfaces between different materials. (b) Three-dimensional rendering of a typical PBPC setup. The edge-enhancement requires a high degree of spatial coherence (i.e., SR). (c) Section from PBPC volume of healthy human AC. Besides the interface AC-air on the top, darker spots in the tissue, attributable to chondrocytes' lacunae, are clearly recognizable. Image adapted from the work of Horng et al. [200], published under Creative Commons license (CC BY 4.0).

Propagation-based phase-contrast (PBPC) imaging is the simplest PC technique to implement, as no optical element is required [201]. PBPC requires increasing sample-to-detector distance to generate a phase shift-induced interference pattern on the detector. This is generally visible as a couple of dark/bright fringes corresponding to interfaces between materials with different refractive index, and it is referred to as edge-enhancement effect.

Since the spatial coherence of the X-ray beam is crucial for PBPC [201], this technique can be implemented with SR, laser-driven systems, or high-end microfocus X-ray tubes [202] (see Table 2.4). A scheme of image formation via PBPC is displayed in Figure 2.5. Images featuring the edge-enhancement effect can be further processed with phase-retrieval algorithms, which enable the recovery of the phase-shift information [203] and enhance the signal-to-noise ratio, hence the visibility, of soft tissue structures [203,204].

Table 2.4. Summary of research papers including X-ray imaging of AC with PBPC protocols, ordered from the most to the least recent. For each paper, the corresponding reference is reported, along with the model for the AC tissue, the size of the specimen S, the source type, the voltage V or associated energy E of the X-ray beam (m. monochromatic, p. polychromatic, p.b. pink beam), the acquisition time T , the voxel size of the reconstructed volume p and the object-to-distance ODD.

ref.	model	S (mm)	source	V /E	T (min)	p (µm)	ODD (cm)
[205]	bovine	Ø 4	synchrotron	21keV m.	0.08-0.66	2.75	40
[206]	bovine	Ø 4-6	synchrotron	17 keV m.	66	3.5	250
[200]	human	Ø 7	synchrotron	60keV m.	NA	6.1	1100
				55keV p.		0.7	120
				17keV m.		0.325-0.1	10
[207]	murine	NA	synchrotron	52 keV m.	8	6.1; 6.06	1100
		NA	X-ray tube	60 kVp	NA		

[208]	bovine	Ø 3-4	X-ray tube	40 kVp	NA	2.02-2.56	NA
[209]	human	Ø 7	synchrotron	26.1 keV p.b.	NA	5.1	500
[210]	murine	NA	synchrotron	12-25 keV p.b.	1.1-7.3	0.8-1.6	NA
				19 keV, m.	37.5	1.1	NA
[211]	human	NA	synchrotron	60 keV m.	1.5	46	700
[212]	murine	NA	synchrotron	NA	NA	NA	NA
[213]	rabbit	NA	synchrotron	5-18 keV p.	NA	10	NA
[214]	murine	NA	synchrotron	14 keV m.	NA	3.7	NA
[215]	human	NA	synchrotron	60 keV m.	90	46	700
[216]	bovine	Ø 2	synchrotron	14 keV m.	60-180	1.752	0.5-30.0
[217]	murine	NA	X-ray tube	80 kVp	30	9/6.6	32.2
[218]	horse	0.2-1	X-ray tube	70 kVp	NA	13	NA
	human			11.2 keV, m.		15	NA
[219]	murine	NA	synchrotron	7-14 keV p.	NA	1.48	5
[54]	bovine	NA	synchrotron	10-15 keV m.	40	1.6	15
[220]	human	20	synchrotron	30 keV m.	NA	NA	NA

In the literature, PBPC has been demonstrated as a suitable imaging technique, not only in visualizing AC without the need for CA, but also in unveiling the most subtle structures. The ability to clearly distinguish AC was confirmed by studies based on planar [218–220] and tomosynthesis approach [212,213]. Reduced thickness and augmented roughness of AC surface have been recognized as hallmarks of AC degeneration in diseased models [211,212]. The transfer of PBPC to tomographic acquisitions confirmed these observations [207,214,217]. Boosting the resolution of the acquisition system down to few µm, the sensitivity of PBPC technique to cellular pattern was further enhanced with specific CAs and validated by independent methods such as histology [60,221,222] (see Table 2.5). Besides the coherence of the beam, the object-to-detector distance is crucial for the visualization of lacunae, namely the interfaces between the inner chondrocytes from the surrounding ECM.

Larger sample-to-detector distances and higher beam energies of the X-ray beam were demonstrated to be beneficial for the optimal visualization of structural details [54]. Noteworthily, the proposed imaging protocol distinguishes also chondrocyte from the surrounding lacunae, as confirmed by scanning electron microscope images [54,216]. Horng et al. further pushed the evaluation of healthy and diseased AC down at sub-cellular level, highlighting even the cellular nucleus and bundles of collagen fibers with the highest spatial resolution of 0.1 µm [200] (see Figure 2.5c).

Table 2.5. Summary of research papers including X-ray imaging of AC with contrast-enhanced PBPC protocols, ordered from the most to the least recent. For each paper, the corresponding reference is reported, along with the contrast agent and its charge q, the model for the AC tissue, the size of the specimen, the source type, the voltage V of the X-ray beam, the acquisition time T , the voxel size of the reconstructed volume p and the object-to-distance ODD.

ref.	contrast agent	q (e)	model	S (mm)	V	T (min)	s (µm)	ODD (cm)
[223]	RHT	NA	murine	NA	NA	NA	NA	NA
	cacodylic acid	NA						
	OsO_4	NA						
[222]	PTA	-3	ovine	Ø10	80 kVp	NA	4.5	9.5
					60 kVp	NA	10.2	17.2
[60]	PTA	-3	bovine	Ø 3	40 kVp	NA	1.97-2.85	4.0-55.8

[224]	PTA	-3	murine	NA	NA	NA	NA	NA
[225]	OsO_4	NA	murine equine	NA	NA	NA	NA	NA
[221]	OsO_4	NA	murine	NA	40-80 kVp	65-1067	0.54-10	2.5-7.5
[226]	OsO_4	NA	murine	NA	40 kVp	NA	4	7.5
[227]	RHT cacodylic acid OsO_4	NA NA NA	murine	NA	NA	NA	NA	NA

Other studies, rather than focusing on cellular-scale details, analyzed the morphology of AC on larger scales. The acquisition of whole cadaveric human joints yielded not only the delineation of several soft tissues, but also the differentiation of AC layers. The latter feature was observed to vary substantially from healthy to osteoarthritic AC. The authors speculated that the loss of chondrocytes associated to the pathology could imply a variation in the electron density associated with the retrieved signal [215].

The quantitative analysis was also carried out with the application of Paganin phase- retrieval, assigning different gray level windows, according to the heterogeneous arrangement of components in ECM [200,206,209]. Unless more complex acquisition schemes are implemented, such as in the case of holotomography [228], a quantitatively accurate phase-retrieval requires strict assumptions on sample composition [229]. Alternatively, the phase information can be accessed with different imaging configurations, making use of optical elements in the imaging setup. These approaches will be discussed in the following subsections.

2.1.3.2. Analyzer-based imaging

Analyzer-based Imaging (ABI) makes use of a perfect crystal, referred to as analyzer, set between the object and the detector [231–233], and requires a monochromatic and laminar X-ray beam. The analyzer crystal acts as an angular filter of the incoming X-ray beam. When the analyzer crystal is set to an angle that satisfies the Bragg's condition with respect to the incoming beam, X-rays are transmitted (i.e., diffracted). The transmission efficiency decreases as the analyzer is rotated off the Bragg's condition. The curve describing the X-ray transmission as a function of the analyzer crystal's angle is called rocking curve [231].

As the angular acceptance of the rocking curve is in the order of some microradians, the analyzer crystal allows the translation of X-ray refraction into intensity modulation with high sensitivity. By acquiring images at different angles of the analyzer crystal, that is, different points on the rocking curve, both attenuation and (differential) phase signal can be obtained via dedicated algorithms.

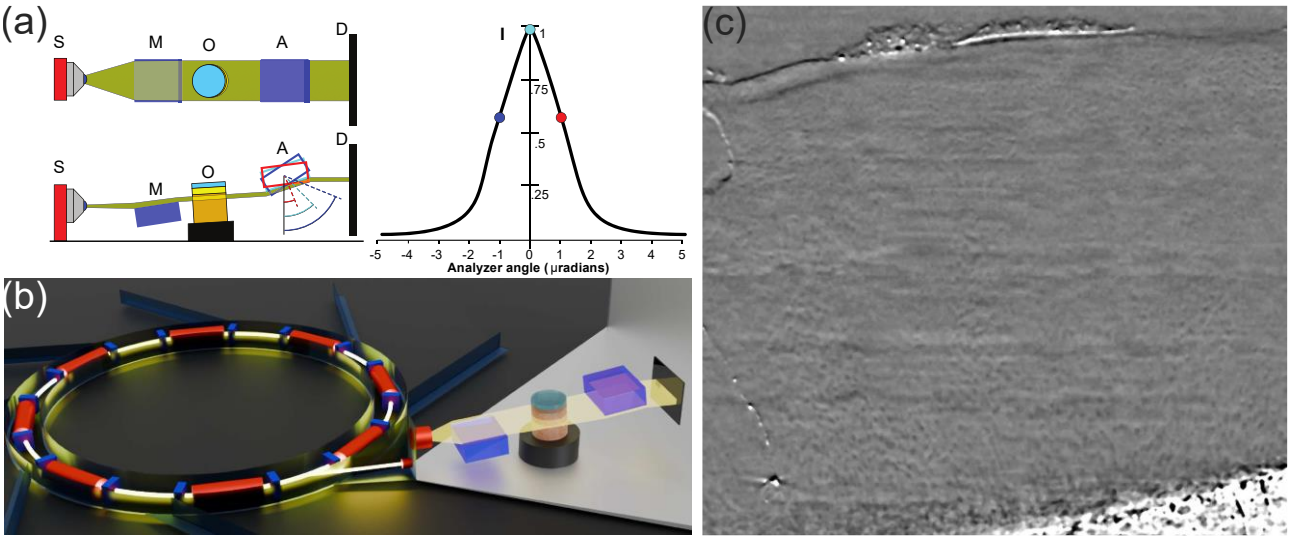

Figure 2.6. (a) Scheme of ABI. The insertion of the analyzer crystal A acts as an angular filter on the photons transmitted by the sample O. Only photons satisfying the angular acceptance, determined by the rocking curve (in the right bottom), are transmitted by the analyzer A and reach the detector D. (b) Three-dimensional rendering of a typical ABI setup. The ABI requires monochromatic and laminar X-ray beam, typically provided by synchrotron facilities. (c) Section from reconstructed ABI volume of healthy human AC. Margins of AC are highlighted, as well as the speckle pattern conferred by the distribution of chondrocytes' lacunae. Image adapted from the work of Nagarajan et al. [230], published under Creative Commons license (CC BY 4.0).

Additionally, if at least three images are acquired in different positions of the rocking curve, ABI allows the extraction of the scattering or dark-field (DF) signal, hence giving access to structures below the system's spatial resolution [232–234]. While ABI is usually associated with high image quality and quantitative accuracy, its use is mostly limited within SR facilities due to the need for intense monochromatic laminar beams. The mechanism behind the image formation of ABI is outlined in Figure 2.6.

The potential of ABI for AC depiction was explored in the first 2000s at different synchrotron facilities. Although the first images were radiographies impressed on radiographic film, they provided robust results in terms of discernability of soft tissues [235–240]. The positioning of the analyzer crystal was crucial for AC visualization. Depending on the analyzer tilting, only those photons emerging from the sample within the angular acceptance range of the rocking curve (order of few μrad) reach the image plane. Therefore, different structures in AC are highlighted at different angular positions of the analyzer, i.e. at different working positions on the rocking curve [241–246] (see Table 6). For example, if the peak of the rocking curve is chosen, only photons experiencing no or little deflection traversing the sample are transmitted by the analyzer, ensuring an optimal scatter rejection. Conversely, by setting the orientation of the analyzer crystal in one slope of the rocking curve, the system becomes sensitive to refracted photons, which are transmitted with a higher (lower)

probability if the refraction angle is towards the top (tail) of the rocking curve [241–243,246]. The overall effect of the analyzer orientation on AC radiographs is the edge enhancement of tissue boundaries and of highly oriented structures such as collagen, delineated as bright or dark fringes. Similarly, defects within AC are noticeable, and rendered differently depending on the analyzer angle [241,247].

With the advent of digital detectors, ABI shifted toward tomographic applications, enabling three-dimensional reconstructions of joints from various models, at superior spatial resolutions compared to CT and MRI [248–250]. The efficacy of ABI was also assessed on whole intact human knee joints, despite the prolonged exposure time and limited vertical aperture of the X- ray beam [251]. Aside from the clear distinction of macroscopic structures, ABI is also suitable for the imaging of AC microarchitecture. The high sensitivity to subtle changes in the refraction index allows for the depiction of collagen arcades [252] and lacunae [253], down to the spatial resolution of few µm. High-resolution ABI further enabled cellular characterization of healthy and osteoarthritic AC, distinguishing chondrocyte alignment, zonal distribution, and fibrillation [230,254–256] (see Figure 2.6c). Different algorithms of phase extraction from ABI images were also studied, and their performance was compared on a common AC sample. Weighting the advantages and pitfalls of the single approaches, those yielding the independent reconstruction of apparent absorption, refraction and scattering signals resulted in the best visualization [257,258]. Interestingly, several studies exploited ABI for its multimodal potential. Rather than the refraction component alone, Muehleman and colleagues applied the method known as multiple- image radiography (MIR) to the visualization of AC. MIR consists in the acquisition of multiple images (namely, more than three) at several positions of the rocking curve. By using eleven different crystal orientations, the researchers explored the suitability of MIR in detecting USAXS signal with high precision. Notably, the scattering image distinguished the connective tissues, owing to their inner collagen arrangement [259]. The latter approach was later extended to conventional and limited-angle tomography techniques [260].

Table 2.6. Summary of research papers including X-ray imaging of AC with ABI protocols, ordered from the most to the least recent. For each paper, the corresponding reference is reported, along with the model for the AC tissue, the size of the specimen, the source type, the energy E of the X-ray beam (m. monochromatic, q.m. quasi-monochromatic), the number of analyzer positions N_A, the acquisition time T and the voxel size of the reconstructed volume p.

ref.	model	size (mm)	source	E	N_A	T (min)	p (µm)
[238]	rat	NA	synchrotron	20-35 keV m.	NA	NA	9
[256]	human	NA	synchrotron	26 keV q.m.	NA	NA	8
[249]	rabbit	NA	synchrotron	51 keV m.	2	10-60	46
[248]	swine	NA	synchrotron	40 keV m.	5	NA	18.7
[230,255]	human	Ø 7	synchrotron	26 keV q.m.	NA	NA	8
[260]	human	NA	synchrotron	40 keV	25	NA	50
[236]	human	NA	synchrotron	40 keV m.	1	5	31.2
[261]	equine	80x35x30	X-ray tube	22.15 keV m.	17	NA	160; 153

[262]	human	NA	X-ray tube	22.15 keV m.	15	240	160; 153
[258]	human	Ø 7	synchrotron	26 keV m.	5	NA	16
[257]	human	Ø 8	synchrotron	25 keV m.	5	NA	16
[250]	guinea pig	NA	synchrotron	52 keV m.	NA	NA	47
[254]	human	Ø 7	synchrotron	26 keV m.	1	NA	8
[263]	human	NA	X-ray tube	59 keV m.	NA	NA	50
[251]	human	NA	synchrotron	51 keV m.	1	1380	56.2
[253]	human	Ø 2.6	synchrotron	20 keV m.	1	7000	3.6
[235]	murine	NA	synchrotron	15 keV m.	2	NA	NA
[237]	canine	NA	synchrotron	40 keV m.	3	NA	50
[259]	human	NA	synchrotron	40 keV m.	11	NA	NA
[239]	human	NA	synchrotron	NA	5	NA	NA
[247]	human	NA	synchrotron	20-50 keV m.	1-3	NA	NA
[240]	human	NA	synchrotron	30 keV m.	3	0.2	50
[246]	human	20	synchrotron	15 keV m.	NA	NA	50
[252]	human	40x60, Ø15	synchrotron	17/25 keV m.	NA	NA	5
[245]	human	NA	synchrotron	40 keV m.	2	NA	50
[244]	human	Ø 15	synchrotron	17 keV m.	NA	NA	NA
[243]	rabbit	NA	synchrotron	30 keV m.	3	NA	NA
[242]	human	NA	synchrotron	40 keV m.	5	10; 0.5	50-75
[241]	human	NA	synchrotron	18/30 keV m.	NA	0.07-0.1	50

Only few studies implemented ABI with table-top systems. The requisite of monochromaticity is satisfied also by kilovoltage tubes with the adoption of monochromator crystals, although the X-ray beam flux results severely reduced [262]. The refraction component clearly depicts AC from other soft tissues in intact joints, and distinguishes AC samples at different degradation stages, with results comparable to histology [261,263]. Nonetheless, the implementation of ABI to table-top systems remains the most challenging compared to other PC techniques.

2.1.3.3. Gratings interferometry

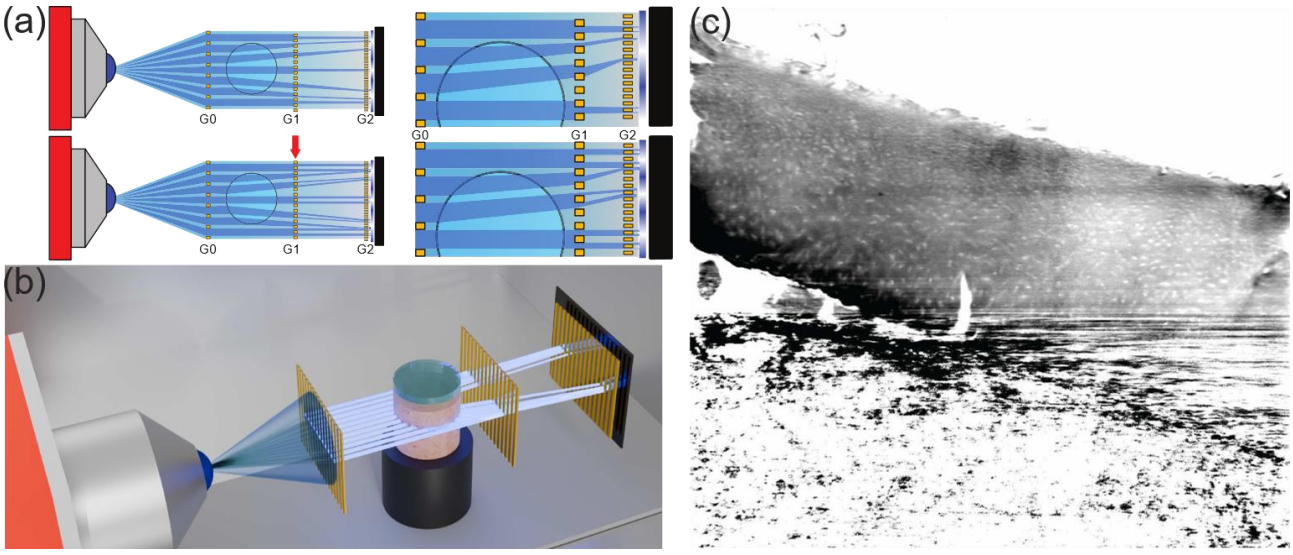

Figure 2.7. (a) Scheme of GI, in Talbot-Lau configuration. Provided the spatial coherence of the X-ray beam, only the sample gratings G1 and the detector gratings G2 are required. Otherwise, source gratings G0 are required, as in the depicted case. The distance of the detector gratings is determined according to the occurrence of the Talbot self-image

effect. The lateral shift of the detector gratings allows to collect the refraction and the scattering signals. (b) Three-dimensional rendering of a typical Talbot-Lau GI setup, featuring a conventional X-ray source (e.g., X-ray tube). (c) Section from reconstructed GI volume of healthy human AC. Within AC, spots featuring higher intensity are distinguishable, attributable to chondrocytes' lacunae. Image adapted from the work of Schulz et al. [264], published under Creative Commons license (CC BY 3.0).

Gratings interferometry (GI) is based on the Talbot self-image effect produced by regular periodic structures with a period in the order of a few micrometers, referred to as gratings, set along the direction of propagation of X-rays. Due to Fresnel diffraction, diffraction patterns with the same periodicity of the grating are formed at specific distances from the grating, which are equal to multiples of the Talbot distance [234]. The first GI studies exploited the spatially- coherent synchrotron X-ray beam and made use of two gratings, referred to as G1 and G2, generally positioned downstream from the sample [265,266]. The grating G1, referred to as phase-grating, is set close to the sample and it is made ideally of X-ray transparent materials, introducing a periodic phase-shift that is responsible for the Talbot diffraction pattern. The grating G2, referred to as absorption grating, is positioned at a multiple of the Talbot distance and acts as an analyzer, partially absorbing the X-rays. As a function of the relative displacement or misalignment of the two gratings, a modulation in the X-ray intensity recorded at the imaging plane is observed. Similarly to ABI, when a sample is introduced in the beam, the recorded intensity is modified according to sample's attenuation, phase, and scattering properties, which can be retrieved though dedicated algorithm [267]. In the wake of these SR-based results, Pfeiffer and colleagues successfully adapted GI to conventional low-brilliance X-ray sources [198]. To overcome the smearing of the diffraction pattern that would occur using a source with limited spatial coherence, a third absorption grating close to the source, is inserted in the so-called Talbot- Lau configuration. The source grating G0 generates a periodic array of repeated sharp line sources which are individually coherent despite being globally non-coherent. This arrangement produces a diffraction pattern which, as in the Talbot case, can be transformed into intensity modulations at the detector plane by displacing G1 and G2 [268]. The Talbot-Lau scheme for GI is displayed in Figure 2.7.

Table 2.7. Summary of research papers including X-ray imaging of AC with GI protocols, ordered from the most to the least recent. For each paper, the corresponding reference is reported, along with the model for the AC tissue, the size of the specimen S, the source type (Mo molybdenum, W tungsten), the focal spot size s_{FS} , the voltage V or associated energy E of the X-ray beam (m. monochromatic), the number of grating positions N_G, the acquisition time T and the voxel size of the reconstructed volume p.

ref.	model	S (mm)	source	S (µm)	V /E	N_G	T (min)	p (µm)
[269]	porcine	Ø 3	synchrotron	NA	20 keV m.	5	20	4.46
[270]	human	NA	X-ray tube (W)	400	40 kVp	NA	0.32	85
[271]	bovine	Ø 6	X-ray tube (Mo)	400	40 kVp	11	NA	41
[272]	human	Ø 5.4	X-ray tube	0.9-2.7	42 kVp	7	NA	23.3
			synchrotron		19 keV	NA	2.3	23.3

			synchrotron		52 keV	NA	5.1	23.3
[264]	human	Ø 5	synchrotron	NA	19 keV	5	NA	2.3
		Ø 5	X-ray tube	NA	40 kVp	5	NA	3
		entire knee	X-ray tube	NA	180 kVp		1020	65
[273]	human	Ø 5	X-ray tube	NA	52 keV	4	NA	5.1
		Ø 10	synchrotron	NA	19 keV	5	NA	2.3
[274]	human	NA	X-ray tube (W)	300	40 kVp	5	0.25	85
[275]	human	NA	X-ray tube (W)	450	40 kVp	3	19	85
[276]	human	NA	X-ray tube (W)	400	40 kVp	3	19	90
[277]	porcine	NA	X-ray tube (W)	300	49 kVp	NA	NA	NA
[278]	porcine	NA	X-ray tube (W)	300	49 kVp	NA	NA	NA
[279]	human	NA	X-ray tube (W)	300	40kVp	5	NA	85
[280]	chicken	NA	synchrotron	NA	17.5 keV m. 35 keV m.	NA	0.008	12
[281]	human	Ø 8	synchrotron	NA	32 keV m.	3	NA	16
[282]	human	NA	X-ray tube (W)	60	40 kVp	NA	NA	50
				300	40 kVp	16	NA	50
[283]	chicken	NA	X-ray tube (W)	300	40 kVp	NA	NA	NA
[284]	chicken	NA	X-ray tube (W)	300	40 kVp	NA	NA	NA
[285]	chicken	NA	X-ray tube (W)	300	40 kVp	NA	0.67	18

Since its inception, GI has been applied to the visualization of articular soft tissues. Synchrotron-radiation implementations of GI allowed a good delineation of the edges of AC [277,278,280]. Similarly, laboratory-based GI setups using polychromatic and non-pointlike focal spot sources has delivered differential PC images enabling the visualization of AC [283–285] (see Table 7). Advances in grating fabrication promoted the translation of GI to clinical settings, with ex-vivo studies on human metacarpophalangeal joints highlighting AC margins [274,276,279,282], followed by optimized low-dose in-vivo imaging of healthy volunteers [274–276,282]. More recently, a conventional X-ray tube-driven GI system has been tested for the assessment of rheumatoid arthritis, to ascertain its sensitivity to tissue alterations. Independent evaluations, namely MRI and clinical scores, have supported the results, suggesting that the GI apparatus distinguishes healthy AC from pathological tissue [270]. Albeit the promising results in terms of AC visibility, the works reported until now have focused on GI to radiography, as the tomographic implementation would raise further concerns on deposited dose.

In the research frame, the translation of GI to tomography delivers three-dimensional maps of absorption, refraction and scattering (or DF) components [272,281]. The refraction-enhanced highlighted AC microstructures such as chondrocyte clusters, while energy-dependent protocols enabled simultaneous imaging of mineralized and soft tissues [264,273] (see Figure 2.7c).

Grating interferometry imaging also reportedly revealed differences in collagen content between superficial and deep AC layers. These variations reflect the gradient of electron density related to collagen content, making GI a quantitative tool complementary to state-of-the-art MRI maps. Interestingly, GI imaging is not prone to biases induced by variation in water content, unlike MRI. In

this aspect, GI could provide sound information of ECM integrity, regardless of the interstitial fluid [271].

2.1.3.4. Edge-illumination imaging

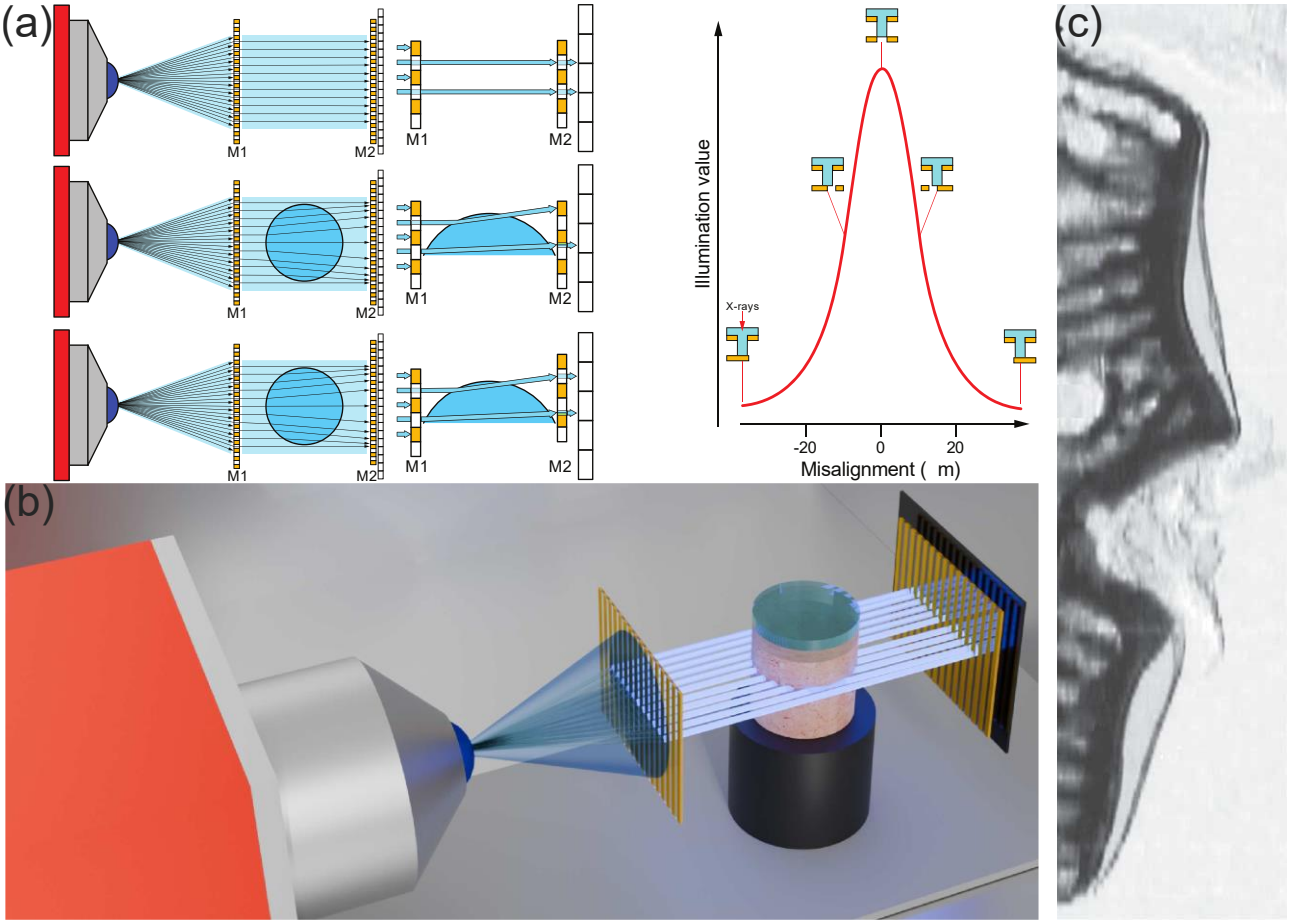

Figure 2.8. (a) Scheme of EI imaging. When illuminated, the sample mask M1 and the detector mask M2 produce an illumination pattern, replicating the periodicity of the masks. The overall effect of masks' lateral displacements on the intensity modulation of a single pixel is summarized by the illumination curve (in the bottom right). The insertion of the sample modifies the illumination pattern, according to interactions of different nature. In particular, the absorption, the refraction and the scattering of photons either attenuate, deviate or broaden the beamlets, and alter the modulation of the illumination curve. The lateral shift of the detector mask M2 allows the retrieval of those signals, as different sensitive areas of detector are differentially exposed. (b) Three-dimensional rendering of a typical EI setup. As reported in literature, nearly all experiments featured conventional X-ray sources (e.g., X-ray tubes). (c) Planar image of 1 mm-section from healthy murine osteochondral tissue. Besides the depiction of mineralized tissues (black structures), the interface of AC is clearly recognizable. Image adapted from the work of Marenzana et al. [286], published under Creative Commons license (CC BY 3.0).

Edge illumination (EI) imaging allows access to phase information by means of regular absorbing structures (i.e. masks) with a period in the order of tens of micrometers, positioned along the X-ray propagation direction [199]. A typical EI setup features two masks, positioned upstream of the sample (M1) and close to the detector (M2), respectively. Each mask is structured as a linear array of

absorbing material, such as gold, interleaved with X-ray transparent septa, or apertures, with a dimension of a few micrometers. Both masks share the same periodicity and aperture size, apart from the geometrical magnification factor depending on their relative position with respect to the X-ray source. The masks' period matches the detector pixel pitch, such that each periodic feature of the mask corresponds to one detector pixel column (or row). The role of the mask M1 is to structure the incoming X-ray beam into a series of independent, non- interfering narrow beams, or beamlets. In the absence of a sample, when the apertures of mask M2 are aligned with the apertures of M1, the beamlets are fully transmitted to the detector. If M1 and M2 are laterally displaced, the transmission decreases (ideally) reaching zero if the apertures are completely misaligned. The curve describing pixel-by-pixel the X-ray transmission across the two masks as a function of their lateral displacement is known as the illumination curve and plays a role conceptually analogous to the rocking curve in ABI. When a sample is introduced, the illumination curve is modulated in terms of area, due to X-ray absorption, lateral position, due to refraction, and width, due to scattering. A scheme of EI principles of image formation is shown in Figure 2.8. By using suitable retrieval algorithms and acquiring images at (at least) three positions on the illumination curve, all these effects can be uncoupled producing attenuation, phase and DF maps of the sample [287]. Although GI and EI share some similarities, EI is a non-interferometric technique as the beamlets are sufficiently spaced to be individually analyzed, hence not relying on the formation of diffraction patterns. As for the Talbot-Lau GI, the EI configuration does not require strict constraints on X-ray source coherence and it is implemented with commercial, polychromatic X-ray sources [184,287].

Table 2.8. Summary of research papers including X-ray imaging of AC with EI protocols, ordered from the most to the least recent. For each paper, the corresponding reference is reported, along with the model for the AC tissue, the size of the specimen, the source type, the voltage V or associated energy E of the X-ray beam (m. monochromatic), the number of mask positions N_M the acquisition time T , the voxel size of the reconstructed volume p and the object-to-distance ODD.

ref.	model	S (mm)	source	V /E	N_M	T (min)	p (μm)
[288]	chicken	NA	X-ray tube	40 kVp	NA	0.03	NA
[286]	murine	NA	X-ray tube	40 kVp	NA	NA	9
		NA	synchrotron	17 keV m.	NA	NA	5
[289]	rat	NA	X-ray tube	NA	NA	NA	NA
[290]	rat	NA	X-ray tube	40 kVp	4	1	20

In the context of AC imaging, EI has been mostly implemented within table-top systems (see Table 8). Notably, differently from all other mentioned techniques, the spatial resolution of an EI system is not related to the size of the X-ray focal spot or to the detector pixel size, but it is ultimately determined by the aperture size of the pre-sample mask, allowing an additional degree of flexibility in trading-off acquisition time and image quality [199,291,292]. The research group at University

College London, who pioneered EI, demonstrated the viability of EI implemented with uncollimated and non-microfocus X-ray tube, for the visualization of small lesions in rat AC [290]. Despite the relatively thin AC layer, EI images provided its visualization in both air and aqueous environments. The measurements of tissue thickness were comparable to CE- based studies and gold standard techniques, such as histology [286,289]. The yield in refraction images are comparable to synchrotron-based ABI system and confirms the soundness of using the refraction signal to highlight the AC layer [286] (see Figure 2.8c). One further implementation of EI has considered the insertion of a structured detector to replace the detector mask (M2), demonstrating a clear visualization of AC in refraction image, similarly to conventional EI setup [288].

2.1.4.Scattering-based X-ray imaging: dark-field imaging

Dark-field imaging conveys contrast from ultra small-angle X-ray scattering (USAXS) photons, which arise from the interaction of primary X-rays with microscopic structures in the sample. These structures are typically not resolved with conventional attenuation-based techniques, owing to insufficient spatial resolution or to the low radiopacity of the structures [268]. Under the ray tracing approximation, USAXS can be understood as the effect of multiple refraction causing locally a diffusion of the X-ray beam. The amount of diffusion can be traced back to quantities such as the average size of the scatterers or the scattering power of the sample, hence giving access to information at a spatial scale below the system's spatial resolution [268,293–295]. As anticipated in the previous subsections, many PC methods including ABI, GI, and EI give access to the scattering signal, generally at the cost of additional exposures at different positions of the optical element.

Table 2.9. Summary of research papers including X-ray imaging of AC with DF protocols, ordered from the most to the least recent. For each paper, the corresponding reference is reported, along with the model for the AC tissue, the size of the specimen S, the source type, the size of the focal spot s_{FS} (Cu copper), the voltage V or associated energy E of the X-ray beam (m. monochromatic, p.b. pink beam), the acquisition time T , the voxel size of the reconstructed volume p and the object-to-distance ODD. *detector pitch size

ref.	model	S (mm)	source	s_{FS} (µm)	V /E	T (min)	p (µm)
[296]	rabbit	1	X-ray tube (Cu)	350	8 keV m.	NA	1.1*
[297]	equine	2x0.5x0.5	synchrotron	NA	25 keV p.b.	5	0.8
			X-ray tube (Cu)	350	8 keV m.	NA	1.1*
[298]	human	NA	synchrotron	NA	20 keV m.	NA	7.4
					12 keV m.	NA	16
[293]	human	NA	synchrotron	NA	35 keV m.	NA	10
[299]	human	NA	synchrotron	NA	36 keV m.	0.92	NA
[300]	human	NA	synchrotron	NA	36 keV m.	NA	NA
[301]	human	NA	synchrotron	NA	34.8 keV m.	NA	NA
					33 keV m.	NA	NA
[302]	human	NA	synchrotron	NA	34.8 keV m.	NA	NA
[303]	human	NA	synchrotron	NA	35 keV m.	NA	10
[304]	human	NA	synchrotron	NA	15 keV m.	NA	NA

Dark-field has been explored as a complementary signal for assessing soft tissues, including AC, alongside PC refraction-based methods. Since the first studies, results demonstrated the ability of DF in depicting features of AC at a sub-pixel spatial resolution. Early applications included film-based DF radiographies acquired with the ABI technique, which highlighted the soft tissue components of excised human joints in different environmental conditions [293,298,303,304]. The same approach was followed also on intact joints, where the differentiation of AC structures resulted optimal, given a careful selection of orientations of the analyzer crystal [301,302]. In particular, different orientations conferred major contrast to AC contour or bulk [300]. Notwithstanding the promising results in radiography, the rather large number of frames required at different orientations of the analyzer significantly increases the radiation dose and the exposure time, thus limiting the translation of ABI-based DF imaging to SR-based CT (see Table 9). On the other hand, tomosynthesis approach requires fewer projection images, compared to CT, while giving a certain level of in-depth information. Notably, past works delivered DF tomosyntheses with doses equivalent to a single DF radiograph [299]. Recently, the feasibility of DF has been demonstrated on alternative experimental designs. Specifically, thanks to the beam-tracking technique, that is an EI variant making use of a high-resolution detector instead of the M2 mask [305], DF, refraction and attenuation images of AC could be obtained simultaneously [271]. From these images, authors speculated the visualization of collagen bundles. Further radiographs performed with the same imaging configuration properly visualized lacunae of AC [296]. Despite the two-dimensional nature, the cellular pattern was compatible to reference images from synchrotron-driven PBPC method and histology [297].

2.2. Towards the in-situ evaluation of articular cartilage

Originally conceived for trabecular bone characterization [306], DVC has been applied to various musculoskeletal tissues [307–310]. Its principles include the tracking recognizable voxel-intensity variations through sequential compression steps, the evaluation of displacement vectors, and the derivation of the strain tensor field [311]. In the case of AC, time-resolved rheologic experiments require multiple rapid tomographic scans, yielding speckled patterns obtained under different compressive steps. To the aims of DVC, the lacunae hosting chondrocytes serve as discrete patterns ideal for strain measurements. Such patterns can be highlighted with several approaches. In absorption mode, CAs such as the polyoxometalates enhance the contrast between the lacunae and the surrounding ECM [93], though fixation and staining alter the mechanical properties of the tissue.

Alternatively, staining protocols could lead to the preservation of the original mechanical behavior of AC [70,78]. Furthermore, DNA-binding stains enhance lacunae visibility [12], but require complex processing procedures and a severe downsizing of the sample. The combination of PC with CAs was also investigated to highlight features of AC and compensate the limited flux and coherence of laboratory microCT systems [60,221–227] (see Table 5). However, the limited X-ray flux implies prolonged scan times, with significant impact on AC properties and sample stability [208]. Synchrotron-radiation microCT overcomes these issues thanks to the availability of high flux X-ray beams.

For instance, a methodology to visualize and quantify cellular structures in compressed AC was recently proposed, along with a dedicated SR beamline [209]. In the same beamline, the compressive method with DVC was also implemented on murine model, and yielded the visualization of hierarchical changes in AC structures. The high spatial resolution reached (0.8 μm) allowed the calculation of displacements with accuracies below 100 nm in knees of healthy and osteoarthritic mice [210].

In addition to PBPC, the investigation of osteochondral samples under compression was accomplished with other PC methods. At the SPring-8 synchrotron facility in Japan, GI- microCT successfully resolved the cellular pattern of porcine AC, as confirmed by histology. The deformation of the cellular pattern served as input for DVC analysis. Remarkably, the density map of sample was shown to change accordingly to the imparted compression [269].

Despite the positive outcome of the above-described implementations, most studies making use of PC techniques require a scanning or stepping of optical elements. As a result, they are focused on imaging of AC in static configuration, because of the longer times related to acquisition procedures and the limited time-resolving capabilities of laboratory-based systems, associated to the limited X-ray flux. Interestingly, the time-resolved approach was successfully implemented with PBPC, exploiting monochromatic SR. Its implementation was demonstrated at TOMCAT beamline, at Paul Scherrer Institute in Switzerland, where a rheometric setup allowed the evaluation of dynamic behavior through time of unprocessed bovine AC samples [205]. The tomographic experiment took advantage of the shortest exposure time to date for the dynamic investigation of connective tissues, resulting in acquisition times ranging from 40 down to 5 seconds. The advantageous experimental condition achieved spatial resolutions compatible with the size of lacunae (2.75 μm), with nearly no radiation damage induced to the tissue. Notwithstanding the detrimental laminarization of the monochromatized beam, the experiment benefited from a field of view large enough to accommodate the whole AC (5.54x3.85 mm against 4-mm diameter samples). According to existing literature, PBPC is the most straight-forward implementation for rheometric measurements. It offers favorable

acquisition time and image quality, while keeping as low as possible the complexity of the experimental setup.

2.3. Benefits, challenges and future perspectives

The above discussed X-ray imaging techniques achieve optimal results in terms of contrast and detail discernability of AC, in a variety of models and experimental conditions. Nevertheless, the choice of the imaging approach should be tailored to the rationale of the investigation. The relatively large number of studies applying CAs reflects the straightforward implementation of CECT to AC imaging. The use of ionic CAs allows for a quantitative analysis of several components of AC (see Table 1). Nevertheless, their possible impact on tissue's mechanical properties draws concerns in rheologic applications. For instance, hyperosmolar CA solutions modifies tissue stiffness [312–314]. Furthermore, certain staining protocols alter the mechanical response of the tissue and introduce significant bias in rheometric evaluation of the whole osteochondral unit [70].

Additionally, the composition of CAs should be chosen to optimize the imaging outcome. The imaging protocol should include X-ray energies compatible with the absorption signature of the selected radiopaque element. In the context of spectral protocols, this aspect becomes more crucial. In fact, mixtures of CAs with different absorbing features facilitate the material discrimination [315]. Furthermore, the CA concentration should be carefully chosen to simultaneously yield the optimal contrast among details and reduce imaging artifacts. Despite its readiness, the use of CAs with conventional microCT scasnners could impair the segmentation of tissues with similar radiopacity, as in the case of contrast-enhanced AC and mineralized tissues [158].

Spectral approaches such as DE technique could circumvent the issue, yet facing several limitations. First, multiple acquisitions require volume co-registration in space or in time, whether images are collected with two sources at different spatial locations simultaneously, or with a single source at different time points, respectively. Second, the span of materials is restricted by the limited flexibility of spectra provided by conventional X-ray sources. Third, the material decomposition worsens if the number of materials entering the composition of the sample exceeds the beam energies [315]. Last, radiation dose increases with the number of energy exposures. Photon-counting detectors overcome these limitations, although their larger pixel sizes and/or smaller field-of-view limit the spatial resolution. The development of the latest PCD technologies (i.e., modular structure and advanced signal clustering) allows larger field of view, and a resolution finer than the pixel pitch [316,317].

Phase-contrast techniques enable the visualization of several structures in AC (namely collagen arcades, lacunae and even chondrocytes) [54,200,205,216,254,256,264,269,273] without exogenous

CAs, though most approaches require high-brilliance sources, ad-hoc optics, or their combination. Propagation-based PC is the most promising method for rheologic evaluation of AC, provided the implementation with SR [205]. The same considerations apply to ABI, plus the additional limitations related to the use of monochromatic X-ray beams, laminar geometry and the need for multiple scans at different analyzer orientations. Similarly to ABI, GI is a multimodal approach sensitive to refraction and scattering signals, delivering promising results in-vivo [270]. In research-oriented applications, GI allows for the visualization of cellular patterns in AC, pushing its applications to in-situ testing of AC [269]. Nonetheless, high-end applications of GI make the implementation with SR essential, to compensate for the prolonged acquisition times associated with multiple-frame grating stepping. The rigorous requirements on X-ray beam decay for non-interferometric EI, as it is easily implemented to compact laboratory-based systems. Furthermore, EI potentially retrieves phase information with only two images, by illuminating the pixels at their opposite sides, compared to GI method [318]. Nevertheless, studies adopting EI for AC imaging are the minority, with no reported experience on in-situ evaluations. Focusing on the scattering signal, DF imaging is still under development, specifically for AC evaluation. Despite the unique nature of the signal, DF imaging has been mainly limited to plain radiographs or tomosynthesis only, as the tomographic approach would significantly increase the acquisition times and the dose fractions.

Aside from in-depth analysis of the single techniques, more general observations arise by considering the examined literature. In general, high resolution is obtained at the cost of reduced sample size, increased photon fluxes and greater radiation doses. Furthermore, the evaluation of mechanical response requires volumes representative of the whole tissue (i.e., ECM), rather than single structures (i.e., collagen bundles). Recently, an imaging protocol has been proposed as optimal trade-off between the sample size and spatial resolution for the visualization of lacunae, in the context of time-resolved in-situ imaging [205].

Another concern arises from the time of exposure to radiation. The scanning time of each technique is largely dependent on the X-ray source characteristics, the presence of optical elements and the geometrical configuration. Synchrotron-radiation generally ensures the fastest exposure times, especially when the full spectrum (i.e., white beam) is used coupled to the PBPC technique. Conversely, the installation of any optical element in the beam generally leads to longer exposure times both at synchrotrons and laboratory-based systems.

Radiation dose remains a major concern. Planar and tomosynthesis studies report mGy- level exposures compatible with clinical translation [215,251,275,279,298], while tomographic experiments may reach several Gy, inducing macroscopic (namely, heating of the sample) [93,319] and microscopic (namely, degradation of ECM, oxidative stress, and cellular degeneration) effects

[60,168,169,205,215,251] (see Table S4 in Supplementary Material for dose values). Furthemore, the evaluation of the whole osteochondral unit should consider significant effect of prolonged X- ray exposures on bone tissues [320,321]. Therefore, any rheologic experiment should consider cryogenic expedients compensating the progressive dose deposition, with special mention to SR studies.

Aside from rheologic applications, more relaxed experimental conditions for AC imaging meet the use of multimodal laboratory-based X-ray systems. Preliminary experiences retrieved successfully attenuation, differential PC and DF channels on biological samples [184]. Similarly to the multimodal X-ray system involved in the work of Olivo et al., the equipment installed at PEPILab features specifications meeting the depiction of AC structures. In the perspective of preclinical applications, a CT prototype has been developed to deliver USAXS images. Its application to lung evaluation on healthy humans and patients with pulmonary disorders yielded results comparable to conventional radiography [322,323]. Analogously, applications of DF could be extended to musculoskeletal imaging. For instance, articular soft tissues might be distinguished, as well as their alteration, thanks to the subpixel spatial resolution inferred by gratings configuration.

2.4. Conclusions

The present scoping review focused on X-ray techniques adopted for AC imaging. One of the main differentiations accounts for the prompt implementation of these approaches with either commercial systems or synchrotron-driven setups. In the first case, CE techniques can be easily implemented with radiopaque CAs. Nonetheless, the use of CAs might alter the pristine properties of the tissue. Conversely, PC methods do not imply any alteration of AC nature, but require stringent specifications for the X-ray source. The sought-after coherence of the X- ray beam, crucial for PC imaging, is achieved with SR. Thanks to the latter implementation, various optical configurations retrieve valuable information of AC, down to the cellular scale. Regardless of the intrinsic contrast enhancement associated with PC, the limited access to SR facilities hinders the full unfolding of refraction-based imaging modalities. A promising option makes use of conventional X-ray sources, together with suitable optical elements. Still, the low brilliance of conventional sources significantly increases the acquisition times. Lastly, the scattering information associated with DF is still under investigation for various biomedical applications, including the musculoskeletal system.

The context becomes further intricated in case rheologic studies are considered. Among the approaches here discussed, PC methods provide visual and quantitative information. According to the existing literature, PBPC and GI successfully depict the inner structures of AC and enable their implementation to DVC analysis. More in detail, PBPC features the shortest acquisition time to

resolve the microscopic lacunae. On the contrary, GI and, in general, PC methods based on optical elements leads to increased exposure times, raising concerns on the deposited radiation dose and sample stability. At present, this limits rheologic evaluation of AC samples mostly to synchrotron-based experiments. However, the development of novel synchrotron-like X-ray sources with sources with a smaller footprint and cost, such as laser-driven system of liquid- metal jet sources, hold the promise to impact AC imaging, enabling advanced applications, such as rheology, in compact laboratory environment.

CHAPTER 3

Contrast-enhanced X-ray imaging of articular cartilage: impact, reversibility and reliability of a cationic contrast agent

The present Chapter reports activities related to contrast-enhanced X-ray imaging. As already mentioned in Chapter 2, the use of contrast agents circumvents the inherent lack of sensitivity to soft tissues. Besides the enhanced discernibility of the overall tissue, inner structures can be highlighted, depending on the nature of the interaction between the contrast agent and the targeted component. In the case of ionic contrast agents, their molecules interact with proteoglycans, owing to the negative fixed charge of the latter. According to existing literature, cationic contrast agents provide superior results compared to anionic formulations. Among all proposed molecules, CA4+ succeeded in properly assessing the proteoglycan content of articular cartilage. Despite its experimental nature, CA4+ proved promising findings in preclinical studies, assessing both healthy and degenerated articular cartilage in a variety of models. The use of CA4+ was favourable for the evaluation of the cellular pattern as well.

In light of such evidence, applications oriented to in-situ mechanical assessment of the tissue could take advantage of the use of CA4+. Nevertheless, several aspects have not been deepened yet. For instance, the use of CA4+ could imply non-negligible effects on articular cartilage, including its mechanical response. Furthermore, the potential retention of CA4+ could be deleterious in the context of in-vivo studies or concurrent analysis with alternative methods (e.g., histology). Such critical aspects were investigated, as outlined hereafter:

- The impact of CA4+ on the mechanical response of articular cartilage was sifted, aiming at ascertaining the suitability of CA4+-based contrast-enhanced protocol to in-situ mechanical applications (Chapter 3, Section 1).
- The reversibility of effects induced by CA4+ on the mechanical behaviour of articular cartilage was investigated to confirm the viability of CA4+ for research-oriented purposes. Aspects such as the complete desorption and restoration of tissue properties were also deepened (Chapter 3, Section 2).
- The test of reliability of contrast-enhanced X-ray imaging of articular cartilage, performed with high-resolution peripheral quantitative computed tomography (HR-pQCT), sought for correlations between imaging data and the mechanical behaviour of the tissue (Chapter 3, Section 3).

Section 1

Assessment of CA4+ impact on mechanical properties of articular cartilage

This section was reproduced from the published manuscript:

"Assessment of CA4+ Impact on Mechanical Properties of Articular Cartilage"
M. Berni, S. Fantoni, R. Fognani, P. Cardarelli, F. Baruffaldi and M. Baleani
Materials, 18(13):2943 (2025). DOI: 10.3390/ma18132943

Contribution disclosure

This study was performed with the support of the Medical Technology Laboratory of IRCCS Istituto Ortopedico Rizzoli, under the supervision of Mr. Massimiliano Baleani. The candidate Simone Fantoni and Dr. Matteo Berni contributed equally to conceptualization, experimental design and execution, and formal data analysis.

Abstract

X-ray imaging of articular cartilage could be a breakthrough for the early diagnosis of tissue degeneration. This approach relies on radiopaque contrast agents to enhance the visualization of soft tissues. The potential impact of contrast agents on the mechanical response of articular cartilage should be considered in the frame of both clinical and research applications. Attention has been drawn to a solution containing molecules with six iodine atoms and four positive charges (CA4+), which has been shown to improve the X-ray visibility of articular cartilage. This study aimed to determine the effects of a CA4+ solution on tissues' mechanical properties. An experimental pipeline based on indentation tests was applied to paired samples of articular cartilage before and after the immersion in either CA4+ or phosphate-buffered saline solution, maintained at a temperature of 22 ± 2 °C, for 22 h to determine the differences in instantaneous, viscous, and equilibrium responses between the articular cartilage of the two groups. The 22 h immersion of articular cartilage in either CA4+ or phosphate-buffered saline solution had a significant detrimental effect on the overall response, including the instantaneous, viscous, and equilibrium responses, of the articular cartilage. However, this detrimental effect was greater with exposure to the CA4+ solution. Specifically, the articular cartilage was found to be less stiff in both the instantaneous response (approximately −25%) and the equilibrium response (approximately −38%). The softening effect could be attributable to an alteration of the interaction between the proteoglycans of articular cartilage, induced by the positive charges within the CA4+ contrast agent. Further investigations are needed to elucidate whether this hypothesised mechanism is reversible.

3.1.1.Introduction

Articular cartilage (AC) is an avascular and aneural tissue that covers the ends of opposing bone segments in diarthroses. Its unique mechanical properties, including the absorption of shocks and distribution of articular contact pressure during locomotion, derive from the interplay between phases, a solid matrix, and an interstitial fluid [324]. The main components of the solid matrix are bundles of collagen fibrils and proteoglycans (PGs), the most abundant of which are aggrecans. The three-dimensional arrangement and concentration of collagen and PGs define the extracellular matrix (ECM) [325], in which a small population of chondrocytes is embedded. The interstitial fluid is primarily composed of water and dissolved electrolytes (mainly Na+ ions) [326].

The response of such a complex structure to the sudden application of a localised pressure to the articular surface must be split into an instantaneous flow-independent and a flow-dependent viscoelastic response [325]. The instantaneous response is determined by the rapid localised deformation of the ECM, resulting in the localised tensioning of the collagen network in the superficial zone [327], reorientation of collagen network in the deep zone [328], and an increase in both the mutual repulsive force of glycosaminoglycans [326] and fluid pressure [329,330]. The localised increase in the fluid pressure drives interstitial fluid flow through the porous ECM and outward across the AC tissue over time. This process continues until the equilibrium between the applied load and the tissue reaction is reached, at which point the fluid flow ceases [56,331]. For the purposes of this study, it is also important to note that the fixed charge density (FCD) of the AC provides an osmotic pressure [332] counterbalanced by the restraining stress in the collagen network. The osmotic pressure, together with the mutual electrostatic repulsion between the PGs, determines the swelling of the AC tissue [325].

The degeneration of the complex structure of AC tissue, whatever the cause, can result in pain and loss of joint function, e.g., as occurs with the onset of osteoarthritis [333]. X-ray imaging is a diagnostic tool commonly used in the evaluation of a wide range of musculoskeletal disorders. However, the X-ray visibility of AC tissue is impaired by its low radiopacity. Two approaches have been proposed for enhancing the X-ray visualization of AC tissue: X-ray phase-contrast imaging and the use of contrast agents (CAs). Although different streams of X-ray phase imaging, e.g., propagation-based, diffraction-enhanced, edge-illumination, and grating interferometry, can be found in the literature [215,254,273,286], almost none have been successfully translated to clinical applications in the management of joint pathologies. Notably, a clinical system implemented with grating interferometry distinguished AC alterations in the metacarpophalangeal joints of patients affected by rheumatoid arthritis [275]. Despite these promising results, its effectiveness on other joints remains untested. On the other hand, CAs are selected for a specific imaging target depending

on the tissue composition [64]. Limited to AC, the imaging outcome strictly depends on the net charge of the molecule composing the considered CA [334]. CAs can be categorised as ionic and non-ionic, based on whether the single molecule carries a net charge or is electrostatically neutral. Ionic CAs can be further subdivided into anionic and cationic, depending on whether the displayed charge is negative or positive, respectively. Non-ionic and anionic CAs have been extensively tested for AC X-ray imaging [90,154,160,189,190,335–339]. Despite their safety certified by regulatory bodies, clinical use of anionic and non-ionic CAs require considerable concentrations, due to the indirect correlation between their distribution and the AC composition cartilage (namely, a direct correlation with water content and an inverse correlation with PGs) [154,160,338,339]. An experimental cationic iodine-based CA, referred to as CA4+, was specifically developed to be electrostatically attracted by the PGs of cartilage tissue [116]. The preliminary results regarding the safety and toxicity of CA4+ are encouraging [116]. Additionally, significant correlations have been reported between the mechanical properties and CA4+-enhanced imaging features on different AC models and several X-ray imaging systems [101,116,128,147,165,167,169,180]. Indeed, CA4+ permeates within AC, in concentrations directly proportional to the PG content [116,128]. However, the exposure of AC tissue to CAs has already highlighted a significant effect on tissue mechanical properties [313]. Therefore, the impact of any new contrast agent, such as CA4+, on tissue mechanics should be thoroughly investigated before its use in clinical practice or biomechanical research, as alterations to the mechanical properties of AC may affect joint function or experimental outcomes.

The aim of this study was to investigate the possible effects of CA4+ on the mechanical behavior of AC tissue. Indentation tests were performed on AC samples exposed to CA4+ to determine the instantaneous, viscous, and equilibrium behavior of the tissue. The results were compared to the behavior of a control group, which underwent the same experimental protocol except for the exposure to the CA.

3.1.2.Materials and Methods

3.1.2.1. Preparation of contrast agent solution

The CA used in the present work is CA4+ (5,50-[Malonylbis(azanediyl)]bis[N1,N3-bis(2-aminoethyl)-2,4,6-triiodoisophthalamide] chloride). CA4+ molecules include six iodine atoms each. They have the following characteristics: molecular weight mw = 1354 g/mol, iodine fraction per molecule f = 0.5084, net positive charge q = +4. Therefore, CA4+ molecules are electrostatically attracted to the negative FCD of PGs.

Synthesis of CA4+ salts was carried out according to the work of Stewart et al. [116]. CA4+ solution was prepared dissolving its salts in phosphate-buffered saline (PBS) solution (7.4 pH, Life

Technologies Europe B.V., Bleiswijk, The Netherlands), to obtain a concentration of 10 mgI/mL. This value is lower than the 12 mgI/mL used in the aforementioned study. The rationale for this reduction is that a concentration of 10 mgI/mL has been proven effective in achieving the X-ray attenuation of AC [83]. Using a lower salt concentration to enhance AC radiopacity may reduce the risk of a possible impact on tissue and side effects in patients. The pH of the obtained solution was adjusted to a value of 7.4 by adding NaOH 4 M. The osmolality (osmometer TypM 10/25 µL, accuracy 1 mOsm/kg, Löser Messtechnik, Berlin, Germany) of the CA4+ solution was 419 mOsm/kg. For comparison, the osmolality of the PBS solution was 307 mOsm/kg.

3.1.2.2. Extraction of osteochondral tissue samples

Parallelepiped shaped samples, approximatively 20 mm in thickness, were excised from fresh tibiofemoral surfaces of bovine stifle joints obtained from a local slaughterhouse within 24 h of slaughter. The parallelepiped shaped samples were taken from regions with different AC thicknesses to capture the full spectrum of thicknesses, and from both the femur and tibia to represent the entire joint. After excision, parallelepiped shaped samples were wrapped in gauzes soaked in PBS solution and frozen at T = −20 °C (first freezing cycle). After thawing in PBS at 4 °C for one hour, osteochondral (OC) cores—10 mm in diameter—were extracted from each excised parallelepiped shaped sample. Depending on its size, two or four OC cores were extracted from each parallelepiped shaped sample. OC cores were extracted by means of a computer numerically controlled milling machine (ProLight 2000, Light Machines Corporation, Manchester, NH, USA) equipped with a diamond-coated coring tool with a 10 mm inner diameter. The parallelepiped shaped sample was kept fully immersed in PBS solution at room temperature during the process. OC cores were extracted at points where the surface was as flat as possible, perpendicular to the local articular surface. Each OC core was cut on the trabecular bone side to adjust its height to approximately 10 mm. Therefore, each OC core included AC tissue, subchondral, and trabecular bone. OC cores from adjacent locations were paired. A total of 36 matched pairs of OC cores were extracted. For each pair of OC cores, one was randomly assigned to the CA4+ treated (contrast-enhanced CE) group while the other was assigned to the PBS-treated (Control) group. After harvesting, each OC core was enveloped in PBS-soaked gauze and frozen at T = −20 °C until Parallelepiped indentation test (second freezing cycle).

3.1.2.3. Indentation tests

Subgroups of six OC cores were thawed in PBS solution at T = 4 °C overnight. The AC thickness was measured prior to testing. Each OC core was blotted from any excess of PBS solution and placed in a custom-made polymethyl methacrylate sample holder. Four planar images of each OC core were

acquired via X-ray μCT system (SkyScan 1072, SkyScan, Aartselaar, Belgium), each after a 90– rotation of the sample (X-ray tube voltage = 50 kV, current = 197 μA, 1-cm Al filter, pixel size = 11.5 μm, exposure time = 5.9 s). AC thickness was determined using a custom-made MATLAB code (MATLAB version R2022b, MathWorks, Natick, MA, USA), according to the following steps: (i) preliminary crop of planar images to exclude residual portion of the sample holder; (ii) differentiation of AC layer from mineralised tissue and air; (iii) binarization of AC layer; (iv) exclusion of possible spurious pixels; (v) counting of the number of pixels within the AC layer in the vertical direction. The counting was limited to a 10 pixel-thick peripheral annulus of the AC layer to avoid the inevitable overlap caused by projecting the 3D curved layer onto the planar image, which could introduce errors to the thickness calculation; (vi) averaging the calculated values over the four planar images.

The six OC cores were then placed in a custom-made polyacetal sample holder with six cavities, with an inner diameter of 10 mm and depth of 20 mm. Before placing the OC cores in the cavities, a small amount of polymethyl methacrylate was poured into the bottom of each cavity to constrain the core on the trabecular bone side, and a silicone-based grease was applied to the lateral surface of AC. It has been proven that a small continuous amount of grease around the entire circumference prevents any leakage of aqueous solution into the small gap between the edge of AC and the inner surface of the cylindrical cavity [83]. Then, 0.5 mL of PBS solution was added to each cavity, i.e., on the top surface of the OC cores, to keep the AC wet. The sample holder was mounted on the X-Y motorised table of the testing machine (Mach-1 V500css, Biomomentum Inc., Laval, QC, Canada). Each OC core underwent the following procedure: (i) a preliminary indentation to precondition the AC tissue, (ii) three indentations, each performed after a resting period of 40 min, (iii) resting for 22 h at a temperature of 22 ± 2 °C, to ensure that diffusion equilibrium had been reached [83] while keeping the sample mounted on the testing machine to ensure that the indentation test is performed in the same position, after replacing the PBS solution with 0.5 mL of CA4+ (CE group) or fresh PBS solution (Control group), (iv) an additional preliminary indentation, (v) three indentations, each performed after a resting period of 40 min (see Figure S1 in the Supplementary Materials Section). This two-groups experimental design was necessary to distinguish the effect of CA4+ from any modifications in the mechanical response of the AC due to tissue alterations over time. The entire process for each subgroup of six OC cores took 30 h, during which the OC cores were kept at room temperature [340].

The indentation test involved applying a 6 mm spherical indenter perpendicular to the articular surface of the OC core (see Figure S2 in the Supplementary Materials Section) at deformation rate of 0.15 s−1, i.e., 15%/s. To ensure consistent preloading at the start of the indentation test, the initial contact between the indenter and AC was defined using a load-based criterion, i.e., when the load

reached 70 mN. The test was conducted to achieve a maximum nominal deformation equal to 15% of AC thickness at the centre of the OC core [341]. The nominal deformation was maintained for 300 s [342] to monitor the stress response over time (relaxation test). A pilot study had previously been carried out to verify that this duration would result in a negligible load relaxation rate (<0.01 N/s) by the end of the period. The above reported protocol was used for both the preliminary indentation and the three indentations employed to determine the mechanical properties of AC (see Figure S1 in the Supplementary Materials Section). The instantaneous response of AC was evaluated in terms of maximum reaction load (S_0) reached during indentation, and instantaneous elastic modulus (E_0). S_0 was measured experimentally by the multiple-axis load cell (accuracy 1% within the measurement range). E_0 was calculated by fitting the load-displacement indentation curve to the Hayes model [343], by setting the Poisson's ratio to 0.45 [344]. The viscous behavior of the AC was evaluated in terms of load decay, starting from the beginning of the test, and speed at which the equilibrium was reached. This behavior was quantified by the time constant (τ) and the stretching parameter (β) of a stretched exponential function [345] used to fit the load–time relaxation curve (see Appendix A). Such a function was implemented by minimizing the root mean square error through a custom-made MATLAB script. The fluid flow-independent property of AC, i.e., when all fluid flow has ceased, was evaluated in term of equilibrium modulus (E_{eq}). Eeq was calculated using the Hayes equation, based on the load measured experimentally by the load cell at equilibrium, i.e., 300 s after the start of the indentation test, and considering the involved geometries [342]. In calculating E_{eq} of AC, a Poisson's ratio of 0.3 was assumed [346,347]. All the values of the five parameters (S_0, E_0, τ, β, E_{eq}) were normalised to the value measured in the first indentation test to determine the percentage change between subsequent indentation tests.

3.1.2.4. Statistical analysis

Differences in AC thickness between the CE and Control groups were assessed using the Wilcoxon signed-rank test.

Differences in S_0, E_0, τ, β, or E_{eq} values measured during the first indentation between the CE and Control groups were also evaluated with the Wilcoxon signed-rank test.

Any upward or downward trend in S_0, E_0, τ, β, or E_{eq} values measured during the first three indentations, i.e., before 22 h of immersion in solution, or the second three indentations, i.e., after 22 h of immersion in solution, were assessed using the Friedman test.

The effect of 22 h immersion in solution on the mechanical behavior of the AC within each group was investigated by applying the Mann–Whitney signed-rank test to the normalised values of S_0, E_0, τ, β, or E_{eq}, i.e., the changes in the values of the five parameters between the two series expressed as

per cent of the initial value (percentage change). Finally, the effect of the CA4+ solution was analyzed by applying the Mann–Whitney test to compare the percentage changes between the CE and Control groups.

3.1.3.Results

The AC thickness values of OC cores for the CE group and Control group were in the range of 0.8–3.1 mm and 0.8–3.0 mm, respectively. No significant difference was found between the two groups (CE group median thickness 1.5 mm, Control group median thickness 1.4 mm, Wilcoxon signed-rank test: $p = 0.82$). By considering a sphere-plane Hertzian contact, the contact radius (a) was calculated to be in the range of 0.8–1.6 mm. Since the AC area affected by indentation extends to less than 3a [341]—which in our series was always smaller than the OC core radius—boundary effects were unlikely to influence the AC tissue response to indentation.

A total of 432 indentation tests were performed, neglecting the preconditioning procedure of AC tissue. The indentation procedure on the untreated AC tissue appeared to be repeatable, as evidenced by the coefficient of variation calculated for the five mechanical parameters (Table 3.1).

Table 3.1. Distribution of the coefficient of variation for the five mechanical parameters across the first three indentation tests (untreated AC tissue).

Percentile	CE Group					Control Group				
	S_0	E_0	τ	β	E_{eq}	S_0	E_0	τ	β	E_{eq}
5^{th}	0.3	0.6	0.4	0.1	0.5	0.6	0.4	0.2	0.1	0.5
25^{th}	0.7	1.3	0.8	0.3	1.0	0.9	1.0	0.8	0.3	1.3
50^{th}	1.3	1.6	1.3	0.5	2.1	1.6	1.9	1.4	0.4	2.2
75^{th}	2.9	3.1	2.8	0.7	3.5	1.9	2.8	2.6	0.7	3.2
95^{th}	6.4	8.0	5.4	1.3	8.5	3.3	4.1	8.0	1.5	4.2

The mechanical response of the AC tissue of the 72 OC cores measured during the first indentation differed by up to an order of magnitude. The range of variability, including the minimum and maximum values, of the computed mechanical parameters are reported in the following: S_0: 0.7–9.9 N; E_0: 0.6–28.9 MPa; τ: 1.0–15.4 s; β: 0.326–0.657; E_{eq}: 0.1–1.2 MPa. No difference was found between the two groups in the S_0 (Wilcoxon signed-rank test: $p = 0.24$), E_0 (Wilcoxon signed-rank test: $p = 0.73$), τ (Wilcoxon signed-rank test: $p = 0.27$), β (Wilcoxon signed-rank test: $p = 0.85$), and E_{eq} (Wilcoxon signed-rank test: $p = 0.08$) values measured during the first indentation.

No significant trends over test repetitions were found in the first three or the second three indentations in both the CE and Control group for all calculated parameters, except E_{eq}: E_{eq} values showed a small, but systematic, downward trend in both the first three and the second three indentations regardless of the group (Friedman test: $p < 0.001$ in all four cases). The downward trend was similar for the two groups in the first three repetition (median reduction between the first and the third indentations about 3%), as was the reduction observed in the CE group in the second three indentations (median reduction between the fourth and the sixth indentations about 3%) The reduction observed in the Control group in the second three indentations was a few percentage points greater (median reduction between the fourth and sixth indentation about 8%). To exclude the effect of such a downward trend, the effect of CA4+ on E_{eq} was calculated as the differences between the medians of the 36 values of the third and fourth indentation sets. Normalised parameter trends across tests are shown in Figures 3.1–3.3.

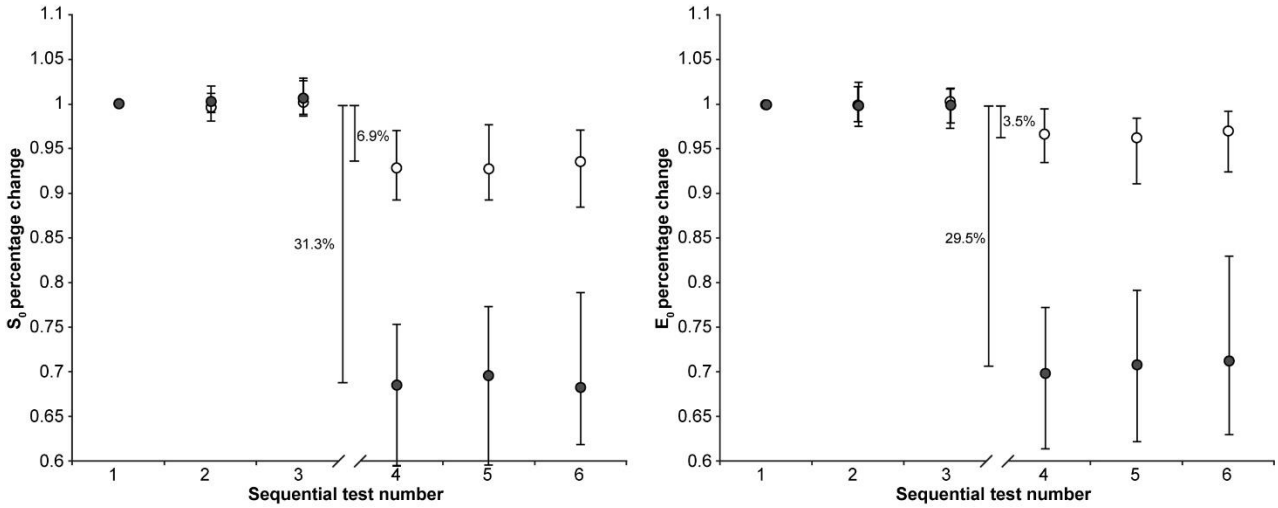

Figure 3.1. The median (markers), 75th percentile (upper edge of error bars), and 25th percentile (lower edge of error bars) of the percentage changes in S_0 (a) and E_0 values (b) before (1st, 2nd, and 3rd indentation test) and after (4th, 5th, and 6th indentation test) 22 hours of immersion in solution are shown (grey markers: CE group; white markers: Control group). The values shown in the figure were calculated as the differences between the medians of the 108 values measured in the first three and the 108 values measured in the second set of indentation tests.

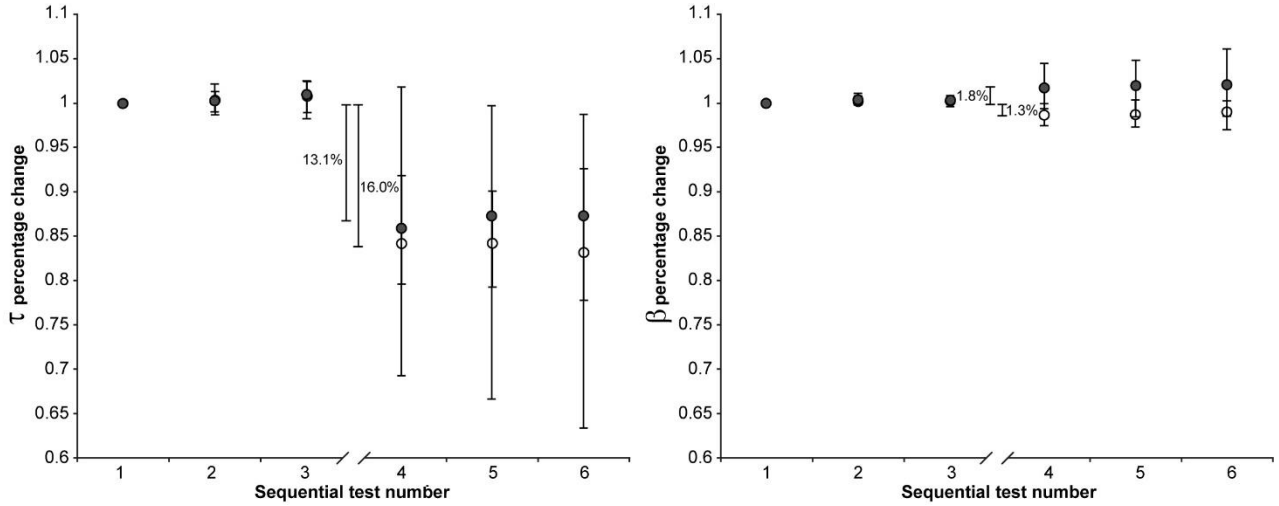

Figure 3.2. The median (markers), 75th percentile (upper edge of error bars), and 25th percentile (lower edge of error bars) of the percentage changes in τ (a) and β values (b) before (1st, 2nd, and 3rd indentation test) and after (4th, 5th, and 6th indentation test) 22 h of immersion in solution are shown (grey markers: CE group; white markers: Control group). The values shown in the figure were calculated as the differences between the medians of the 108 values measured in the first three and the 108 values measured in the second set of indentation tests. Reproduced under the terms of the CC BY 4.0 license. © 2025 Berni et al.

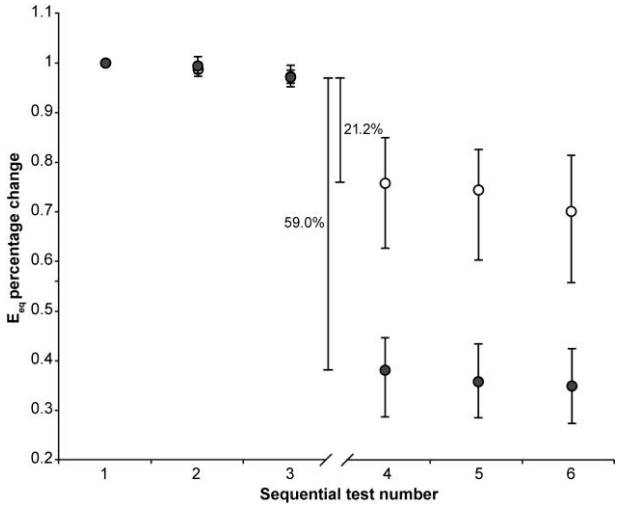

Figure 3.3. The median (markers), 75th percentile (upper edge of error bars), and 25th percentile (lower edge of error bars) of the percentage changes in E_{eq} values before (1st, 2nd, and 3rd in-dentation test) and after (4th, 5th, and 6th indentation test) 22 h of immersion in solution are shown (grey markers: CE group; white markers: Control group). The values shown in the figure were calculated as the differences between the medians of the 36 values measured in the third and the 36 values measured in the fourth set of indentation tests to exclude the effect of the downward trend. Reproduced under the terms of the CC BY 4.0 license. © 2025 Berni et al.

The 22 h immersion of AC in the CA4+ solution had the following significant effects (Mann–Whitney signed-rank test: $p < 0.001$ in all five cases): 31.3% reduction in S_0, 29.5% reduction in E_0, 13.1% reduction in τ, 1.8% increase in β, 59.0% reduction in E_{eq}, with the latter calculated as the difference between the medians of the 3rd and 4th indentation tests.

On the other hand, keeping the AC immersed in the PBS solution had the following significant effects (Mann–Whitney signed-rank test: $p < 0.001$ in all five cases): 6.9% reduction in S_0, 3.5% reduction

in E_0, 16.0% reduction in τ, 1.3% reduction in β, 21.2% reduction in E_{eq}, with the latter calculated as the difference between the medians of the 3rd and 4th indentation tests.

When comparing the percentage changes between the two groups, immersion in CA4+ solution led to the following significant differences relative to immersion in PBS solution: a 24.4% reduction in S_0 (Mann–Whitney: $p < 0.001$), a 26.0% reduction in E_0 (Mann–Whitney: $p < 0.001$), 37.8% reduction in and E_{eq} (Mann–Whitney: $p < 0.001$), and a 3.1% increase in β (Mann–Whitney: $p < 0.001$). No significant difference was found in the τ values between the two groups (Mann–Whitney: $p = 0.76$). Figure 3.4 is representative of the response measured on matched paired OC cores after 22 h of immersion in CA4+ or PBS solution.

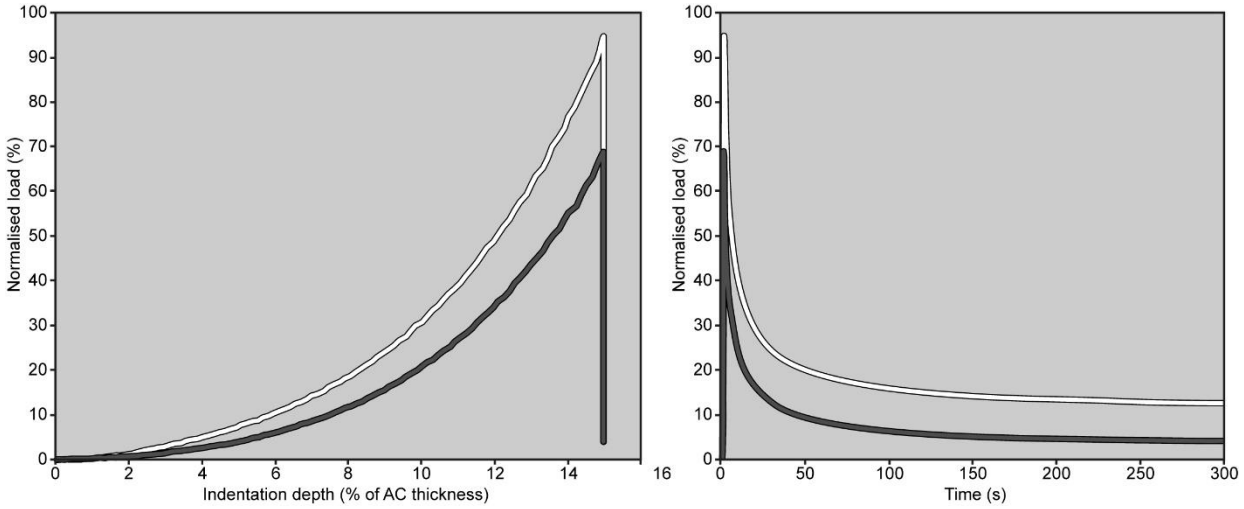

Figure 3.4. Load trends measured on matched paired OC cores (grey line: OC core immersed in CA4+ solution; white line: OC core immersed in PBS solution) during the 4th indentation are shown as a function of indentation depth, up to 15% of AC thickness (a), and as a function of time (b). The peak load is reached in 1 s. In both graphs, the load values have been normalised to the maximum load measured on the same OC core during the 1st indentation (note: if there were no alterations in the mechanical response of the AC, the peak load should have reached 100%).

3.1.4.Discussion

The aim of the present study was to investigate possible alterations in the AC mechanical response related to the use of a cationic iodine-based contrast agent CA4+.

The design of this study attempted to account for the altered mechanical response of the AC resulting from simply managing the tissue. Indeed, immersion in PBS solution, maintained at a temperature of 22 ± 2 °C, for 22 h, alters the AC tissue response, though to a lesser extent than immersion in CA4+ solution. This result deserves a brief discussion before addressing the effect of CA4+ on the tissue. It has been found that immersion of AC in PBS solution, maintained at a temperature of 4 °C, for 6 days does not significantly alter the mechanical behavior of the tissue, while a significant effect has been

found after 12 days [348]. It is also known that increasing the temperature of the solution increases the degradation rate [349]. Therefore, it is reasonable to assume that the temperature of 22 °C used in this study accelerated the process reported by Changor et al [348]. On the other hand, it must also be considered that the sample size of this study, along with the statistical analysis method—which tracks variations in each specimen—allows for the detection of statistically significant, even small percentage changes, even if of small entities. This is supported by the E_{eq} variation found in all 72 OC cores across the first three repetitions (Figure 3.3), which show a small but systematic decrease in E_{eq}. In any case, the design of this study includes the control group with the aim of isolating the effect of the CA4+ on the mechanical properties of AC.

The comparison between the data acquired from the two groups suggest that the exposure to CA4+ alters both the instantaneous and equilibrium response of AC to a localised compression (i.e., indentation). As both the responses do not imply any fluid flow, it can be inferred that the altered response is due to a modification in the ECM tridimensional arrangement and, thus, a reaction to an external impulse. PGs located within the ECM confer FCD to its structure. When the AC is immersed in saline solution, FCD determines the Donnan osmotic pressure, AC swelling, and, ultimately, the collagen framework pretension [314]. The key role of FCD in the compressive behavior of AC is therefore heavily influenced by both the concentration and type (i.e., valence) of dissolved cations [350]. Indeed, it has been demonstrated that AC immersed in a physiological concentration solution in which monovalent ions (Na+) were replaced by divalent ions (Ca^{2+}) leads to a compaction of the PG layers as well as bridging between the opposing PG layers [314]. The compaction of the adjacent PG layers, and the subsequent softening of AC, is expected to be further increased after AC immersion in a solution with a higher ion concentration also containing quadrivalent cations [351]. This is the case of the interaction between the positively charged molecules of CA4+ and negatively charged PGs. As a result, the PG molecules crimp, decreasing their spatial extension and, thus, the pretension applied to collagen bundles. The direct consequence of such a phenomenon could be associated with a decrease in the fluid-independent mechanical response of AC, i.e., the instantaneous and equilibrium response [352]. The osmolality of the solution is also a contributing factor to the softening mechanism. Indeed, it has been demonstrated that the immersion of bovine AC in a hyperosmolar solution of anionic CA induces an overall softening of the tissue. Such an effect was attributed to a decrease in pressure between the tissue and the CA bath, along with diminished repulsive forces exerted by PGs. Furthermore, the immersion in this hypertonic CA solution determined a net water flow exiting the tissue. Overall, the tension among collagen fibres decreased, resulting in a reduced fluid pressure under loading [312]. Although in the present study, the difference in osmolality between the CA4+ solution and PBS (100 mOsm/kg) is smaller if compared to the aforementioned

study (300 mOsm/kg), the described softening mechanism may have played a reduced, but still present, role.

On the other hand, the exposure to CA4+ seems to have a minimal effect on the viscous properties of AC tissue. Indeed, small variations—a slight increase in the value of the stretch parameter β—were observed in the shape of the decay, specifically the final phase of the relaxation when the pressure gradients within AC are reduced. It is worth noting that all other parameters—therefore, S_0 and τ—being equal, a slight increase in the stretch parameter β results in a slightly steeper knee of the curve, leading to a shorter time to reach the horizontal asymptote (see Appendix A). However, not significant variations were observed in the initial transient, i.e., in the fast initial decrease in the curve of Figure 3.4b, perhaps due to the large scatter of this response. On the other hand, the initial transient depends on the pressure impulse produced by the indentation. As CA4+-treated AC exhibits smaller values of instantaneous modulus, and therefore lower pressure impulse, it cannot be excluded a priori that under similar pressure gradients, the initial transient might provide different results. Otherwise, the following can also be hypothesised (i) the distorted ECM, due to the exposure to CA4+, was less effective at counteracting the fluid flow through the AC layers than the undistorted ECM and/or (ii) the amount of fluid that must flow is reduced due to the immersion in a hypertonic CA4+ solution, which determined the aforementioned net water flow exiting the tissue. Whatever the cause, it seems to be a minor effect compared to the effect on the instantaneous and equilibrium response.

This study has some limitations. First, OC cores were extracted from bovine stifle joints. This choice was driven by the wide sample size of the paired OC cores—including intact AC—that needed to be collected in a reasonable timeframe. Opting for OC cores from human knees would have made it impossible to comply with the project timeline. Nevertheless, bovine AC presents similar viscoelastic trends to those of human AC [353]. Therefore, the findings retrieved by the present study can be extrapolated to human OC cores. Second, the AC of the OC cores exhibited highly variable mechanical behavior, despite the preliminary optimised indentation testing protocol. The high variability in the mechanical response has already been reported for AC [353–357] and was expected, given the criterion used for OC core extraction. However, by pairing OC cores, it was possible to obtain two groups with comparable mechanical properties. In addition, by using each OC core as its own reference, it was possible to calculate the relative variation in percentage points of the computed parameters, thus equalizing all OC cores regardless of the absolute mechanical response of their AC [341]. Third, all OC cores underwent two freeze–thaw cycles. Previous studies have suggested that freeze–thaw cycles may affect the mechanical properties of AC [358,359]. The design of this study involved the paired OC cores of the Control and CE group undergoing the same procedure. Thus, any effects of freeze–thaw cycles on the tissue mechanical properties should be equally reflected in both

groups. Fourth, indentation tests were performed at a deformation rate of 0.15 s−1, i.e., 15%/s. Given that the AC thickness ranged from 0.8 to 3.1 mm, the corresponding indenter speed required to achieve this deformation rate was between 0.120 and 0.465 mm/s. To simulate impact loading conditions, these values should be increased by two orders of magnitude [360]. However, it has been demonstrated that the indenter speeds within the range used in this study ensure interstitial fluid support [361], therefore are appropriate for evaluating the AC instantaneous response. Additionally, the set deformation level of 15% is just one of the possible values that may occur in vivo. Nevertheless, this value is representative of the AC deformation under full body weight [362,363] and therefore is suitable for, and already adopted in, comparative biomechanical testing of the knee AC [364]. Fifth, possible effects due to differences in the osmolality of the CA4+ solution were not investigated. The investigation of modifications in osmolality would have introduced an additional source of variability, making unfeasible the study of all the possible combinations. However, the osmolality of the CA4+ solution used in the present study fell within the range reported in the literature and was selected due to the efficacy of such a formulation in enhancing the radiopacity of AC [116,338].

Despite these limitations, the acquired data enabled the evaluation, through comparison, of the effect of the exposure to CA4+ on the response of AC to indentation, highlighting significant alterations in both the instantaneous and equilibrium responses.

3.1.5.Conclusions

The exposure of AC to a CA4+ solution with an osmolarity of 419 mOsm/kg significantly alters both the instantaneous and equilibrium responses of AC to indentation. The effect appears to be a softening of the AC tissue, likely due to the interaction between the three-dimensional distribution of positive charges within CA4+ and the PGs in the ECM, which may alter the PG–PG interaction contributing to AC compressive behavior. Whether this hypothesised mechanism damages AC, or whether the effects of CA4+ exposure are reversible through articular lavage, remains to be demonstrated.

3.1.6.Supplementary Materials

The following supporting information can be downloaded at: https://www.mdpi.com/article/10.3390/ma18132943/s1, Figure S1: flow chart showing the experimental design of this study. Figure S2: schematic of the indentation test. Annex S1: dataset of S_0 values normalized to the value measured in the first indentation; Annex S2: dataset of E_0 values normalized to the value measured in the first indentation; Annex S3: dataset of τ values normalized

to the value measured in the first indentation; Annex S4: dataset of β values normalized to the value measured in the first indentation; Annex S5: dataset of E_{eq} values normalized to the value measured in the first indentation.

Appendix A

The stretched exponential model [66] is described by the function:

$$S(t) = (S_0 - S_{eq})\, e^{-(t/\tau)\beta} + S_{eq}$$

where

S(t) is the load value at time t;

S_0 is the maximum load value reached at the end of the indentation test;

τ is the time constant;

β is the stretching parameter ($0 < \beta < 1$);

S_{eq} is the equilibrium load value reached at the end of the relaxation.

The load cell of the testing machine measured the load value S0 at the end of the indentation test, which was the initial load from which load relaxation began. It also recorded the load S(t) at a given time t and the equilibrium load S_{eq} at the end of the relaxation test. The two parameters τ and β were determined using a non-linear least-squares fitting routine.

Figure A1 shows the effect of variations in the time constant τ. A reduction in τ results in a larger value of 1/τ and, consequently, a faster drop in S(t) at the beginning of the relaxation test.

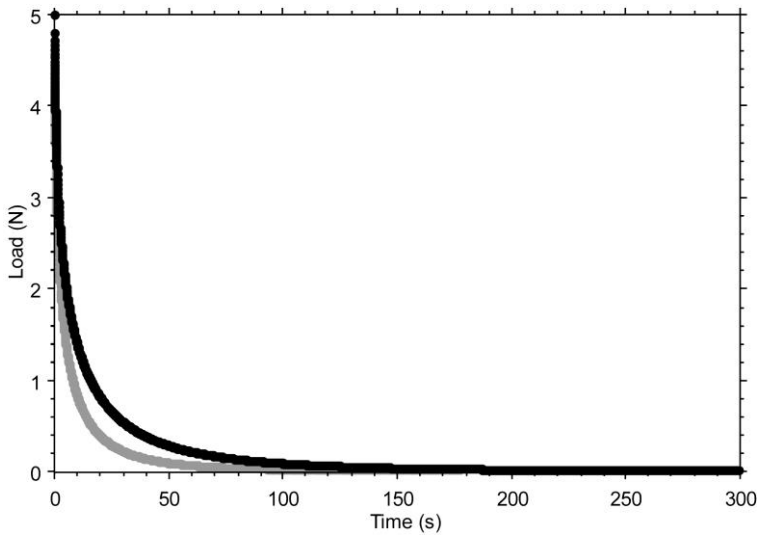

Figure A1. The effect of varying the time constant τ is shown by comparing τ = 6 s (black curve) and τ = 3 s (grey curve), while keeping all other parameters of the stretched exponential function unchanged (S_0 = 5 N; β = 0.5; S_{eq} = 0 N). Note: The 50% reduction in the time constant was made for illustrative purposes only, to make the effect of the variation visible in the graph. S_{eq} was set to zero to better highlight how the final part of the curve tends toward a horizontal asymptote.

Figure A2 shows the effect of variations in the stretching parameter β. A reduction in β causes the curve to stretch more, thereby modifying the rate of decay, making it more gradual after the initial rapid drop.

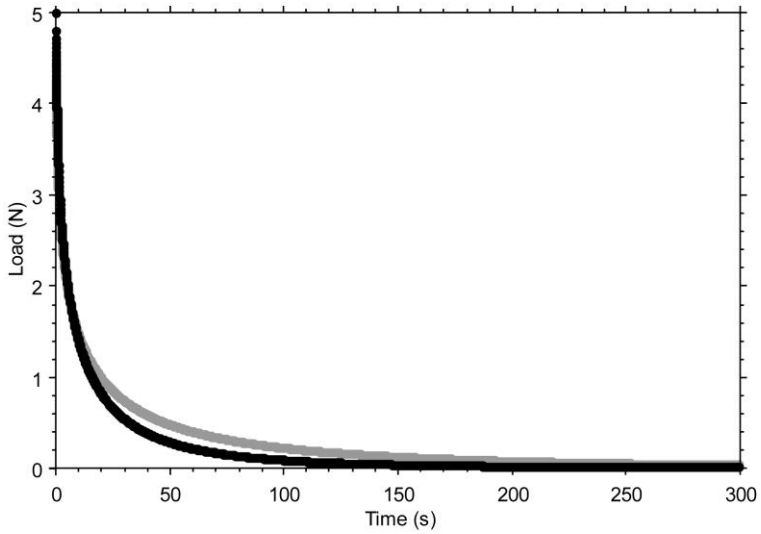

Figure A2. The effect of varying the stretching parameter β is shown by comparing β = 0.5 (black curve) and β = 0.4 (grey curve), while keeping all other parameters of the stretched exponential function unchanged (S_0 = 5 N; τ = 6 s; S_{eq} = 0 N). Note: The 20% reduction in the stretching parameter was made for illustrative purposes only, to make the effect of the variation visible in the graph. S_{eq} was set to zero to better highlight how the final part of the curve tends toward a horizontal asymptote.

Section 2

Reversibility of effects of CA4+ on mechanical properties of articular cartilage: preliminary results

Abstract

Articular cartilage is a specialised soft tissue essential for the smooth operation of synovial joints. Its mechanical performance—shock absorption, load distribution to subchondral bone, and low-friction lubrication—arises from the coordinated interaction of its structural components. The hierarchical organisation of collagen mesh and PGs, combined with the reconfiguration of the interstitial fluid, enables resistance to both compressive and tensile stresses. Degenerative alterations, such as those occurring in osteoarthritis, impair these mechanisms and compromise the mechanical integrity of the tissue.

Although conventional X-ray imaging techniques offer limited intrinsic sensitivity to soft tissues, their high spatial resolution remains crucial for resolving the internal architecture of tissues such as AC. Within advanced X-ray modalities, contrast-enhanced protocols can be readily implemented on commercial micro-CT systems. The use of CAs enables quantitative assessment of specific tissue components. For AC, cationic CAs—particularly CA4+—are preferred due to their electrostatic affinity for proteoglycans. Despite its proven efficacy in visualising both healthy and degenerated AC, CA4+ has been shown to alter the mechanical response of the tissue. This makes the CA4+ radiopaque AC unsuitable for rheological applications. Nevertheless, CA4+ remains a valuable probe for preclinical studies, such as in-vivo animal models. However, its resorption and the reversibility of its mechanical effects on AC have not been investigated yet. The present study aims to assess the reversibility of CA4+-induced effects. Secondly, the washout time (required for total resorption of CA4+ from AC) was assessed.

The indentation-based experimental protocol, illustrated in Section 1 of Chapter 3, included an additional washout step and a final indentation test cycle. Such pipeline was applied to paired AC samples before and after 22 h immersion in either CA4+ or PBS to compare their instantaneous, viscous, and equilibrium mechanical responses.

The washout time, estimated as equal to 19 hours, confirmed the effective resorption of CA4+ from AC. Indentation tests performed on small sample size groups revealed no significant differences in all mechanical parameters between the treated and control groups. While these results must be considered preliminary, the current findings suggest that the effects on the mechanical behaviour of AC are largely, if not entirely, reversible.

3.2.1.Introduction

Articular cartilage is a heterogeneous soft tissue, whose unique mechanical properties result from the interaction of its components. Collagen and PGs build up the ECM, i.e., the solid phase of the tissue [325]. The interstitial fluid, mainly composed of water and solutes, constitutes the fluid phase [326]. Owing to the packed, intertwined arrangement of collagen bundles and PGs, AC optimally responds to both compressive and tensile stimuli [324]. The FCD, associated with the net negative charge of GAGs, is mainly responsible for generating Donnan osmotic pressure and the pre-tensioning of the matrix, following the osmotic balance between water content and solute concentration [332]. The interstitial fluid, contained within the matrix, plays a crucial role in the tissue's response to mechanical loading. Under compressive stress, the fluid is forced through the matrix, creating interstitial pressure that resists deformation. This hydrodynamic resistance is critical during the initial stages of compression, with the fluid contributing to the energy dissipation due to its viscosity [365]. On the other hand, the interstitial fluid contributes to tensile resistance to a lesser extent, mainly by helping to dissipate energy and reduce deformation, with the solid matrix playing a dominant role in resisting tensile stresses [330]. The interaction between the interstitial fluid and the solid matrix ensures that AC efficiently handles both compressive and tensile forces, maintaining its structural integrity and function.

The way such a complex structure responds to the sudden application of a localised pressure on the articular surface can be separated into two main components, namely an instantaneous, flow-independent reaction and a flow-dependent viscoelastic response [325].

Following the rapid deformation of AC in a localised region, the immediate response includes the tensioning of the collagen network in the superficial layer [327], the reorientation of collagen fibres in the deeper layers [328], which accounts for the solid fibrillar component, and an increase in the repulsive forces between GAGs [326]. The FCD of the GAGs contributes to the osmotic pressure, which is crucial for withstanding further stresses transmitted through the collagen network [332]. Concomitantly, the fluid pressure within the matrix increases [329,330].

The mechanical competence of AC declines with the onset of tissue degeneration. Hallmarks of its alterations (i.e., PG loss, fibrillation of collagen bundles, increased water content) progressively disrupt the synovial environment and impact on the whole osteochondral unit [366]. Severe complications derived from advanced stages of joint degenerative diseases such as osteoarthritis, leading to the jeopardised functionality of the tissue, with significant impact on individuals' daily routine [333].

Early detection of such alterations could prevent the irreversible disruption of AC. Diagnostic tools such as X-ray imaging ensure satisfactory spatial resolution in reasonable acquisition times.

Nevertheless, approaches alternative to conventional absorption are demanded to circumvent the radio-transparency of AC to X-rays.

Straightforward implementations to commercial X-ray scanners are offered using CAs. They are radiopaque substances whose interaction with one or more components of the target tissues enhance its overall X-ray visibility. In particular, the net molecular charge determines the interaction with the tissue, and in turn the imaging outcome. Existing literature reports potential use of anionic clinical CAs, as they distribute in the ECM in an inverse fashion with the PGs distribution. Nevertheless, this class of CAs requires significant concentration to compensate for the electrostatic repulsion.

Experimental cationic CAs have been recently designed to be electrostatically attracted by PGs. Among their main advantages, cationic CAs require less concentrations, and distribute according to the PGs depth-dependent arrangement [116,128]. Previous works highlighted the positive outcome related to the use of CA4+, considering in-vitro, ex-vivo and in-vivo studies [101,116,128,147,165,167,169,180].

Despite the promising results in terms of safety and cytotoxicity of CA4+ [116], no clue on its potential impact on AC has been retrieved yet. Literature provides few evidence pointing out the potential alteration of AC mechanical response due to the use of hyperosmolar CA solution [312] . Recently, a study evaluating the impact of CA4+ in iso-osmolar conditions highlighted an overall softening of bovine AC [367]. Apart from these findings, no information has been provided yet about a possible reversal of the alteration induced by CAs exposure to the AC mechanical response.

The aim of this study was to investigate the potential reversibility of such effects, by focusing on the mechanical response of bovine AC. The latter was assessed via indentation tests. Elastic, viscous and equilibrium behaviour of the tissue was studied before and after the CA4+ exposure. Subsequently, samples were immersed in PBS bath to achieve the complete washout of CA4+. To this end, the washout time (i.e., the time required for AC to clear out CA4+) was also estimated. Similarly to the previous study of Berni et al., the protocol included parallel testing on control samples, to single out potential spurious phenomena affecting the native condition of AC.

3.2.2.Materials and Methods

3.2.2.1. Preparation of contrast agent solution

CA4+ (5,50-[Malonylbis(azanediyl)]bis[N1,N3-bis(2-aminoethyl)-2,4,6-triiodoisophthalamide] chloride) is the cationic probe used in this study. Among the molecule properties (molecular weight mw = 1354 g/mol, iodine fraction per molecule f = 0.5084), net positive charge q = +4 is responsible for the electrostatic attraction of CA4+ to PGs.

CA4+ solution was prepared by dissolving salts (synthetised according to the work of Stewart et al. [116] in PBS solution (7.4 pH, Life Technologies Europe B.V., Bleiswijk, The Netherlands), to obtain a concentration of 10 mgI/mL. Further adding of NaOH led to the desired pH value of 7.4, and an osmolality of 419 mOsm/kg (osmometer TypM 10/25 µL, accuracy 1 mOsm/kg, Löser Messtechnik, Berlin, Germany).

3.2.2.2. Extraction of osteochondral tissue samples

Osteoarticular specimens were collected from bovine stifle joints, at a local abattoir within 24 hours from slaughter. Parallelepiped shaped samples were harvested from both femur and tibia, to address the heterogeneous thickness of AC. Following their collection, samples were stored at T = −20 °C, wrapped in gauzes soaked in PBS solution, until the excision of osteochondral (OC) cores. Following the thawing process, OC cores (10-mm diameter and 10-mm height) were obtained with the aid of a computer numerically controlled milling machine (ProLight 2000, Light Machines Corporation, Manchester, NH, USA) mounting a diamond-coated coring tool. Extraction of cylindrical OC cores was performed by keeping the parallelepiped shaped samples fully immersed in PBS solution at room temperature. Site of extraction was chosen to obtain AC surface as flat as possible. The design of the experiment foresaw pairs of OC cores, each destining one to the CA4+ exposure (CE group) and the remaining to the PBS bath (Control group). Cylindrical OC cores underwent second freezing cycle, following the same freezing storage conditions.

3.2.2.3. Washout time

The washout time was assessed first, to establish the most suitable resorption time for the following investigation of reversal. A set of N=10 cylindrical OC cores was immersed in CA4+ solution for 22 hours. Afterwards, they were acquired via X-ray microCT system (SkyScan 1072, SkyScan, Aartselaar, Belgium). Volumetric reconstructions were retrieved from datasets collected with the following imaging protocol: X-ray tube voltage = 50 kV, current = 197 µA, 1-cm Al filter, pixel size = 11.5 µm, exposure time per frame = 5.9 s, angular step = 0.9°, angle range = 180°. The final pixel size corresponded to 11.5 µm. The resulting microCT reconstruction was considered as the reference volume for the following post-processing analysis. From it, the AC volume was semi-automatically segmented, to yield a volumetric mask able to single out AC tissue from subsequent microCT scans. Specimens were then immersed in a mechanically agitated bath of 100 ml of PBS, and microCT scans were performed at several times (namely, 2 h, 4 h, 6 h, 22 h, 24 h, 26 h, 28 h). For each sample, volumetric reconstructions at progressive washout time points underwent rigid volume registration to the reference volume, taking advantage of the underlying trabecular bone. Following the

segmentation of AC volumes, the radiopacity (i.e., CT numbers) was assessed at each washout time point.

According to the diffusion of solutes in a membrane, the washout process was modelled as the Fick's second law:

$$c = c_0 e^{-\frac{t}{\tau_w}}$$

Provided that c is the final concentration of solute, c_0 the initial concentration of solute and τ_w the characteristic time.

In this framework, the washout time was defined as the time required to achieve after washout a decrease in the AC radiopacity of 99% of the value, resulting from the acquisition immediately after the 22 hours exposure to CA4+:

$$t_w = 5\,\tau_w$$

3.2.2.4. Indentation protocol

The experiment followed a modified version of the protocol illustrated in Subsection 3.1.2.3. At time of writing, a total of N=42 samples were included in the experimental protocol, subdivided into CE (N=21) and Control (N=21) group. This two-groups experimental design was necessary as samples exposed to CA4+ undergo modifications in the mechanical response of the AC due to tissue alterations over time, and therefore could not be treated in the same manner as the Control group. Subgroups of up to six osteochondral cores were thawed in PBS solution at T = 4 °C overnight. Steps of assessment of AC thickness and indentation test followed the experimental conditions already illustrated in Subsection 3.1.2.3. Following the estimation of AC thickness, the specimens were collocated in a custom-made polyacetal sample-holder, mounted on the testing machine (Mach-1 V500css, Biomomentum Inc., Laval, QC, Canada) and underwent the first indentation session, consisting of a preliminary preconditioning indentation and three indentations, each performed after a resting period of 40 min. Thus, the PBS solution was replaced with 0.5 mL of CA4+ (CE group) or fresh PBS solution (Control group). Diffusion of the target solution was left for 22 h at a temperature of 22 ± 2 °C [83]. Thus, the PBS solution was replaced with 0.5 mL of CA4+ (CE group) or fresh PBS solution (Control group).

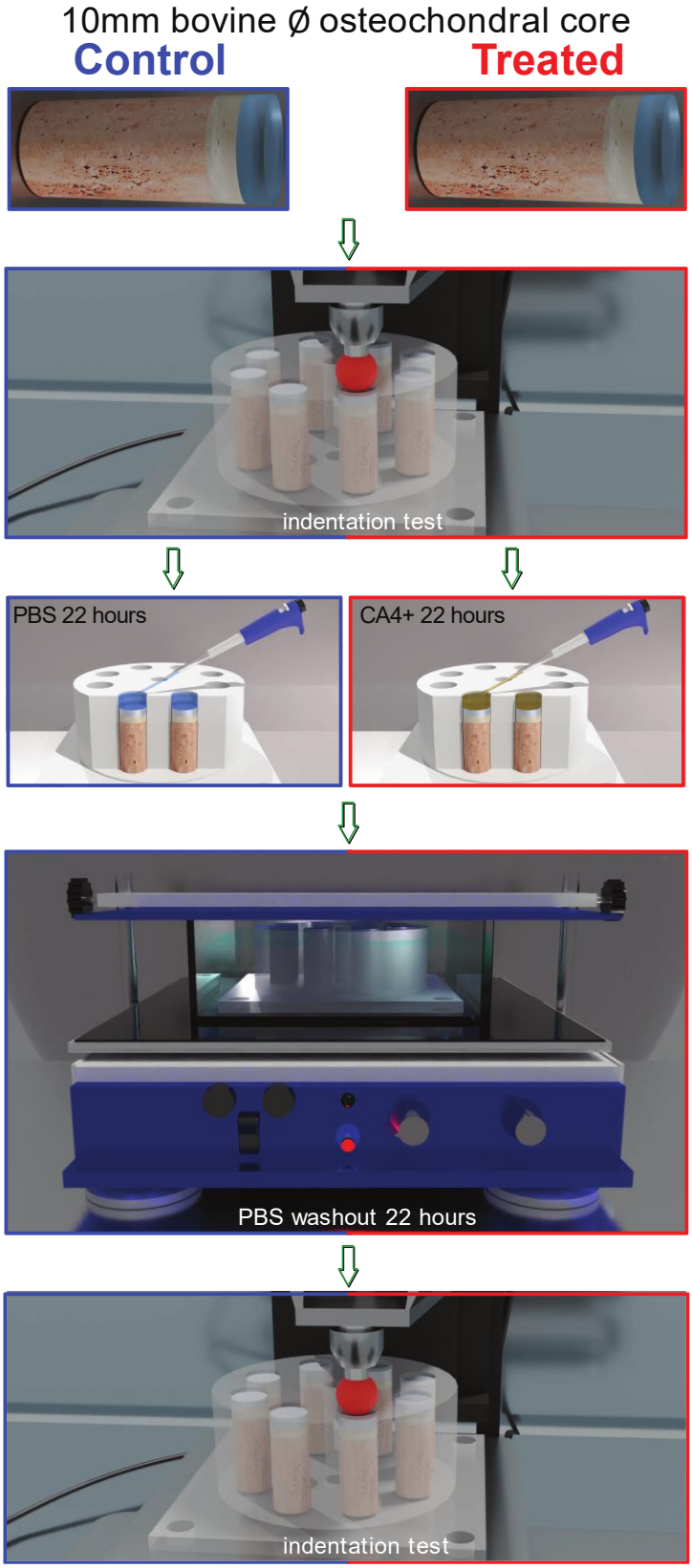

Figure 3.5. Scheme of the indentation protocol. After their collection, samples were subdivided into treated (i.e., samples undergoing contrast enhancement) and control (i.e., samples exposed to PBS only). Regardless of the group, osteochondral samples underwent a preliminary cycle of indentation tests. After a 22 h-bath in the respective solution baths, followed the 22-h washout in PBS. Eventually, samples from both groups were tested via indentation, following the same protocol performed preliminarily.

Afterwards, the polyacetal sample-holder carrying the specimens was immersed in dynamical bath for 22 hours at room temperature, in a volume of 380 ml of PBS, placed on a laboratory stirrer. In the end, a second cycle of indentation test, again consisting of one pre-conditioning and three indentations, was performed, with specifications identical to the first mechanical test session. For each subgroup of N=6 osteochondral cores, the experimental protocol lasted 50 hours. The indentation protocol is schematised in Figure 3.5.

The mechanical properties of AC were extrapolated from the indentations performed during the first and second test sessions. The instantaneous mechanical response of AC was assessed by analysing the peak reaction load (S_0) recorded during indentation and the instantaneous elastic modulus (E_0). The value of S_0 was obtained experimentally using a multi-axis load cell with an accuracy of 1% within its operational range. E_0 was determined by fitting the indentation load–displacement data to the Hayes analytical model [343], assuming a Poisson's ratio of 0.45 [344].

To characterise the viscoelastic properties of AC, load relaxation behaviour was evaluated in terms of the initial load decay and the time required to reach equilibrium. This behaviour was quantified by fitting the load–time relaxation curve with a stretched exponential function [345], from which the time constant (τ) and the stretch parameter (β) were extracted. Curve fitting was carried out by minimising the root mean square error using a custom MATLAB script.

The fluid flow-independent mechanical response—after complete fluid exudation—was characterised by the equilibrium modulus (E_{eq}). E_{eq} was computed via the Hayes model, using the equilibrium load measured at 300 seconds from the start of the indentation test and accounting for the geometry of the setup [342]. For this calculation, a Poisson's ratio of 0.3 was used [346,347].

All five parameters (S_0, E_0, τ, β, E_{eq}) were normalised to the values obtained in the initial indentation test to express the relative changes observed in subsequent tests.

3.2.2.5. Statistical analysis

The relationship between the characteristic time τ_w and AC features was deepened. Monotonic trends with AC thickness and radiopacity were investigated with Spearman ρ.

To assess differences in AC thickness between the CE and Control groups, the Wilcoxon signed-rank test was used. Similarly, differences in the values of S_0, E_0, τ, β, or E_{eq} measured during the first indentation were evaluated between the two groups using the Wilcoxon signed-rank test. Trends in S_0, E_0, τ, β, or E_{eq} values observed during the first three indentations (before 22 hours of immersion in solution) or the subsequent three indentations (after 22 hours of immersion) were examined using the Friedman test. The impact of 22-hour immersion on the mechanical properties of the AC within each group was analysed by applying the Mann–Whitney signed-rank test to the normalised values

of S_0, E_0, τ, β, or E_{eq}, where the percentage change in these parameters between the two series was calculated relative to their initial values. Finally, the effect of the CA4+ solution on these parameters was assessed by applying the Mann–Whitney test to compare the percentage changes between the CE and Control groups.

3.2.3.Results

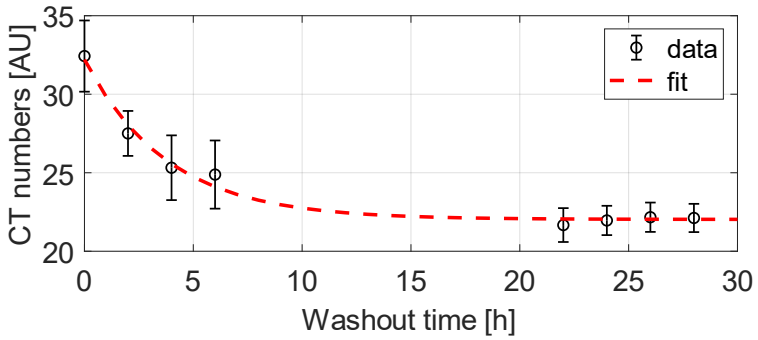

Figure 3.6. Fit of experimental data to Fick's law, modelling the resorption of CA4+ from AC.

Characteristic time τ was estimated from fitting of resorption from single samples to Fick's law (Figure 3.6), showcasing thickness in range 0.4-1.4 mm. A median value of τ_w resulted 3.85 hours (provided with 25th and 75th percentile value of 2.62 hours and 9.26 hours, respectively). The washout time resulted in 19.3 hours. Upon the investigation of possible relations to AC features, median values τ_w shown monotonic increasing trend as a function of AC thickness (Spearman $\rho = 0.91$, $p < 0.001$). On the contrary, a monotonic decreasing trend was observed to CT numbers (Spearman $\rho = -0.83$, $p < 0.01$).

The AC thickness values of OC cores for the CE group and Control group were in the range of 1.1–2.9 mm and 0.8–3.0 mm, respectively. No significant difference was found between the two groups (CE group median thickness 1.7 mm, Control group median thickness 1.6 mm, Wilcoxon signed-rank test: $p = 0.54$).

A total of 126 indentation tests were performed, neglecting the preconditioning procedure of AC tissue. The indentation procedure on the untreated AC tissue appeared to be repeatable, as evidenced by the coefficient of variation calculated for the five mechanical parameters (Table 3.2).

Table 3.2. Distribution of the coefficient of variation for the five mechanical parameters – S_0 peak reaction load, E_0 instantaneous elastic modulus, τ time constant, β stretch parameter, E_{eq} equilibrium modulus – across the first three indentation tests (untreated AC tissue).

Percentile	CE Group					Control Group				
	S_0	E_0	τ	β	E_{eq}	S_0	E_0	τ	β	E_{eq}
5th	0.68	0.68	2.25	0.37	0.10	0.89	0.93	1.86	0.38	0.07
25th	1.47	1.52	3.86	0.39	0.17	1.62	1.34	3.30	0.40	0.22
50th	2.23	3.01	4.68	0.41	0.28	2.48	3.94	5.10	0.41	0.27
75th	2.99	4.74	6.62	0.41	0.36	3.48	6.65	6.87	0.43	0.35
95th	7.30	15.67	9.78	0.50	0.45	5.57	12.59	8.63	0.52	0.52

The mechanical response of the AC tissue of the 21 OC cores measured during the first indentation differed by up to two orders of magnitude. The range of variability, including the minimum and maximum values, of the computed mechanical parameters are reported in the following: S_0: 0.6–11.8 N; E_0: 0.4–24.1 MPa; τ: 1.4–10.7 s; β: 0.35–0.58; E_{eq}: 0.05–0.67 MPa. No difference was found between the two groups in the S_0 (Wilcoxon signed-rank test: $p = 0.50$), E_0 (Wilcoxon signed-rank test: $p = 0.47$), τ (Wilcoxon signed-rank test: $p = 0.62$), β (Wilcoxon signed-rank test: $p = 0.56$), and E_{eq} (Wilcoxon signed-rank test: $p = 0.82$) values measured during the first indentation.

Significant trends over test repetitions were found in the first three or the second three indentations in both the CE and Control group for all calculated parameters. In particular S_0 in the second three repetitions of the Control group (Friedman test: $p < 0.001$), E_0 in the second three repetitions of the CE group (Friedman test: $p < 0.001$), τ in the second three repetitions of both groups (Friedman test: $p < 0.001$ for both groups), β in the first three repetitions of the CE group (Friedman test: $p < 0.001$ for both groups) and E_{eq} in the first three repetitions of the Control group (Friedman test: $p < 0.001$). Contrasting trends were observed along with significant Friedman test (median variation between the first and the third indentations up to 15%). To exclude the effect of such contrasting trends, the reversibility of CA4+ effects on mechanical parameters were calculated as the differences between the medians of the 21 values of the third and fourth indentation sets. Normalised parameter trends across tests are shown in Figure 3.7.

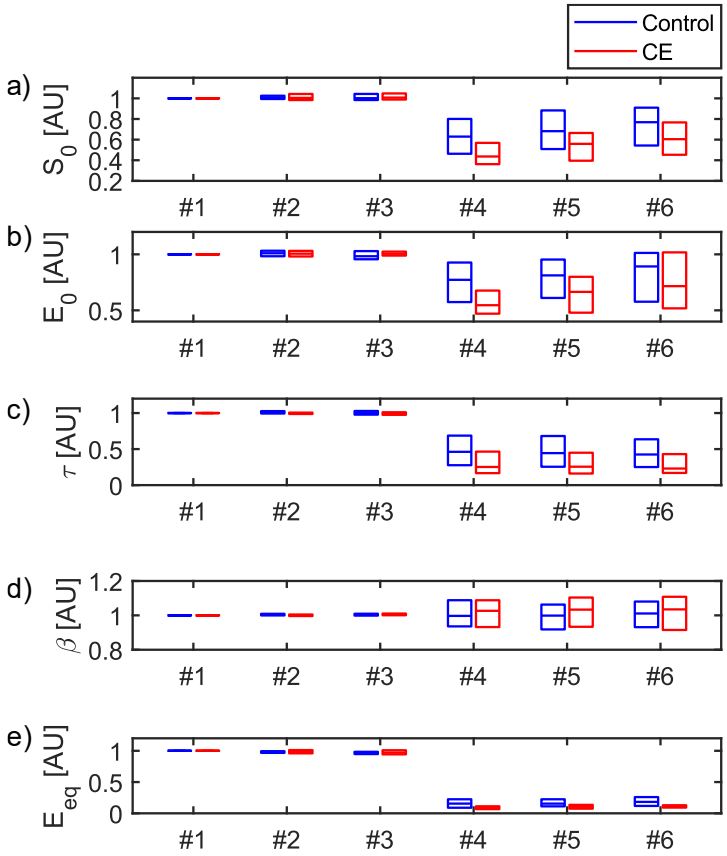

Figure 3.7. The median (markers), 75th percentile (upper edge of error bars), and 25th percentile (lower edge of error bars) of the percentage changes in S_0 (a) and E_0 (b), τ (c), β (d) and E_{eq} (e) values before (1st, 2nd, and 3rd indentation test) and after (4th, 5th, and 6th indentation test) washout are shown (grey markers: CE group; white markers: Control group). The values shown in the figure were calculated as the differences between the medians of the 63 values measured in the first three and the 63 values measured in the second set of indentation tests.

The washout had the following significant effects on CE group (Mann–Whitney signed-rank test: $p < 0.001$ in all five cases), except for β: 57.1% reduction in S_0, 46.0% reduction in E_0, 43.1% reduction in τ, 87.2% reduction in E_{eq}, all calculated as the difference between the medians of the 3rd and 4th indentation tests. Similarly, significant effects were highlighted on Control group as well, except for β (Mann–Whitney signed-rank test: $p < 0.001$): 29.1% reduction in S_0, 21.7% reduction in E_0, 55.8% reduction in τ, 83.9% reduction in E_{eq}.

When comparing the percentage changes between the two groups, the washout procedure led to the significant 6.4% reduction in E_{eq} with respect to the Control group. Contrariwise, the remaining parameters showed no significant differences between the two groups (S_0: Mann–Whitney: $p = 0.07$, E_0: Mann–Whitney: $p = 0.26$, τ: Mann–Whitney: $p = 0.10$, β: Mann–Whitney: $p = 0.78$).

3.2.4.Discussion

The aim of the study was to explore the potential reversal of alterations observed in AC mechanical response, caused by its exposure to the cationic iodine-based contrast agent CA4+. The potential

resorption of CA4+ was also investigated, pointing out the successful removal of CA4+ from AC. This result supports the reversible nature of the electrostatic attraction exerted from negative FCD of PGs on CA4+ molecules [160,154,116]. Despite the potential segregation of CA4+ molecules occurring with such interaction, the concentration imbalance prevails and successfully vehicles the exogenous substance out of the tissue. Rather than reporting the exact estimation of the washout time, existing literature limits to mention the removal of CA4+ [133,120,107,89,83]. Nevertheless, contrasting evidence urged a rigorous investigation of the phenomenon [368].

A few considerations regarding the washout time t_w (and consequently the characteristic time τ_w) warrant discussion in the light of their significant relationship with specific properties of AC. In this framework, AC may be conceptualised as a permeable membrane separating two distinct compartments, characterised by high and negligible concentrations of the target solute CA4+ (i.e., AC and PBS, respectively).

In general, phenomena such as diffusion or resorption in such membrane are governed by the combination of solute properties (namely, molecular size, charge, and concentration) and structural features of the tissue itself (namely thickness and zonal organisation).

The faster resorption of CA4+ from more radiopaque AC (namely, tissue with higher PG content) was observed to occur despite the electrostatic attraction. Other factors, such as molecular size, could explain such trend. Smaller molecules diffuse more rapidly and penetrate deeper into the ECM. In particular, studies using fluorescent tracers and radiolabelled molecules showed a size-dependent decrease in diffusivity, particularly for macromolecules with consistent molecular weight [369,370]. Furthermore, the inverse relation between the diffusion coefficient and the solute molecular weight confirmed that steric hindrance from the dense ECM limits the mobility of larger molecules [371]. The limited diffusivity of large molecules due to steric hindrance of ECM could be exacerbated by AC thickness.

The thickness of AC has a direct influence on both the extent and kinetics of solute diffusion and desorption. In diffusion-controlled systems, the characteristic time for solute transport scales with the square of tissue thickness. A comparative study between rat and rabbit AC (namely, model presenting significant differences in AC thickness) showed that the retention half-life of a cationic large molecule, such as avidin, increased from ~29 hours in thin rat cartilage to ~154 hours in thicker rabbit AC [372]. Alternative methodologies investigated the contribution of steric hindrance independently of solute properties. For example, reduced water diffusivity and shortened relaxation times, as measured by single-sided high-resolution nuclear magnetic resonance, were associated with a denser ECM in the deep zone of AC [373]. This evidence supports the positive trend relating longer τ_w with thicker AC.

In the wake of independent methods, the possible retention of CA4+ molecules was analysed in the context of histological assessment of AC. In this regard, CA4+ was hypothesised to compete in binding to PGs with Safranin-O, a cationic histological stain used in the standard assessment of PG content [89]. Cartilage samples subjected to different environmental conditions (i.e., hydrated or fixed in formalin) underwent CA4+ exposure, PBS bath and subsequent histological analysis. Interestingly, only the hydrated samples exhibited optimal histological staining. Contrariwise, the poor staining obtained on fixed samples indirectly pointed out the retention of CA4+ molecules [89]. Therefore, the environmental conditions (i.e., suspension in PBS or fixation) impacts on the subsequent assessment of the tissue using alternative methods, such as histology. In this scenario, the concurrent microCT and histological analysis would require smaller batches of test animals, involving fewer ethical concerns.

The confirmation of clearance of the CA from the tissue and the recovery of tissue's pristine properties evaluations would make the translation viable to in-vivo animal studies. In this sense, previous studies addressed no adverse effects (i.e., cytotoxicity, renal clearance and inflammation) on animals in-vivo, following the administration of CA4+ [68,107,116] . Concordance is met with a previous study, demonstrating the removal of CA4+ from equine AC samples following an overnight bath in PBS. However, no details on the precise process were provided [107]. Analogously, murine femurs incubated in CA4+ underwent PBS bath overnight, exposing no differences in radiopacity before CA4+ incubation and after PBS washout [120]. Desorption procedures of human AC samples in saline solution allowed the subsequent Safranin-O histological staining as well [133].

Besides evidence suggesting the possible removal of CA4+ from AC, the present study shows little to no difference in mechanical parameters between CE and Control groups following CA4+ washout. The study was designed to single out any bias that could not be addressed to the exclusive alteration of AC mechanical properties due to CA4+. In this regard, providing groups with similar features is crucial to implement studies aiming to evaluate and compare the effect of different treatments on biological tissues, i.e., AC. The approach of pairing samples harvested from nearby locations allowed to provide experimental groups with comparable mechanical response [353–357].

The present study comes along with some limitations. Notwithstanding the complete desorption of CA4+ from AC, the washout time evaluated might not be compatible with in vivo animal applications. On the other hand, the washout time was measured under conditions far from the physiological ones. For instance, thermal body temperature, integral synovial environment and motion protocols could ideally shorten the washout time.

Long experimental times, associated with the use of no preservation agents (i.e., antifungal, antibiotics, antiprotease) lead to a progressive deterioration of AC, as highlighted by the Control

group. This phenomenon adds to the multiple freeze-thaw cycles withstood by OC cores. Despite the impact of freeze–thaw cycles on the mechanical properties of AC has been proved [358,359], such an effect should have equally affected both groups investigated by this study.

The limited sample size constitutes one further limitation and underpins the preliminary nature of the results presented. Increasing the sample size would improve the statistical power and could either confirm that the small differences between the two groups are statistically significant or show that the small significant difference found in E_{eq} values is not actually significant.

Notwithstanding these weaknesses, these preliminary results suggest that even if a residual effect of CA4+ on AC exists, it is small – only a few percentage points.

3.2.5.Conclusions

The preliminary results presented in this study support the reversible nature of interaction involving CA4+ molecules and PGs in AC. The experimental study was performed on bovine OC cores obtained from stifle joints, to demonstrate the resorption of CA4+ from AC and the reversibility of its effects on tissue mechanical response. The analysis of resorption of CA4+ in time resulted in a almost complete removal of the molecule from the tissue. Paired samples harvested from adjacent locations of either tibial plate or femoral condyles were used to ensure comparable baseline conditions. The inclusion of a control group was essential to distinguish the effects of CA4+ from potential changes related to prolonged sample handling and tissue degeneration throughout the whole experiment. Following the removal of CA, most differences between treated and control samples were no longer significant, with the exception of a small residual difference (approximately 6%). Overall, these findings support the hypothesis that CA4+-induced mechanical alterations are largely reversible. Further studies should be carried out to further clarify whether this reversibility is complete, minimising as much as possible uncertainties related to residual non-significant differences observed in instantaneous response, together with sample variability and limited sample size.

Section 3

Contrast-enhanced X-ray imaging of articular cartilage: reliability of a cationic contrast agent in combination with high-resolution peripheral quantitative computed tomography system

This section was reproduced from the manuscript:

"Contrast-enhanced X-ray imaging of articular cartilage: reliability of a cationic contrast agent in combination with high-resolution peripheral quantitative computed tomography system"
S. Fantoni, M. Berni, R. Fognani, G. Fraterrigo, P. Cardarelli, F. Baruffaldi and M. Baleani

Submitted to *Frontiers in Bioengineering and Biotechnology*

The preprint version of the manuscript has already been published on ArXiv repository:
https://arxiv.org/abs/2510.20391

The external reviewers asked to describe the novelty of this manuscript. Here such a description is provided. These novelties will be included in the revision of the manuscript upon submission, but to respect the integrity of the preprint, they will be added here and not in the body of the chapter.
Nickmanesh et al. found a correlation between stiffness and attenuation of the tissue following the contrast enhancement. However, in this study, AC stiffness was defined as "*the ratio of peak normal load to normal displacement*". This definition assumes a linear tissue response and, therefore, may represent a relatively simplified indicator of tissue mechanical behaviour. Lakin et al. found a strong positive correlation between the contrast-enhanced attenuation of the tissue and its compressive modulus. However, the imaging was performed using microCT, which cannot be implemented in clinical practice.

Abstract

Articular cartilage exhibits distinctive mechanical behaviour, attributable to its biphasic composition and hierarchical organization. Proteoglycans, essential constituents of the extracellular matrix, contribute to tissue swelling, stiffness, and viscoelasticity, thanks to their fixed charge density. Degenerative alterations in proteoglycan content and collagen structure compromise the mechanical integrity of articular cartilage. Early detection of these alterations is essential to increase the chance of effectiveness of any innovative treatment. Although magnetic resonance imaging provides valuable compositional information, its limited spatial resolution restricts its effectiveness in capturing subtle alterations in articular cartilage. As an alternative, contrast-enhanced X-ray imaging circumvents such limitation, resorting to the use of radiopaque contrast agents. In this context, cationic contrast agents, like CA4+, enable the quantitative assessment of proteoglycan content via electrostatic attraction. High-resolution peripheral quantitative computed tomography offers an optimal compromise between spatial resolution and radiation exposure, making it a promising tool for clinical use. This study aimed to explore the relationship between proteoglycan content—quantified through contrast-enhanced high-resolution peripheral quantitative computed tomography combined with the use of CA4+—and the viscoelastic properties of healthy bovine articular cartilage, assessed via indentation testing. These preliminary data from a small sample size group support significant correlations between cartilage enhanced radiopacity and parameters representing the tissue's mechanical behaviour. These findings should be confirmed in a larger sample size group.

3.3.1.Introduction

Articular cartilage (AC) is a soft tissue showcasing unique mechanical properties, arising from its composition and hierarchical structure. More precisely, two phases can be distinguished [9]. The solid phase includes collagen network and proteoglycans (PGs), as the main components of the extracellular matrix (ECM). The collagen network is composed by fibres locally collected into bundles, anchored to the calcified cartilage, and expanding towards the articular surface in an arcade-like configuration [325]. PG are macromolecules including glycosaminoglycan chains, featuring a negative charge unbalance, the fixed charge density (FCD) [374]. Intertwined with collagen network, PGs outstretch owing to the mutual repulsion, and distribute along the tissue depth according to a characteristic concentration gradient [325]. The fluid phase, represented by the interstitial fluid, is mainly composed of water and positively-charged ions [326].

Due to the interplay of those hierarchically arranged phases, AC responds to any local stimulus with an instantaneous flow-independent response and a flow-dependent viscoelastic response [15]. The instantaneous response originates from the tensile deformation of collagen bundles in the superficial layer of the tissue, the rearrangement of the collagen network in the deep layer, the mutual repulsion of glycosaminoglycans bound to PGs and fluid pressure. The originated fluid pressure triggers the flow of interstitial fluid across the ECM. Viscous phenomena exhaust when the equilibrium between the mechanical stimulus and the tissue reaction is reached [17]. The FCD of PGs plays a crucial role in pretensioning the collagen network and, moreover, originates the osmotic pressure. The combination of both phenomena induces the swelling of AC [332].

The degradation of AC owed to musculoskeletal diseases, i.e., osteoarthritis, leads to a progressive decline of the tissue mechanical competence [1] Several alterations of AC serve as hallmarks for potential identification of tissue degeneration, among which the loss of PG content implicates a decrease in the tissue stiffness [375]. Moreover, the fibrillation of collagen network induces the augmented permeability of ECM, held accountable for altering both the instantaneous and viscous response of the tissue [376].

The early detection of any alteration of AC could be crucial in the field of regenerative medicine and pharmacological treatments. For instance, the capability to monitor their impact on disease progression could delay the need for invasive solutions such as prosthetic implant [377]. In this frame, diagnostic techniques sensitive to one or more AC components should be considered in the perspective of identifying early degenerative hallmarks. Magnetic resonance imaging (MRI) delivers high-contrast images of hydrated tissues and enables the quantitative assessment of several parameters signalling the tissue condition. For instance, T1ρ and T2 relate with the PG content and state of collagen mesh, respectively [378]. Nevertheless, clinical MRI systems suffer from low spatial

resolution, with major implications for the evaluation of thin layers of tissues, as in the case of AC [379].

Conventional X-ray imaging methods have proved their reliability mainly in the evaluation of mineralised tissues [380]. Although such methods can overcome the MRI limitation related to spatial resolution [381], they are not suitable to identify soft tissues' features due to their low electron density.

To enhance the X-ray visibility of soft tissues, the use of radiopaque exogenous substances is required. Contrast agents (CAs) are compounds that include electron-dense elements (e.g., iodine) and are employed in both research and clinical context to increase the radiopacity of a target organ or tissue [64]. Clinical CAs feature chemical properties (e.g., pH and osmolality) meeting strict requirements for patient safety [382]. In the research context, CAs include polyoxometalate-based histological stains, nanoparticles or experimental formulations, adopted in both ex vivo and in vitro studies [383]. Regardless of the CA type, it is the net molecular charge that determines the CA affinity for a specific tissue or component. Focusing on AC, cationic CAs provide superior results in terms of imaging outcome, as demonstrated for CA4+. This formulation is an experimental iodine-based cationic CA that allows the quantitative assessment of PG content in AC thanks to the electrostatic attraction exerted by FCD of glycosaminoglycans [116]. Previous studies have reported a correlation between CA4+ contrast enhancement and tissue properties, namely stiffness, compressive modulus, and torsional coefficient of friction [114,147]. Therefore, contrast enhanced X-ray imaging protocols implemented with CA4+ could predict the mechanical competence of AC, providing essential outcomes in both preclinical and clinical contexts. In deploying such a framework clinical X-ray imaging systems should be privileged, prioritizing the acquisition of patient limbs at acceptable spatial resolutions and low radiation doses. High-resolution peripheral quantitative computed tomography (HR-pQCT) scanners represent an optimal trade-off between relatively high spatial resolution (i.e., from 40 to 60 μm) and minimal radiation dose [384]. Nevertheless, insights about the deep connection between the composition and mechanical competence of the tissue must be provided first, e.g., by focusing on ex vivo experiments. The aim of this study was to investigate the relationship between information related to the PG content of healthy bovine AC – retrieved by a contrast-enhanced HR-pQCT clinical protocol – and the tissue viscoelastic properties, derived from indentation test.

3.3.2.Materials and Methods

3.3.2.1. Preparation of contrast agent solution

The CA employed by this study is CA4+, i.e., with formulation (5,50-[Malonylbis(azanediyl)]bis[N1,N3-bis(2-aminoethyl)-2,4,6-triiodoisophthalamide] chloride). One molecule of CA4+ includes six iodine atoms, and displays iodine fraction per molecule f = 0.5084, net positive charge q = +4, molecular weight mw = 1354 g/mol. CA4+ salts synthesis was performed according to literature [116]. CA solution was prepared by dissolving CA4+ salts in phosphate-buffered saline (PBS) solution (1X, 7.4 pH, Life Technologies Europe B.V., Bleiswijk, The Netherlands) until reaching a concentration of 10 mgI/mL, effective to enhance significantly the X-ray attenuation of AC [385]. The pH of the CA solution was balance by adding NaOH 4M, i.e., up to a value of 7.4. The osmolarity of PBS and CA solution was measured with an osmometer (TypM 10/25 µL, accuracy 1 mOsm/kg, Löser Messtechnik, Berlin, Germany), yielding 307 mOsm/kg and 419 mOsm/kg, respectively.

3.3.2.2. Osteochondral Tissue Samples

Osteochondral (OC) cuboids (N = 11) were excised from tibiofemoral surfaces of N = 6 fresh bovine stifle joints, obtained from a local slaughterhouse within 24 hours post-slaughter for food production purposes. Cuboid samples were obtained through the use of a diamond-coated blade mounted assembled on a circular saw (MDP200 and TR60, respectively; Remet, Italy). The process was performed under continuous water irrigation, to avoid the dehydration and heating of the OC tissues. OC cuboids were then wrapped in gauzes soaked in PBS 1X and frozen at −20 °C (1st freezing cycle). On a different day, OC cuboids were thawed at 4°C in PBS 1X for one hour, after which cylindrical OC cores (10-mm in diameter and height, including AC, SB and TB) were excised by means of a computer numerically controlled milling machine (ProLight 2000, Light Machines Corporation, Manchester, NH, USA) equipped with a diamond-coated coring tool (10 mm inner diameter). Prior to coring, OC cuboids were spatially tilted to retrieve cores with an AC surface as flat as possible. A total of N = 18 OC cores were excised. OC cores were then stored at -20°C in a PBS 1X-soaked gauze until indentation test (2nd freezing cycle).

3.3.2.3. Indentation test

OC cores, in subgroups of N = 6, were thawed in PBS 1X at T = 4 °C overnight. The AC thickness was estimated before indentation by means of X-ray imaging. After placing each OC core in a custom-made polymethyl methacrylate sample holder, four planar images (each after a 90–rotation of the core) were acquired via X-ray microCT system (SkyScan 1072, SkyScan, Aartselaar, Belgium) by applying a previously developed protocol [367], i.e., with a pixel size = 11.5 µm. AC thickness was

estimated by using a custom-made MATLAB code (MATLAB version R2022b, MathWorks, Natick, MA, USA) [367].

Afterwards, subgroups of N = 6 OC cores were placed in a custom-made polyacetal sample holder with six cavities [367]. Then, PBS 1X (0.5 mL) was poured on the top surface of the OC cores to keep the AC hydrated.

The sample holder was mounted on the testing machine (Mach-1 V500css, Biomomentum Inc., Laval, QC, Canada), and each OC core underwent the following procedure: (i) a preconditioning of the AC, i.e., preliminary indentation, (ii) three indentations, each performed after a resting period of 40 min, (iii) substitution of the PBS solution with 0.5 mL of CA solution, followed by a 22 h rest at a room temperature (22 ± 2 °C) to reach equilibrium of the diffusion phenomena [385].

The indentation test foresaw the application by a 6 mm spherical indenter of a maximum nominal deformation equal to 15% of AC thickness, at a deformation rate of 15%/s, perpendicular to the articular surface and at the centre of each OC core [386]. The nominal deformation was held for 300 s [342] to assess variation of stress over time. This protocol was employed to investigate the following parameters: maximum reaction load (S_0), instantaneous elastic modulus (E_0), time constant (τ) and the stretching parameter (β) of the load–time relaxation curve, and equilibrium modulus (E_{eq}). Full details regarding the computation of these parameters have been published elsewhere [386].

3.3.2.4. High-resolution peripheral quantitative computed tomography imaging

Following the exposure to CA solution, the subgroup of N = 6 OC cores was acquired using a HR-pQCT system (XtremeCT II, SCANCO Medical AG, Brüttisellen, Switzerland). After removing the CA solution from the top surface of each OC core, the sample holder was placed within HR-pQCT, i.e., by aligning the OC cores' axial direction to the scanning axis, and the cores were acquired (X-ray tube voltage = 68 kV, current = 1.47 mA, filtration = 1 mm Al + 0.2 mm Cu, pixel size = 60.7 μm, scan time = 10 min). Afterward, OC cores were removed from the samples holder, wrapped in gauzes soaked in PBS 1X, and stored at -20°C. HR-pQCT images were reconstructed using a multithreaded Feldkamp-Davis-Kress reconstruction program [387]. The reconstructed volumes underwent semi-automatic segmentation of contrast-enhanced AC. The segmented AC volumes were further processed by a custom-made Matlab code to estimate i) the AC thickness, and ii) the depth-dependent distribution of CA4+ across such a tissue, i.e., in term of attenuation – CT number (HU) – profile.

3.3.2.5. Statistical analysis

The distribution of AC thickness, assessed by microCT and HR-pQCT, mechanical parameters, and volumetric distribution of CA4+ across AC samples was assessed via Kolmogorov-Smirnov test.
The replicability of measuring AC thickness by two different imaging approaches, i.e., microCT and HR-pQCT, was investigated by Pearson correlation.
Eventual trend, i.e., upward or downward, of S_0, E_0, τ, β, or E_{eq} values over the indentations was assessed through the Friedman test ($p < 0.05$).
In absence of trend in the mechanical parameters' values computed starting by the three indentations, their median values were considered to investigate relationships with the volumetric distribution of CA4+ within AC (Spearman correlation, $p < 0.05$).

3.3.3.Results

The AC thickness of OC cores computed by microCT- and HR-pQCT approaches was in the range (0.8 ÷ 3.0) mm and (0.6 ÷ 2.7) mm, respectively. Both the approaches provided non-normal distributed values (Kolmogorov-Smirnov test, $p < 0.001$; Table 3.3).

Table 3.3. Distribution of the AC thickness estimated by microCT and HR-pQCT approaches.

Percentile	AC thickness (mm)	
	microCT	**HR-pQCT**
5^{th}	0.8	0.9
25^{th}	1.1	1.2
50^{th}	1.8	1.8
75^{th}	2.6	2.4
95^{th}	3.0	2.7

The replicability of measuring AC thickness by the two imaging approaches was investigated by Pearson correlation, which highlighted a significant and strong ($\rho > 0$, $\rho^2 = 0.98$; $p < 0.001$) relationship between microCT and HR-pQCT estimates.
Concerning the indentation of OC cores, a total of 54 tests were performed (neglecting the preconditioning indentation). The testing procedure proved to be repeatable (see the percentage coefficient of variation calculated for the mechanical parameters in Table 3.4).

Table 3.4. Distribution of the coefficient of variation (CV%) for the mechanical parameters across the three indentations.

Percentile	S_0	E_0	τ	β	E_{eq}
5^{th}	0.4	0.9	0.5	0.9	0.5
25^{th}	1.1	1.5	0.7	1.0	1.2
50^{th}	2.0	2.0	1.2	1.0	1.8

75th	3.2	3.7	3.1	1.0	3.3
95th	5.2	5.2	4.3	1.0	14.1

The range of variability, i.e., minimum and maximum values, of the computed parameters are reported in the following: S_0: (0.8÷4.3) N; E_0: (0.6÷9.2) MPa; τ: (1.7÷10.3) s; β: (0.342÷0.499); E_{eq}: (0.1÷0.6) MPa.

No significant trends over the three test repetitions were found regardless the parameter.

Considering the obtained results, the median value of the mechanical parameters across the three indentations was analysed for each OC core, with the aim of investigating its correlation with the volumetric distribution of CA4+ within AC.

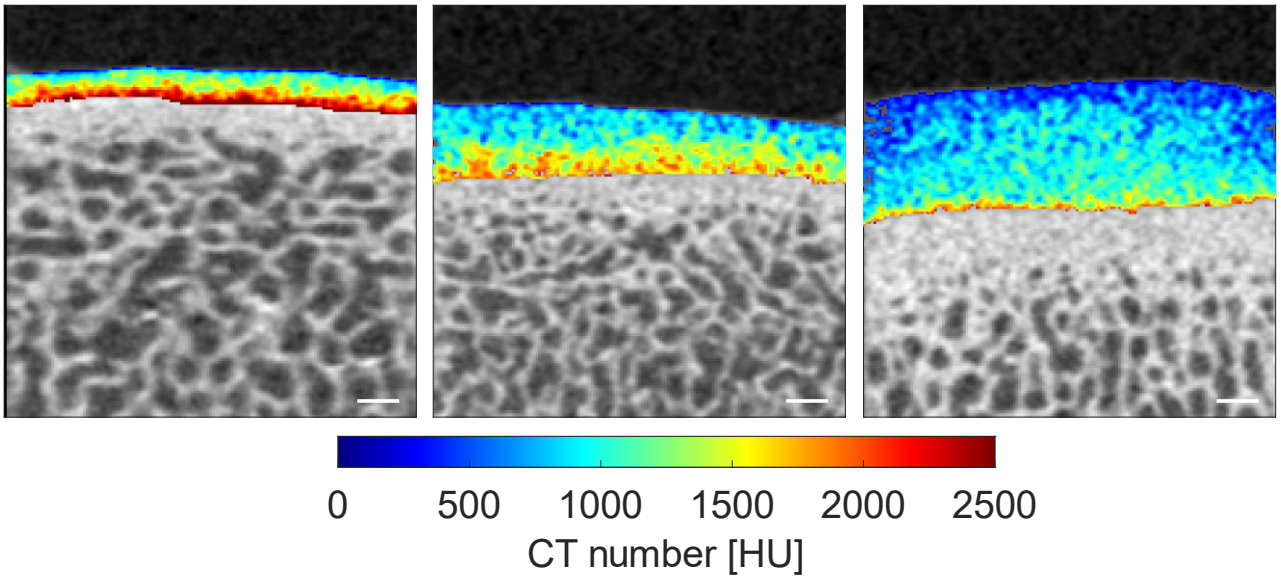

Figure 3.8. Sections of reconstructed volumes from HR-pQCT acquisitions. Samples representative of thin (left), average (centre) and thick (right) tissue are reported, displaying the radiopacity of contrast-enhanced AC. White line bar = 1 mm.

In the context of HR-pQCT assessment, the range of CA concentration in AC tissue, defined by the minimum and maximum CT numbers, was found to be comparable across OC cores with varying AC thicknesses (Figure 3.8). Regarding the distribution of CT numbers across the AC thickness, an increasing trend in attenuation values was observed from the articular surface to the deep zone (Figure 3.9).

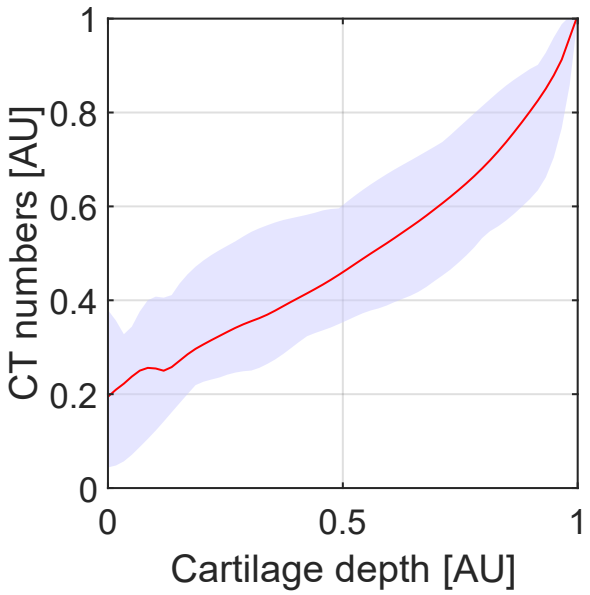

Figure 3.9. Average profile (red line) of radiopacity, evaluated on N=18 samples previously normalised to their maximum CT number. The average profile points out an increasing radiopacity from the surface (i.e., tissue depth = 0) towards the deep layer (i.e., tissue depth = 1) of AC.

Focusing on the relationship between AC morphology (thickness), composition (PG content), and functionality (viscoelastic properties), several key findings were identified (Table 3.5, 3.6 and 3.7). Regarding the relationship between AC morphology and composition, a significant negative correlation was observed, specifically between tissue thickness and CT number: $\rho = -0.888$ ($p < 0.001$) (Table 3.5).

Table 3.5. Spearman's correlation coefficients (ρ) between AC morphology – i.e., tissue thickness, computed by HR-pQCT approach – and functionality – i.e., viscoelastic properties. * $p < 0.05$; ** $p < 0.01$; *** $p < 0.001$.

	E_0	**S_0**	**τ**	**β**	**E_{eq}**
AC Thickness	ρ = -0.926 ***	ρ = -0.685 **	ρ = 0.661 **	ρ = -0.683 **	ρ = -0.323

Moving to the relationship between AC composition and functionality, significant, weak to strong, positive correlations were found between CT number and tissue elastic properties (Table 3.6).

Table 3.6. Spearman's correlation coefficients (ρ) between AC composition – i.e., PG content, computed by CE HR-pQCT – and functionality – i.e., elastic properties. * $p < 0.05$; ** $p < 0.01$; *** $p < 0.001$.

	E_0	**S_0**	**E_{eq}**
CT number	ρ = 0.943 ***	ρ = 0.752 ***	ρ = 0.455

Furthermore, significant, weak to moderate relationships were highlighted between CT number and AC viscous properties (Table 3.7).

Table 3.7. Spearman's correlation coefficients (ρ) between AC composition – i.e., PG content, computed by CE HR-pQCT – and functionality – i.e., viscous properties. * $p < 0.05$; ** $p < 0.01$; *** $p < 0.001$.

	τ	**β**
CT number	ρ = -0.589 *	ρ = 0.660 **

3.3.4.Discussion

The purpose of the present study was to investigate possible correlations between mechanical properties and data achievable from high-resolution X-ray scan of the contrast-enhanced AC.

The findings for AC thickness estimates highlighted consistency between the microCT and HR-pQCT approaches, supporting the reliability of HR-pQCT for evaluating contrast-enhanced AC thickness. Minor discrepancies observed between the two modalities are likely attributable to differences in image acquisition—planar in the case of microCT and volumetric for HR-pQCT—as well as variations in spatial resolution. Specifically, the higher resolution of microCT allows for the detection of finer structural features within the tissue.

The design of the study involved the investigation of the AC mechanical properties prior to performing the protocol required by contrast-enhanced HR-pQCT. This choice was based on the known effect of the contrast agent on the mechanical response of AC [367], which could have introduced bias into the findings of the study.

The findings derived from contrast-enhanced HR-pQCT revealed a depth-dependent distribution of CT numbers within the AC tissue. Owing to the cationic nature of the contrast agent employed in this study, the observed increase in CT number with depth indicates a corresponding progressive increase in PG content across the AC thickness [385]. These results align with previous evidence on PG distribution, as demonstrated by a range of ex vivo reference techniques—including histology [388], histochemistry [389], digital densitometry [390], FT-IR spectroscopy [391], and Raman spectroscopy [392]—as well as imaging modalities such as contrast-enhanced X-ray techniques [114,116,147,179,179].

The present study highlighted a significant negative correlation between AC thickness and tissue PG content. This suggests that PGs play a crucial contribute in supporting compressive loads particularly in healthy, thin AC. This evidence is at odds with the findings of a previous study, which showed an increase in PG content as a function of AC thickness [393]. Such a discrepancy might be ascribed to

both the nature of the species being investigated and sample size, rather than the specific approach employed to estimate the amount of PG content. The correlations between AC thickness and mechanical properties – i.e., considering the negative correlations with the elastic response support the hypothesis that a high PG content within thin AC provides a stiff response to external, compressive stimuli. Of course, these evidence and hypotheses are limited to healthy AC – as the one herein investigated. They cannot be generalised to pathological tissue, in which a decrease in thickness and PG content results in a progressive deterioration of the tissue mechanical properties as the disease progresses [394–396].

Proteoglycans contribute significantly to the load bearing capacity of AC. Their FCD [397] generates osmotic pressure within the interstitial fluid, which is crucial to withstand external compressive stimuli [9]. By accounting for both electrostatic and non-electrostatic interactions, proteoglycans contribute substantially to the overall modulus of AC. In addition to their role in stiffness, proteoglycans are also involved in the tissue's viscous behaviour, particularly through flow-independent intrinsic mechanical responses of the ECM constituents [398]. AC is composed of biological polymers engaged in heterogeneous and complex interactions. According to such heterogeneity, different polymers and interactions are involved in the diverse phase of viscous phenomenon, i.e., reptation of monodisperse polymers, and transient binding of polydisperse polymers (macromolecules) [399].

In agreement with the available evidence, the results obtained in this study from a small sample support the existence of correlations between CT number (PG content) and AC mechanical properties, considering both elastic and viscous parameters.

Regarding the elastic properties, the positive correlations between CT number and S_0, E_0, and E_{eq} (see Table 3.6) suggest that the higher the PG content, the stiffer the instantaneous and equilibrium response of the AC. Such evidence are in strong agreements with the literature, considering both the instantaneous [147,180,400,401] and equilibrium [87,169,180,402] elastic parameters and regardless the approach employed to estimate the PG content.

Concerning the viscous parameters, correlations were found between CT number and τ or β suggesting that the higher the CT number (PG content), the faster the exhaustion of the viscous phenomena. Due to the complex nature of the phenomena underlying fluid-independent viscosity, the topic deserves further discussion.

The relaxation time τ is linked to the physical features of the polymers composing the system, e.g., concentration, mobility and stiffness. According to the theory of polymer dynamics, faster stress-relaxation (i.e., lower τ values) is associated with an increased molecular mobility and a decreased molecular stiffness [350].This suggests that fluid-independent relaxation processes reach an

equilibrium more rapidly in systems composed of more compliant polymers. This hypothesis is supported by the findings of this study, where i) faster relaxation was observed in more compliant AC, as evidence by a significant negative correlation between τ and E_0 ($\rho = -0.544$, $p < 0.05$), and ii) thicker tissue exhibited a more compliant mechanical response. In summary, the following trend was observed: increased AC thickness is associated with lower CT numbers (i.e., lower PG content), which in turn suggests higher molecular mobility of polymers, a more compliant tissue response, and consequently, a more rapid dissipation of viscous phenomena.

The stretching parameter β depends on the type of polymers composing AC and on their relative motion [396]. A previous study suggested that a decrease in β is associated to an increase in the molecular weight of the entangled polymers [403]. The positive correlation between CT number (PG content) and β herein highlighted is supported by existing literature [87].

This study presents several limitations that should be acknowledged. First, no gold standard techniques for the assessment of PG content were employed to validate the data obtained from contrast-enhanced HR-pQCT. Nevertheless, it is important to note that the electrostatic affinity between CA4+ molecules and the fixed negative charges of PG is a well-established and extensively studied phenomenon, consistently confirmed across numerous studies [61,160,170,179,338].

Second, the time interval between the mechanical characterization of AC via indentation testing and the estimation of PG content through HR-pQCT—approximately 22 hours—may have led to progressive tissue degradation, potentially affecting its compositional integrity. However, this time frame was previously identified as the minimum duration required to achieve equilibrium in CA4+ diffusion within AC [385], and thus represents the necessary condition for reliable volumetric PG quantification.

Third, the sample size of the present study is limited. A larger cohort would be necessary to more accurately characterise and statistically validate the correlations observed between morphological, compositional, and mechanical parameters.

Moreover, the correlations reported in this work pertain exclusively to healthy AC. The onset and progression of joint pathologies, such as osteoarthritis, are known to alter the principal features of AC, notably reducing PG content and modifying its mechanical response [346,404–406]. Nonetheless, it is worth noting that findings from comparable studies investigating both healthy and pathological AC report consistent results, suggesting that degenerative conditions do not corroborate the fundamental relationships among tissue morphology, composition, and mechanics [87,407].

Despite the above limitations, the present study supports the existence of significant correlations among the morphology, composition and the mechanical response of healthy AC. These findings lay

the groundwork for a more comprehensive and integrative evaluation of key cartilage features in both research and clinical contexts.

3.3.5.Conclusions

Contrast-enhanced X-ray imaging allows for the identification of a significant correlation between AC thickness, PG content, and its viscoelastic mechanical properties. This approach holds considerable potential for the prediction of critical tissue characteristics in future clinical contexts. The methodologies introduced in this study may contribute to improving the early diagnosis of AC degeneration. Furthermore, they offer a valuable tool for assessing the effectiveness of therapeutic strategies and biomaterials aimed at AC repair and regeneration. Ultimately, these methods could inform and refine tissue engineering strategies, supporting the development of scaffolds that more accurately replicate the mechanical behaviour of native AC.

CHAPTER 4

Quantitative spectral micro-CT of a CA4+ loaded osteochondral sample with a tabletop system

This chapter was reproduced from the published manuscript:

"Quantitative spectral micro-CT of a CA4+ loaded osteochondral sample with a tabletop system"
S. Fantoni, F. Brun, P. Cardarelli, F. Baruffaldi, V. Cristofori, A. Taibi, C. Trapella, L. Brombal
Eur. Phys. J. Plus 139, 735 (2024). DOI: 10.1140/epjp/s13360-024-05428-0

Abstract

Micro-computed tomography (µCT) is the gold standard for nondestructive 3D imaging of biomedical samples in the centimeter scale, but it has limited effectiveness in revealing intricate soft tissue details due to the limited attenuation contrast. Radiopaque contrast agents that accumulate in the structures of interest are employed to enhance their visibility. However, the increased attenuation provided by the contrast agents does not guarantee discrimination among tissues. This issue can be solved by spectral µCT (SµCT) systems employing small-pixel chromatic photon-counting detectors. These detectors, combined with material decomposition algorithms, allow the generation of high-resolution material-specific 3D maps. This work aims to demonstrate the potential of photon-counting X-ray SµCT on osteochondral samples loaded with a cationic iodinated contrast agent (CA4+) at a spatial resolution below 50 µm, and to compare the results against a conventional µCT system. An osteochondral sample extracted from a bovine stifle joint was loaded with CA4+ and imaged with a novel multimodal X-ray imaging system, featuring a 62 µm pixel CdTe spectral detector (Pixirad1-PixieIII). After material decomposition, quantitative 3D density maps of iodine and hydroxyapatite were reconstructed. The same sample was also scanned with a commercial µCT scanner with matched spectrum and exposure time. SCTµ images at a (measured) spatial resolution comparable with the commercial scanner (~45 µm) were obtained. Spectral images allowed for a fully automatic segmentation of cartilage and subchondral bone. The unambiguous discrimination between iodine and hydroxyapatite revealed a more realistic representation of proteoglycan distribution compared to conventional imaging.

4.1. Introduction

Articular cartilage (AC) is a soft tissue conferring nearly frictionless and smooth motion at the articular level. The interplay among its constituents, namely collagen, proteoglycans (PGs), and interstitial fluid, delivers excellent mechanical properties to healthy AC [55]. Compositional and morphological modifications of AC, identified as fibrillation of collagen fibers and depletion of PGs, alter the homeostasis of AC with a severe negative impact on its mechanics. As a consequence, progressive wear of AC triggers the onset of joint-affecting diseases such as osteoarthritis [333]. Further hallmarks of AC degeneration are also detected on the subchondral bone, the dense mineralized layer supporting AC in load-bearing events [408]. For these reasons, the availability of imaging tools enabling the identification and monitoring of the progression of osteoarthritis on both AC and subchondral bone is of paramount importance. Nowadays, X-ray micro-computed tomography (μCT) provides high-spatial resolution 3D reconstructions of biological samples.

For advanced systems featuring synchrotron radiation, spatial resolution reaches even the cellular level [409,410]. Several studies demonstrated that μCT is a powerful tool for the evaluation of mineralized tissues [411]. However, the low radiopacity of AC hinders the evaluation of the progression of the pathological state through μCT. Recently, the adoption of dedicated contrast agents (CAs) allowed advances in terms of qualitative and quantitative assessment of AC. In fact, CAs based on high atomic number (Z) elements, such as iodine and gadolinium, significantly enhance X-ray visualization of soft tissues [162]. Depending on the electrostatic properties of CAs, they can be categorized into non-ionic and ionic CAs. Ionic CAs can be further subdivided into anionic and cationic, if the corresponding molecules host negative or positive charge density, respectively. The ionic nature of CA molecules determines the electrostatic interaction with biological structures [64]. In this context, conventional commercial non-ionic and anionic CAs were tested for X-ray visualization of AC, displaying negative or weak correlation to PG content, which exhibits a negative fixed charge density [334]. As a result, high concentrations and long exposure times were required to yield an effective AC imaging [154]. In recent times, dedicated CAs have been developed to improve cartilage visualization, as in the case of cationic iodine-based CA4+ [160]. The positive charge density generates electrostatic attraction between CA4+ molecules and negatively-charged PGs, resulting in shorter diffusion times, lower CA concentrations required, and direct correlation of CA distribution with PG content [154].

Although the use of CAs addresses the poor visibility of the cartilage, contrast-enhanced μCT (CEμCT) still fails in distinguishing

tissues exhibiting similar X-ray attenuation, such as contrast-enhanced AC from subchondral bone, potentially hindering their exact segmentation, quantification, and, more generally, a detailed evaluation of osteoarthritis progression [158]. This limitation can be overcome by using X-ray spectral imaging (XSI). XSI relies on measurements at two (or more) X-ray energy levels (or bins) and provides tissue separation by exploiting the different attenuation energy dependence of the CA.

Historically, XSI has been implemented by using dual-energy or multi-energy methods based on acquisitions of the sample performed with different X-ray spectra [175]. This typically implies the use of complex dual source or fast kilovoltage switching systems or, alternatively, requires multiple scans, posing concerns in terms of image registration and, for in-vivo applications, of deposited radiation dose [412]. Along with studies based on conventional X-ray tubes, various XSI tests have been carried out at synchrotron facilities for the visualization of AC with different combinations of ionic contrast media [165,167–169]. Despite the demonstration of high-quality imaging, the peculiar features of synchrotron radiation are hardly reproducible in laboratory-based setups.

The recent advent of photon-counting detectors (PCDs) is going to revolutionize XSI in preclinical and clinical imaging applications, thus overcoming these concerns [181,413,414]. In fact, the adoption of PCD devices brings a simplification in the hardware and, by employing a broad X-ray spectrum, allows to target applications making use of different contrast media by simply adjusting the energy-calibrated thresholds. The possibility of acquiring images over multiple energy bins in a single shot guarantees exact spatial and temporal registration of spectral images and does not require additional radiation dose [415]. Moreover, with respect to conventional integration devices, the design of PCDs implies advantages in terms of electronic noise suppression (Poisson-dominated noise), artifact suppression, and contrast-to-noise-ratio, the latter due to their intrinsic absence of spectral weighting upon detection [414]. Even more recently, spectral μCT (SμCT) has been made possible by the availability of devices featuring a small pixel size

(~50 μm) and charge-sharing compensation or clustering mechanisms guaranteeing both spectral performance and high-spatial resolution [416,417].

Focusing on AC applications, previous studies implemented XSI of AC with anionic and non-ionic CAs, exploiting the anti-correlation between their distribution across the tissue and PG content [189,190]. Cationic CAs were considered for quantitative imaging of AC with dual-energy techniques implemented with indirect conversion detectors by using monochromatic synchrotron radiation [166,168,169] and recently with a PCD-based CT system by Paakkari et al. [180], although in the latter attention was drawn exclusively to the assessment of AC and not to the underlying subchondral bone, and the achieved spatial resolution was in the order of 200 μm.

In this framework, our research work demonstrates the potential of SμCT based on a novel system integrating a chromatic PCD
(Pixirad1-PixieIII) in the context of osteoarticular imaging at a spatial resolution below 50 μm. Following the treatment to CA4+ targeting PG's structures, osteochondral samples were scanned with scan time and X-ray spectrum, matched to a conventional state-of-the-art μCT scanner. Spectral decomposition has been performed in two basis materials, and imaging performance on the same sample was directly compared to a commercial CEμCT system. Results provide a simultaneous evaluation (both qualitative and quantitative) of cartilage and bone tissues, with the smallest pixel size reported so far referring to a tabletop PCD system, to the best of the authors' knowledge. Noteworthily, the SμCT system allowed a better understanding of the distribution of CA4+ at the bone/CA interface and enabled the automatic segmentation of cartilage and subchondral bone.

4.2. Materials and Methods

4.2.1. Preparation of sample and contrast agent

The imaged sample was one cylindrical osteochondral plug (Ø = 10 mm, height= 10 mm) extracted from a bovine stifle joint, provided by a local slaughterhouse, and stored in phosphate-buffered saline (PBS) solution-soaked lint at T = −20◦C. Before the image acquisition, the sample was thawed in PBS solution at T = 4◦C overnight, inserted in a custom-made polymethyl-metacrylate (PMMA) sample holder and immersed in CA solution [83]. The sample holder had an inner diameter of 10 mm, so that a single cylindrical sample could fit inside, and a height of 30 mm, to fit both the sample and the CA bath.
The used contrast agent was CA4+ (5, 50-[Malonylbis(azanediyl)]bis[N1,N3-bis(2-aminoethyl)-2, 4, 6-triiodoisophthalamide] chloride), which contains six iodine atoms per molecule. The net positive charge (q = +4 per molecule) confers the characteristic affinity of CA4+ to PGs, which have instead a negative fixed charge density. CA4+ salts were synthesized according to the work of Stewart et al. [116], and dissolved in PBS solution to reach the desired iodine concentration of 10 mgI/ml. The pH of the resulting aqueous compound was balanced to 7.4 by adding NaOH 4 M. The CA4+ solution was poured on the surface of the cartilage tissue after the insertion of the plug in the sample holder. In addition to the 10 mgI/ml solution, three other CA4+ solutions, with iodine concentrations of 20 mgI/ml, 15 mgI/ml, 5 mgI/ml, and 0 mgI/ml (pure water), respectively, were prepared and used for the calibration of the SμCT system.

4.2.2. μCT acquisition

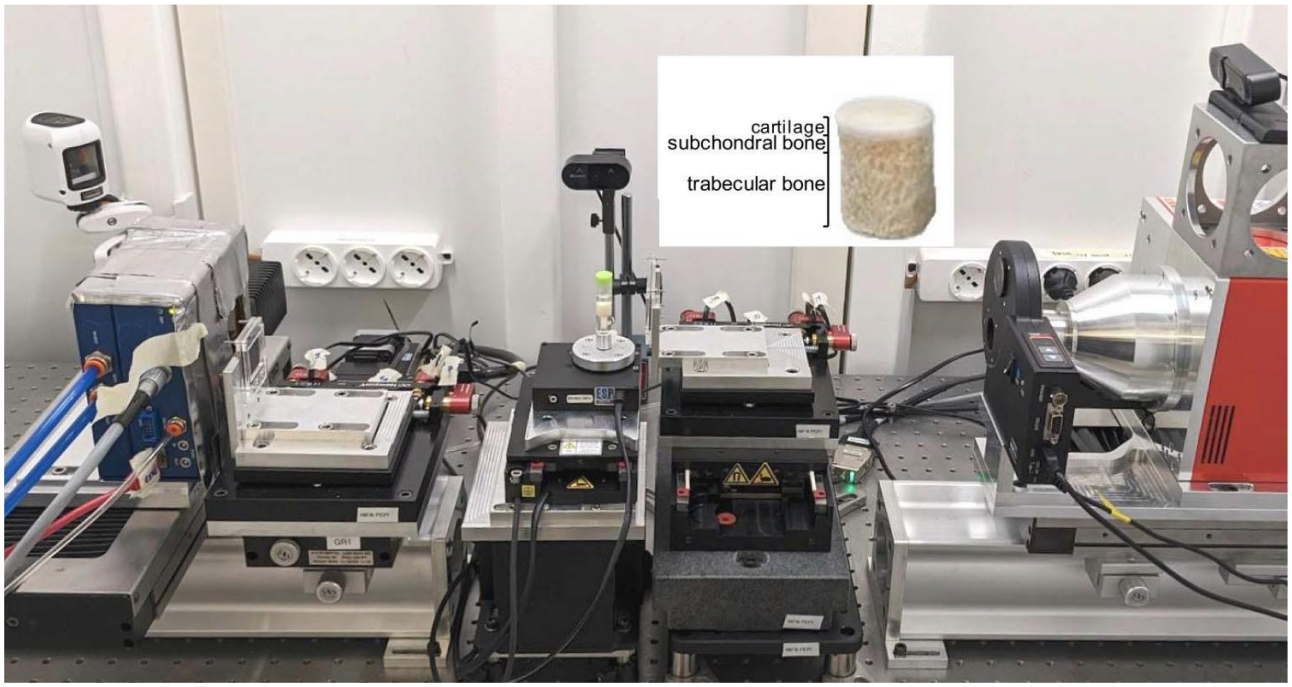

Fig. 4.1 Photograph of the SμCT experimental setup at PEPILab. The inset shows a zoomed image of the osteochondral sample where its main components are outlined. Reproduced under the terms of the CC BY 4.0 license. © 2024 Fantoni et al.

SμCT acquisitions were performed at the multipurpose X-ray laboratory PEPILab [184] at the Italian National Institute for Nuclear Physics (INFN) in Trieste: the experimental setup used for the acquisition is shown in Fig. 4.1. X-rays are produced by a conventional microfocus source (Hamamatsu L10101), operated at 50 kV and 200 μA. A filtration of 0.12 mm of Cu and 0.2 mm of Al was introduced, resulting in a spectrum peaked at the iodine K-edge energy (33.2 keV). From previous characterization measurements, the focal spot size was estimated to be 16±3 μm for the used voltage and current settings [184]. The used chromatic PCD is a Pixirad1-PixieIII, featuring a 62 μm pixel size and a sensitive area of 512×402 pixels, corresponding to 31.7×24.9 mm^2 [417].

The overall source-to-detector distance was set to 65 cm, while geometric magnification was 1.83, corresponding to a reconstruction voxel size of 34 μm and a field-of-view of 17.2×13.7 mm2. The detector was operated in the charge-summing mode that compensates for the effect of charge sharing and optimizes the intrinsic spatial resolution, corresponding to the dimension of one pixel [418]. Spectral images were generated by using the two-color mode, which yields two independent images corresponding to low and high-energy bins. Bins are defined by two energy-calibrated thresholds, which were set to 26 keV and 33 keV. The second threshold was chosen to maximize the iodine signal, while the first was adjusted to reject the cadmium fluorescence (Kα at 23.2 keV), hence reducing the spectral cross-talk between energy bins. It should be noted that in a CdTe sensor also tellurium fluorescence is produced. However, it is locally self-absorbed in the sensor with high probability as its energy (Kα at 27.5 keV) is just above the cadmium K-edge (26.7 keV) [418].

Exposure time was set to 7.2 s per projection and 1000 projections were acquired over a 360-degree rotation, corresponding to an overall acquisition time of 120 min. No relevant polarization time-dependent effects [419] were observed during the acquisition, owing to the relatively low X-ray flux (order of 500 photons/pixel/s) and the fast polariza- tion/depolarization cycles between consecutive projections enabled by the step-and-shoot acquisition procedure. A random jittering motion of the detector was introduced in between projections to mitigate ring artifacts [420].

In addition to the osteochondral sample, two calibration phantoms were imaged to achieve accurate quantification of iodine concentration and bone density. The first was an epoxy resin phantom (QRM, Moehrendorf, Germany) containing five inserts with different hydroxyapatite (HA) densities. The second was custom-made phantom including five cuvettes filled with different concentrations of CA+, as described in the previous section.

After the spectral scan, the same osteochondral core was acquired with a commercial µCT system (Skyscan 1072, SkyScan, Aartselaar, Belgium) at the Medical Technology Laboratory of Istituto Ortopedico Rizzoli in Bologna. Between acquisitions (∼ 48 h), the sample was stored in CA4+ solution at T = 4◦C. CEµCT acquisitions were performed with the parameters routinely used for osteochondral samples. The X-ray tube was operated at a voltage of 50 kV and 200 µ A (as for the SµCT scan) with an added filtration of 1 mm-Al. 410 projections over 185◦ were acquired with an exposure time of 11.8 s per frame, leading to a total scan time (including dead time) of 112 min, which is comparable to the SµCT scan. Given the similar X-ray beam quality, total exposure time and source-to-sample distance of SµCT and commercial CEµCT, the number of projections used matched the integrated fluence at the sample. Images were collected with an energy-integrating detector (Hamamatsu C4742-55), consisting of a CCD camera coupled to a scintillator. The CCD array features a pixel size of 6.7 µm, and an active area of 1024 × 1024 pixels. The scintillator is coupled to the sensor with optical fibers and a 3.7:1 size ratio. Provided a source-to-detector distance of 84 cm and geometric magnification of 2.2, the final reconstruction voxel size was 11.5 µm and the field-of-view 11.8 × 11.8 mm^2.

4.2.3. Calibration, data processing, and analysis

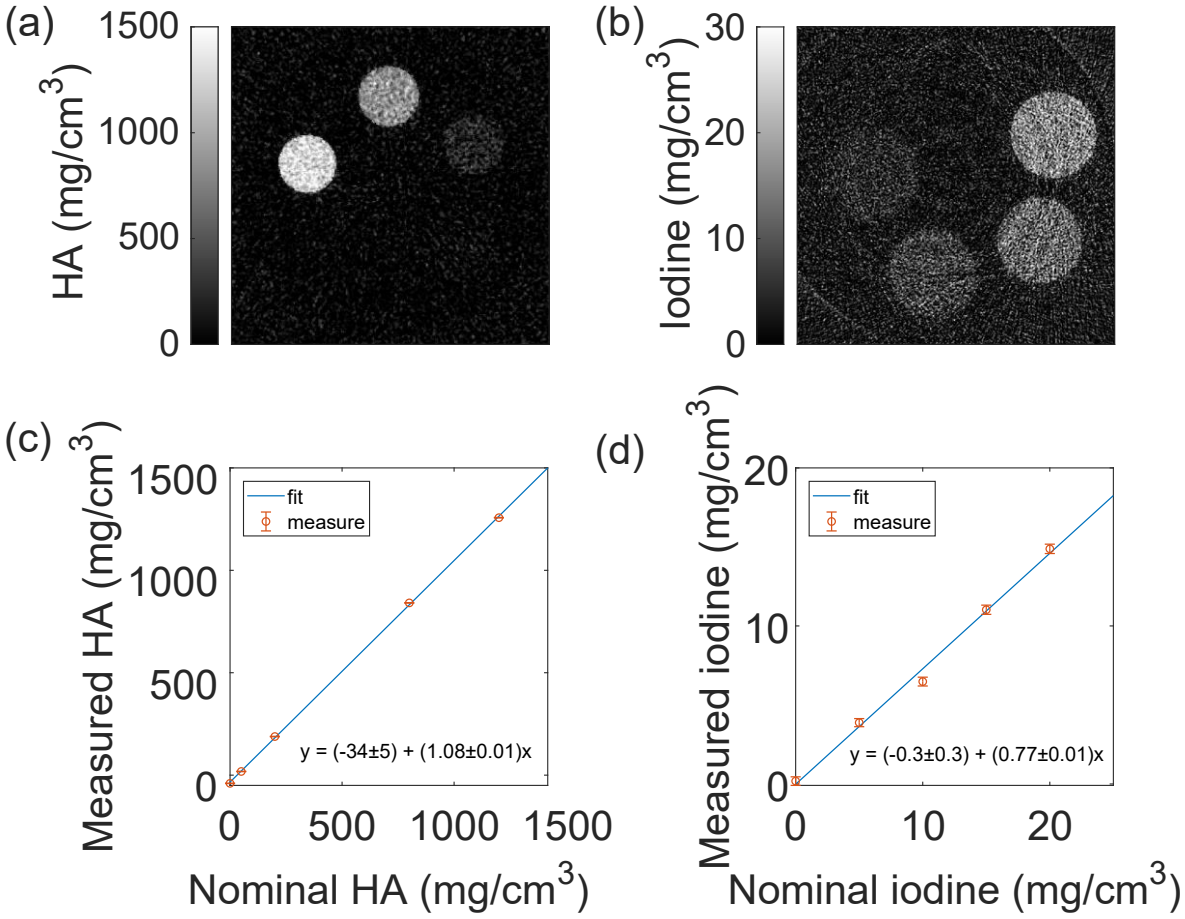

Fig. 4.2 HA (a) and iodine (b) density maps of the two calibration phantoms, respectively. In (c) and (d), the respective measured against nominal density values and the linear fit functions. Fit parameters and associated uncertainties are reported in the plots. Reproduced under the terms of the CC BY 4.0 license. © 2024 Fantoni et al.

High- and low-energy projection images of the two calibration phantoms underwent a dedicated preprocessing procedure to mitigate detector-specific artifacts [421]. Preprocessed projections were reconstructed via conventional cone-beam FDK [422] with Shepp-Logan filtering, by using the implementation available in the open-source software library TIGRE [423]. Spectral basis material decomposition was performed on the 3D reconstructed volumes through matrix inversion. The mass attenuation coefficient system matrix accounts for the X-ray spectrum and the detector spectral response (including fluorescence), which is obtained with an experimentally validated custom simulation software [424,425]. The basis materials chosen for the decomposition of the two phantoms were HA and iodine. From the resulting HA and iodine maps, shown in Fig. 4.2 a and b, mean densities were measured from circular areas within the inserts/cuvettes and plotted against their nominal value. Uncertainty on the measured data was calculated as the standard error of the mean. Data were fitted with a linear function, whose parameters are used to calibrate the osteochondral sample's images. Calibration results are reported in Fig. 4.2 c and d.

The osteochondral sample's data followed the same pipeline described for the calibration phantom except for the addition of a self- supervised deep denoising procedure that is applied to reconstructed datasets [421]. This processing step is carried out to mitigate noise amplification occurring in the following spectral decomposition step [426]. Consistently with the calibration, the materials chosen for the spectral decomposition of the osteochondral core were iodine and HA, for cartilage and bone tissues, respectively. The former element accounts for the radiopacity of CA4+ targeting PGs in the cartilage tissue. The latter is a mineral constituent of bone tissue and hosts calcium as its radiopaque counterpart. As a result, mass density 3D maps of iodine and HA were obtained from the reconstructed volumes. To carry out the direct comparison with CEμCT, a non-spectral attenuation reconstruction was produced by summing high- and low-energy projections prior to processing. The availability of spectrally decomposed volumes allowed for the implementation of an automatic segmentation procedure for separating bone and cartilage based on the Otsu thresholding algorithm [427]. The obtained volumetric masks were then applied on both (non-spectral) attenuation and material decomposition volumes.

The CEμCT reconstruction was performed by using the manufacturer's software (NRecon, Skyscan, Aartselaar, Belgium). Since the two scans feature different voxel sizes and detector technologies, the spatial resolution has been estimated from the reconstructed images for both CEμCT and (attenuation) SμCT scans. Spatial resolution was evaluated by fitting with an error function (erf) the intensity profile obtained across a sharp bone detail, and defined as the full width at half maximum (FWHM) of the Gaussian obtained deriving the erf fit. Additionally, to apply the same segmentation masks on the CEμCT image, the reconstructed attenuation volumes were co-registered. The registration of volumes was performed in Matlab, by using the function imregister. Among the possible registration methods, the similarity criterion was selected, which allows for rotation, translation and dilation of target volume together with the erf fit. Profiles are extracted from the yellow line ROI drawn in (a) and (b), respectively, pointed out by the arrows (CEμCT) to the reference volume (SμCT). The metrics used is the mean square difference and the optimizer is regular step gradient descent. The results of the registration were evaluated by visual inspection of the voxel-by-voxel subtraction of the registered and target volumes.

After registration, the depth-wise intensity concentration profiles across the cartilage were extracted and compared for both attenuation images obtained with the two systems and for the iodine decomposed image of the SμCT system. Attention was focused on the differences between attenuation and iodine density (i.e., PG) distributions close to the AC tidemark, which is the narrow region of interface between calcified cartilage and subchondral bone. In fact, modifications to the cartilage tidemark can be considered as a hallmark for recognition of osteoarticular pathologies like

osteoarthritis [408]. For this reason, the tidemark voxels of all the images were realigned to a planar surface via translation in order to study the profiles across the whole volume as a function of the distance from the cartilage-bone interface. The tidemark position for each voxel column was identified as the first pixel separating the subchondral bone from the segmented volume of cartilage.

4.3. Results

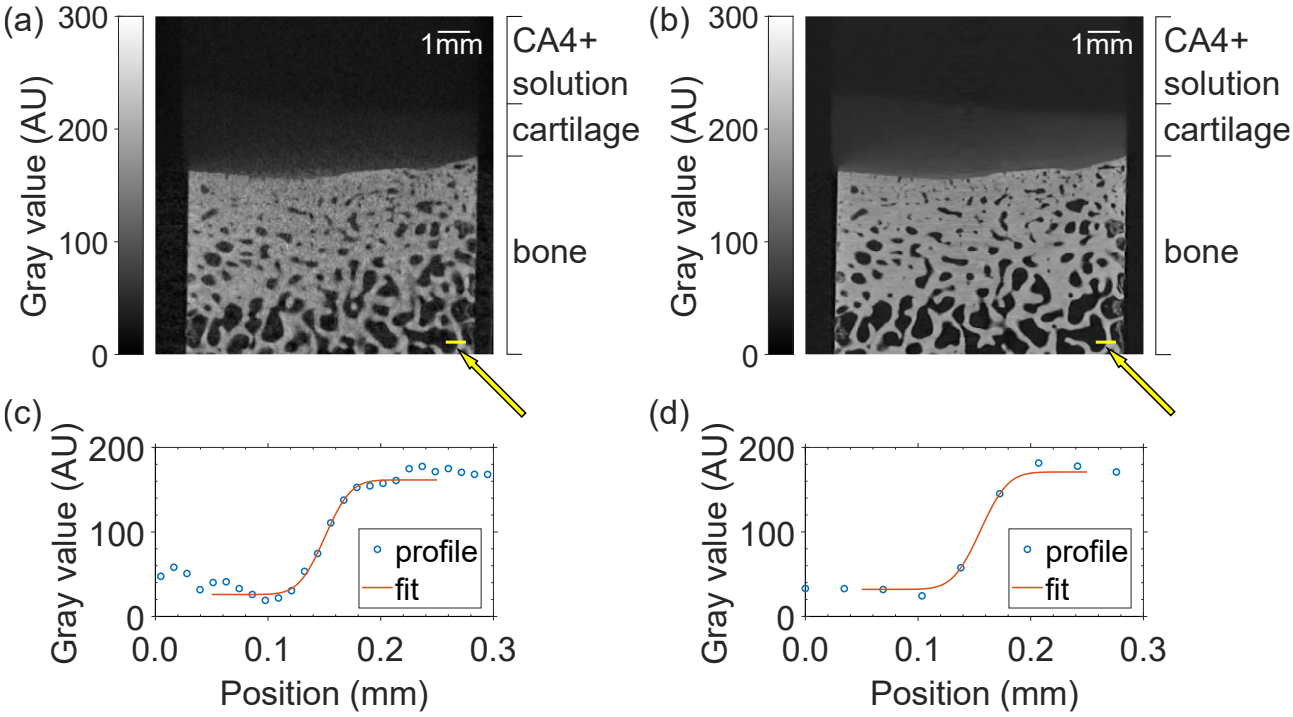

Fig. 4.3 Section of reconstructed volume from CEμCT (a) and from SμCT (b). In both sections, the three main layers of the osteochondral plug, namely CA4+ bath, cartilage, and bone are highlighted. In the bottom panels, the line profiles for CEμCT (c) and SμCT (d) are reported together with the erf fit. Profiles are extracted from the yellow line ROI drawn in (a) and (b), respectively, pointed out by the arrows. Reproduced under the terms of the CC BY 4.0 license. © 2024 Fantoni et al.

One transverse slice obtained from the CEμCT reconstruction and the corresponding detail from the (nonspectral) attenuation volume obtained with the SμCT are reported in Fig. 4.3. In both images, three layers of the sample are fairly visible, corresponding (from top to bottom) to the CA4+ bath, the contrast-enhanced cartilage, and the underlying bone tissue. As demonstrated by the line profiles across a sharp bone detail, the spatial resolution of the two systems is similar and the FWHM is estimated to be 45±15 μm for the SμCT and 43±15 μm for the CEμCT, where uncertainties correspond to the 95% confidence level given by the fitting procedure.

The same transverse slice reconstructed from the high- and low-energy bins of the SμCT dataset is shown in panels (a) and (b) of Fig. 4.4. From the images, it is clear that, while the bone tissue signal

decreases at high energy, the cartilage signal has an opposite behavior due to the presence of CA4+. Panels (c) and (d) show the iodine and HA mass density maps after spectral decomposition and automatic segmentation.

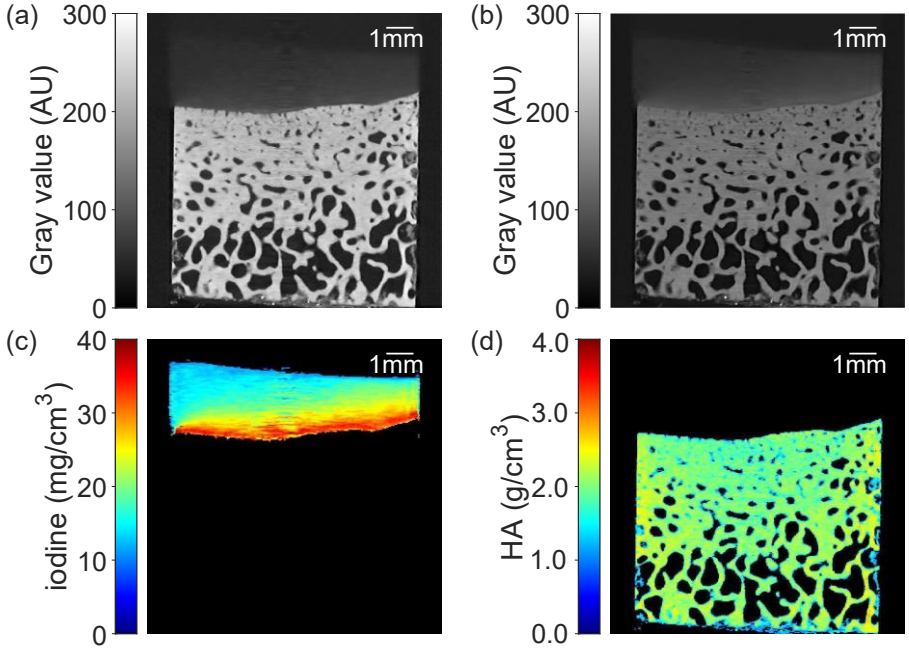

Fig. 4.4 Section of the reconstructed volume of laboratory SμCT, taken from low-energy (a) and high-energy bins reconstructions (b). Spectral decomposition in iodine (c) and HA basis (d) after the application of the automatic segmentation. Reproduced under the terms of the CC BY 4.0 license. © 2024 Fantoni et al.

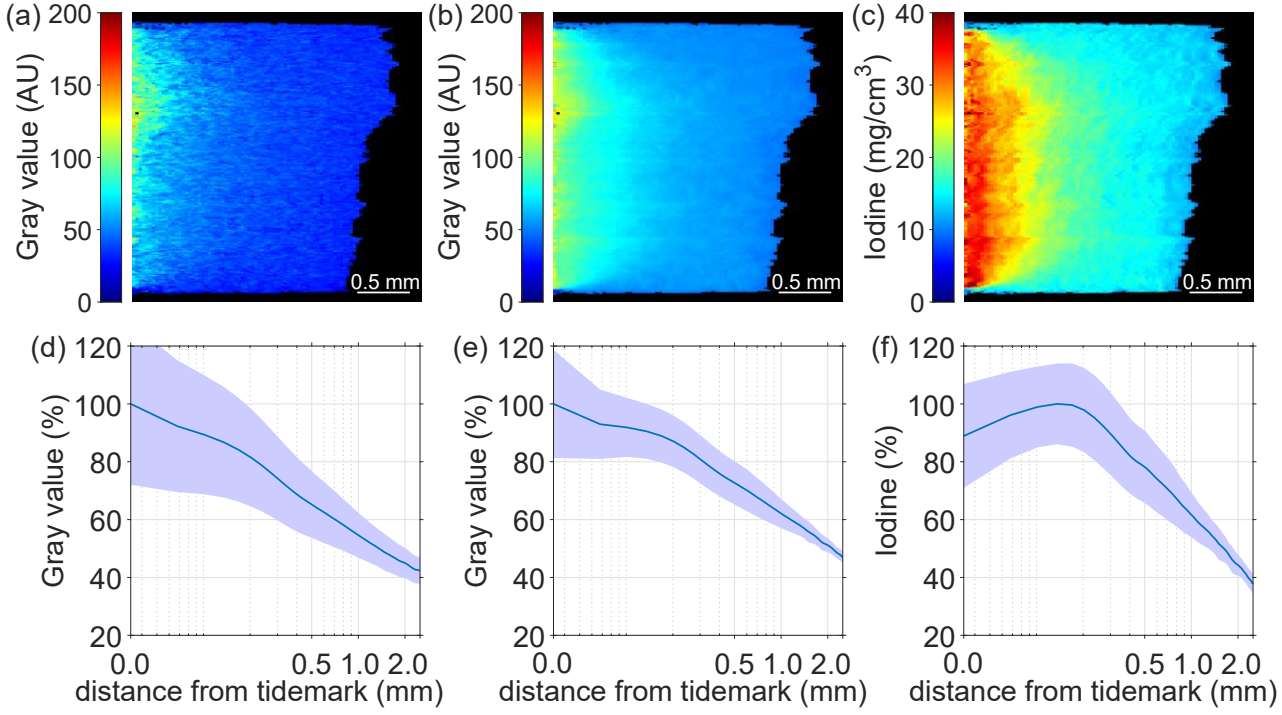

Fig. 4.5 Sections from volumes realigned to a planar tidemark surface, from CEμCT (a), and absorption (b) and iodine-base decomposition (c) from SμCT. Their respective intensity profiles (solid lines), corresponding to the volume average as a function of the distance from the tidemark, are shown in (d), (e), and (f). Similarly, for each profile, the data dispersion (shaded area) corresponds to one standard deviation. For comparison, each profile is normalized to its maximum value.

The distance from the tidemark position (0 mm) is reported in logarithmic scale in plots (d), (e), and (f). Reproduced under the terms of the CC BY 4.0 license. © 2024 Fantoni et al.

The intensity distributions across the cartilage volumes obtained from the CEμCT, (non-spectral) attenuation SμCT, and the iodine mass density distribution obtained from the SμCT are shown in panels (a) to (c) of Fig. 4.5, respectively.
Their respective normalized intensity profiles are reported in panels (d) to (f). From the profiles, it can be noted that, regardless of the system used, attenuation-only μCT images have a signal peaked at the bone/cartilage interface, while the spectral image reveals an iodine peaking approximately 150 μm above the interface. Albeit this value can be affected by possible misregistration errors (order of 1 pixel), the fact that the shift in the peak appears systematically across the whole volume indicates a clear difference between the SμCT and CEμCT profiles.

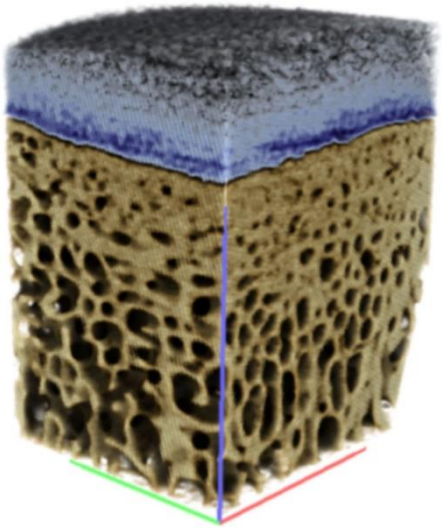

Fig. 4.6 3D rendering of the sample acquired with the SμCT system. The blue palette displays iodine content (darker at higher concentrations), the light brown palette displays the HA distribution. Reproduced under the terms of the CC BY 4.0 license. © 2024 Fantoni et al.

Starting from material decomposition volumes, a 3D rendering of the scanned sample was also produced, as shown in Fig. 4.6. The CA4+ perfused cartilage has been rendered in blue, where a darker color is related to a higher concentration, while the underlying bone structure is rendered with a light brown palette.

4.4. Discussion

Given similar parameters in terms of acquisition time and X-ray spectrum, a qualitative comparison between the conventional CEμCT and the (non-spectral) attenuation images acquired with the SμCT

reveals comparable results in terms of image appearance, as seen in Fig. 4.3. This also demonstrates that the sample was not significantly altered in the time elapsed between the two scans (48 h).

Quantitatively, the two systems revealed a similar spatial resolution in the order of 45µm, despite a factor of 3 difference in voxel size. This is related to the high efficiency and sharp response of the PCD detector used in the SµCT. In both scans, features within the mineralized tissue, namely the characteristic trabeculae found in cancellous bone, could be easily distinguished. On the other hand, even if the SµCT image shows a generally higher image quality, the interface between cartilage and CA4+ remained ambiguous. The same observation holds for the interface between cartilage tissue and subchondral bone.

This limitation is overcome by spectral images delivered by the SµCT. A higher intensity of dense structures is found in the low-energy channel with respect to the high-energy one, while the opposite behavior is observed in the presence of iodine. This allows for the discrimination between the cartilage and the mineralized tissue as well as for masking out the CA4+ bath that contains a lower iodine concentration with respect to the cartilage, as reported in panel (c) of Fig. 4.4. Moreover, further quantitative examination of bone tissue, based on quantification of the mineral density, is promptly accessible in spectral modality, as shown in panel (d), while calibration curves are required in attenuation modality.

Focusing on the cartilage layer, a depth-wise intensity/concentration dependence could be observed, generally decreasing from the deep cartilage, rich in PG, to the superficial layer, as demonstrated in Fig. 4.5. Noteworthily, the comparison between profiles from absorption and spectral imaging outlines the potential of material decomposition. In particular, while the attenuation-based CTs show a similar monotonically decreasing behavior regardless of the used imaging system, the peak in the spectral density profile is shifted with respect to the bone/cartilage interface. This is due to the fact that only the spectral decomposition can discriminate between different contributions to the attenuation at the cartilage tidemark, distinguishing between the iodine, related to PG concentration, and the calcified tissue. From a biological perspective, the PG distribution shown in the material decomposition can be understood by considering that the cartilage tissue close to the tidemark shows increased content of calcification, at the expense of PG concentration. These results are consistent with previous literature. The work of Bansal et al. [154] demonstrated the correlation between CA4+ uptake and GAG overall content in the cartilage in bovine osteochondral samples from the femoral condyles. The 3D CA4+ distribution reported in their study showed a clear gradient, with increasing CA uptake in the deeper layer of cartilage. Similarly, the work by Honkanen et al [169] performed on human cadaver samples showed that, at diffusion equilibrium (72 h of immersion), CA4+ distribution at increasing depths in the cartilage correlates with PG concentration. The hypothesis that

the PG concentration decreases in calcified cartilage close to the tidemark is supported in the literature by independent methods, which provided direct measurements of thickness of calcified cartilage. Values of the order of 200 µm were found in Kauppinen et al. [428], by segmenting histological images from healthy human tissues.

In this context, the calcium quantification capabilities enabled by SµCT, could provide a powerful tool for the nondestructive 3D assessment of the calcified cartilage region. Indeed, the simultaneous but differentiated assessment of cartilage and subchondral bone is considered to be of great importance for the understanding of pathologies such as osteoarthritis, which concurrently develops in both tissues [408]. In previous works, the use of cationic CA4+ for the evaluation of cartilage tissue [94] was extensively validated using reference methods [101], conventional CT, and synchrotron µCT [147,166,171,339], but it was faced with the problem of comparable radiopacity of contrast-enhanced cartilage and calcified tissue [158]. This further implies that manual segmentation procedures are typically used for the delineation of articulating surfaces and cartilage-bone surfaces [165,167–169], potentially being imprecise and/or subject to operator-dependent bias. On the other hand, spectral data-based material decomposition enables the automatic segmentation of heterogeneous structures as demonstrated, for instance, in the 3D rendering of Fig. 4.6.

Despite only few studies making use of detector-based spectral systems have been reported in the literature on osteochondral samples, those works focused either on the diffusion of anionic CAs, which anticorrelates with PG [189], or on PG-affine CA4+ but at a much coarser spatial resolution (order of 200 µm) [180]. In this framework, to the best of the authors' knowledge, our work reports the first SµCT on an osteochondral sample loaded with an iodine-based cationic contrast agent to be scanned with a laboratory spectral PCD system at a (measured) spatial resolution below 50 µm.

It is understood that the promising results demonstrated in this paper have been obtained on a single sample, and need to be confirmed on a larger number of samples. This should also account for the fact that the features in the articular cartilage strongly depend on the location in articulating sites [173], hence differences in morphology (i.e., thickness) and composition (i.e., PG content) might impact the imaging outcome. Another limitation of the study is the simplified (cylindrical) geometry of osteochondral samples. In fact, the relatively small size and constrained geometry might overestimate the potential of automatic segmentation provided by spectral imaging. A comprehensive evaluation should include samples with complex geometries and greater size or, alternatively, whole-sized condyles from small animal models.

4.5. Conclusion

The present study investigated the potential of the SμCT on an osteochondral sample perfused with the iodine-based cationic contrast agent CA4+ and compared the results against a commercial CEμCT system. For similar acquisition time and spectrum, the results demonstrate that the SμCT provides a better distinction among tissues, also enabling automatic segmentation, at comparable spatial resolution. Spectral capabilities allowed for a more realistic description of proteoglycan distribution across the cartilage. The material decomposition approach makes possible the unambiguous discrimination between iodine and hydroxyhapatite at the cartilage/bone interface, having a potential impact for the assessment of osteoarticular pathologies. Future studies will be aimed at extending the analysis to a larger number of samples and sample types, while further improving spatial resolution (by a factor between 1.5 and 2) using a higher magnification and the extended field-of-view acquisition modality.

CHAPTER 5

Synchrotron-radiation based phase-contrast imaging: impact on mechanical behaviour of articular cartilage

Abstract

The heterogeneous and anisotropic arrangement of the AC microstructure confers peculiar strain gradients within the tissue under loads. Upon uniaxial compression, AC showcases a depth-dependent strain distribution. For instance, higher strains in superficial layer manifest, compared to the deeper zones, which feature higher compressive modulus. A comprehensive understanding of strain distribution is crucial for a clearer picture of the aetiology of pathologies such as osteoarthritis, besides the design of osteochondral scaffolds and tailored approaches for AC regeneration. Digital volume correlation is a full-field technique that computes the fields of displacements and the three-dimensional strain map by processing time-lapsed volumes acquired during in-situ mechanical testing. The key condition for a successful employment of DVC relies upon the detection of features that can be tracked within the structure-of-interest during mechanical testing, based on subsequent steps. Phase-contrast already proved to clearly highlight chondrocyte lacunae of AC (namely, the pericellular environment surrounding AC cells). Commercial microCT systems do not access resolutions high enough to visualise the lacunae of a large portion of tissue in a reasonable time, without affecting the viscoelastic properties of the osteochondral tissues. Indeed, the scan of small samples is not representative of the in-vivo situation, as the sample size affects the mechanical load distribution and the tissue deformation. Additionally, while a few commercial X-ray systems implementing phase-contrast exist, they feature poor X-ray fluxes. In this context, contrast enhancement of the relevant structures of AC can be achieved via radiopaque CAs, which, however, can affect the mechanical properties of the tissue. The aim of the present study was to investigate the potential impact of SR on the mechanical properties of AC. SR imaging was used during in-situ experiment, involving multiple scans to capture the tissue's deformation at different levels.

5.1. Introduction

The hierarchical multiphasic structure of AC allows the tissue to withstand a variety of stresses (namely, compressive, shear, tensile). The mechanical competence of the tissue depends on the integrity of the ECM. When the homeostasis of AC is disrupted (i.e., as a consequence of traumatic events), the mechanical response is compromised. For instance, wear of collagen mesh reduces the shear stiffness of AC [18]. The progressive loss of PGs leads to a diminished fixed charge density (FCD), corresponding to a weakened compressive strength of the tissue [429]. Furthermore, the altered porosity associated with the packed, entwined mesh of collagen bundles and PGs implies an increased water content. When this microstructure is altered, this delicate balance is disrupted, and the applied loads result in tissue damage [430].

Osteoarthritis represents a severe manifestation of AC degeneration, affecting the whole osteochondral unit. In fact, OA interests the underlying mineralised tissue, especially at its late stages. Tidemark duplication, increased thickness of calcified cartilage, and angiogenesis reflect the progressive evolution of the disease. Eventually, pain manifests when the whole osteochondral unit is irreversibly compromised [431].

To understand the aetiology of OA and to relate the progressive degradation of AC mechanical quality, the combination of complementary approaches is essential. Mechanical testing provides insights into the response of AC to external stimuli. In the case of incremental compressions being imparted to the tissue, the imaging of AC could relate the morphological and compositional features to the mechanical response. Consequently, displacements transmitted from external compression to the internal architecture of AC may provide insight into the strain distribution in relation to the tissue's functionality. In terms of visually detectable features, the most suitable structure is the chondrocyte lacuna, the pericellular environment in which chondrocytes are enclosed. Nevertheless, the scarce X-ray radiopacity of AC obliges the adoption of non-conventional imaging approaches. Contrast-enhanced protocols are the most straightforward approach to the assessment of soft tissues, as the use of CAs can be easily implemented on table-top X-ray scanners with no hardware modifications to the setup. Several studies investigated the morphology and distribution of lacunae following the diffusion of CAs [61,63,93,119]. Nonetheless, research-oriented studies confirmed the alterations of the AC mechanical response, following the contrast enhancement [93,367,432,433]. Additionally, staining procedures require processing (i.e., fixation) that alters the tissue properties [65]. In conclusion, evidence discourages the use of CAs in rheologic studies, unless non-invasive approaches are adopted [93,432].

Phase-contrast imaging represents a valuable alternative to the contrast-enhanced approach, owing to the superior contrast conferred to structures without the use of any CA. For instance, the interface between chondrocytes and the surrounding pericellular environment gives rise to the sought-after edge-enhancement effect at the fundamentals of PC imaging [54]. As already discussed in Chapters 1 and 2, the spatial coherence of the X-ray beam is crucial in generating the phase modulation, thanks to the interference phenomena induced by the passage of wavefronts through the sample [434]. Laboratory-based microCTs allow the depiction of lacunae during in-situ mechanical compression, provided the installation of nanofocus X-ray tubes featuring adequate lateral coherence. Nevertheless, table-top microCT-driven imaging protocols are affected by prolonged exposure times, due to the limited fluence of bremsstrahlung emission-based X-ray tubes [60,93].

This limitation is easily overcome with synchrotron radiation (SR), thanks to its unsurpassed brilliance [435]. Several works have reported the successful outcome of rheologic studies carried out at synchrotron facilities, investigating the mechanical response of osteochondral tissues to step-wise increase of applied deformation [205,208–210,269]. Still, the radiation dose represents a major drawback, especially in the case of large SR fluxes that irradiate the sample in a reduced time lapse [436,437]. This controversial aspect is well documented for bone tissues, but still deserves further investigation for AC.

The aim of the study was to investigate the potential impact of SR on the mechanical properties of AC. SR imaging was used as the light source in a PC protocol to image bovine AC subjected to incremental compressive steps. The experiment was carried out in SYRMEP (SYnchrotron Radiation for MEdical Physics) beamline at Elettra synchrotron facility. In this frame, attention was addressed in evaluating the potential effect of SR on the mechanical behaviour of irradiated AC.

5.2. Materials and Methods

5.2.1.Extraction of osteochondral tissue samples

Bovine stifle joints (N=8) were collected at a local slaughterhouse, within 24 hours of the culling. Both femoral condyles and tibial plates were considered to address the varying morphological features (i.e., thickness) of AC. Parallelepiped-shaped sections were collected from the sites of interest, wrapped in PBS-soaked gauze and stored at -20°C until the extraction of osteochondral samples. Once thawed, from parallelepiped-shaped sections 10 mm in diameter by 10 mm in height, cylindrical cores were drilled out by means of a computer numerically controlled milling machine (ProLight 2000, Light Machines Corporation, Manchester, NH, USA), equipped with a diamond-

coated coring tool. The whole extraction procedure was carried out in a PBS bath to prevent heating and dehydration of tissues. The procedure also accounted for the surface geometry of AC, aiming at harvesting cores with the flattest configuration. As the experiment included the investigation of SR effects, osteochondral cores were extracted in pairs to minimise the morphological differences. From each pair, one sample was destined for the irradiated and the control group, respectively. Following harvesting, specimens were frozen under the same storage conditions as the parallelepiped-shaped sections.

5.2.2.Pre-irradiation indentation tests

The whole experimental pipeline is schematised in Figure 5.1. Samples from both irradiated and control groups underwent a second thaw cycle overnight in PBS at 4°C, in preparation for the mechanical testing. The thickness of AC was assessed via X-ray microCT imaging (SkyScan 1072, SkyScan, Aartselaar, Belgium) and quantified using a custom MATLAB algorithm (MATLAB version R2022b, MathWorks, Natick, MA, USA), which processed four planar images per sample to compute the mean thickness of AC [367]. Specimens were embedded in a custom polyacetal holder, secured with polymethyl methacrylate at their base, and sealed laterally with silicone grease. Additional PBS was poured on the AC to prevent dehydration during the mechanical test. The polyacetal holder was mounted on the X-Y motorised table of the testing machine (Mach-1 V500css, Biomomentum Inc., Laval, QC, Canada). Each osteochondral core underwent an initial preconditioning indentation, followed by three tests with 40-minute intervals.

Indentation was performed with a 6 mm spherical indenter at 0.15 s^{-1}, reaching 15% of AC thickness and held for 300 s [341]. Instantaneous response was characterised by S_0 and E_0 (via the Hayes model, Poisson's ratio = 0.45) [343], while viscoelastic behaviour was described by the time constant (τ) and stretching exponent (β) from a stretched-exponential fit [430]. The equilibrium modulus (E_{eq}) was calculated using the Hayes model at 300 s, assuming Poisson's ratio = 0.3 [346]. All parameters were normalised to the first indentation to express relative changes across tests.

Afterwards, samples were stored at 20°C, wrapped in PBS-soaked gauze, until the imaging session at the SYRMEP beamline.

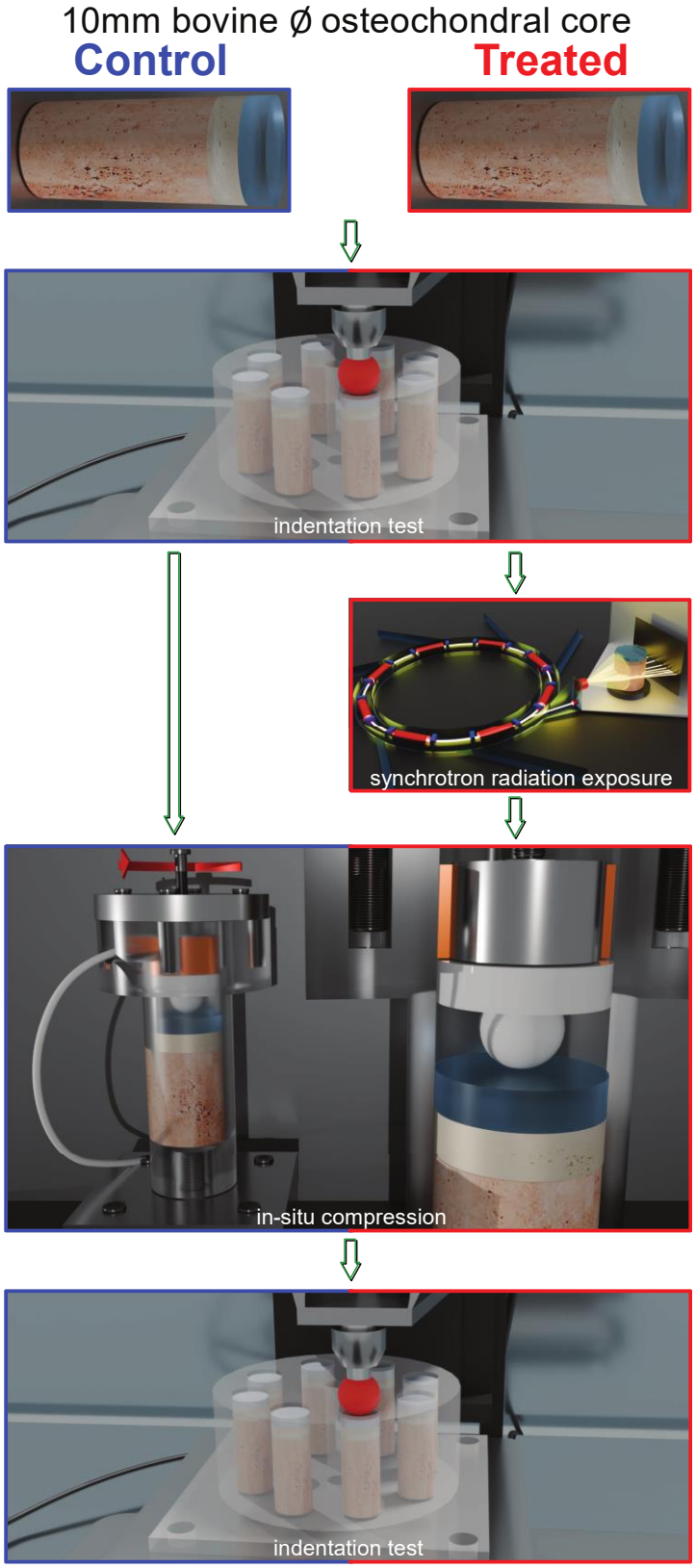

Figure 5.1. Samples were divided into two groups: treated and control. All samples underwent a preliminary cycle of indentation tests. Samples of the treated group were compressed at different deformation levels while being imaged at the SYRMEP beamline (Elettra synchrotron facility, Trieste, Italy). Samples of the control group were compressed at different deformation levels without being irradiated. Compression of the samples was accomplished using a dedicated device. A polyethylene sphere, moved orthogonally to the articular surface via a micrometric screw, applied compression to the articular surface. All samples underwent a final indentation test using the same protocol of the preliminary cycle.

5.2.3.In-situ compression device

An ad hoc compression device was designed and realised to perform the rheological experiment at the SYRMEP beamline. To minimise the absorption of X-rays, a polymethylmethacrylate (PMMA) cylindrical holder was obtained, with a wall thickness of 1 mm. The design accounted for the mechanical compression of cylindrical samples in a humid environment. In particular, the inner diameter of the holder facing the AC was enlarged to host the PBS and the indenter. The latter consisted of a 6-mm diameter polyethylene sphere, solidly attached to a PMMA cylinder fitting the inner edge of the wet chamber. The indenter was surmounted by the load cell to measure the load applied to the AC. A screw was used to apply a controlled axial displacement to the indenter, resulting in a controlled deformation of the cartilage.

5.2.4.In-situ testing protocol

In preparation for PC imaging, each sample was thawed in PBS at 6°C (third thaw cycle) 22 hours before the imaging session. Following the pouring of PBS, each sample was carefully placed in the in-situ compressive device to avoid the trapping of air bubbles in the chamber. The whole assembled device was plugged into the rotational stage, mounted on a six-degree-of-freedom hexapod. The SYRMEP beamline comprises a Hamamatsu Orca Flash sCMOS camera (Hamamatsu Photonics, Shizuoka, Japan, 2048 pixels × 2048 pixels matrix with physical pixel size of 6.5 μm × 6.5 μm) coupled with an optical magnification system. The magnification 5x provided the smallest pixel size (i.e., 1.3 μm) and a field-of-view (FOV) of 5x5 mm. To maximise the FOV without affecting the pixel size, the fly-scan method was adopted, provided the scan over 360° (3600 projections).

To maximise the photon flux, the polychromatic beam was selected, with a mean energy of 20 keV. The configuration selected for the experiment was propagation-based phase-contrast (PBPC), namely the simplest one pivoting exclusively on the propagation distance. The latter, defined as the sample-to-detector distance, was set to 25 cm. Provided the propagation distance and the beam features, an optimal exposure time per projection was 150 ms.

Following the automated alignment procedure [438], each sample of the irradiated group underwent five irradiation cycles. Except for the first repetition, the deformation level was increased by 15% of the original thickness at each subsequent step, reaching a maximum of 45%. Following each deformation increment, a 20-minute resting period was respected to allow the AC to reach equilibrium. The control group underwent the same experimental pipeline, except for the SR irradiation.

After the session, each sample of the irradiated group was rinsed in PBS, enveloped in PBS-soaked gauze and stored at -20°C

5.2.5.Post-irradiation indentation tests

Following the fourth thaw cycle, samples underwent the identical protocol of indentation tests illustrated in Subsection 5.2.2.

5.2.6.Statistical analysis

Statistical analyses were conducted as follows. Variations in AC thickness between the irradiated and control groups were analysed using the Wilcoxon signed-rank test. The same test was employed to compare the initial values of the mechanical parameters (S_0, E_0, τ, β, and E_{eq}) obtained during the first indentation cycle between the two groups. The influence of in-situ mechanical protocol within each group was evaluated by applying the Wilcoxon signed-rank test to the normalised parameter values, calculated as percentage changes relative to baseline (namely, the very first indentation). Lastly, to determine the effect of the SR, inter-group comparisons of these percentage changes were performed using the Mann–Whitney U test.

5.3. Results

The AC thickness values of OC cores for the irradiated group and control group were in the range of 0.8–2.3 mm and 1.0–2.0 mm, respectively. No significant difference was found between the two groups (irradiated group median thickness 1.5 mm, Control group median thickness 1.6 mm, Wilcoxon signed-rank test: $p = 0.96$).

A total of 48 indentation tests were performed, neglecting the preconditioning procedure of AC tissue. No significant difference was found between the parameters of the irradiated and control groups, calculated from the first three indentations. Normalised parameter trends across tests are shown in Figure 5.2.

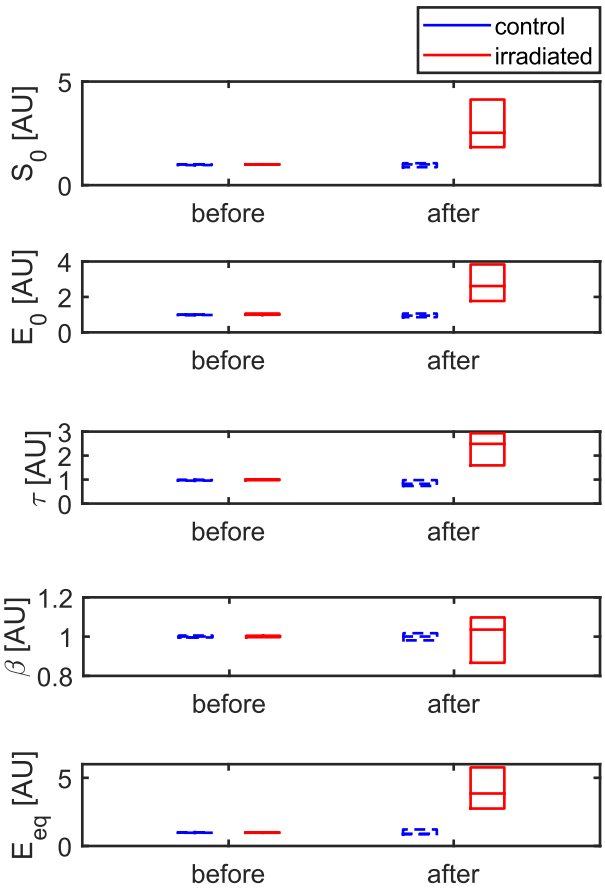

Figure 5.2. The median (central marker), 75th percentile (upper edge), and 25th percentile (lower edge) of the percentage changes in S_0, E_0, τ, β and E_{eq} values before and after in-situ testing protocol are shown. The values shown in the figure were calculated as the differences between the medians of the 24 values measured in the first three and the 24 values measured in the second set of indentation tests.

The exposure of AC to SR had the following significant effects on samples of the irradiated group (Mann–Whitney signed-rank test) for the following parameters: 149% increase in S_0 ($p < 0.01$), 160% increase in E_0 ($p < 0.01$), 149% increase in τ ($p < 0.01$), 286% increase in E_{eq} ($p < 0.01$). A statistically non-significant 4% increase in β ($p = 0.43$) was found.

On the other hand, in-situ mechanical compression without irradiation induced no significant differences in control samples (Mann–Whitney signed-rank test): 3% apparent decrease in S_0 ($p = 0.87$), 6% apparent decrease in E_0 ($p = 0.51$), 17% apparent decrease in τ ($p = 0.06$), 0.3% apparent increase in β ($p = 0.60$), 8% apparent decrease in E_{eq} ($p = 0.51$).

When comparing the percentage changes between the two groups, exposure to SR led to the following significant differences relative to unexposed samples: a 152% increase in S_0 (Mann–Whitney: $p < 0.01$), a 166% increase in E_0 (Mann–Whitney: $p < 0.01$), a 166% increase in τ (Mann–Whitney: $p < 0.001$), 294% increase in (Mann–Whitney: $p < 0.001$). No significant difference was found in the β values between the two groups (Mann–Whitney: $p = 0.44$).

5.4. Discussions

The aim of this study was to validate a PC imaging protocol at the SYRMEP beamline of Elettra. The protocol included the sequential acquisition of bovine osteochondral samples under several compressive steps. The inclusion of control samples, paired to the irradiated twins, aimed at evaluating the potential impact of SR on the mechanical response of AC.

Considering rheological studies alone, PBPC modality allowed for scan times shorter than one minute [205]. First, SR different specifications depend on the beamline of extraction. For instance, the different design of storage rings (i.e., radius) and extraction devices (i.e., undulators and wigglers), confers beam characteristics varying from beamline to beamline. The most important discrepancy is primarily found in beam brilliance, which in turn directly impacts the acquisition time. Comparing the brilliance of various X-ray imaging-dedicated beamlines around the world, SYRMEP features average values. The study featuring the shortest acquisition time was conducted at the TOMCAT beamline, in the Swiss Light Source of the Paul Scherrer Institute, based in Switzerland. Despite the monochromatisation of the beam, a procedure known for hampering the fluence of the resulting beam, the imaging protocol proposed in the work of Dejea et al. resulted in strikingly short exposure times [205]. The almost two orders of magnitude discrepancy between the exposure time in the present study and the one from Dejea et al. (i.e., 150 ms and 2.5 ms, respectively) is attributable to the fluence of the beamlines employed [438]. Therefore, the present study maximised the beam fluence by deliberately selecting the polychromatic modality. Second, to minimise the pixel size, the acquisition protocol foresaw a 360° scan instead of a 180° scan by exploiting the fly-scan method [439].

In light of the benefits and limitations of the proposed protocol, a few considerations can be made on the impact of SR on the mechanical response of AC. Statistical analysis confirmed that samples from irradiated and control groups show comparable morphological and mechanical native features. That said, a significant increase in mean values and variance of E_0, τ and E_{eq} was observed in the irradiated group, in response to a localised compression imparted via indentation tests. As both groups underwent the identical incremental compressive steps, it is plausible to attribute the overall increase of the aforementioned values to SR exposure.

The increase of E_0 reflects the stiffening of tissue upon the localised compression, pointing out apparent modifications interesting the ECM. In general, literature reports contrasting evidence over the impact of indirect ionising radiation on the mechanical properties of AC. Such discrepancies could be addressed to potential inconsistencies in the type of radiation, the dosage of radiation, the dose rate, and the model used. Independent of the aforementioned parameters, ionising radiation exerts

effects across multiple scales, from mesoscopic (i.e., molecular-level alterations) to macroscopic levels (i.e., structural changes affecting the tissue as a whole).

The fractioning of therapeutic X-rays on rabbit stifle joints in vivo was associated with no apparent alterations in the mechanical properties of AC [440]. Contrariwise, studies based on nano- and micro-indentation uncovered a diminished compressive stiffness of AC [441]. Independent imaging approaches such as T2 mapping were considered, owing to their sensitivity to water interacting with collagen of the ECM [442]. For instance, the study of Hutchinson et al. revealed decreased values of T2 relaxations, indicative of collagen cross-linking in rat stifle AC [443]. The latter effect, artificially induced in mature bovine AC, was associated with increased equilibrium stiffness [444], in line with the results of the present study.

Interestingly, the relaxation time τ shows increased values as well, meaning that the viscous phenomena are exhausted in longer time lapses. This effect could result from the cleavage of GAGs from PGs. The deposition of low radiation doses is associated with a release of GAGs from the ECM, as confirmed by biochemical essays [441], resulting in a weakened electrostatic repulsion and softening of the tissue. On the other hand, experimentally induced cross-linking of collagen mesh was responsible for increased FCD [442] and mechanical stiffness of the bovine and human AC [442,445]. Additionally, a study based on Fourier-transform infrared (FTIR) analysis found denaturation of proteins. Upon irradiation, it was suggested that water molecules decompose into unstable species which, in cascade, form GAG free radicals and oxygen reactive species, with potential impact on AC viscoelasticity [446]. Further modification of FTIR spectra suggested that collagen loses its characteristic structure in favour of an amyloid-like shape, no longer functional in withstanding external stresses [446].

In contrast with the aforementioned evidence, a recent rheologic study involving bovine AC found no apparent impact of SR on the mechanical response of the tissue [205]. In the same study, the use of a monochromatic beam could avoid the deposition of undesired energy components to the tissue. Additionally, the very short acquisition times prevent the development of heat in the sample, renowned as a macroscopic manifestation of radiation deposition, along with high dose rates. Heat could potentially lead to alterations in the state of AC. Literature mainly addresses the impact of heat on cell viability rather than the mechanical behaviour of AC. Notably, morphological alterations have been reported following radiation exposure, potentially translating to AC functionality [447]. Compared to the study of Dejea et al., the present study was based on polychromatic radiation and relatively long acquisition times to maximise the beam fluence. Such a choice could imply larger radiation doses, together with the already outlined longer exposure times.

The present study comes with several limitations. Above all, the limited sample size could bias the soundness of statistical analysis and the reliability of results. Still, the number of samples accommodated the limited beamtime available. Additionally, the design of the experiment sensibly downsized the number of specimens to be included. As already mentioned, single samples underwent several image acquisitions after the disposal of each compressive step. Furthermore, the choice to include relaxation time, essential for the complete exhaustion of viscous phenomena in AC, was made at the expense of the beamtime available.

Further considerations should be made regarding the AC model. The bovine model provides healthy osteochondral tissues within reasonable timeframes. On the other hand, human osteochondral tissue should be considered in the light of future investigation of OA progression. In this sense, the morphological features of AC from the selected model rule the imaging outcome and, in turn, the subsequent rheologic analysis. The site-dependent and interspecies variations in tissue morphology have already been revealed in a comparative study, comparing human and bovine AC [173]. For instance, histological inspections of human and bovine AC highlighted lacunae sizes corresponding to 16.9±3.0 and 19.7±2.6 μm, respectively [173]. Except for the morphological differences between the bovine and the human model, both provide AC with comparable viscoelastic properties [448]. For inference, the impact of SR should manifest in a similar way on human AC as well.

Besides the morphological aspects, the site-dependent variability of mechanical behaviour exhibited by AC should be considered [314,391,448–450]. Provided that the indentation protocol was optimised, along with the criterion of specimen extraction. As a result, samples showed comparable mechanical properties, regardless of the group. Eventually, the normalisation of mechanical parameters to the very first indentation contributed to lowering the inherent variability of absolute mechanical features [341].

As concerns the handling of specimens, a total of four freeze–thaw cycles were performed throughout the whole experiment. The deleterious impact of such a procedure on the mechanical properties of AC has already been addressed by previous studies [358,359]. Because the freeze-thaw procedure was identical across groups, its effects are unlikely to bias comparisons between treated and control samples. This supports the interpretation that observed differences between groups are attributable to the radiation exposure rather than to specimen handling.

Despite the abovementioned pitfalls, significant alterations in the viscoelastic response of bovine AC were highlighted, following the comparative evaluation of the SR effect on AC response to indentation.

5.5. Conclusions

The present study proposed an experimental protocol for the rheological evaluation of AC at the SYRMEP beamline, in the Elettra synchrotron facility. The illustrated protocol combined high-resolution PBPC imaging of chondrocyte lacunae with the application of incremental compressive steps. The proposed protocol was implemented with indentation tests before and after irradiation, to investigate the potential impact of SR on the mechanical response of AC. To this purpose, the experimental design included irradiated and control groups.

The analysis of mechanical data highlighted a significant effect of SR on the mechanical response of AC to localised compression. For instance, increased instantaneous modulus and equilibrium modulus were associated with the stiffening of AC. Viscous phenomena were observed to exhaust in longer time lapses. The comparison to the control group confirmed that the effects observed on the irradiated group are attributable to SR.

Further improvements to the proposed imaging protocol could include the use of monochromatic beams to lower the detrimental effect of unwanted components of X-rays. This could be possible after the planned upgrade of Elettra synchrotron infrastructure, including SYRMEP. The beamline will provide advanced X-ray imaging, including phase-contrast and monochromatic microCT with a superior beam energy range (namely, 10–130 keV), enabling research in fields such as palaeontology, materials science, and medicine. High flux will also allow fast 4D microCT scans within seconds, crucial for concurrent in-situ mechanical investigations.

CHAPTER 6

Conclusions

This Chapter provides a comprehensive summary of the main outcomes of the PhD work, with particular emphasis on the original contributions made to the application of advanced X-ray imaging techniques for the study of articular cartilage. Subsequently, the principal limitations of the conducted studies are discussed. Finally, potential future developments and implications arising from the presented findings are outlined.

6.1. Summary

The aim of the present PhD thesis was to evaluate the feasibility of X-ray techniques alternative to the conventional imaging of AC. A high-resolution depiction of the inner structure is essential both when the early effects of a pathology need to be investigated or when full-field techniques are employed. For instance, chondrocyte lacunae allow the punctual evolution of three-dimensional displacements in the tissue upon the application of external mechanical stresses on the sample. To this end, several approaches have been sifted, ranging from contrast-enhanced imaging (Chapter 3), detector-based spectral microCT (Chapter 4), to SR-based PBPC imaging (Chapter 5).
Aiming at the validation of the single protocols proposed in this work, ex-vivo approaches were considered.

Prior to any experimental attempt, an extensive review of existing literature focused on evidence supporting the application of advanced X-ray techniques to high-resolution imaging of AC (Chapter 2). Briefly, the X-ray imaging field distinguishes among absorption-based, refraction-based and scattering-based approaches. Absorption-based methods resort to the use of radiopaque CAs to selectively enhance the discernibility of inner structures, allowing for a quantitative assessment of the tissue, even with a table-top conventional X-ray scanner. In the light of such contrast improvements, cutting-edge approaches such as spectral imaging further boost the visibility of details in one or more tissues. Nevertheless, such implementations come at the cost of potential alterations of the investigated tissue, increased radiation doses or low-resolution devices. Refraction-based approaches circumvent these pitfalls. Notably, the intrinsic enhancement of interfaces at mesoscopic and macroscopic scales substitutes the use of CAs. Essential requirements, such as the spatial coherence of the X-ray beam, the insertion of dedicated optical elements, or their combination, limit their implementation to a limited number of SR facilities or custom laboratory-based X-ray systems. Scattering-based methods, implementable in most of the refraction-based configurations, retrieve unique mesoscale information, typically not reached by other imaging approaches. Nevertheless, the application of scattering-based methods suffers from the same limitations as refraction-based configurations, and their potential has only been demonstrated in two-dimensional imaging approaches. Pondering the advantages and limitations of their applications to AC imaging, PBPC demonstrated the most promising results, especially in light of rheologic investigations, thanks to the simplest experimental setup and the shortest acquisition time.

Chapter 3 focused on the use of an experimental iodine-based cationic CA, CA4+. The latter exhibits a superior imaging outcome compared to other existing CA formulations, as it provides direct insight into the PG content of AC. Furthermore, CA4+ use demonstrated the depiction of chondrocyte

lacunae [61]. Aiming at the potential combination of CA4+ to rheologic assessment of AC, the definition of experimental activities included multidisciplinary approaches, namely X-ray imaging and mechanical testing. The following aspects were deepened:

1. The impact of CA4+ on the mechanical response of AC (Chapter 3, Section 1). This aspect is crucial in establishing the suitability of CA4+ with in-situ testing of bovine AC. In this sense, indentation testing was performed on two distinct groups of samples (namely, contrast-enhanced and control) to single out effects solely attributable to the use of CA4+. The experimental pipeline attempted to minimise jeopardising factors such as variability of AC morphology and mechanical properties. Results highlighted significant alterations of AC following the exposure to CA4+, pointing out an overall softening of the tissue (i.e., decreased instantaneous and equilibrium response) to localised compressions. Such evidence discourages any mechanical assessment of AC after its contrast-enhancement with CA4+. Still, contrast-enhanced protocols could find remarkable applications in the research field, aiming at either research-oriented or preclinical investigation of AC. To these aims, the potential resorption of CA4+ from AC is required for downstream evaluations, such as histology or for potential in-vivo animal studies. To date, no rigorous analysis has focused on the reversibility of CA4+ effects highlighted here.
2. The reversibility of CA4+ effects on the mechanical response of AC (Chapter 3, Section 2). To this end, the effective resorption of CA4+ from bovine AC was investigated first. Dynamical washout in PBS bath was effective in clearing out CA4+ from the tissue in a specific time (namely, washout time). This information contributed to refining the experimental pipeline, as reprised from Section 1, Chapter 3. Indentation tests demonstrated that samples undergoing a dynamical washout cycle in PBS bath share a similar mechanical response, regardless of the group assignment.
3. The reliability of CA4+ on preclinical assessment of AC, resorting to HR-pQCT (Chapter 3, Section 3). High-resolution peripheral quantitative computed tomography represents a viable option for imaging of limbs, meeting unsurpassed spatial resolution and negligible radiation doses, compared to other clinical X-ray scanners. In this study, the combination of CA4+-enhanced HR-pQCT with indentation testing aimed at proving the potential predictability of AC mechanical features, based on quantitative imaging data. The latter reflected the characteristic concentration of PGs in the tissue, thanks to the electrostatic attraction exerted from negatively charged GAGs on CA4+ molecules. Results provided correlations between several mechanical parameters – accounting for the instantaneous, viscous and equilibrium behaviour of AC in response to localised compressions – and the imaging data. In other words,

the proposed contrast-enhanced imaging protocol supports the ability to predict AC mechanical properties.

Chapter 4 investigated the feasibility of detector-based spectral imaging applied to CA4+-exposed osteochondral samples. Despite the beneficial outcomes of CA4+ on AC assessment, its use could face limitations if the whole osteochondral unit is considered. For instance, the comparable radiopacity between contrast-enhanced AC and the underlying bone tissues could hinder their discrimination [158]. Such a limitation can be overcome with detector-based spectral imaging. This novel approach was possible at PEPILab, a multimodal X-ray imaging system equipped with a PCD. Thanks to the direct discrimination of photons based on their energy, such technology provided multiple datasets, serving as input for material-decomposition algorithms. Results provided density maps of AC and bone tissue, reconstructed from a single X-ray exposure. Notably, the density maps obtained featured the smallest spatial resolution retrieved from AC, according to the existing literature. Additionally, further analysis of AC profiles indirectly highlighted structural features at the AC-bone interface. For instance, the calcified cartilage, anchoring AC to the underlying subchondral bone, is recognised as a hallmark in the onset of osteoarthritis. Hence, detector-based X-ray spectral imaging could be a valuable tool in preclinical studies. Yet, the imaging performance depends on both the selection of the CA and the energy optimization. The choice of the CA governs the biochemical specificity and diffusion features within AC. In contrast, the selection of certain energy thresholds primarily determines the effectiveness with which the CA can be spectrally separated from pristine tissue, thereby affecting the quantification accuracy and robustness. On the side of CAs, current developments are focusing on improving the specificity to AC, favourable diffusion kinetics, and spectral signatures well matched to clinically feasible energy ranges. Recently, attention has been drawn to the development of smaller molecules (i.e., NPs) and different customisations (i.e., insertion of functional groups). Elements with spectral features different from those of conventionally used clinical formulations (i.e., iodine and gadolinium) could provide enhanced contrast and distinguishability between contrast-enhanced AC and the underlying bone. Furthermore, the use of high-atomic-number elements (e.g., tantalum, gold, bismuth) would enable acquisitions at higher X-ray energies, with particular attention on radiation dose optimisation. On the side of instrumentation, advances in detector technology, energy bin optimisation and dose-efficient acquisition strategies will be critical to fully exploit existing and emerging CAs. Manufacturing aspects, including pixel size, still offer significant potential for optimization, to deliver sensors with inherently enhanced sensitivity to even finer structural details.

In light of the results provided in Section 1, Chapter 3, any approach potentially altering the mechanical behaviour of AC should be avoided. As already mentioned, refraction-based X-ray imaging serves as a valuable alternative to contrast-enhanced approaches. The last activity, reported in Chapter 5, reported the experiment carried out in the SYRMEP beamline, at the Elettra synchrotron facility. The aim was to develop a protocol for in-situ loading of AC, combined with high-resolution PBPC imaging. Similar to previous studies, attention was addressed to the depiction of chondrocyte lacunae. The latter serves as an excellent marker for advanced full-field analysis, such as DVC. Additionally, the potential impact of SR on the mechanical response of AC was investigated to shed light on the contrasting evidence reported in the literature. Results provided a valuable outcome in terms of lacunae depiction. Indentation tests pointed out a significant effect of SR on the instantaneous, viscous and equilibrium behaviour of AC. Interestingly, the resulting stiffening could be associated with modifications occurring at the mesoscopic scale, following the exposure to ionising radiation. On the other hand, previous studies evidence no clear impact of SR in the context of rheologic assessment of AC. The origin of these contrasting results could lie in the different imaging protocols. For instance, the X-ray spectrum, the exposure time per projection and the dose rate play a major role in determining potential alterations of the irradiated tissue.

In summary, the imaging approaches included in the present PhD thesis delivered valuable results under several aspects, but the applications are limited to the preclinical field. In the more circumscribed context of rheological investigations, PBPC imaging meets demanding requirements such as no alterations due to any CA, high spatial resolution and short acquisition times.

6.2. Limitations and future perspectives

Limitations and potential improvements of each study are presented hereafter.

Above all, a critical limitation of all the reported activities is the use of bovine AC. The use of animal tissue was driven by its availability – bovine tissues can be obtained within a few hours of slaughter – and the absence of ethical implications – no animals were sacrificed specifically for the aims of the studies. Comparative studies have reported similarities between bovine and human tissues in terms of both morphological and mechanical features [173]. Therefore, bovine tissues have been widely used in studies exploring the potential of several imaging approaches. By inference, results demonstrating the soundness of these imaging approaches on bovine AC would imply equally robust outcome also for human AC. While bovine AC represents a widely accepted and convenient model

for ex vivo experimentation, it cannot fully substitute human tissue. Investigated bovine AC obtained from the food industry consistently represents a healthy physiological state, lacking the spectrum of degenerative changes typically observed in human specimens. In contrast, human AC samples encompass a broad range of conditions, from intact to severely degraded, offering a more comprehensive representation of the tissue's pathological variability. Therefore, the validation of experimental protocols, regardless of their specific nature, should not rely exclusively on healthy tissue, but should also be extended to pathological samples to ensure translational relevance and robustness of the reported findings.

Focusing on contrast-enhanced protocols included in Chapters 3 and 4, some considerations should be addressed to the CA used. As already mentioned in Chapter 2, cationic CAs (CA4+ included) lead to superior contrast of AC when compared to non-ionic and anionic counterparts, due to their preferential accumulation in negatively charged regions of the ECM. This electrostatic interaction improves the visualisation of PG-rich zones and has been shown to correlate with tissue composition [116]. However, this work relied on a single CA formulation at a fixed concentration, following a standardised preparation protocol. While this choice ensured consistency across experiments and simplified data interpretation, it inherently limited the scope of the findings. Exploring alternative CA types, featuring different nature (i.e., NPs), charge, molecular size, or X-ray attenuation properties, could have provided a broader understanding of contrast dynamics and sensitivity. Similarly, varying concentrations might have revealed optimal trade-offs between imaging contrast, diffusion time, and potential effects on tissue mechanics. In this sense, recent works highlighted the suitability of polyoxometalates to mechanical probing of AC, granting the native mechanical properties of the tissue [70].

Additional aspects regarding mechanical testing are included in Chapters 3. The integration of X-ray imaging with indentation testing using millimetre-scale indenters (namely, 6 mm) enabled a spatially resolved assessment of AC mechanical behaviour. The approach here adopted ensured consistent indentation conditions across heterogeneous specimens, relatable to the intrinsic regional variations of AC. All indentation tests reported in this PhD thesis were performed under displacement-controlled condition, on the base of preliminary estimation of AC thickness. In healthy AC, there is no issue applying such an approach. However, the thinner the residual AC layer, the more difficult it becomes to apply this procedure. Indeed, the resulting load may exceed the physiological range in stiffer regions, potentially limiting the direct biomechanical relevance of the measured responses, and, in turn, of the correlations with the parameters derived from imaging data.

Despite the novelty of detector-based spectral imaging presented in Chapter 4, several limitations should be underlined. First, the experiment was carried out on a single osteochondral

sample. Second, the evidence provided on calcified cartilage was not confirmed by reference methods (i.e., histology). On the other hand, the study proposed itself as a methodology work, highlighting the benefits of detector-based spectral imaging over conventional approaches. Insights on calcified cartilage could be replicated on multiple samples, possibly from alternative models to bovine. For instance, the inclusion of samples with increasing stages of degeneration would deepen the suitability of such a protocol in recognising several hallmarks of osteoarthritis, on the scale of the whole osteochondral unit. Third, the spatial resolution of the reconstructed volume is incompatible with rheological applications, owing to the relatively large physical pixel size of PCD. Laboratory-based experiments based on conventional EID technology were carried out at significantly higher spatial resolutions. Still, improvements in geometrical configuration and field of view would improve the final spatial resolution.

As for Chapter 5, the main limitations regard the protocol design. Considering the potential impact of SR on the mechanical properties of AC, an optimal trade-off between beam features (namely, monochromaticity and fluence) and in-situ protocol (namely, number of acquisitions) should be contemplated. Furthermore, incorporating the underlying bone tissues into the experimental protocol could yield a more complete understanding of the mechanical load transfer and stress distribution throughout the entire osteochondral unit, capturing the interactions between AC, calcified cartilage, and subchondral bone under physiological and pathological conditions. Another significant limitation of the study presented in Chapter 5 is the absence of image analysis, which, at the time of writing, remained in an early and exploratory phase

In conclusion, the present PhD thesis analysed several X imaging approaches for AC imaging, integrating mechanical tests to validate or corroborate the suitability of each for potential rheologic applications. Considering advantages and limitations, the following aspects emerged:

- Contrast-enhancement with CA4+ allows for quantitative imaging of AC, with potential towards the predictability of tissue mechanical behaviour, in the frame of localised compression. Nevertheless, the impact of CA4+ on the mechanical response of AC is not suitable for any application to in-situ mechanical evaluation of the tissue.
- Detector-based spectral imaging distinguishes among tissues in a single X-ray exposure, thanks to the photon energy discrimination performed by PCD technology. Notably, this approach implemented at a laboratory-based X-ray microCT provided insights into calcified cartilage. On the other hand, the limited spatial resolution hinders the adoption of the proposed experimental setup for rheological studies on AC.
- Propagation-based phase-contrast imaging of AC successfully depicted chondrocyte lacunae, following the design and testing of an in-situ mechanical protocol in the SYRMEP beamline.

Refinements to the protocol could reduce the effect of SR on the mechanical response of AC, including a remodulation of compressive steps and the adoption of monochromatic X-ray beams.

As general remarks for this PhD thesis, PG content and chondrocyte lacunae were successfully characterised. Conversely, collagen bundles remained unresolved due to their submicron dimensions. For example, spatial resolutions as fine as 0.1 µm, reported in the context of AC imaging, could not resolve collagen bundles [200]. In light of advancements in X-ray imaging, novel SR-based techniques have been developed to probe sub-micron structural features that are typically beyond the resolution limits of high-resolution microCT. Noteworthily, SAXS tensor tomography combines scattering-based measurements with tomographic reconstruction to provide three-dimensional maps of nanoscale anisotropic structures within tissues [451]. This method could enable the quantitative assessment of collagen fibre orientation and organisation at length scales inaccessible to conventional microCT.

References

1. Setton, L.A.; Elliott, D.M.; Mow, V.C. Altered Mechanics of Cartilage with Osteoarthritis: Human Osteoarthritis and an Experimental Model of Joint Degeneration. *Osteoarthritis and Cartilage* **1999**, *7*, 2–14, doi:10.1053/joca.1998.0170.
2. Kurtz, S.; Ong, K.; Lau, E.; Mowat, F.; Halpern, M. Projections of Primary and Revision Hip and Knee Arthroplasty in the United States from 2005 to 2030: *The Journal of Bone and Joint Surgery-American Volume* **2007**, *89*, 780–785, doi:10.2106/00004623-200704000-00012.
3. Scheuing, W.J.; Reginato, A.M.; Deeb, M.; Acer Kasman, S. The Burden of Osteoarthritis: Is It a Rising Problem? *Best Practice & Research Clinical Rheumatology* **2023**, *37*, 101836, doi:10.1016/j.berh.2023.101836.
4. Kanamoto, T.; Mae, T.; Yokoyama, T.; Tanaka, H.; Ebina, K.; Nakata, K. Significance and Definition of Early Knee Osteoarthritis. *Ann Joint* **2020**, *5*, 4–4, doi:10.21037/aoj.2019.09.02.
5. Leskinen, H.P.P.; Hänninen, N.E.; Nissi, M.J. T_2 Orientation Anisotropy Mapping of Articular Cartilage Using qMRI. *Phys. Med. Biol.* **2023**, *68*, 085004, doi:10.1088/1361-6560/acc169.
6. Badar, F.; Xia, Y. The Interface Region between Articular Cartilage and Bone by MMRI and PLM at Microscopic Resolutions. *Microscopy Res & Technique* **2022**, *85*, 1483–1493, doi:10.1002/jemt.24011.
7. Florkow, M.C.; Willemsen, K.; Mascarenhas, V.V.; Oei, E.H.G.; Van Stralen, M.; Seevinck, P.R. Magnetic Resonance Imaging Versus Computed Tomography for Three-Dimensional Bone Imaging of Musculoskeletal Pathologies: A Review. *Magnetic Resonance Imaging* **2022**, *56*, 11–34, doi:10.1002/jmri.28067.
8. Davis, S.; Karali, A.; Zekonyte, J.; Roldo, M.; Blunn, G. Development of a Method to Investigate Strain Distribution across the Cartilage-Bone Interface in Guinea Pig Model of Spontaneous Osteoarthritis Using Lab-Based Contrast Enhanced X-Ray-Computed Tomography and Digital Volume Correlation. *Journal of the Mechanical Behavior of Biomedical Materials* **2023**, *144*, 105999, doi:10.1016/j.jmbbm.2023.105999.
9. Sophia Fox, A.J.; Bedi, A.; Rodeo, S.A. The Basic Science of Articular Cartilage: Structure, Composition, and Function. *Sports Health* **2009**, *1*, 461–468, doi:10.1177/1941738109350438.
10. Eyre, D. Collagen of Articular Cartilage. *Arthritis Res* **2002**, *4*, 30, doi:10.1186/ar380.
11. Bloebaum, R.D.; Wilson, A.S.; Martin, W.N. A Review of the Collagen Orientation in the Articular Cartilage. *CARTILAGE* **2021**, *13*, 367S-374S, doi:10.1177/1947603520988770.
12. Alcaide-Ruggiero, L.; Cugat, R.; Domínguez, J.M. Proteoglycans in Articular Cartilage and Their Contribution to Chondral Injury and Repair Mechanisms. *IJMS* **2023**, *24*, 10824, doi:10.3390/ijms241310824.
13. Akkiraju, H.; Nohe, A. Role of Chondrocytes in Cartilage Formation, Progression of Osteoarthritis and Cartilage Regeneration. *JDB* **2015**, *3*, 177–192, doi:10.3390/jdb3040177.
14. Maroudas, A. Physicochemical Properties of Cartilage in the Light of Ion Exchange Theory. *Biophysical Journal* **1968**, *8*, 575–595, doi:10.1016/S0006-3495(68)86509-9.
15. Mow, V.C.; Kuei, S.C.; Lai, W.M.; Armstrong, C.G. Biphasic Creep and Stress Relaxation of Articular Cartilage in Compression: Theory and Experiments. *Journal of Biomechanical Engineering* **1980**, *102*, 73–84, doi:10.1115/1.3138202.
16. Lai, W.M.; Hou, J.S.; Mow, V.C. A Triphasic Theory for the Swelling and Deformation Behaviors of Articular Cartilage. *Journal of Biomechanical Engineering* **1991**, *113*, 245–258, doi:10.1115/1.2894880.
17. Mow, V.C.; Holmes, M.H.; Michael Lai, W. Fluid Transport and Mechanical Properties of Articular Cartilage: A Review. *Journal of Biomechanics* **1984**, *17*, 377–394, doi:10.1016/0021-9290(84)90031-9.
18. Wyse Jackson, T.; Michel, J.; Lwin, P.; Fortier, L.A.; Das, M.; Bonassar, L.J.; Cohen, I. Structural Origins of Cartilage Shear Mechanics. *Sci. Adv.* **2022**, *8*, eabk2805, doi:10.1126/sciadv.abk2805.

19. Ateshian, G.A. The Role of Interstitial Fluid Pressurization in Articular Cartilage Lubrication. *Journal of Biomechanics* **2009**, *42*, 1163–1176, doi:10.1016/j.jbiomech.2009.04.040.
20. Buckwalter, J.A.; Mankin, H.J. Articular Cartilage: Degeneration and Osteoarthritis, Repair, Regeneration, and Transplantation. *Instr Course Lect* **1998**, *47*, 487–504.
21. Peters, A.E.; Akhtar, R.; Comerford, E.J.; Bates, K.T. The Effect of Ageing and Osteoarthritis on the Mechanical Properties of Cartilage and Bone in the Human Knee Joint. *Sci Rep* **2018**, *8*, 5931, doi:10.1038/s41598-018-24258-6.
22. Buckwalter, J.A.; Mankin, H.J.; Grodzinsky, A.J. Articular Cartilage and Osteoarthritis. *Instr Course Lect* **2005**, *54*, 465–480.
23. Nelson, F.; Billinghurst, R.C.; Pidoux, I.; Reiner, A.; Langworthy, M.; McDermott, M.; Malogne, T.; Sitler, D.F.; Kilambi, N.R.; Lenczner, E.; et al. Early Post-Traumatic Osteoarthritis-like Changes in Human Articular Cartilage Following Rupture of the Anterior Cruciate Ligament. *Osteoarthritis and Cartilage* **2006**, *14*, 114–119, doi:10.1016/j.joca.2005.08.005.
24. Li, G.; Yin, J.; Gao, J.; Cheng, T.S.; Pavlos, N.J.; Zhang, C.; Zheng, M.H. Subchondral Bone in Osteoarthritis: Insight into Risk Factors and Microstructural Changes. *Arthritis Res Ther* **2013**, *15*, 223, doi:10.1186/ar4405.
25. Martel-Pelletier, J.; Lajeunesse, D.; Reboul, P.; Pelletier, J.-P. The Role of Subchondral Bone in Osteoarthritis. *Osteoarthritis: a companion to rheumatology* **2007**, *1*, 15–32.
26. Röntgen, W.C. On a New Kind of Rays. *Science* **1896**, *3*, 227–231, doi:10.1126/science.3.59.227.
27. Kalender, W.A. X-Ray Computed Tomography. *Phys. Med. Biol.* **2006**, *51*, R29–R43, doi:10.1088/0031-9155/51/13/R03.
28. Hsieh, J.; Flohr, T. Computed Tomography Recent History and Future Perspectives. *J. Med. Imag.* **2021**, *8*, doi:10.1117/1.JMI.8.5.052109.
29. Zink, F.E. X-Ray Tubes. *RadioGraphics* **1997**, *17*, 1259–1268, doi:10.1148/radiographics.17.5.9308113.
30. Willmott, P. *An Introduction to Synchrotron Radiation: Techniques and Applications*; 1st ed.; Wiley, 2019; ISBN 978-1-119-28039-2.
31. Lewis, R. Medical Applications of Synchrotron Radiation X-Rays. *Phys. Med. Biol.* **1997**, *42*, 1213–1243, doi:10.1088/0031-9155/42/7/001.
32. Spahn, M. X-Ray Detectors in Medical Imaging. *Nuclear Instruments and Methods in Physics Research Section A: Accelerators, Spectrometers, Detectors and Associated Equipment* **2013**, *731*, 57–63, doi:10.1016/j.nima.2013.05.174.
33. Lee, D.L.Y.; Cheung, L.K.; Jeromin, L.S. New Digital Detector for Projection Radiography.; Van Metter, R.L., Beutel, J., Eds.; San Diego, CA, May 8 1995; pp. 237–249.
34. Taguchi, K.; Iwanczyk, J.S. Vision 20/20: Single Photon Counting x-Ray Detectors in Medical Imaging: Vision 20/20: Photon Counting Detectors. *Med. Phys.* **2013**, *40*, 100901, doi:10.1118/1.4820371.
35. Barth, H.D.; Launey, M.E.; MacDowell, A.A.; Ager, J.W.; Ritchie, R.O. On the Effect of X-Ray Irradiation on the Deformation and Fracture Behavior of Human Cortical Bone. *Bone* **2010**, *46*, 1475–1485, doi:10.1016/j.bone.2010.02.025.
36. Rueckel, J.; Stockmar, M.; Pfeiffer, F.; Herzen, J. Spatial Resolution Characterization of a X-Ray microCT System. *Applied Radiation and Isotopes* **2014**, *94*, 230–234, doi:10.1016/j.apradiso.2014.08.014.
37. Huda, W.; Abrahams, R.B. X-Ray-Based Medical Imaging and Resolution. *American Journal of Roentgenology* **2015**, *204*, W393–W397, doi:10.2214/AJR.14.13126.
38. Howansky, A.; Mishchenko, A.; Lubinsky, A.R.; Zhao, W. Comparison of CsI:Tl and Gd_2O_2S:Tb Indirect Flat Panel Detector X-ray Imaging Performance in Front- and Back-irradiation Geometries. *Medical Physics* **2019**, *46*, 4857–4868, doi:10.1002/mp.13791.

39. Belluzzi, E.; Todros, S.; Pozzuoli, A.; Ruggieri, P.; Carniel, E.L.; Berardo, A. Human Cartilage Biomechanics: Experimental and Theoretical Approaches towards the Identification of Mechanical Properties in Healthy and Osteoarthritic Conditions. *Processes* **2023**, *11*, 1014, doi:10.3390/pr11041014.
40. Patel, J.M.; Wise, B.C.; Bonnevie, E.D.; Mauck, R.L. A Systematic Review and Guide to Mechanical Testing for Articular Cartilage Tissue Engineering. *Tissue Engineering Part C: Methods* **2019**, *25*, 593–608, doi:10.1089/ten.tec.2019.0116.
41. Gao, L.; Liu, G.; Tan, Y.; Li, R.; Zhang, C.; Gao, H.; Zhao, B. Creep-Recovery Behaviors of Articular Cartilage under Uniaxial and Biaxial Tensile Loadings. *Front. Bioeng. Biotechnol.* **2023**, *10*, 1085062, doi:10.3389/fbioe.2022.1085062.
42. Ahsanizadeh, S.; Li, L. Strain-Rate-Dependent Non-Linear Tensile Properties of the Superficial Zone of Articular Cartilage. *Connective Tissue Research* **2015**, *56*, 469–476, doi:10.3109/03008207.2015.1066779.
43. Li, L.P.; Buschmann, M.D.; Shirazi-Adl, A. Strain-Rate Dependent Stiffness of Articular Cartilage in Unconfined Compression. *Journal of Biomechanical Engineering* **2003**, *125*, 161–168, doi:10.1115/1.1560142.
44. Eschweiler, J.; Horn, N.; Rath, B.; Betsch, M.; Baroncini, A.; Tingart, M.; Migliorini, F. The Biomechanics of Cartilage—An Overview. *Life* **2021**, *11*, 302, doi:10.3390/life11040302.
45. Chan, D.D.; Cai, L.; Butz, K.D.; Trippel, S.B.; Nauman, E.A.; Neu, C.P. In Vivo Articular Cartilage Deformation: Noninvasive Quantification of Intratissue Strain during Joint Contact in the Human Knee. *Sci Rep* **2016**, *6*, 19220, doi:10.1038/srep19220.
46. Hamsayeh Abbasi Niasar, E.; Li, L.P. Characterizing Site-Specific Mechanical Properties of Knee Cartilage with Indentation-Relaxation Maps and Machine Learning. *Journal of the Mechanical Behavior of Biomedical Materials* **2023**, *142*, 105826, doi:10.1016/j.jmbbm.2023.105826.
47. Sim, S.; Chevrier, A.; Garon, M.; Quenneville, E.; Lavigne, P.; Yaroshinsky, A.; Hoemann, C.D.; Buschmann, M.D. Electromechanical Probe and Automated Indentation Maps Are Sensitive Techniques in Assessing Early Degenerated Human Articular Cartilage. *Journal Orthopaedic Research* **2017**, *35*, 858–867, doi:10.1002/jor.23330.
48. Bae, W.C.; Schumacher, B.L.; Sah, R.L. Indentation Probing of Human Articular Cartilage: Effect on Chondrocyte Viability. *Osteoarthritis and Cartilage* **2007**, *15*, 9–18, doi:10.1016/j.joca.2006.06.007.
49. Simha, N.K.; Jin, H.; Hall, M.L.; Chiravarambath, S.; Lewis, J.L. Effect of Indenter Size on Elastic Modulus of Cartilage Measured by Indentation. *Journal of Biomechanical Engineering* **2007**, *129*, 767–775, doi:10.1115/1.2768110.
50. Novakofski, K.D.; Pownder, S.L.; Koff, M.F.; Williams, R.M.; Potter, H.G.; Fortier, L.A. High-Resolution Methods for Diagnosing Cartilage Damage *In Vivo*. *CARTILAGE* **2016**, *7*, 39–51, doi:10.1177/1947603515602307.
51. Brenneman Wilson, E.C.; Quenneville, C.E.; Maly, M.R. Integrating MR Imaging with Full-Surface Indentation Mapping of Femoral Cartilage in an Ex Vivo Porcine Stifle. *Journal of the Mechanical Behavior of Biomedical Materials* **2023**, *139*, 105651, doi:10.1016/j.jmbbm.2023.105651.
52. Lakin, B.A.; Grasso, D.J.; Shah, S.S.; Stewart, R.C.; Bansal, P.N.; Freedman, J.D.; Grinstaff, M.W.; Snyder, B.D. Cationic Agent Contrast-Enhanced Computed Tomography Imaging of Cartilage Correlates with the Compressive Modulus and Coefficient of Friction. *Osteoarthritis and Cartilage* **2013**, *21*, 60–68, doi:10.1016/j.joca.2012.09.007.
53. Mizutani, R.; Suzuki, Y. X-Ray Microtomography in Biology. *Micron* **2012**, *43*, 104–115, doi:10.1016/j.micron.2011.10.002.
54. Zehbe, R.; Haibel, A.; Riesemeier, H.; Gross, U.; Kirkpatrick, C.J.; Schubert, H.; Brochhausen, C. Going beyond Histology. Synchrotron Micro-Computed Tomography as a Methodology for

Biological Tissue Characterization: From Tissue Morphology to Individual Cells. *J. R. Soc. Interface.* **2010**, *7*, 49–59, doi:10.1098/rsif.2008.0539.
55. Mow, V.C.; Ratcliffe, A.; Poole, A.R. Cartilage and Diarthrodial Joints as Paradigms for Hierarchical Materials and Structures. *Biomaterials* **1992**, *13*, 67–97, doi:10.1016/0142-9612(92)90001-5.
56. Ateshian, G.A. The Role of Interstitial Fluid Pressurization in Articular Cartilage Lubrication. *Journal of Biomechanics* **2009**, *42*, 1163–1176, doi:10.1016/j.jbiomech.2009.04.040.
57. Mahjoub, M.; Berenbaum, F.; Houard, X. Why Subchondral Bone in Osteoarthritis? The Importance of the Cartilage Bone Interface in Osteoarthritis. *Osteoporos Int* **2012**, *23*, 841–846, doi:10.1007/s00198-012-2161-0.
58. Dall'Ara, E.; Peña-Fernández, M.; Palanca, M.; Giorgi, M.; Cristofolini, L.; Tozzi, G. Precision of Digital Volume Correlation Approaches for Strain Analysis in Bone Imaged with Micro-Computed Tomography at Different Dimensional Levels. *Front. Mater.* **2017**, *4*, 31, doi:10.3389/fmats.2017.00031.
59. Mourad, C.; Gallego Manzano, L.; Viry, A.; Booij, R.; Oei, E.H.G.; Becce, F.; Omoumi, P. Chances and Challenges of Photon-Counting CT in Musculoskeletal Imaging. *Skeletal Radiol* **2024**, *53*, 1889–1902, doi:10.1007/s00256-024-04622-6.
60. Clark, J.N.; Garbout, A.; Ferreira, S.A.; Javaheri, B.; Pitsillides, A.A.; Rankin, S.M.; Jeffers, J.R.T.; Hansen, U. Propagation Phase-Contrast Micro-Computed Tomography Allows Laboratory-Based Three-Dimensional Imaging of Articular Cartilage down to the Cellular Level. *Osteoarthritis and Cartilage* **2020**, *28*, 102–111, doi:10.1016/j.joca.2019.10.007.
61. Karhula, S.S.; Finnilä, M.A.; Freedman, J.D.; Kauppinen, S.; Valkealahti, M.; Lehenkari, P.; Pritzker, K.P.H.; Nieminen, H.J.; Snyder, B.D.; Grinstaff, M.W.; et al. Micro-Scale Distribution of CA4+ in Ex Vivo Human Articular Cartilage Detected with Contrast-Enhanced Micro-Computed Tomography Imaging. *Frontiers in Physics* **2017**, *5*.
62. Ojanen, S.P.; Finnilä, M.A.J.; Herzog, W.; Saarakkala, S.; Korhonen, R.K.; Rieppo, L. Micro-Computed Tomography-Based Collagen Orientation and Anisotropy Analysis of Rabbit Articular Cartilage. *Ann Biomed Eng* **2023**, *51*, 1769–1780, doi:10.1007/s10439-023-03183-4.
63. Danalache, M.; Beutler, K.R.; Rolauffs, B.; Wolfgart, J.M.; Bonnaire, F.C.; Fischer, S.; Greving, I.; Hofmann, U.K. Exploration of Changes in Spatial Chondrocyte Organisation in Human Osteoarthritic Cartilage by Means of 3D Imaging. *Scientific Reports* **2021**, *11*, doi:10.1038/s41598-021-89582-w.
64. Lusic, H.; Grinstaff, M.W. X-Ray-Computed Tomography Contrast Agents. *Chem. Rev.* **2013**, *113*, 1641–1666, doi:10.1021/cr200358s.
65. Pauwels, E.; Van Loo, D.; Cornillie, P.; Brabant, L.; Van Hoorebeke, L. An Exploratory Study of Contrast Agents for Soft Tissue Visualization by Means of High Resolution X-Ray Computed Tomography Imaging: CONTRAST AGENTS FOR SOFT TISSUE VISUALIZATION WITH MICROCT. *Journal of Microscopy* **2013**, *250*, 21–31, doi:10.1111/jmi.12013.
66. Majda, D.; Bhattarai, A.; Riikonen, J.; Napruszewska, B.D.; Zimowska, M.; Michalik-Zym, A.; Töyräs, J.; Lehto, V.-P. New Approach for Determining Cartilage Pore Size Distribution: NaCl-Thermoporometry. *Microporous and Mesoporous Materials* **2017**, *241*, 238–245, doi:10.1016/j.micromeso.2017.01.005.
67. Omelchenko, A.I.; Dyachkova, I.G.; Zolotov, D.A.; Kaloyan, A.A.; Shepeleva, V.O.; Podurets, K.M. New Approaches in the Tomographic Visualization of Joints Using X-Ray Contrast Nanoparticles and Laser Radiation. *Crystallogr. Rep.* **2024**, *69*, 214–219, doi:10.1134/S106377452460011X.
68. Nelson, B.B.; Mäkelä, J.T.A.; Lawson, T.B.; Patwa, A.N.; Snyder, B.D.; McIlwraith, C.W.; Grinstaff, M.W.; Seabaugh, K.A.; Barrett, M.F.; Goodrich, L.R.; et al. Longitudinal in Vivo Cationic Contrast-enhanced Computed Tomography Classifies Equine Articular Cartilage Injury and Repair. *Journal Orthopaedic Research* **2024**, *42*, 2264–2276, doi:10.1002/jor.25869.

69. Jäntti, J.; Joenathan, A.; Fugazzola, M.; Tuppurainen, J.; Honkanen, J.T.J.; Töyräs, J.; Van Weeren, R.; Snyder, B.D.; Grinstaff, M.W.; Matikka, H.; et al. Cationic Tantalum Oxide Nanoparticle Contrast Agent for Micro Computed Tomography Reveals Articular Cartilage Proteoglycan Distribution and Collagen Architecture Alterations. *Osteoarthritis and Cartilage* **2024**, *32*, 299–309, doi:10.1016/j.joca.2023.11.020.
70. Davis, S.; Karali, A.; Balcaen, T.; Zekonyte, J.; Pétré, M.; Roldo, M.; Kerckhofs, G.; Blunn, G. Comparison of Two Contrast-Enhancing Staining Agents for Use in X-Ray Imaging and Digital Volume Correlation Measurements across the Cartilage-Bone Interface. *Journal of the Mechanical Behavior of Biomedical Materials* **2024**, *152*, 106414, doi:10.1016/j.jmbbm.2024.106414.
71. Valerio, M.S.; Edwards, J.B.; Dolan, C.P.; Motherwell, J.M.; Potter, B.K.; Dearth, C.L.; Goldman, S.M. Effect of Targeted Cytokine Inhibition on Progression of Post-Traumatic Osteoarthritis Following Intra-Articular Fracture. *INTERNATIONAL JOURNAL OF MOLECULAR SCIENCES* **2023**, *24*, doi:10.3390/ijms241713606.
72. Lin, A.S.P.; Reece, D.S.; Thote, T.; Sridaran, S.; Stevens, H.Y.; Willett, N.J.; Guldberg, R.E. Intra-Articular Delivery of Micronized Dehydrated Human Amnion/Chorion Membrane Reduces Degenerative Changes after Onset of Post-Traumatic Osteoarthritis. *Frontiers in Bioengineering and Biotechnology* **2023**, *11*, doi:10.3389/fbioe.2023.1224141.
73. Jo, S.Y.; Sebro, R.A. In Vivo Intra-Articular Contrast Enhanced μCT Imaging of Mouse Knee Cartilage. *Bone* **2023**, *167*, doi:10.1016/j.bone.2022.116632.
74. Jin, Y.J.; Park, D.Y.; Noh, S.; Kwon, H.; Shin, D.I.; Park, J.H.; Min, B.-H. Effects of Glycosaminoglycan Content in Extracellular Matrix of Donor Cartilage on the Functional Properties of Osteochondral Allografts Evaluated by Micro-CT Nondestructive Analysis. *PLoS ONE* **2023**, *18*, doi:10.1371/journal.pone.0285733.
75. Honkanen, M.K.M.; Mohammadi, A.; te Moller, N.C.R.; Ebrahimi, M.; Xu, W.; Plomp, S.; Pouran, B.; Lehto, V.-P.; Brommer, H.; van Weeren, P.R.; et al. Dual-Contrast Micro-CT Enables Cartilage Lesion Detection and Tissue Condition Evaluation Ex Vivo. *Equine Veterinary Journal* **2023**, *55*, 315–324, doi:10.1111/evj.13573.
76. Fleischer, M.M.; Hartner, S.E.; Newton, M.D.; Baker, K.C.; Maerz, T. Early Patellofemoral Cartilage and Bone Pathology in a Rat Model of Noninvasive Anterior Cruciate Ligament Rupture. *Connective Tissue Research* **2023**, *64*, 175–185, doi:10.1080/03008207.2022.2136571.
77. Durongbhan, P.; Silva, M.O.; Li, Z.; Ansari, N.; Kour, R.Y.N.; Davey, C.E.; Stok, K.S. A microCT Imaging Protocol for Reproducible and Efficient Quantitative Morphometric Analysis (QMA) of Joint Structures of the in Situ Mouse Tibio-Femoral Joint. *Bone* **2023**, *166*, doi:10.1016/j.bone.2022.116606.
78. Davis, S.; Karali, A.; Zekonyte, J.; Roldo, M.; Blunn, G. Development of a Method to Investigate Strain Distribution across the Cartilage-Bone Interface in Guinea Pig Model of Spontaneous Osteoarthritis Using Lab-Based Contrast Enhanced X-Ray-Computed Tomography and Digital Volume Correlation. *Journal of the Mechanical Behavior of Biomedical Materials* **2023**, *144*, doi:10.1016/j.jmbbm.2023.105999.
79. Chan, D.D.; Mashiatulla, M.; Li, J.; Ross, R.D.; Pendyala, M.; Patwa, A.; Grinstaff, M.W.; Plaas, A.; Sumner, D.R. Contrast-Enhanced Micro-Computed Tomography of Compartment and Time-Dependent Changes in Femoral Cartilage and Subchondral Plate in a Murine Model of Osteoarthritis. *Anatomical Record* **2023**, *306*, 92–109, doi:10.1002/ar.25027.
80. Bhattarai, A.; Lok, J.G.-T.; Sun, H.; Vardhanabhuti, V. Computed Tomography of Cartilage: An Exploration of Novel Cationic Bismuth Contrast Agent. *Annals of Biomedical Engineering* **2023**, *51*, 977–986, doi:10.1007/s10439-022-03110-z.
81. McKinney, J.M.; Pucha, K.A.; Doan, T.N.; Wang, L.; Weinstock, L.D.; Tignor, B.T.; Fowle, K.L.; Levit, R.D.; Wood, L.B.; Willett, N.J. Sodium Alginate Microencapsulation of Human Mesenchymal Stromal Cells Modulates Paracrine Signaling Response and Enhances Efficacy

for Treatment of Established Osteoarthritis. *Acta Biomaterialia* **2022**, *141*, 315–332, doi:10.1016/j.actbio.2021.12.034.
82. Fowkes, M.M.; Das Neves Borges, P.; Cacho-Nerin, F.; Brennan, P.E.; Vincent, T.L.; Lim, N.H. Imaging Articular Cartilage in Osteoarthritis Using Targeted Peptide Radiocontrast Agents. *PLoS ONE* **2022**, *17*, e0268223, doi:10.1371/journal.pone.0268223.
83. Fantoni, S.; Gabucci, I.; Cardarelli, P.; Paternò, G.; Taibi, A.; Cristofori, V.; Trapella, C.; Bazzani, A.; Assenza, M.; Zanna Bonacorsi, A.; et al. A Cationic Contrast Agent in X-Ray Imaging of Articular Cartilage: Pre-Clinical Evaluation of Diffusion and Attenuation Properties. *Diagnostics* **2022**, *12*, doi:10.3390/diagnostics12092111.
84. Zhu, Y.; Ponjevic, D.; Matyas, J.R.; Boyd, S.K. Contrast-Enhanced x-Ray Microscopy of Articular Cartilage. *Connective Tissue Research* **2021**, *62*, 542–553, doi:10.1080/03008207.2020.1813121.
85. Ve Koon, K.T.; Grenier, D.; Taborik, F.; Perrier, A.-L.; Mahieu-Williame, L.; Magnier, L.; Chuzel, T.; Contamin, H.; Chereul, E.; Beuf, O. Comparison of High-Resolution Magnetic Resonance Imaging and Micro-Computed Tomography Arthrography for in-Vivo Assessment of Cartilage in Non-Human Primate Models. *Quantitative Imaging in Medicine and Surgery* **2021**, *11*, 3431–3447, doi:10.21037/qims-20-116.
86. Nelson, B.B.; Stewart, R.C.; Kawcak, C.E.; Freedman, J.D.; Patwa, A.N.; Snyder, B.D.; Goodrich, L.R.; Grinstaff, M.W. Quantitative Evaluation of Equine Articular Cartilage Using Cationic Contrast-Enhanced Computed Tomography. *Cartilage* **2021**, *12*, 211–221, doi:10.1177/1947603518812562.
87. Nelson, B.B.; Mäkelä, J.T.A.; Lawson, T.B.; Patwa, A.N.; Snyder, B.D.; McIlwraith, C.W.; Grinstaff, M.W.; Goodrich, L.R.; Kawcak, C.E. Cationic Contrast-enhanced Computed Tomography Distinguishes between Reparative, Degenerative, and Healthy Equine Articular Cartilage. *Journal Orthopaedic Research* **2021**, *39*, 1647–1657, doi:10.1002/jor.24894.
88. Lawson, T.; Joenathan, A.; Patwa, A.; Snyder, B.D.; Grinstaff, M.W. Tantalum Oxide Nanoparticles for the Quantitative Contrast-Enhanced Computed Tomography of Ex Vivo Human Cartilage: Assessment of Biochemical Composition and Biomechanics. *ACS Nano* **2021**, *15*, 19175–19184, doi:10.1021/acsnano.1c03375.
89. Gao, X.; Patwa, A.N.; Deng, Z.; Utsunomiya, H.; Grinstaff, M.W.; Ruzbarsky, J.J.; Snyder, B.D.; Ravuri, S.; Philippon, M.J.; Huard, J. Influence of Fixation on CA4+ Contrast Enhanced microCT of Articular Cartilage and Subsequent Feasibility for Histological Evaluation. *Am J Transl Res* **2021**, *13*, 8921–8937.
90. Flynn, C.; Hurtig, M.; Linden, A. zur Anionic Contrast–Enhanced MicroCT Imaging Correlates with Biochemical and Histological Evaluations of Osteoarthritic Articular Cartilage. *CARTILAGE* **2021**, *13*, 1388S-1397S, doi:10.1177/1947603520924748.
91. Dunham, C.L.; Steenbock, H.; Brinckmann, J.; Reiter, A.J.; Castile, R.M.; Chamberlain, A.M.; Lake, S.P. Increased Volume and Collagen Crosslinks Drive Soft Tissue Contribution to Post-Traumatic Elbow Contracture in an Animal Model. *Journal of Orthopaedic Research* **2021**, *39*, 1800–1810, doi:10.1002/jor.24781.
92. Dufour, A.; Lafont, J.E.; Buffier, M.; Verset, M.; Cohendet, A.; Contamin, H.; Confais, J.; Sankar, S.; Rioult, M.; Perrier-Groult, E.; et al. Repair of Full-Thickness Articular Cartilage Defects Using IEIK13 Self-Assembling Peptide Hydrogel in a Non-Human Primate Model. *Scientific Reports* **2021**, *11*, doi:10.1038/s41598-021-83208-x.
93. Clark, J.N.; Tavana, S.; Clark, B.; Briggs, T.; Jeffers, J.R.T.; Hansen, U. High Resolution Three-Dimensional Strain Measurements in Human Articular Cartilage. *Journal of the Mechanical Behavior of Biomedical Materials* **2021**, *124*, 104806, doi:10.1016/j.jmbbm.2021.104806.
94. Boos, M.A.; Grinstaff, M.W.; Lamandé, S.R.; Stok, K.S. Contrast-Enhanced Micro–Computed Tomography for 3D Visualization and Quantification of Glycosaminoglycans in Different Cartilage Types. *CARTILAGE* **2021**, *13*, 486S-494S, doi:10.1177/19476035211053820.

95. Blom, R.P.; Mol, D.; van Ruijven, L.J.; Kerkhoffs, G.M.M.J.; Smit, T.H. A Single Axial Impact Load Causes Articular Damage That Is Not Visible with Micro-Computed Tomography: An Ex Vivo Study on Caprine Tibiotalar Joints. *Cartilage* **2021**, *13*, 1490S-1500S, doi:10.1177/1947603519876353.
96. Besler, B.A.; Schadow, J.E.; Durongbhan, P.; Steiner, T.H.; Choo, R.J.; Zulliger, M.A.; Wilke, M.; Atal, K.; Firminger, C.; Quintin, A.; et al. Quantitative Measures of Bone Shape, Cartilage Morphometry and Joint Alignment Are Associated with Disease in an ACLT and MMx Rat Model of Osteoarthritis. *Bone* **2021**, *146*, doi:10.1016/j.bone.2021.115903.
97. ter Voert, C.E.M.; Kour, R.Y.N.; van Teeffelen, B.C.J.; Ansari, N.; Stok, K.S. Contrast-Enhanced Micro-Computed Tomography of Articular Cartilage Morphology with Ioversol and Iomeprol. *Journal of Anatomy* **2020**, *237*, 1062–1071, doi:10.1111/joa.13271.
98. Sugasawa, T.; Kuji, T.; Aoki, K.; Yanazawa, K.; Takenouchi, A.; Watanabe, M.; Tome, Y.; Takeuchi, Y.; Aita, Y.; Yahagi, N.; et al. Characterization of Osteoarthritis in a Medial Meniscectomy-Induced Animal Model Using Contrast-Enhanced X-Ray Microtomography. *Biomedicines* **2020**, *8*, doi:10.3390/biomedicines8030056.
99. Reece, D.S.; Burnsed, O.A.; Parchinski, K.; Marr, E.E.; White, R.M.; Salazar-Noratto, G.E.; Lin, A.S.P.; Willett, N.J.; Guldberg, R.E. Reduced Size Profile of Amniotic Membrane Particles Decreases Osteoarthritis Therapeutic Efficacy. *Tissue Engineering - Part A* **2020**, *26*, 28–37, doi:10.1089/ten.tea.2019.0074.
100. Meng, H.; Quan, Q.; Yuan, X.; Zheng, Y.; Peng, J.; Guo, Q.; Wang, A.; Lu, S. Diffusion of Neutral Solutes within Human Osteoarthritic Cartilage: Effect of Loading Patterns. *Journal of Orthopaedic Translation* **2020**, *22*, 58–66, doi:10.1016/j.jot.2019.10.013.
101. Freedman, J.D.; Ellis, D.J.; Lusic, H.; Varma, G.; Grant, A.K.; Lakin, B.A.; Snyder, B.D.; Grinstaff, M.W. dGEMRIC and CECT Comparison of Cationic and Anionic Contrast Agents in Cadaveric Human Metacarpal Cartilage. *J Orthop Res* **2020**, *38*, 719–725, doi:10.1002/jor.24511.
102. Cubria, M.B.; Suarez, S.; Masoudi, A.; Oftadeh, R.; Kamalapathy, P.; DuBose, A.; Erdos, M.R.; Cabral, W.A.; Karim, L.; Collins, F.S.; et al. Evaluation of Musculoskeletal Phenotype of the G608G Progeria Mouse Model with Lonafarnib, Pravastatin, and Zoledronic Acid as Treatment Groups. *Proceedings of the National Academy of Sciences of the United States of America* **2020**, *117*, doi:10.1073/pnas.1906713117.
103. Zhang, H.; Belev, G.; Stewart, R.C.; Grinstaff, M.W.; Snyder, B.D.; Wilson, D.R. Protocol Development for Synchrotron Contrast-Enhanced CT of Human Hip Cartilage. *Medical Engineering & Physics* **2019**, *73*, 1–8, doi:10.1016/j.medengphy.2019.08.003.
104. Ylitalo, T.; Finnilä, M.A.J.; Gahunia, H.K.; Karhula, S.S.; Suhonen, H.; Valkealahti, M.; Lehenkari, P.; Hæggström, E.; Pritzker, K.P.H.; Saarakkala, S.; et al. Quantifying Complex Micro-Topography of Degenerated Articular Cartilage Surface by Contrast-Enhanced Micro-Computed Tomography and Parametric Analyses. *Journal of Orthopaedic Research* **2019**, *37*, 855–866, doi:10.1002/jor.24245.
105. Tsai, L.-C.; Cooper, E.S.; Hetzendorfer, K.M.; Warren, G.L.; Chang, Y.-H.; Willett, N.J. Effects of Treadmill Running and Limb Immobilization on Knee Cartilage Degeneration and Locomotor Joint Kinematics in Rats Following Knee Meniscal Transection. *Osteoarthritis and Cartilage* **2019**, *27*, 1851–1859, doi:10.1016/j.joca.2019.08.001.
106. Steppacher, S.D.; Hanke, M.S.; Zurmühle, C.A.; Haefeli, P.C.; Klenke, F.M.; Tannast, M. Ultrasonic Cartilage Thickness Measurement Is Accurate, Reproducible, and Reliable - Validation Study Using Contrast-Enhanced Micro-CT. *Journal of Orthopaedic Surgery and Research* **2019**, *14*, doi:10.1186/s13018-019-1099-8.
107. Nelson, B.B.; Mäkelä, J.T.A.; Lawson, T.B.; Patwa, A.N.; Barrett, M.F.; McIlwraith, C.W.; Hurtig, M.B.; Snyder, B.D.; Moorman, V.J.; Grinstaff, M.W.; et al. Evaluation of Equine Articular Cartilage Degeneration after Mechanical Impact Injury Using Cationic Contrast-

Enhanced Computed Tomography. *Osteoarthritis and Cartilage* **2019**, *27*, 1219–1228, doi:10.1016/j.joca.2019.04.015.
108. Michalak, G.J.; Walker, R.; Boyd, S.K. Concurrent Assessment of Cartilage Morphology and Bone Microarchitecture in the Human Knee Using Contrast-Enhanced HR-pQCT Imaging. *Journal of Clinical Densitometry* **2019**, *22*, 74–85, doi:10.1016/j.jocd.2018.07.002.
109. McKinney, J.M.; Doan, T.N.; Wang, L.; Deppen, J.; Reece, D.S.; Pucha, K.A.; Ginn, S.; Levit, R.D.; Willett, N.J. Therapeutic Efficacy of Intra-Articular Delivery of Encapsulated Human Mesenchymal Stem Cells on Early Stage Osteoarthritis. *European cells & materials* **2019**, *37*, 42–59, doi:10.22203/eCM.v037a04.
110. Kwok, A.T.; Moore, J.E.; Rosas, S.; Kerr, B.A.; Andrews, R.N.; Nguyen, C.M.; Lee, J.; Furdui, C.M.; Collins, B.E.; Munley, M.T.; et al. Knee and Hip Joint Cartilage Damage from Combined Spaceflight Hazards of Low-Dose Radiation Less than 1 Gy and Prolonged Hindlimb Unloading. *Radiation Research* **2019**, *191*, 497–506, doi:10.1667/RR15216.1.
111. Gatenholm, B.; Lindahl, C.; Brittberg, M.; Stadelmann, V.A. Spatially Matching Morphometric Assessment of Cartilage and Subchondral Bone in Osteoarthritic Human Knee Joint with Micro-Computed Tomography. *Bone* **2019**, *120*, 393–402, doi:10.1016/j.bone.2018.12.003.
112. Dourthe, B.; Nickmanesh, R.; Wilson, D.R.; D'Agostino, P.; Patwa, A.N.; Grinstaff, M.W.; Snyder, B.D.; Vereecke, E. Assessment of Healthy Trapeziometacarpal Cartilage Properties Using Indentation Testing and Contrast-Enhanced Computed Tomography. *Clinical Biomechanics* **2019**, *61*, 181–189, doi:10.1016/j.clinbiomech.2018.12.015.
113. Reece, D.S.; Thote, T.; Lin, A.S.P.; Willett, N.J.; Guldberg, R.E. Contrast Enhanced μCT Imaging of Early Articular Changes in a Pre-Clinical Model of Osteoarthritis. *Osteoarthritis and Cartilage* **2018**, *26*, 118–127, doi:10.1016/j.joca.2017.10.017.
114. Nickmanesh, R.; Stewart, R.C.; Snyder, B.D.; Grinstaff, M.W.; Masri, B.A.; Wilson, D.R. Contrast-enhanced Computed Tomography (CECT) Attenuation Is Associated with Stiffness of Intact Knee Cartilage. *Journal Orthopaedic Research* **2018**, *36*, 2641–2647, doi:10.1002/jor.24022.
115. Mirahmadi, F.; Koolstra, J.H.; Fazaeli, S.; Lobbezoo, F.; van Lenthe, G.H.; Snabel, J.; Stoop, R.; Arbabi, V.; Weinans, H.; Everts, V. Aging Does Not Change the Compressive Stiffness of Mandibular Condylar Cartilage in Horses. *Osteoarthritis and Cartilage* **2018**, *26*, 1744–1752, doi:10.1016/j.joca.2018.08.007.
116. Stewart, R.C.; Patwa, A.N.; Lusic, H.; Freedman, J.D.; Wathier, M.; Snyder, B.D.; Guermazi, A.; Grinstaff, M.W. Synthesis and Preclinical Characterization of a Cationic Iodinated Imaging Contrast Agent (CA4+) and Its Use for Quantitative Computed Tomography of Ex Vivo Human Hip Cartilage. *J. Med. Chem.* **2017**, *60*, 5543–5555, doi:10.1021/acs.jmedchem.7b00234.
117. Saukko, A.E.A.; Honkanen, J.T.J.; Xu, W.; Väänänen, S.P.; Jurvelin, J.S.; Lehto, V.-P.; Töyräs, J. Dual Contrast CT Method Enables Diagnostics of Cartilage Injuries and Degeneration Using a Single CT Image. *Annals of Biomedical Engineering* **2017**, *45*, 2857–2866, doi:10.1007/s10439-017-1916-3.
118. Raines, A.L.; Shih, M.-S.; Chua, L.; Su, C.-W.; Tseng, S.C.; O'Connell, J. Efficacy of Particulate Amniotic Membrane and Umbilical Cord Tissues in Attenuating Cartilage Destruction in an Osteoarthritis Model. *Tissue engineering. Part A* **2017**, *23*, 12–19, doi:10.1089/ten.TEA.2016.0088.
119. Nieminen, H.J.; Gahunia, H.K.; Pritzker, K.P.H.; Ylitalo, T.; Rieppo, L.; Karhula, S.S.; Lehenkari, P.; Hæggström, E.; Saarakkala, S. 3D Histopathological Grading of Osteochondral Tissue Using Contrast-Enhanced Micro-Computed Tomography. *Osteoarthritis and Cartilage* **2017**, *25*, 1680–1689, doi:10.1016/j.joca.2017.05.021.
120. Mashiatulla, M.; Moran, M.M.; Chan, D.; Li, J.; Freedman, J.D.; Snyder, B.D.; Grinstaff, M.W.; Plaas, A.; Sumner, D.R. Murine Articular Cartilage Morphology and Compositional Quantification with High Resolution Cationic Contrast-Enhanced μCT. *Journal of Orthopaedic Research* **2017**, *35*, 2740–2748, doi:10.1002/jor.23595.

121. Kün-Darbois, J.-D.; Manero, F.; Rony, L.; Chappard, D. Contrast Enhancement with Uranyl Acetate Allows Quantitative Analysis of the Articular Cartilage by microCT: Application to Mandibular Condyles in the BTX Rat Model of Disuse. *Micron* **2017**, *97*, 35–40, doi:10.1016/j.micron.2017.03.008.
122. Karhula, S.S.; Finnilä, M.A.; Lammi, M.J.; Ylärinne, J.H.; Kauppinen, S.; Rieppo, L.; Pritzker, K.P.H.; Nieminen, H.J.; Saarakkala, S. Effects of Articular Cartilage Constituents on Phosphotungstic Acid Enhanced Micro-Computed Tomography. *PLoS ONE* **2017**, *12*, doi:10.1371/journal.pone.0171075.
123. de Visser, H.M.; Weinans, H.; Coeleveld, K.; van Rijen, M.H.P.; Lafeber, F.P.J.G.; Mastbergen, S.C. Groove Model of Tibia-Femoral Osteoarthritis in the Rat. *Journal of Orthopaedic Research* **2017**, *35*, 496–505, doi:10.1002/jor.23299.
124. Willett, N.J.; Thote, T.; Hart, M.; Moran, S.; Guldberg, R.E.; Kamath, R.V. Quantitative Pre-Clinical Screening of Therapeutics for Joint Diseases Using Contrast Enhanced Micro-Computed Tomography. *Osteoarthritis and Cartilage* **2016**, *24*, 1604–1612, doi:10.1016/j.joca.2016.04.021.
125. van Tiel, J.; Siebelt, M.; Reijman, M.; Bos, P.K.; Waarsing, J.H.; Zuurmond, A.-M.; Nasserinejad, K.; van Osch, G.J.V.M.; Verhaar, J.A.N.; Krestin, G.P.; et al. Quantitative in Vivo CT Arthrography of the Human Osteoarthritic Knee to Estimate Cartilage Sulphated Glycosaminoglycan Content: Correlation with Ex-Vivo Reference Standards. *Osteoarthritis and Cartilage* **2016**, *24*, 1012–1020, doi:10.1016/j.joca.2016.01.137.
126. Stok, K.S.; Besler, B.A.; Steiner, T.H.; Escudero, A.V.V.; Zulliger, M.A.; Wilke, M.; Atal, K.; Quintin, A.; Koller, B.; Müller, R.; et al. Three-Dimensional Quantitative Morphometric Analysis (QMA) for in Situ Joint and Tissue Assessment of Osteoarthritis in a Preclinical Rabbit Disease Model. *PLoS ONE* **2016**, *11*, doi:10.1371/journal.pone.0147564.
127. Mittelstaedt, D.; Kahn, D.; Xia, Y. Topographical and Depth-Dependent Glycosaminoglycan Concentration in Canine Medial Tibial Cartilage 3 Weeks after Anterior Cruciate Ligament Transection Surgery - A Microscopic Imaging Study. *Quantitative Imaging in Medicine and Surgery* **2016**, *6*, 648–660, doi:10.21037/qims.2016.06.12.
128. Lakin, B.A.; Patel, H.; Holland, C.; Freedman, J.D.; Shelofsky, J.S.; Snyder, B.D.; Stok, K.S.; Grinstaff, M.W. Contrast-Enhanced CT Using a Cationic Contrast Agent Enables Non-Destructive Assessment of the Biochemical and Biomechanical Properties of Mouse Tibial Plateau Cartilage. *Journal of Orthopaedic Research* **2016**, *34*, 1130–1138, doi:10.1002/jor.23141.
129. Honkanen, J.T.J.; Turunen, M.J.; Freedman, J.D.; Saarakkala, S.; Grinstaff, M.W.; Ylärinne, J.H.; Jurvelin, J.S.; Töyräs, J. Cationic Contrast Agent Diffusion Differs Between Cartilage and Meniscus. *Annals of Biomedical Engineering* **2016**, *44*, 2913–2921, doi:10.1007/s10439-016-1629-z.
130. Wang, V.M.; Karas, V.; Lee, A.S.; Yin, Z.; Van Thiel, G.S.; Hussey, K.; Sumner, D.R.; Chubinskaya, S.; Magin, R.L.; Verma, N.N.; et al. Assessment of Glenoid Chondral Healing: Comparison of Microfracture to Autologous Matrix-Induced Chondrogenesis in a Novel Rabbit Shoulder Model. *Journal of Shoulder and Elbow Surgery* **2015**, *24*, 1789–1800, doi:10.1016/j.jse.2015.06.008.
131. Nieminen, H.J.; Ylitalo, T.; Karhula, S.; Suuronen, J.-P.; Kauppinen, S.; Serimaa, R.; Hæggström, E.; Pritzker, K.P.H.; Valkealahti, M.; Lehenkari, P.; et al. Determining Collagen Distribution in Articular Cartilage Using Contrast-Enhanced Micro-Computed Tomography. *Osteoarthritis and Cartilage* **2015**, *23*, 1613–1621, doi:10.1016/j.joca.2015.05.004.
132. Li, X.-F.; Cai, X.-R.; Fan, F.; Niu, H.-J.; Li, S.-Y.; Li, D.-Y.; Fan, Y.-B.; Qin, Y.-X. Observation of sGAG Content of Human Hip Joint Cartilage in Different Old Age Groups Based on EPIC Micro-CT. *Connective Tissue Research* **2015**, *56*, 99–105, doi:10.3109/03008207.2015.1009052.

133. Lakin, B.A.; Ellis, D.J.; Shelofsky, J.S.; Freedman, J.D.; Grinstaff, M.W.; Snyder, B.D. Contrast-Enhanced CT Facilitates Rapid, Non-Destructive Assessment of Cartilage and Bone Properties of the Human Metacarpal. *Osteoarthritis and Cartilage* **2015**, *23*, 2158–2166, doi:10.1016/j.joca.2015.05.033.
134. Fan, F.; L, X.; R, P.; C, X.; Y, Y.; F, Y.; N, H. Correlations between X-Ray Attenuation and GAG Content of Different Cartilage Layers Based on Contrast Agent Enhanced Micro-CT. *Annual International Conference of the IEEE Engineering in Medicine and Biology Society. IEEE Engineering in Medicine and Biology Society. Annual International Conference* **2015**, *2015*, 6366–6369, doi:10.1109/EMBC.2015.7319849.
135. Bagi, C.M.; Zakur, D.E.; Berryman, E.; Andresen, C.J.; Wilkie, D. Correlation between μCT Imaging, Histology and Functional Capacity of the Osteoarthritic Knee in the Rat Model of Osteoarthritis. *Journal of Translational Medicine* **2015**, *13*, doi:10.1186/s12967-015-0641-7.
136. Bagi, C.M.; Berryman, E.; Zakur, D.E.; Wilkie, D.; Andresen, C.J. Effect of Antiresorptive and Anabolic Bone Therapy on Development of Osteoarthritis in a Posttraumatic Rat Model of OA. *Arthritis Research and Therapy* **2015**, *17*, doi:10.1186/s13075-015-0829-5.
137. Siebelt, M.; Waarsing, J.H.; Groen, H.C.; Müller, C.; Koelewijn, S.J.; de Blois, E.; Verhaar, J.A.N.; de Jong, M.; Weinans, H. Inhibited Osteoclastic Bone Resorption through Alendronate Treatment in Rats Reduces Severe Osteoarthritis Progression. *Bone* **2014**, *66*, 163–170, doi:10.1016/j.bone.2014.06.009.
138. Siebelt, M.; Van der Windt, A.E.; Groen, H.C.; Sandker, M.; Waarsing, J.H.; Müller, C.; De Jong, M.; Jahr, H.; Weinans, H. FK506 Protects against Articular Cartilage Collagenous Extra-Cellular Matrix Degradation. *Osteoarthritis and Cartilage* **2014**, *22*, 591–600, doi:10.1016/j.joca.2014.02.003.
139. Renders, G.A.P.; Mulder, L.; Lin, A.S.; Langenbach, G.E.J.; Koolstra, J.H.; Guldberg, R.E.; Everts, V. Contrast-Enhanced microCT (EPIC-μCT) Ex Vivo Applied to the Mouse and Human Jaw Joint. *Dentomaxillofacial Radiology* **2014**, *43*, doi:10.1259/dmfr.20130098.
140. Kerckhofs, G.; Sainz, J.; Maréchal, M.; Wevers, M.; Van de Putte, T.; Geris, L.; Schrooten, J. Contrast-Enhanced Nanofocus X-Ray Computed Tomography Allows Virtual Three-Dimensional Histopathology and Morphometric Analysis of Osteoarthritis in Small Animal Models. *Cartilage* **2014**, *5*, 55–65, doi:10.1177/1947603513501175.
141. Fu, M.; Liu, J.; Huang, G.; Huang, Z.; Zhang, Z.; Wu, P.; Wang, B.; Yang, Z.; Liao, W. Impaired Ossification Coupled with Accelerated Cartilage Degeneration in Developmental Dysplasia of the Hip: Evidences from μcT Arthrography in a Rat Model. *BMC Musculoskeletal Disorders* **2014**, *15*, doi:10.1186/1471-2474-15-339.
142. Freedman, J.D.; Lusic, H.; Snyder, B.D.; Grinstaff, M.W. Tantalum Oxide Nanoparticles for the Imaging of Articular Cartilage Using X-Ray Computed Tomography: Visualization of Ex Vivo/in Vivo Murine Tibia and Ex Vivo Human Index Finger Cartilage. *Angewandte Chemie - International Edition* **2014**, *53*, 8406–8410, doi:10.1002/anie.201404519.
143. Entezari, V.; Bansal, P.N.; Stewart, R.C.; Lakin, B.A.; Grinstaff, M.W.; Snyder, B.D. Effect of Mechanical Convection on the Partitioning of an Anionic Iodinated Contrast Agent in Intact Patellar Cartilage. *Journal of Orthopaedic Research* **2014**, *32*, 1333–1340, doi:10.1002/jor.22662.
144. Das Neves Borges, P.; Forte, A.E.; Vincent, T.L.; Dini, D.; Marenzana, M. Rapid, Automated Imaging of Mouse Articular Cartilage by microCT for Early Detection of Osteoarthritis and Finite Element Modelling of Joint Mechanics. *Osteoarthritis and Cartilage* **2014**, *22*, 1419–1428, doi:10.1016/j.joca.2014.07.014.
145. Thote, T.; Lin, A.S.P.; Raji, Y.; Moran, S.; Stevens, H.Y.; Hart, M.; Kamath, R.V.; Guldberg, R.E.; Willett, N.J. Localized 3D Analysis of Cartilage Composition and Morphology in Small Animal Models of Joint Degeneration. *Osteoarthritis and Cartilage* **2013**, *21*, 1132–1141, doi:10.1016/j.joca.2013.05.018.

146. Stewart, R.C.; Bansal, P.N.; Entezari, V.; Lusic, H.; Nazarian, R.M.; Snyder, B.D.; Grinstaff, M.W. Contrast-Enhanced CT with a High-Affinity Cationic Contrast Agent for Imaging Ex Vivo Bovine, Intact Ex Vivo Rabbit, and in Vivo Rabbit Cartilage. *Radiology* **2013**, *266*, 141–150, doi:10.1148/radiol.12112246.
147. Lakin, B.A.; Grasso, D.J.; Shah, S.S.; Stewart, R.C.; Bansal, P.N.; Freedman, J.D.; Grinstaff, M.W.; Snyder, B.D. Cationic Agent Contrast-Enhanced Computed Tomography Imaging of Cartilage Correlates with the Compressive Modulus and Coefficient of Friction. *Osteoarthritis Cartilage* **2013**, *21*, 60–68, doi:10.1016/j.joca.2012.09.007.
148. Wang, J.; Gao, Y.; Hou, Y.; Zhao, F.; Pu, F.; Liu, X.; Wu, Z.; Fan, Y. Evaluation on Cartilage Morphology after Intra-Articular Injection of Titanium Dioxide Nanoparticles in Rats. *Journal of Nanomaterials* **2012**, *2012*, 452767, doi:10.1155/2012/452767.
149. Van Tiel, J.; Siebelt, M.; Waarsing, J.H.; Piscaer, T.M.; Van Straten, M.; Booij, R.; Dijkshoorn, M.L.; Kleinrensink, G.J.; Verhaar, J.A.N.; Krestin, G.P.; et al. CT Arthrography of the Human Knee to Measure Cartilage Quality with Low Radiation Dose. *Osteoarthritis and Cartilage* **2012**, *20*, 678–685, doi:10.1016/j.joca.2012.03.007.
150. Kotwal, N.; Li, J.; Sandy, J.; Plaas, A.; Sumner, D.R. Initial Application of EPIC-μCT to Assess Mouse Articular Cartilage Morphology and Composition: Effects of Aging and Treadmill Running. *Osteoarthritis and Cartilage* **2012**, *20*, 887–895, doi:10.1016/j.joca.2012.04.012.
151. Kerckhofs, G.; Sainz, J.; Wevers, M.; Van De Putte, T.; Schrooten, J. Contrast-Enhanced Nanofocus Computed Tomography Images the Cartilage Subtissue Architecture in Three Dimensions. *European Cells and Materials* **2012**, *25*, 179–189, doi:10.22203/eCM.v025a13.
152. Siebelt, M.; Waarsing, J.H.; Kops, N.; Piscaer, T.M.; Verhaar, J.A.N.; Oei, E.H.G.; Weinans, H. Quantifying Osteoarthritic Cartilage Changes Accurately Using In Vivo MicroCT Arthrography in Three Etiologically Distinct Rat Models. *JOURNAL OF ORTHOPAEDIC RESEARCH* **2011**, *29*, 1788–1794, doi:10.1002/jor.21444.
153. Siebelt, M.; van Tiel, J.; Waarsing, J.H.; Piscaer, T.M.; van Straten, M.; Booij, R.; Dijkshoorn, M.L.; Kleinrensink, G.J.; Verhaar, J.A.N.; Krestin, G.P.; et al. Clinically Applied CT Arthrography to Measure the Sulphated Glycosaminoglycan Content of Cartilage. *Osteoarthritis and Cartilage* **2011**, *19*, 1183–1189, doi:10.1016/j.joca.2011.07.006.
154. Bansal, P.N.; Stewart, R.C.; Entezari, V.; Snyder, B.D.; Grinstaff, M.W. Contrast Agent Electrostatic Attraction Rather than Repulsion to Glycosaminoglycans Affords a Greater Contrast Uptake Ratio and Improved Quantitative CT Imaging in Cartilage. *Osteoarthritis and Cartilage* **2011**, *19*, 970–976, doi:10.1016/j.joca.2011.04.004.
155. Bansal, P.N.; Joshi, N.S.; Entezari, V.; Malone, B.C.; Stewart, R.C.; Snyder, B.D.; Grinstaff, M.W. Cationic Contrast Agents Improve Quantification of Glycosaminoglycan (GAG) Content by Contrast Enhanced CT Imaging of Cartilage. *Journal of Orthopaedic Research* **2011**, *29*, 704–709, doi:10.1002/jor.21312.
156. Xie, L.; Lin, A.S.P.; Guldberg, R.E.; Levenston, M.E. Nondestructive Assessment of sGAG Content and Distribution in Normal and Degraded Rat Articular Cartilage via EPIC-μCT. *Osteoarthritis and Cartilage* **2010**, *18*, 65–72, doi:10.1016/j.joca.2009.07.014.
157. Bansal, P.N.; Joshi, N.S.; Entezari, V.; Grinstaff, M.W.; Snyder, B.D. Contrast Enhanced Computed Tomography Can Predict the Glycosaminoglycan Content and Biomechanical Properties of Articular Cartilage. *Osteoarthritis and Cartilage* **2010**, *18*, 184–191, doi:10.1016/j.joca.2009.09.003.
158. Xie, L.; Lin, A.S.P.; Levenston, M.E.; Guldberg, R.E. Quantitative Assessment of Articular Cartilage Morphology via EPIC-μCT. *Osteoarthritis and Cartilage* **2009**, *17*, 313–320, doi:10.1016/j.joca.2008.07.015.
159. Taylor, C.; Carballido-Gamio, J.; Majumdar, S.; Li, X. Comparison of Quantitative Imaging of Cartilage for Osteoarthritis: T2, T1rho, dGEMRIC and Contrast-Enhanced Computed Tomography. *Magn Reson Imaging* **2009**, *27*, 779–784, doi:10.1016/j.mri.2009.01.016.

160. Joshi, N.S.; Bansal, P.N.; Stewart, R.C.; Snyder, B.D.; Grinstaff, M.W. Effect of Contrast Agent Charge on Visualization of Articular Cartilage Using Computed Tomography: Exploiting Electrostatic Interactions for Improved Sensitivity. *J. Am. Chem. Soc.* **2009**, *131*, 13234–13235, doi:10.1021/ja9053306.
161. Piscaer, T.M.; Waarsing, J.H.; Kops, N.; Pavljasevic, P.; Verhaar, J.A.N.; van Osch, G.J.V.M.; Weinans, H. *In Vivo* Imaging of Cartilage Degeneration Using μCT-Arthrography. *OSTEOARTHRITIS AND CARTILAGE* **2008**, *16*, 1011–1017, doi:10.1016/j.joca.2008.01.012.
162. Palmer, A.W.; Guldberg, R.E.; Levenston, M.E. Analysis of Cartilage Matrix Fixed Charge Density and Three-Dimensional Morphology via Contrast-Enhanced Microcomputed Tomography. *Proc Natl Acad Sci U S A* **2006**, *103*, 19255–19260, doi:10.1073/pnas.0606406103.
163. Nemetschek, Th.; Riedl, H.; Jonak, R. Topochemistry of the Binding of Phosphotungstic Acid to Collagen. *Journal of Molecular Biology* **1979**, *133*, 67–83, doi:10.1016/0022-2836(79)90251-1.
164. Zhang, C.; Vedadghavami, A.; He, T.; Charles, J.F.; Bajpayee, A.G. Cationic Carrier Mediated Delivery of Anionic Contrast Agents in Low Doses Enable Enhanced Computed Tomography Imaging of Cartilage for Early Osteoarthritis Diagnosis. *ACS Nano* **2023**, *17*, 6649–6663, doi:10.1021/acsnano.2c12376.
165. Bhattarai, A.; Honkanen, J.T.J.; Myller, K.A.H.; Prakash, M.; Korhonen, M.; Saukko, A.E.A.; Virén, T.; Joukainen, A.; Patwa, A.N.; Kröger, H.; et al. Quantitative Dual Contrast CT Technique for Evaluation of Articular Cartilage Properties. *Annals of Biomedical Engineering* **2018**, *46*, 1038–1046, doi:10.1007/s10439-018-2013-y.
166. Saukko, A.E.A.; Turunen, M.J.; Honkanen, M.K.M.; Lovric, G.; Tiitu, V.; Honkanen, J.T.J.; Grinstaff, M.W.; Jurvelin, J.S.; Töyräs, J. Simultaneous Quantitation of Cationic and Non-Ionic Contrast Agents in Articular Cartilage Using Synchrotron MicroCT Imaging. *Scientific Reports* **2019**, *9*, 7118, doi:10.1038/s41598-019-43276-6.
167. Bhattarai, A.; Pouran, B.; Mäkelä, J.T.A.; Shaikh, R.; Honkanen, M.K.M.; Prakash, M.; Kröger, H.; Grinstaff, M.W.; Weinans, H.; Jurvelin, J.S.; et al. Dual Contrast in Computed Tomography Allows Earlier Characterization of Articular Cartilage over Single Contrast. *Journal of Orthopaedic Research* **2020**, *38*, 2230–2238, doi:10.1002/jor.24774.
168. Honkanen, M.K.M.; Saukko, A.E.A.; Turunen, M.J.; Xu, W.; Lovric, G.; Honkanen, J.T.J.; Grinstaff, M.W.; Lehto, V.-P.; Töyräs, J. Triple Contrast CT Method Enables Simultaneous Evaluation of Articular Cartilage Composition and Segmentation. *Annals of Biomedical Engineering* **2020**, *48*, 556–567, doi:10.1007/s10439-019-02362-6.
169. Honkanen, M.K.M.; Saukko, A.E.A.; Turunen, M.J.; Shaikh, R.; Prakash, M.; Lovric, G.; Joukainen, A.; Kröger, H.; Grinstaff, M.W.; Töyräs, J. Synchrotron MicroCT Reveals the Potential of the Dual Contrast Technique for Quantitative Assessment of Human Articular Cartilage Composition. *Journal of Orthopaedic Research* **2020**, *38*, 563–573, doi:10.1002/jor.24479.
170. Bhattarai, A.; Mäkelä, J.T.A.; Pouran, B.; Kröger, H.; Weinans, H.; Grinstaff, M.W.; Töyräs, J.; Turunen, M.J. Effects of Human Articular Cartilage Constituents on Simultaneous Diffusion of Cationic and Nonionic Contrast Agents. *Journal of Orthopaedic Research* **2021**, *39*, 771–779, doi:10.1002/jor.24824.
171. Saukko, A.E.A.; Nykänen, O.; Sarin, J.K.; Nissi, M.J.; Te Moller, N.C.R.; Weinans, H.; Mancini, I.A.D.; Visser, J.; Brommer, H.; Weeren, P.R.; et al. Dual-contrast Computed Tomography Enables Detection of Equine Posttraumatic Osteoarthritis in Vitro. *Journal Orthopaedic Research* **2022**, *40*, 703–711, doi:10.1002/jor.25066.
172. Hsu, J.C.; Nieves, L.M.; Betzer, O.; Sadan, T.; Noël, P.B.; Popovtzer, R.; Cormode, D.P. Nanoparticle Contrast Agents for X-ray Imaging Applications. *WIREs Nanomed Nanobiotechnol* **2020**, *12*, doi:10.1002/wnan.1642.

173. Pedersen, D.R.; Goetz, J.E.; Kurriger, G.L.; Martin, J.A. Comparative Digital Cartilage Histology for Human and Common Osteoarthritis Models. *Orthop Res Rev* **2013**, *2013*, 13–20, doi:10.2147/ORR.S38400.
174. Alvarez, R.E.; Macovski, A. Energy-Selective Reconstructions in X-Ray Computerised Tomography. *Phys. Med. Biol.* **1976**, *21*, 733–744, doi:10.1088/0031-9155/21/5/002.
175. Lehmann, L.A.; Alvarez, R.E.; Macovski, A.; Brody, W.R.; Pelc, N.J.; Riederer, S.J.; Hall, A.L. Generalized Image Combinations in Dual KVP Digital Radiography. *Med. Phys.* **1981**, *8*, 659–667, doi:10.1118/1.595025.
176. Thomlinson, W.; Elleaume, H.; Porra, L.; Suortti, P. K-Edge Subtraction Synchrotron X-Ray Imaging in Bio-Medical Research. *Physica Medica* **2018**, *49*, 58–76, doi:10.1016/j.ejmp.2018.04.389.
177. Perion, P.; Brombal, L.; Delogu, P.; Di Trapani, V.; Menk, R.H.; Oliva, P.; Arfelli, F. A High Sensitivity Wide Bandwidth Spectral System for Multiple K-Edge Imaging. *J. Phys. D: Appl. Phys.* **2024**, *57*, 355402, doi:10.1088/1361-6463/ad4f9b.
178. Kulpe, S.; Dierolf, M.; Günther, B.; Busse, M.; Achterhold, K.; Gleich, B.; Herzen, J.; Rummeny, E.; Pfeiffer, F.; Pfeiffer, D. K-Edge Subtraction Computed Tomography with a Compact Synchrotron X-Ray Source. *Sci Rep* **2019**, *9*, 13332, doi:10.1038/s41598-019-49899-z.
179. Honkanen, M.K.M.; Matikka, H.; Honkanen, J.T.J.; Bhattarai, A.; Grinstaff, M.W.; Joukainen, A.; Kröger, H.; Jurvelin, J.S.; Töyräs, J. Imaging of Proteoglycan and Water Contents in Human Articular Cartilage with Full-Body CT Using Dual Contrast Technique. *Journal of Orthopaedic Research* **2019**, *37*, 1059–1070, doi:10.1002/jor.24256.
180. Paakkari, P.; Inkinen, S.I.; Honkanen, M.K.M.; Prakash, M.; Shaikh, R.; Nieminen, M.T.; Grinstaff, M.W.; Mäkelä, J.T.A.; Töyräs, J.; Honkanen, J.T.J. Quantitative Dual Contrast Photon-Counting Computed Tomography for Assessment of Articular Cartilage Health. *Scientific Reports* **2021**, *11*, 5556, doi:10.1038/s41598-021-84800-x.
181. Flohr, T.; Petersilka, M.; Henning, A.; Ulzheimer, S.; Ferda, J.; Schmidt, B. Photon-Counting CT Review. *Physica Medica* **2020**, *79*, 126–136, doi:10.1016/j.ejmp.2020.10.030.
182. Rajendran, K.; Baffour, F.; Powell, G.; Glazebrook, K.; Thorne, J.; Larson, N.; Leng, S.; McCollough, C.; Fletcher, J. Improved Visualization of the Wrist at Lower Radiation Dose with Photon-Counting-Detector CT. *Skeletal Radiol* **2023**, *52*, 23–29, doi:10.1007/s00256-022-04117-2.
183. Rajendran, K.; Petersilka, M.; Henning, A.; Shanblatt, E.R.; Schmidt, B.; Flohr, T.G.; Ferrero, A.; Baffour, F.; Diehn, F.E.; Yu, L.; et al. First Clinical Photon-Counting Detector CT System: Technical Evaluation. *Radiology* **2022**, *303*, 130–138, doi:10.1148/radiol.212579.
184. Brombal, L.; Arfelli, F.; Menk, R.H.; Rigon, L.; Brun, F. PEPI Lab: A Flexible Compact Multi-Modal Setup for X-Ray Phase-Contrast and Spectral Imaging. *Sci Rep* **2023**, *13*, 4206, doi:10.1038/s41598-023-30316-5.
185. Luetkens, K.S.; Grunz, J.-P.; Kunz, A.S.; Huflage, H.; Weissenberger, M.; Hartung, V.; Patzer, T.S.; Gruschwitz, P.; Erguen, S.; Bley, T.A.; et al. Ultra-High-Resolution Photon-Counting Detector CT Arthrography of the Ankle: A Feasibility Study. *DIAGNOSTICS* **2023**, *13*, doi:10.3390/diagnostics13132201.
186. Kim, D.-Y.; Yoon, J.-M.; Park, G.Y.; Kang, H.W.; Lee, D.-O.; Lee, D.Y. Computed Tomography Arthrography versus Magnetic Resonance Imaging for Diagnosis of Osteochondral Lesions of the Talus. *Archives of Orthopaedic and Trauma Surgery* **2023**, *143*, 5631–5639, doi:10.1007/s00402-023-04871-5.
187. Paakkari, P.; Inkinen, S.I.; Jäntti, J.; Tuppurainen, J.; Fugazzola, M.C.; Joenathan, A.; Ylisiurua, S.; Nieminen, M.T.; Grinstaff, M.W.; Kröger, H.; et al. Tantalum And Iodine Based Dual-Contrast Photon-Counting Computed Tomography Method For Assessment Of Articular Cartilage Composition. *Osteoarthritis and Cartilage* **2023**, *31*, S273, doi:10.1016/j.joca.2023.01.278.

188. Tuppurainen, J.; Paakkari, P.; Jäntti, J.; Nissinen, M.T.; Fugazzola, M.C.; Van Weeren, R.; Ylisiurua, S.; Nieminen, M.T.; Kröger, H.; Snyder, B.D.; et al. Revealing Detailed Cartilage Function Through Nanoparticle Diffusion Imaging: A Computed Tomography & Finite Element Study. *Ann Biomed Eng* **2024**, *52*, 2584–2595, doi:10.1007/s10439-024-03552-7.
189. Rajendran, K.; Löbker, C.; Schon, B.S.; Bateman, C.J.; Younis, R.A.; de Ruiter, N.J.A.; Chernoglazov, A.I.; Ramyar, M.; Hooper, G.J.; Butler, A.P.H.; et al. Quantitative Imaging of Excised Osteoarthritic Cartilage Using Spectral CT. *European Radiology* **2017**, *27*, 384–392, doi:10.1007/s00330-016-4374-7.
190. Baer, K.; Kieser, S.; Schon, B.; Rajendran, K.; Ten Harkel, T.; Ramyar, M.; Löbker, C.; Bateman, C.; Butler, A.; Raja, A.; et al. Spectral CT Imaging of Human Osteoarthritic Cartilage via Quantitative Assessment of Glycosaminoglycan Content Using Multiple Contrast Agents. *APL Bioengineering* **2021**, *5*, 026101, doi:10.1063/5.0035312.
191. Fantoni, S.; Brun, F.; Cardarelli, P.; Baruffaldi, F.; Cristofori, V.; Taibi, A.; Trapella, C.; Brombal, L. Quantitative Spectral Micro-CT of a CA4+ Loaded Osteochondral Sample with a Tabletop System. *Eur. Phys. J. Plus* **2024**, *139*, 735, doi:10.1140/epjp/s13360-024-05428-0.
192. Zhou, S.-A.; Brahme, A. Development of Phase-Contrast X-Ray Imaging Techniques and Potential Medical Applications. *Physica Medica* **2008**, *24*, 129–148, doi:10.1016/j.ejmp.2008.05.006.
193. Momose, A.; Takeda, T.; Itai, Y. Blood Vessels: Depiction at Phase-Contrast X-Ray Imaging without Contrast Agents in the Mouse and Rat—Feasibility Study. *Radiology* **2000**, *217*, 593–596, doi:10.1148/radiology.217.2.r00oc14593.
194. Peterzol, A.; Olivo, A.; Rigon, L.; Pani, S.; Dreossi, D. The Effects of the Imaging System on the Validity Limits of the Ray-optical Approach to Phase Contrast Imaging. *Medical Physics* **2005**, *32*, 3617–3627, doi:10.1118/1.2126207.
195. Cloetens, P.; Barrett, R.; Baruchel, J.; Guigay, J.-P.; Schlenker, M. Phase Objects in Synchrotron Radiation Hard X-Ray Imaging. *J. Phys. D: Appl. Phys.* **1996**, *29*, 133–146, doi:10.1088/0022-3727/29/1/023.
196. Momose, A.; Takeda, T.; Itai, Y.; Hirano, K. Phase–Contrast X–Ray Computed Tomography for Observing Biological Soft Tissues. *Nat Med* **1996**, *2*, 473–475, doi:10.1038/nm0496-473.
197. Snigirev, A.; Snigireva, I.; Kohn, V.; Kuznetsov, S.; Schelokov, I. On the Possibilities of X-ray Phase Contrast Microimaging by Coherent High-energy Synchrotron Radiation. *Review of Scientific Instruments* **1995**, *66*, 5486–5492, doi:10.1063/1.1146073.
198. Pfeiffer, F.; Weitkamp, T.; Bunk, O.; David, C. Phase Retrieval and Differential Phase-Contrast Imaging with Low-Brilliance X-Ray Sources. *Nature Phys* **2006**, *2*, 258–261, doi:10.1038/nphys265.
199. Olivo, A.; Speller, R. A Coded-Aperture Technique Allowing x-Ray Phase Contrast Imaging with Conventional Sources. *Appl. Phys. Lett.* **2007**, *91*, 074106, doi:10.1063/1.2772193.
200. Horng, A.; Stroebel, J.; Geith, T.; Milz, S.; Pacureanu, A.; Yang, Y.; Cloetens, P.; Lovric, G.; Mittone, A.; Bravin, A.; et al. Multiscale X-Ray Phase Contrast Imaging of Human Cartilage for Investigating Osteoarthritis Formation. *Journal of Biomedical Science* **2021**, *28*, 42, doi:10.1186/s12929-021-00739-1.
201. Wilkins, S.W.; Gureyev, T.E.; Gao, D.; Pogany, A.; Stevenson, A.W. Phase-Contrast Imaging Using Polychromatic Hard X-Rays. *Nature* **1996**, *384*, 335–338, doi:10.1038/384335a0.
202. Ikeura-Sekiguchi, H.; Kuroda, R.; Yasumoto, M.; Toyokawa, H.; Koike, M.; Yamada, K.; Sakai, F.; Mori, K.; Maruyama, K.; Oka, H.; et al. In-Line Phase-Contrast Imaging of a Biological Specimen Using a Compact Laser-Compton Scattering-Based x-Ray Source. *Appl. Phys. Lett.* **2008**, *92*, 131107, doi:10.1063/1.2903148.
203. Brombal, L.; Donato, S.; Dreossi, D.; Arfelli, F.; Bonazza, D.; Contillo, A.; Delogu, P.; Di Trapani, V.; Golosio, B.; Mettivier, G.; et al. Phase-Contrast Breast CT: The Effect of Propagation Distance. *Phys. Med. Biol.* **2018**, *63*, 24NT03, doi:10.1088/1361-6560/aaf2e1.

204. Gureyev, T.E.; Nesterets, Y.I.; Kozlov, A.; Paganin, D.M.; Quiney, H.M. On the "Unreasonable" Effectiveness of Transport of Intensity Imaging and Optical Deconvolution. *J. Opt. Soc. Am. A* **2017**, *34*, 2251, doi:10.1364/JOSAA.34.002251.
205. Dejea, H.; Pierantoni, M.; Orozco, G.A.; B. Wrammerfors, E.T.; Gstöhl, S.J.; Schlepütz, C.M.; Isaksson, H. In Situ Loading and Time-Resolved Synchrotron-Based Phase Contrast Tomography for the Mechanical Investigation of Connective Knee Tissues: A Proof-of-Concept Study. *Advanced Science* **2024**, *11*, 2308811, doi:10.1002/advs.202308811.
206. Bissardon, C.; Zhang, Y.; Labriet, H.R.; Berujon, S.; Charlet, L.; Khan, I.M.; Brun, E.; Bohic, S. In Vitro Preparation of Actively Maturing Bovine Articular Cartilage Explants for X-Ray Phase Contrast Imaging. *Journal of Visualized Experiments* **2022**, *2022*, doi:10.3791/61607.
207. Broche, L.; Favier, B.; Rougé-Labriet, H.; Drevet, S.; Lardy, B.; Brun, E.; Lemasson, B. Calcified Cartilage Revealed in Whole Joint by X-Ray Phase Contrast Imaging. *Osteoarthritis and Cartilage Open* **2021**, *3*, 100168, doi:10.1016/j.ocarto.2021.100168.
208. Tozzi, G.; Fernández, M.P.; Davis, S.; Karali, A.; Kao, A.P.; Blunn, G. Full-Field Strain Uncertainties and Residuals at the Cartilage-Bone Interface in Unstained Tissues Using Propagation-Based Phase-Contrast XCT and Digital Volume Correlation. *Materials* **2020**, *13*, doi:10.3390/ma13112579.
209. Rack, A.; Stroebel, J.; Rack, T.; Dabin, Y.; Knabe, C.; Stiller, M.; Coan, P.; Bleuet, P. TomoPress—In Situ Synchrotron-Based Microtomography under Axial Load. *Instruments* **2020**, *4*, 11, doi:10.3390/instruments4020011.
210. Madi, K.; Staines, K.A.; Bay, B.K.; Javaheri, B.; Geng, H.; Bodey, A.J.; Cartmell, S.; Pitsillides, A.A.; Lee, P.D. In Situ Characterization of Nanoscale Strains in Loaded Whole Joints via Synchrotron X-Ray Tomography. *Nature Biomedical Engineering* **2020**, *4*, 343–354, doi:10.1038/s41551-019-0477-1.
211. Geith, T.; Brun, E.; Mittone, A.; Gasilov, S.; Weber, L.; Adam-Neumair, S.; Bravin, A.; Reiser, M.; Coan, P.; Horng, A. Quantitative Assessment of Degenerative Cartilage and Subchondral Bony Lesions in a Preserved Cadaveric Knee: Propagation-Based Phase-Contrast CT versus Conventional MRI and CT. *American Journal of Roentgenology* **2018**, *210*, 1317–1322, doi:10.2214/AJR.17.18286.
212. Yoon, J.S.; Won, S.J.; Kim, S.J.; Hong, S.J.; Kim, G.S.; Kim, J.M. Phase-Contrast Radiography Enables Detection of Early Changes in Articular Cartilage in a Mouse Model of Osteoarthritis. *American Journal of Physical Medicine and Rehabilitation* **2015**, *94*, 644–648, doi:10.1097/PHM.0000000000000232.
213. Sun, W.; Zhang, Y.; Gao, F.; Li, Z.; Li, G.; Pan, L. Phase-Contrast Imaging with Synchrotron Hard X-Ray of Micro Lesions of the Cartilage of the Femoral Head in Rabbits. *International Journal of Clinical and Experimental Medicine* **2015**, *8*, 20086–20091.
214. Li, J.; Yuan, H.; Wu, M.; Dong, L.; Zhang, L.; Shi, H.; Luo, S. Quantitative Assessment of Murine Articular Cartilage and Bone Using X-Ray Phase-Contrast Imaging. *PLoS ONE* **2014**, *9*, doi:10.1371/journal.pone.0111939.
215. Horng, A.; Brun, E.; Mittone, A.; Gasilov, S.; Weber, L.; Geith, T.; Adam-Neumair, S.; Auweter, S.D.; Bravin, A.; Reiser, M.F.; et al. Cartilage and Soft Tissue Imaging Using X-Rays: Propagation-Based Phase-Contrast Computed Tomography of the Human Knee in Comparison with Clinical Imaging Techniques and Histology. *Investigative Radiology* **2014**, *49*, 627–634, doi:10.1097/RLI.0000000000000063.
216. Zehbe, R.; Riesemeier, H.; Kirkpatrick, C.J.; Brochhausen, C. Imaging of Articular Cartilage - Data Matching Using X-Ray Tomography, SEM, FIB Slicing and Conventional Histology. *Micron* **2012**, *43*, 1060–1067, doi:10.1016/j.micron.2012.05.001.
217. Lee, Y.S.; Heo, E.-A.; Jun, H.Y.; Kang, S.H.; Kim, H.S.; Lee, M.S.; Byun, S.-J.; Lee, S.H.; Park, S.H.; Yoon, K.-H. Articular Cartilage Imaging by the Use of Phase-Contrast Tomography in a Collagen-Induced Arthritis Mouse Model. *Academic Radiology* **2010**, *17*, 244–250, doi:10.1016/j.acra.2009.09.015.

218. Ismail, E.C.; Kaabar, W.; Garrity, D.; Gundogdu, O.; Bunk, O.; Pfeiffer, F.; Farquharson, M.J.; Bradley, D.A. X-Ray Phase Contrast Imaging of the Bone-Cartilage Interface. *Applied Radiation and Isotopes* **2010**, *68*, 767–771, doi:10.1016/j.apradiso.2009.09.042.
219. Choi, C.-H.; Kim, H.-T.; Choe, J.-Y.; Kim, S.-K.; Choi, G.-W.; Jheon, S.; Kim, J.-K. In Vivo High-Resolution Synchrotron Radiation Imaging of Collagen-Induced Arthritis in a Rodent Model. *Journal of Synchrotron Radiation* **2010**, *17*, 393–399, doi:10.1107/S0909049510009581.
220. Shimao, D.; Mori, K.; Sigiyama, H.; Hyodo, K. Refraction-Contrast Articular Cartilage Image: Comparison of Depiction Abilities between in-Line Holographic Method and a Laue Type Analyzer Method. *Japanese Journal of Applied Physics, Part 1: Regular Papers and Short Notes and Review Papers* **2005**, *44*, 450–451, doi:10.1143/JJAP.44.450.
221. Ruan, M.Z.C.; Dawson, B.; Jiang, M.-M.; Gannon, F.; Heggeness, M.; Lee, B.H.L. Quantitative Imaging of Murine Osteoarthritic Cartilage by Phase-Contrast Micro-Computed Tomography. *Arthritis and Rheumatism* **2013**, *65*, 388–396, doi:10.1002/art.37766.
222. Clark, J.N.; Heyraud, A.; Tavana, S.; Al-Jabri, T.; Tallia, F.; Clark, B.; Blunn, G.W.; Cobb, J.P.; Hansen, U.; Jones, J.R.; et al. Exploratory Full-Field Mechanical Analysis across the Osteochondral Tissue—Biomaterial Interface in an Ovine Model. *Materials* **2020**, *13*, doi:10.3390/ma13183911.
223. Jayaram, P.; Liu, C.; Dawson, B.; Ketkar, S.; Patel, S.J.; Lee, B.H.; Grol, M.W. Leukocyte-Dependent Effects of Platelet-Rich Plasma on Cartilage Loss and Thermal Hyperalgesia in a Mouse Model of Post-Traumatic Osteoarthritis. *Osteoarthritis and Cartilage* **2020**, *28*, 1385–1393, doi:10.1016/j.joca.2020.06.004.
224. Stone, A.; Grol, M.W.; Ruan, M.Z.C.; Dawson, B.; Chen, Y.; Jiang, M.-M.; Song, I.; Jayaram, P.; Cela, R.; Gannon, F.; et al. Combinatorial *Prg4* and *Il-1ra* Gene Therapy Protects Against Hyperalgesia and Cartilage Degeneration in Post-Traumatic Osteoarthritis. *Human Gene Therapy* **2019**, *30*, 225–235, doi:10.1089/hum.2018.106.
225. Nixon, A.J.; Grol, M.W.; Lang, H.M.; Ruan, M.Z.C.; Stone, A.; Begum, L.; Chen, Y.; Dawson, B.; Gannon, F.; Plutizki, S.; et al. Disease-Modifying Osteoarthritis Treatment With Interleukin-1 Receptor Antagonist Gene Therapy in Small and Large Animal Models. *Arthritis & Rheumatology* **2018**, *70*, 1757–1768, doi:10.1002/art.40668.
226. Ruan, M.Z.C.; Erez, A.; Guse, K.; Dawson, B.; Bertin, T.; Chen, Y.; Jiang, M.-M.; Yustein, J.; Gannon, F.; Lee, B.H.L. Proteoglycan 4 Expression Protects Against the Development of Osteoarthritis. *Sci. Transl. Med.* **2013**, *5*, doi:10.1126/scitranslmed.3005409.
227. Ruan, M.Z.C.; Patel, R.M.; Dawson, B.C.; Jiang, M.-M.; Lee, B.H.L. Pain, Motor and Gait Assessment of Murine Osteoarthritis in a Cruciate Ligament Transection Model. *Osteoarthritis and Cartilage* **2013**, *21*, 1355–1364, doi:10.1016/j.joca.2013.06.016.
228. Cloetens, P.; Ludwig, W.; Baruchel, J.; Van Dyck, D.; Van Landuyt, J.; Guigay, J.P.; Schlenker, M. Holotomography: Quantitative Phase Tomography with Micrometer Resolution Using Hard Synchrotron Radiation x Rays. *Applied Physics Letters* **1999**, *75*, 2912–2914, doi:10.1063/1.125225.
229. Paganin, D.; Mayo, S.C.; Gureyev, T.E.; Miller, P.R.; Wilkins, S.W. Simultaneous Phase and Amplitude Extraction from a Single Defocused Image of a Homogeneous Object. *J Microsc* **2002**, *206*, 33–40, doi:10.1046/j.1365-2818.2002.01010.x.
230. Nagarajan, M.B.; Coan, P.; Huber, M.B.; Diemoz, P.C.; Wismüller, A. Integrating Dimension Reduction and Out-of-Sample Extension in Automated Classification of Ex Vivo Human Patellar Cartilage on Phase Contrast X-Ray Computed Tomography. *PLoS ONE* **2015**, *10*, doi:10.1371/journal.pone.0117157.
231. Ingal, V.N.; Beliaevskaya, E.A. X-Ray Plane-Wave Topography Observation of the Phase Contrast from a Non-Crystalline Object. *J. Phys. D: Appl. Phys.* **1995**, *28*, 2314–2317, doi:10.1088/0022-3727/28/11/012.

232. Davis, T.J.; Gao, D.; Gureyev, T.E.; Stevenson, A.W.; Wilkins, S.W. Phase-Contrast Imaging of Weakly Absorbing Materials Using Hard X-Rays. *Nature* **1995**, *373*, 595–598, doi:10.1038/373595a0.
233. Chapman, D.; Thomlinson, W.; Johnston, R.E.; Washburn, D.; Pisano, E.; Gmür, N.; Zhong, Z.; Menk, R.; Arfelli, F.; Sayers, D. Diffraction Enhanced X-Ray Imaging. *Phys. Med. Biol.* **1997**, *42*, 2015–2025, doi:10.1088/0031-9155/42/11/001.
234. Talbot, H.F. LXXVI. *Facts Relating to Optical Science. No. IV*. *The London, Edinburgh, and Dublin Philosophical Magazine and Journal of Science* **1836**, *9*, 401–407, doi:10.1080/14786443608649032.
235. Crittell, S.; Cheung, K.C.; Hall, C.; Ibison, M.; Nolan, P.; Page, R.; Scraggs, D.; Wilkinson, S. Diffraction Enhanced Imaging of Normal and Arthritic Mice Feet. *NUCLEAR INSTRUMENTS & METHODS IN PHYSICS RESEARCH SECTION A-ACCELERATORS SPECTROMETERS DETECTORS AND ASSOCIATED EQUIPMENT* **2007**, *573*, 126–128, doi:10.1016/j.nima.2006.11.044.
236. Li, J.; Wilson, N.; Zelazny, A.; Meyer, J.; Zhong, Z.; Muehleman, C. Assessment of Diffraction-Enhanced Synchrotron Imaging for Cartilage Degeneration of the Human Knee Joint. *Clinical Anatomy* **2013**, *26*, 621–629, doi:10.1002/ca.22106.
237. Muehleman, C.; Li, J.; Zhong, Z. Preliminary Study on Diffraction Enhanced Radiographic Imaging for a Canine Model of Cartilage Damage. *Osteoarthritis and Cartilage* **2006**, *14*, 882–888, doi:10.1016/j.joca.2006.02.011.
238. Miki, H.; Hirano, K.; Ninomiya, T.; Arai, Y.; Honda, K. Visualization of Temporomandibular Joint Articular Cartilage Using Synchrotron-Radiation X-Ray Phase-Contrast Imaging. *Nuclear Instruments and Methods in Physics Research Section A: Accelerators, Spectrometers, Detectors and Associated Equipment* **2023**, *1049*, 168005, doi:10.1016/j.nima.2022.168005.
239. Wagner, A.; Aurich, M.; Stoessel, M.; Sieber, N.; Wetzel, W.; Mollenhauer, J.; Schmuck, K.; Muehleman, C.; Lohmann, M.; Reime, B.; et al. Chance and Limit of Imaging of Articular Cartilage in Vitro in Healthy and Arthritic Joints - DEI (Diffraction Enhanced Imaging) in Comparison with MRI, CT and Ultrasound. *MEDICAL IMAGING 2005: PHYSIOLOGY, FUNCTION, AND STRUCTURE FROM MEDICAL IMAGES, PTS 1 AND 2* **2005**, *5746*, 542–549, doi:10.1117/12.589614.
240. Li, J.; Williams, J.M.; Zhong, Z.; Kuettner, K.E.; Aurich, M.; Mollenhauer, J.; Muehleman, C. Reliability of Diffraction Enhanced Imaging for Assessment of Cartilage Lesions, Ex Vivo. *Osteoarthritis and Cartilage* **2005**, *13*, 187–197, doi:10.1016/j.joca.2004.11.003.
241. Mollenhauer, J.; Aurich, M.E.; Zhong, Z.; Muehleman, C.; Cole, A.A.; Hasnah, M.; Oltulu, O.; Kuettner, K.E.; Margulis, A.; Chapman, L.D. Diffraction-Enhanced X-Ray Imaging of Articular Cartilage. *Osteoarthritis and Cartilage* **2002**, *10*, 163–171, doi:10.1053/joca.2001.0496.
242. Li, J.; Zhong, Z.; Lidtke, R.; Kuettner, K.E.; Peterfy, C.; Aliyeva, E.; Muehleman, C. Radiography of Soft Tissue of the Foot and Ankle with Diffraction Enhanced Imaging. *Journal of Anatomy* **2003**, *202*, 463–470, doi:10.1046/j.1469-7580.2003.00175.x.
243. Muehleman, C.; Chapman, L.D.; Kuettner, K.E.; Rieff, J.; Mollenhauer, J.A.; Massuda, K.; Zhong, Z. Radiography of Rabbit Articular Cartilage with Diffraction-Enhanced Imaging. *Anatomical Record - Part A Discoveries in Molecular, Cellular, and Evolutionary Biology* **2003**, *272*, 392–397, doi:10.1002/ar.a.10043.
244. Majumdar, S.; Issever, A.S.; Burghardt, A.; Lotz, J.; Arfelli, F.; Rigon, L.; Heitner, G.; Menk, R.-H. Diffraction Enhanced Imaging of Articular Cartilage and Comparison with Micro-Computed Tomography of the Underlying Bone Structure. *European Radiology* **2004**, *14*, 1440–1448, doi:10.1007/s00330-004-2355-8.
245. Muehleman, C.; Li, J.; Wernick, M.; Brankov, J.; Kuettner, K.; Zhong, Z. Yes, You Can See Cartilage with x-Rays; Diffraction Enhanced x-Ray Imaging for Soft and Hard Tissues. *Journal of Musculoskeletal Neuronal Interactions* **2004**, *4*, 369–370.

246. Shimao, D.; Mori, K.; Hyodo, K.; Sugiyama, H.; Ando, M. Application of X-Ray Refraction-Contrast to Medical Joint Imaging. *SYNCHROTRON RADIATION INSTRUMENTATION* **2004**, *705*, 1324–1327, doi:10.1063/1.1758045.
247. Wagner, A.; Aurich, M.; Sieber, N.; Stoessel, M.; Wetzel, W.; Schmuck, K.; Lohmann, M.; Reime, B.; Metge, J.; Coan, P.; et al. Options and Limitations of Joint Cartilage Imaging: DEI in Comparison to MRI and Sonography. *NUCLEAR INSTRUMENTS & METHODS IN PHYSICS RESEARCH SECTION A-ACCELERATORS SPECTROMETERS DETECTORS AND ASSOCIATED EQUIPMENT* **2005**, *548*, 47–53, doi:10.1016/j.nima.2005.03.064.
248. Rhoades, G.W.; Belev, G.S.; Chapman, L.D.; Wiebe, S.P.; Cooper, D.M.; Wong, A.T.F.; Rosenberg, A.M. Diffraction-Enhanced Computed Tomographic Imaging of Growing Piglet Joints by Using a Synchrotron Light Source. *Comparative Medicine* **2015**, *65*, 342–347.
249. Gasilov, S.; Mittone, A.; Horng, A.; Geith, T.; Bravin, A.; Baumbach, T.; Coan, P. Hard X-Ray Index of Refraction Tomography of a Whole Rabbit Knee Joint: A Feasibility Study. *Physica Medica* **2016**, *32*, 1785–1789, doi:10.1016/j.ejmp.2016.10.001.
250. Coan, P.; Wagner, A.; Bravin, A.; Diemoz, P.C.; Keyrilainen, J.; Mollenhauer, J. *In Vivo* x-Ray Phase Contrast Analyzer-Based Imaging for Longitudinal Osteoarthritis Studies in Guinea Pigs. *PHYSICS IN MEDICINE AND BIOLOGY* **2010**, *55*, 7649–7662, doi:10.1088/0031-9155/55/24/017.
251. Li, J.; Zhong, Z.; Connor, D.; Mollenhauer, J.; Muehleman, C. Phase-Sensitive X-Ray Imaging of Synovial Joints. *Osteoarthritis and Cartilage* **2009**, *17*, 1193–1196, doi:10.1016/j.joca.2009.03.005.
252. Muehleman, C.; Majumdar, S.; Sema Issever, A.; Arfelli, F.; Menk, R.-H.; Rigon, L.; Heitner, G.; Reime, B.; Metge, J.; Wagner, A.; et al. X-Ray Detection of Structural Orientation in Human Articular Cartilage. *Osteoarthritis and Cartilage* **2004**, *12*, 97–105, doi:10.1016/j.joca.2003.10.001.
253. Issever, A.S.; Diederichs, G.; Majumdar, S.; Rogalla, P.; Hamm, B.K.; Lange, A.; Harwardt, M.; Hentschel, M.P.; Mueller, B.R. Analyser-Based Tomography Images of Cartilage. *Journal of Synchrotron Radiation* **2008**, *15*, 525–527, doi:10.1107/S0909049508014829.
254. Coan, P.; Bamberg, F.; Diemoz, P.C.; Bravin, A.; Timpert, K.; Mützel, E.; Raya, J.G.; Adam-Neumair, S.; Reiser, M.F.; Glaser, C. Characterization of Osteoarthritic and Normal Human Patella Cartilage by Computed Tomography X-Ray Phase-Contrast Imaging: A Feasibility Study. *Investigative Radiology* **2010**, *45*, 437–444, doi:10.1097/RLI.0b013e3181e193bd.
255. Nagarajan, M.B.; Coan, P.; Huber, M.B.; Diemoz, P.C.; Wismüller, A. Volumetric Quantitative Characterization of Human Patellar Cartilage with Topological and Geometrical Features on Phase-Contrast X-Ray Computed Tomography. *Medical and Biological Engineering and Computing* **2015**, *53*, 1211–1220, doi:10.1007/s11517-015-1340-5.
256. Abidin, A.Z.; Deng, B.; DSouza, A.M.; Nagarajan, M.B.; Coan, P.; Wismüller, A. Deep Transfer Learning for Characterizing Chondrocyte Patterns in Phase Contrast X-Ray Computed Tomography Images of the Human Patellar Cartilage. *Computers in Biology and Medicine* **2018**, *95*, 24–33, doi:10.1016/j.compbiomed.2018.01.008.
257. Diemoz, P.C.; Bravin, A.; Glaser, C.; Coan, P. Comparison of Analyzer-Based Imaging Computed Tomography Extraction Algorithms and Application to Bone-Cartilage Imaging. *Physics in Medicine and Biology* **2010**, *55*, 7663–7679, doi:10.1088/0031-9155/55/24/018.
258. Diemoz, P.C.; Coan, P.; Glaser, C.; Bravin, A. Absorption, Refraction and Scattering in Analyzer-Based Imaging: Comparison of Different Algorithms. *OPTICS EXPRESS* **2010**, *18*, 3494–3509, doi:10.1364/OE.18.003494.
259. Muehleman, C.; Li, J.; Zhong, Z.; Brankov, J.G.; Wernick, M.N. Multiple-Image Radiography for Human Soft Tissue. *Journal of Anatomy* **2006**, *208*, 115–124, doi:10.1111/j.1469-7580.2006.00502.x.

260. Majidi, K.; Wernick, M.N.; Li, J.; Muehleman, C.; Brankov, J.G. Limited-Angle Tomography for Analyzer-Based Phase-Contrast x-Ray Imaging. *Physics in Medicine and Biology* **2014**, *59*, 3483–3500, doi:10.1088/0031-9155/59/13/3483.
261. Fogarty, D.P.; Reinhart, B.; Tzvetkov, T.; Nesch, I.; Williams, C. In-Laboratory Diffraction-Enhanced X-Ray Imaging of an Equine Hoof. *Journal of Equine Veterinary Science* **2011**, *31*, 365–369, doi:10.1016/j.jevs.2011.03.015.
262. Muehleman, C.; Fogarty, D.; Reinhart, B.; Tzvetkov, T.; Li, J.; Nesch, I. In-Laboratory Diffraction-Enhanced X-Ray Imaging for Articular Cartilage. *Clinical Anatomy* **2010**, *23*, 530–538, doi:10.1002/ca.20993.
263. Muehleman, C.; Li, J.; Connor, D.; Parham, C.; Pisano, E.; Zhong, Z. Diffraction-Enhanced Imaging of Musculoskeletal Tissues Using a Conventional X-Ray Tube. *Academic Radiology* **2009**, *16*, 918–923, doi:10.1016/j.acra.2009.04.006.
264. Schulz, G.; Gotz, C.; Muller-Gerbl, M.; Zanette, I.; Zdora, M.-C.; Khimchenko, A.; Deyhle, H.; Thalmann, P.; Mueller, B. Multimodal Imaging of the Human Knee down to the Cellular Level. *X-RAY MICROSCOPY CONFERENCE 2016 (XRM 2016)* **2017**, *849*, doi:10.1088/1742-6596/849/1/012026.
265. David, C.; Nöhammer, B.; Solak, H.H.; Ziegler, E. Differential X-Ray Phase Contrast Imaging Using a Shearing Interferometer. *Applied Physics Letters* **2002**, *81*, 3287–3289, doi:10.1063/1.1516611.
266. Momose, A.; Kawamoto, S.; Koyama, I.; Hamaishi, Y.; Takai, K.; Suzuki, Y. Demonstration of X-Ray Talbot Interferometry. *Jpn. J. Appl. Phys.* **2003**, *42*, L866–L868, doi:10.1143/JJAP.42.L866.
267. Brombal, L.; Rigon, L. Hybrid Imaging Detectors in X-Ray Phase-Contrast Applications. In *Advanced X-Ray Radiation Detection:*; Iniewski, K., Ed.; Springer International Publishing: Cham, 2023; pp. 51–74 ISBN 978-3-030-92988-6.
268. Pfeiffer, F.; Bech, M.; Bunk, O.; Kraft, P.; Eikenberry, E.F.; Brönnimann, Ch.; Grünzweig, C.; David, C. Hard-X-Ray Dark-Field Imaging Using a Grating Interferometer. *Nature Mater* **2008**, *7*, 134–137, doi:10.1038/nmat2096.
269. Kawano, S.; (Osawa) Yagi, T.; Hoshino, M.; Matsumoto, T. In-Situ Deformation Imaging of Articular Cartilage Using Grating-Based Phase-Contrast X-Ray CT at a Synchrotron Light Source. *Journal of Biorheology* **2022**, *36*, 51–57, doi:10.17106/jbr.36.51.
270. Yoshioka, H.; Kadono, Y.; Kim, Y.T.; Oda, H.; Maruyama, T.; Akiyama, Y.; Mimura, T.; Tanaka, J.; Niitsu, M.; Hoshino, Y.; et al. Imaging Evaluation of the Cartilage in Rheumatoid Arthritis Patients with an X-Ray Phase Imaging Apparatus Based on Talbot-Lau Interferometry. *Scientific Reports* **2020**, *10*, doi:10.1038/s41598-020-63155-9.
271. Herzen, J.; Karampinos, D.C.; Foehr, P.; Birnbacher, L.; Viermetz, M.; Burgkart, R.; Baum, T.; Lohoefer, F.; Wildgruber, M.; Schilling, F.; et al. 3D Grating-Based X-Ray Phase-Contrast Computed Tomography for High-Resolution Quantitative Assessment of Cartilage: An Experimental Feasibility Study with 3T MRI, 7T MRI and Biomechanical Correlation. *PLoS ONE* **2019**, *14*, doi:10.1371/journal.pone.0212106.
272. Khimchenko, A.; Schulz, G.; Thalmann, P.; Müller, B. Implementation of a Double-Grating Interferometer for Phase-Contrast Computed Tomography in a Conventional System Nanotom® m. *APL Bioengineering* **2018**, *2*, doi:10.1063/1.5022184.
273. Schulz, G.; Goetz, C.; Deyhle, H.; Mueller-Gerbl, M.; Zanette, I.; Zdora, M.-C.; Khimchenko, A.; Thalmann, P.; Rack, A.; Mueller, B. Hierarchical Imaging of the Human Knee. *DEVELOPMENTS IN X-RAY TOMOGRAPHY X* **2016**, *9967*, doi:10.1117/12.2238089.
274. Nagashima, M.; Tanaka, J.; Kiyohara, J.; Makifuchi, C.; Kido, K.; Momose, A. Application of X-Ray Grating Interferometry for the Imaging of Joint Structures. *Anatomical Science International* **2014**, *89*, 95–100, doi:10.1007/s12565-013-0204-z.
275. Momose, A.; Yashiro, W.; Kido, K.; Kiyohara, J.; Makifuchi, C.; Ito, T.; Nagatsuka, S.; Honda, C.; Noda, D.; Hattori, T.; et al. X-Ray Phase Imaging: From Synchrotron to Hospital.

Philosophical Transactions of the Royal Society A: Mathematical, Physical and Engineering Sciences **2014**, *372*, doi:10.1098/rsta.2013.0023.
276. Tanaka, J.; Nagashima, M.; Kido, K.; Hoshino, Y.; Kiyohara, J.; Makifuchi, C.; Nishino, S.; Nagatsuka, S.; Momose, A. Cadaveric and in Vivo Human Joint Imaging Based on Differential Phase Contrast by X-Ray Talbot-Lau Interferometry. *Zeitschrift fur Medizinische Physik* **2013**, *23*, 222–227, doi:10.1016/j.zemedi.2012.11.004.
277. Tada, T.; Murakoshi, D.; Ishii, H.; Hashimoto, A.; Kaneko, Y.; Ito, W.; Agano, T. Fabrication of High Aspect Grating Using Bonded Substrate for X-Ray Refraction Imaging by Talbot-Lau Interferometer. *INTERNATIONAL WORKSHOP ON X-RAY AND NEUTRON PHASE IMAGING WITH GRATINGS* **2012**, *1466*, 181–186, doi:10.1063/1.4742289.
278. Murakoshi, D.; Tada, T.; Ishii, H.; Hashimoto, A.; Kaneko, Y.; Ito, W.; Agano, T. Feasibility Study of the Sub-Pixel Scanning Method for Single-Exposure X-Ray Refraction Imaging by Talbot-Lau Interferometer Using an a-Se Direct Conversion Type FPD. *MEDICAL IMAGING 2012: PHYSICS OF MEDICAL IMAGING* **2012**, *8313*, doi:10.1117/12.910886.
279. Kiyohara, J.; Makifuchi, C.; Kido, K.; Nagatsuka, S.; Tanaka, J.; Nagashima, M.; Endo, T.; Ichihara, S.; Yashiro, W.; Momose, A. Development of the Talbot-Lau Interferometry System Available for Clinical Use. *INTERNATIONAL WORKSHOP ON X-RAY AND NEUTRON PHASE IMAGING WITH GRATINGS* **2012**, *1466*, 97–102, doi:10.1063/1.4742275.
280. Itoh, H.; Nagai, K.; Sato, G.; Yamaguchi, K.; Nakamura, T.; Kondoh, T.; Ouchi, C.; Teshima, T.; Setomoto, Y.; Den, T. Two-Dimensional Grating-Based X-Ray Phase-Contrast Imaging Using Fourier Transform Phase Retrieval. *Optics Express* **2011**, *19*, 3339–3346, doi:10.1364/OE.19.003339.
281. Diemoz, P.C.; Coan, P.; Zanette, I.; Bravin, A.; Lang, S.; Glaser, C.; Weitkamp, T. A Simplified Approach for Computed Tomography with an X-Ray Grating Interferometer. *Optics Express* **2011**, *19*, 1691–1698, doi:10.1364/OE.19.001691.
282. Stutman, D.; TJ, B.; JA, C.; CO, B. Talbot Phase-Contrast x-Ray Imaging for the Small Joints of the Hand. *Physics in medicine and biology* **2011**, *56*, 5697–5720, doi:10.1088/0031-9155/56/17/015.
283. Makifuchi, C.; Kido, K.; Kiyohara, J.; Ito, T.; Nagatsuka, S.; Momose, A. Development of X-Ray Talbot-Lau Interferometer with a Practical X-Ray Tube for Medical Imaging. *INTERNATIONAL CONFERENCE ON ADVANCED PHASE MEASUREMENT METHODS IN OPTICS AN IMAGING* **2010**, *1236*, 203-+, doi:10.1063/1.3426112.
284. Kido, K.; Makifuchi, C.; Kiyohara, J.; Itou, T.; Honda, C.; Momose, A. Bone Cartilage Imaging with X-Ray Interferometry Using a Practical X-Ray Tube. *MEDICAL IMAGING 2010: PHYSICS OF MEDICAL IMAGING* **2010**, *7622*, doi:10.1117/12.843655.
285. Momose, A.; Yashiro, W.; Kuwabara, H.; Kawabata, K. Grating-Based X-Ray Phase Imaging Using Multiline X-Ray Source. *Japanese Journal of Applied Physics* **2009**, *48*, doi:10.1143/JJAP.48.076512.
286. Marenzana, M.; Hagen, C.K.; Borges, P.D.N.; Endrizzi, M.; Szafraniec, M.B.; Vincent, T.L.; Rigon, L.; Arfelli, F.; Menk, R.-H.; Olivo, A. Synchrotron- and Laboratory-Based X-Ray Phase-Contrast Imaging for Imaging Mouse Articular Cartilage in the Absence of Radiopaque Contrast Agents. *Philosophical Transactions of the Royal Society A: Mathematical, Physical and Engineering Sciences* **2014**, *372*, 20130127, doi:10.1098/rsta.2013.0127.
287. Endrizzi, M.; Diemoz, P.C.; Millard, T.P.; Louise Jones, J.; Speller, R.D.; Robinson, I.K.; Olivo, A. Hard X-Ray Dark-Field Imaging with Incoherent Sample Illumination. *Appl. Phys. Lett.* **2014**, *104*, 024106, doi:10.1063/1.4861855.
288. Massimi, L.; Kallon, G.K.; Buchanan, I.; Endrizzi, M.; Dobrosz, P.; Brooks, R.; Brau, D.; Bullard, E.; Olivo, A. Replacing the Detector Mask with a Structured Scintillator in Edge-Illumination x-Ray Phase Contrast Imaging. *Journal of Applied Physics* **2022**, *131*, doi:10.1063/5.0090139.

289. Endrizzi, M.; Diemoz, P.C.; Szafraniec, M.B.; Hagen, C.K.; Millard, T.P.; Zapata, C.E.; Munro, P.R.T.; Ignatyev, K.; Marenzana, M.; Speller, R.D.; et al. Edge Illumination and Coded-Aperture X-Ray Phase-Contrast Imaging: Increased Sensitivity at Synchrotrons and Lab-Based Translations into Medicine, Biology and Materials Science. *MEDICAL IMAGING 2013: PHYSICS OF MEDICAL IMAGING* **2013**, *8668*, doi:10.1117/12.2007893.
290. Marenzana, M.; Hagen, C.K.; Borges, P.D.N.; Endrizzi, M.; Szafraniec, M.B.; Ignatyev, K.; Olivo, A. Visualization of Small Lesions in Rat Cartilage by Means of Laboratory-Based x-Ray Phase Contrast Imaging. *Physics in Medicine and Biology* **2012**, *57*, 8173–8184, doi:10.1088/0031-9155/57/24/8173.
291. Diemoz, P.C.; Endrizzi, M.; Hagen, C.K.; Millard, T.P.; Vittoria, F.A.; Olivo, A. Angular Sensitivity and Spatial Resolution in Edge Illumination X-Ray Phase-Contrast Imaging. *Nuclear Instruments and Methods in Physics Research Section A: Accelerators, Spectrometers, Detectors and Associated Equipment* **2015**, *784*, 538–541, doi:10.1016/j.nima.2014.12.027.
292. Olivo, A.; Arfelli, F.; Cantatore, G.; Longo, R.; Menk, R.H.; Pani, S.; Prest, M.; Poropat, P.; Rigon, L.; Tromba, G.; et al. An Innovative Digital Imaging Set-up Allowing a Low-Dose Approach to Phase Contrast Applications in the Medical Field. *Med. Phys.* **2001**, *28*, 1610–1619, doi:10.1118/1.1388219.
293. Kunisada, T.; Shimao, D.; Sugiyama, H.; Takeda, K.; Ozaki, T.; Ando, M. X-Ray Dark Field Imaging of Human Articular Cartilage: Possible Clinical Application to Orthopedic Surgery. *European Journal of Radiology* **2008**, *68*, S18–S21, doi:10.1016/j.ejrad.2008.04.034.
294. Zanette, I.; Bech, M.; Rack, A.; Le Duc, G.; Tafforeau, P.; David, C.; Mohr, J.; Pfeiffer, F.; Weitkamp, T. Trimodal Low-Dose X-Ray Tomography. *Proc. Natl. Acad. Sci. U.S.A.* **2012**, *109*, 10199–10204, doi:10.1073/pnas.1117861109.
295. Rigon, L.; Arfelli, F.; Menk, R.-H. Three-Image Diffraction Enhanced Imaging Algorithm to Extract Absorption, Refraction, and Ultrasmall-Angle Scattering. *Appl. Phys. Lett.* **2007**, *90*, 114102, doi:10.1063/1.2713147.
296. Esposito, M.; Buchanan, I.; Massimi, L.; Ferrara, J.D.; Shearing, P.R.; Olivo, A.; Endrizzi, M. Laboratory-Based x-Ray Dark-Field Microscopy. *Physical Review Applied* **2023**, *20*, doi:10.1103/PhysRevApplied.20.064039.
297. Esposito, M.; Astolfo, A.; Cipiccia, S.; Jones, C.M.; Savvidis, S.; Ferrara, J.D.; Endrizzi, M.; Dudhia, J.; Olivo, A. Technical Note: Cartilage Imaging with Sub-Cellular Resolution Using a Laboratory-Based Phase-Contrast x-Ray Microscope. *Medical Physics* **2023**, *50*, 6130–6136, doi:10.1002/mp.16599.
298. Ando, M.; Sunaguchi, N.; Shimao, D.; Pan, A.; Yuasa, T.; Mori, K.; Suzuki, Y.; Jin, G.; Kim, J.-K.; Lim, J.-H.; et al. Dark-Field Imaging: Recent Developments and Potential Clinical Applications. *Physica Medica* **2016**, *32*, 1801–1812, doi:10.1016/j.ejmp.2016.11.103.
299. Shimao, D.; Kunisada, T.; Sugiyama, H.; Ando, M. Refraction-Enhanced Tomosynthesis of a Finger Joint by X-Ray Dark-Field Imaging. *Japanese Journal of Applied Physics, Part 2: Letters* **2007**, *46*, L608–L610, doi:10.1143/JJAP.46.L608.
300. Shimao, D.; Sugiyama, H.; Kunisada, T.; Ando, M. Articular Cartilage Depicted at Optimized Angular Position of Laue Angular Analyzer by X-Ray Dark-Field Imaging. *Applied Radiation and Isotopes* **2006**, *64*, 868–874, doi:10.1016/j.apradiso.2006.03.004.
301. Shimao, D.; Sugiyama, H.; Kunisada, T.; Maksimenko, A.; Toyofuku, F.; Ueno, E.; Yamasaki, K.; Obayashi, C.; Hyodo, K.; Li, G.; et al. X-Ray Dark-Field Imaging and Potential of Its Clinical Application. *Medical Imaging 2005: Physics of Medical Imaging, Pts 1 and 2* **2005**, *5745*, 32–39, doi:10.1117/12.595021.
302. Shimao, D.; Sugiyama, H.; Hyodo, K.; Kunisada, T.; Ando, M. Evaluation of X-Ray Dark-Field Imaging in Visualization of Nearly Clinical Articular Cartilage. *NUCLEAR INSTRUMENTS & METHODS IN PHYSICS RESEARCH SECTION A-ACCELERATORS SPECTROMETERS DETECTORS AND ASSOCIATED EQUIPMENT* **2005**, *548*, 129–134, doi:10.1016/j.nima.2005.03.079.

303. Ando, M.; Sugiyama, H.; Kunisada, T.; Shimao, D.; Takeda, K.; Hashizume, H.; Inoue, H. Construction of X-Ray Dark-Field Imaging with a View Size of 80mm Square and First Visualization of Human Articular Cartilage of Femoral Head under a Nearly Clinical Condition. *Japanese Journal of Applied Physics, Part 2: Letters* **2004**, *43*, L1175–L1177, doi:10.1143/JJAP.43.L1175.
304. Shimao, D.; Mori, K.; Sugiyama, H.; Hyodo, K. Imaging of Ligament and Articular Cartilage Due to Refraction-Contrast Using a Laue Geometry Analyzer Crystal. *Japanese Journal of Applied Physics, Part 1: Regular Papers and Short Notes and Review Papers* **2003**, *42*, 5874–5875, doi:10.1143/jjap.42.5874.
305. Vittoria, F.A.; Kallon, G.K.N.; Basta, D.; Diemoz, P.C.; Robinson, I.K.; Olivo, A.; Endrizzi, M. Beam Tracking Approach for Single–Shot Retrieval of Absorption, Refraction, and Dark–Field Signals with Laboratory x–Ray Sources. *Applied Physics Letters* **2015**, *106*, 224102, doi:10.1063/1.4922189.
306. Bay, B.K. Texture Correlation: A Method for the Measurement of Detailed Strain Distributions within Trabecular Bone. *Journal Orthopaedic Research* **1995**, *13*, 258–267, doi:10.1002/jor.1100130214.
307. Karali, A.; Kao, A.P.; Zekonyte, J.; Blunn, G.; Tozzi, G. Micromechanical Evaluation of Cortical Bone Using in Situ XCT Indentation and Digital Volume Correlation. *Journal of the Mechanical Behavior of Biomedical Materials* **2021**, *115*, 104298, doi:10.1016/j.jmbbm.2020.104298.
308. Costa, M.C.; Tozzi, G.; Cristofolini, L.; Danesi, V.; Viceconti, M.; Dall'Ara, E. Micro Finite Element Models of the Vertebral Body: Validation of Local Displacement Predictions. *PLoS ONE* **2017**, *12*, e0180151, doi:10.1371/journal.pone.0180151.
309. Disney, C.M.; Eckersley, A.; McConnell, J.C.; Geng, H.; Bodey, A.J.; Hoyland, J.A.; Lee, P.D.; Sherratt, M.J.; Bay, B.K. Synchrotron Tomography of Intervertebral Disc Deformation Quantified by Digital Volume Correlation Reveals Microstructural Influence on Strain Patterns. *Acta Biomaterialia* **2019**, *92*, 290–304, doi:10.1016/j.actbio.2019.05.021.
310. Pierantoni, M.; Sharma, K.; Kok, J.; Novak, V.; Eliasson, P.; Isaksson, H. Quantification of 3D Microstructures in Achilles Tendons during in Situ Loading Reveals Anisotropic Fiber Response. *Acta Biomaterialia* **2025**, *194*, 246–257, doi:10.1016/j.actbio.2025.01.023.
311. Bay, B.K.; Smith, T.S.; Fyhrie, D.P.; Saad, M. Digital Volume Correlation: Three-Dimensional Strain Mapping Using X-Ray Tomography. *Experimental Mechanics* **1999**, *39*, 217–226, doi:10.1007/BF02323555.
312. Turunen, M.J.; Töyräs, J.; Lammi, M.J.; Jurvelin, J.S.; Korhonen, R.K. Hyperosmolaric Contrast Agents in Cartilage Tomography May Expose Cartilage to Overload-Induced Cell Death. *Journal of Biomechanics* **2012**, *45*, 497–503, doi:10.1016/j.jbiomech.2011.11.049.
313. Pouran, B.; Arbabi, V.; Zadpoor, A.A.; Weinans, H. Isolated Effects of External Bath Osmolality, Solute Concentration, and Electrical Charge on Solute Transport across Articular Cartilage. *Medical Engineering & Physics* **2016**, *38*, 1399–1407, doi:10.1016/j.medengphy.2016.09.003.
314. Zimmerman, B.K.; Nims, R.J.; Chen, A.; Hung, C.T.; Ateshian, G.A. Direct Osmotic Pressure Measurements in Articular Cartilage Demonstrate Nonideal and Concentration-Dependent Phenomena. *Journal of Biomechanical Engineering* **2021**, *143*, 041007, doi:10.1115/1.4049158.
315. Paternò, G.; Cardarelli, P.; Gambaccini, M.; Taibi, A. Dual-Energy X-Ray Medical Imaging with Inverse Compton Sources: A Simulation Study. *Crystals* **2020**, *10*, 834, doi:10.3390/cryst10090834.
316. Procz, S.; Avila, C.; Fey, J.; Roque, G.; Schuetz, M.; Hamann, E. X-Ray and Gamma Imaging with Medipix and Timepix Detectors in Medical Research. *Radiation Measurements* **2019**, *127*, 106104, doi:10.1016/j.radmeas.2019.04.007.

317. Ramilli, M.; Bergamaschi, A.; Andrae, M.; Brückner, M.; Cartier, S.; Dinapoli, R.; Fröjdh, E.; Greiffenberg, D.; Hutwelker, T.; Lopez-Cuenca, C.; et al. Measurements with MÖNCH, a 25 Mm Pixel Pitch Hybrid Pixel Detector. *J. Inst.* **2017**, *12*, C01071–C01071, doi:10.1088/1748-0221/12/01/C01071.
318. Munro, P.R.T.; Rigon, L.; Ignatyev, K.; Lopez, F.C.M.; Dreossi, D.; Speller, R.D.; Olivo, A. A Quantitative, Non-Interferometric X-Ray Phase Contrast Imaging Technique. *Opt. Express* **2013**, *21*, 647, doi:10.1364/OE.21.000647.
319. Cicek, E. Effect of X-Ray Irradiation on Articular Cartilage Mechanical Properties. *Acta Phys. Pol. A* **2016**, *129*, 200–202, doi:10.12693/APhysPolA.129.200.
320. Peña Fernández, M.; Cipiccia, S.; Dall'Ara, E.; Bodey, A.J.; Parwani, R.; Pani, M.; Blunn, G.W.; Barber, A.H.; Tozzi, G. Effect of SR-microCT Radiation on the Mechanical Integrity of Trabecular Bone Using in Situ Mechanical Testing and Digital Volume Correlation. *Journal of the Mechanical Behavior of Biomedical Materials* **2018**, *88*, 109–119, doi:10.1016/j.jmbbm.2018.08.012.
321. Barth, H.D.; Zimmermann, E.A.; Schaible, E.; Tang, S.Y.; Alliston, T.; Ritchie, R.O. Characterization of the Effects of X-Ray Irradiation on the Hierarchical Structure and Mechanical Properties of Human Cortical Bone. *Biomaterials* **2011**, *32*, 8892–8904, doi:10.1016/j.biomaterials.2011.08.013.
322. Willer, K.; Fingerle, A.A.; Noichl, W.; De Marco, F.; Frank, M.; Urban, T.; Schick, R.; Gustschin, A.; Gleich, B.; Herzen, J.; et al. X-Ray Dark-Field Chest Imaging for Detection and Quantification of Emphysema in Patients with Chronic Obstructive Pulmonary Disease: A Diagnostic Accuracy Study. *The Lancet Digital Health* **2021**, *3*, e733–e744, doi:10.1016/S2589-7500(21)00146-1.
323. Gassert, F.T.; Urban, T.; Frank, M.; Willer, K.; Noichl, W.; Buchberger, P.; Schick, R.; Koehler, T.; Von Berg, J.; Fingerle, A.A.; et al. X-Ray Dark-Field Chest Imaging: Qualitative and Quantitative Results in Healthy Humans. *Radiology* **2021**, *301*, 389–395, doi:10.1148/radiol.2021210963.
324. Eschweiler, J.; Horn, N.; Rath, B.; Betsch, M.; Baroncini, A.; Tingart, M.; Migliorini, F. The Biomechanics of Cartilage—An Overview. *Life* **2021**, *11*, 302, doi:10.3390/life11040302.
325. Muir, H. Proteoglycans as Organizers of the Intercellular Matrix. *Biochemical Society Transactions* **1983**, *11*, 613–622, doi:10.1042/bst0110613.
326. Setton, L.A.; Zhu, W.; Mow, V.C. The Biphasic Poroviscoelastic Behavior of Articular Cartilage: Role of the Surface Zone in Governing the Compressive Behavior. *Journal of Biomechanics* **1993**, *26*, 581–592, doi:10.1016/0021-9290(93)90019-B.
327. Quiroga, J.M.P.; Wilson, W.; Ito, K.; Van Donkelaar, C.C. Relative Contribution of Articular Cartilage's Constitutive Components to Load Support Depending on Strain Rate. *Biomech Model Mechanobiol* **2017**, *16*, 151–158, doi:10.1007/s10237-016-0807-0.
328. Hu, J.; Zheng, K.; Sherlock, B.E.; Zhong, J.; Mansfield, J.; Green, E.; Toms, A.D.; Winlove, C.P.; Chen, J. Zonal Characteristics of Collagen Ultrastructure and Responses to Mechanical Loading in Articular Cartilage. *Acta Biomaterialia* **2025**, *195*, 104–116, doi:10.1016/j.actbio.2025.01.047.
329. Hayes, W.C.; Bodine, A.J. Flow-Independent Viscoelastic Properties of Articular Cartilage Matrix. *Journal of Biomechanics* **1978**, *11*, 407–419, doi:10.1016/0021-9290(78)90075-1.
330. Huang, C.-Y.; Mow, V.C.; Ateshian, G.A. The Role of Flow-Independent Viscoelasticity in the Biphasic Tensile and Compressive Responses of Articular Cartilage. *Journal of Biomechanical Engineering* **2001**, *123*, 410–417, doi:10.1115/1.1392316.
331. Mow, V.C.; Guo, X.E. Mechano-Electrochemical Properties Of Articular Cartilage: Their Inhomogeneities and Anisotropies. *Annu. Rev. Biomed. Eng.* **2002**, *4*, 175–209, doi:10.1146/annurev.bioeng.4.110701.120309.

332. Lai, W.M.; Hou, J.S.; Mow, V.C. A Triphasic Theory for the Swelling and Deformation Behaviors of Articular Cartilage. *Journal of Biomechanical Engineering* **1991**, *113*, 245–258, doi:10.1115/1.2894880.
333. Martel-Pelletier, J. Pathophysiology of Osteoarthritis. *Osteoarthritis and Cartilage* **2004**, *12*, 31–33, doi:10.1016/j.joca.2003.10.002.
334. de Bournonville, S.; Vangrunderbeeck, S.; Kerckhofs, G. Contrast-Enhanced MicroCT for Virtual 3D Anatomical Pathology of Biological Tissues: A Literature Review. *Contrast Media & Molecular Imaging* **2019**, *2019*, 8617406, doi:10.1155/2019/8617406.
335. Aula, A.S.; Jurvelin, J.S.; Töyräs, J. Simultaneous Computed Tomography of Articular Cartilage and Subchondral Bone. *Osteoarthritis Cartilage* **2009**, *17*, 1583–1588, doi:10.1016/j.joca.2009.06.010.
336. Silvast, T.S.; Jurvelin, J.S.; Aula, A.S.; Lammi, M.J.; Töyräs, J. Contrast Agent-Enhanced Computed Tomography of Articular Cartilage: Association with Tissue Composition and Properties. *Acta Radiol* **2009**, *50*, 78–85, doi:10.1080/02841850802572526.
337. Silvast, T.S.; Jurvelin, J.S.; Lammi, M.J.; Töyräs, J. pQCT Study on Diffusion and Equilibrium Distribution of Iodinated Anionic Contrast Agent in Human Articular Cartilage – Associations to Matrix Composition and Integrity. *Osteoarthritis and Cartilage* **2009**, *17*, 26–32, doi:10.1016/j.joca.2008.05.012.
338. Bansal, P.N.; Joshi, N.S.; Entezari, V.; Malone, B.C.; Stewart, R.C.; Snyder, B.D.; Grinstaff, M.W. Cationic Contrast Agents Improve Quantification of Glycosaminoglycan (GAG) Content by Contrast Enhanced CT Imaging of Cartilage. *Journal of Orthopaedic Research* **2011**, *29*, 704–709, doi:10.1002/jor.21312.
339. Stewart, R.C.; Bansal, P.N.; Entezari, V.; Lusic, H.; Nazarian, R.M.; Snyder, B.D.; Grinstaff, M.W. Contrast-Enhanced CT with a High-Affinity Cationic Contrast Agent for Imaging Ex Vivo Bovine, Intact Ex Vivo Rabbit, and in Vivo Rabbit Cartilage. *Radiology* **2013**, *266*, 141–150, doi:10.1148/radiol.12112246.
340. Jin, H.; Lewis, J.L. Determination of Poisson's Ratio of Articular Cartilage by Indentation Using Different-Sized Indenters. *Journal of Biomechanical Engineering* **2004**, *126*, 138–145, doi:10.1115/1.1688772.
341. Berni, M.; Erani, P.; Lopomo, N.F.; Baleani, M. Optimization of In Situ Indentation Protocol to Map the Mechanical Properties of Articular Cartilage. *Materials* **2022**, *15*, doi:10.3390/ma15186425.
342. Mohammadi, A.; Te Moller, N.C.R.; Ebrahimi, M.; Plomp, S.; Brommer, H.; Van Weeren, P.R.; Mäkelä, J.T.A.; Töyräs, J.; Korhonen, R.K. Site- and Zone-Dependent Changes in Proteoglycan Content and Biomechanical Properties of Bluntly and Sharply Grooved Equine Articular Cartilage. *Ann Biomed Eng* **2022**, *50*, 1787–1797, doi:10.1007/s10439-022-02991-4.
343. Hayes, W.C.; Keer, L.M.; Herrmann, G.; Mockros, L.F. A Mathematical Analysis for Indentation Tests of Articular Cartilage. *Journal of Biomechanics* **1972**, *5*, 541–551, doi:10.1016/0021-9290(72)90010-3.
344. Li, G.; Lopez, O.; Rubash, H. Variability of a Three-Dimensional Finite Element Model Constructed Using Magnetic Resonance Images of a Knee for Joint Contact Stress Analysis. *Journal of Biomechanical Engineering* **2001**, *123*, 341–346, doi:10.1115/1.1385841.
345. Kumar, R.; Pierce, D.; Isaksen, V.; Davies, C.; Drogset, J.; Lilledahl, M. Comparison of Compressive Stress-Relaxation Behavior in Osteoarthritic (ICRS Graded) Human Articular Cartilage. *IJMS* **2018**, *19*, 413, doi:10.3390/ijms19020413.
346. Ebrahimi, M.; Ojanen, S.; Mohammadi, A.; Finnilä, M.A.; Joukainen, A.; Kröger, H.; Saarakkala, S.; Korhonen, R.K.; Tanska, P. Elastic, Viscoelastic and Fibril-Reinforced Poroelastic Material Properties of Healthy and Osteoarthritic Human Tibial Cartilage. *Ann Biomed Eng* **2019**, *47*, 953–966, doi:10.1007/s10439-019-02213-4.

347. Kiviranta, P.; Rieppo, J.; Korhonen, R.K.; Julkunen, P.; Töyräs, J.; Jurvelin, J.S. Collagen Network Primarily Controls Poisson's Ratio of Bovine Articular Cartilage in Compression. *J. Orthop. Res.* **2006**, *24*, 690–699, doi:10.1002/jor.20107.
348. Changoor, A.; Fereydoonzad, L.; Yaroshinsky, A.; Buschmann, M.D. Effects of Refrigeration and Freezing on the Electromechanical and Biomechanical Properties of Articular Cartilage. *Journal of Biomechanical Engineering* **2010**, *132*, doi:10.1115/1.4000991.
349. Pereira-Lobato, C.; Echeverry-Rendón, M.; Fernández-Blázquez, J.P.; González, C.; LLorca, J. Mechanical Properties, in Vitro Degradation and Cytocompatibility of Woven Textiles Manufactured from PLA/PCL Commingled Yarns. *Journal of the Mechanical Behavior of Biomedical Materials* **2024**, *150*, 106340, doi:10.1016/j.jmbbm.2023.106340.
350. June, R.K.; Mejia, K.L.; Barone, J.R.; Fyhrie, D.P. Cartilage Stress–Relaxation Is Affected by Both the Charge Concentration and Valence of Solution Cations. *Osteoarthritis and Cartilage* **2009**, *17*, 669–676, doi:10.1016/j.joca.2008.09.011.
351. Han, L.; Dean, D.; Mao, P.; Ortiz, C.; Grodzinsky, A.J. Nanoscale Shear Deformation Mechanisms of Opposing Cartilage Aggrecan Macromolecules. *Biophysical Journal* **2007**, *93*, L23–L25, doi:10.1529/biophysj.107.114025.
352. Lu, X.L.; Sun, D.D.N.; Guo, X.E.; Chen, F.H.; Lai, W.M.; Mow, V.C. Indentation Determined Mechanoelectrochemical Properties and Fixed Charge Density of Articular Cartilage. *Annals of Biomedical Engineering* **2004**, *32*, 370–379, doi:10.1023/B:ABME.0000017534.06921.24.
353. Temple, D.K.; Cederlund, A.A.; Lawless, B.M.; Aspden, R.M.; Espino, D.M. Viscoelastic Properties of Human and Bovine Articular Cartilage: A Comparison of Frequency-Dependent Trends. *BMC Musculoskelet Disord* **2016**, *17*, 419, doi:10.1186/s12891-016-1279-1.
354. Li, H.; Li, J.; Yu, S.; Wu, C.; Zhang, W. The Mechanical Properties of Tibiofemoral and Patellofemoral Articular Cartilage in Compression Depend on Anatomical Regions. *Scientific Reports* **2021**, *11*, 6128, doi:10.1038/s41598-021-85716-2.
355. Thambyah, A.; Nather, A.; Goh, J. Mechanical Properties of Articular Cartilage Covered by the Meniscus. *Osteoarthritis and Cartilage* **2006**, *14*, 580–588, doi:10.1016/j.joca.2006.01.015.
356. Moshtagh, P.R.; Pouran, B.; Korthagen, N.M.; Zadpoor, A.A.; Weinans, H. Guidelines for an Optimized Indentation Protocol for Measurement of Cartilage Stiffness: The Effects of Spatial Variation and Indentation Parameters. *Journal of Biomechanics* **2016**, *49*, 3602–3607, doi:10.1016/j.jbiomech.2016.09.020.
357. Kabir, W.; Di Bella, C.; Choong, P.F.M.; O'Connell, C.D. Assessment of Native Human Articular Cartilage: A Biomechanical Protocol. *CARTILAGE* **2021**, *13*, 427S-437S, doi:10.1177/1947603520973240.
358. Peters, A.E.; Comerford, E.J.; Macaulay, S.; Bates, K.T.; Akhtar, R. Micromechanical Properties of Canine Femoral Articular Cartilage Following Multiple Freeze-Thaw Cycles. *Journal of the Mechanical Behavior of Biomedical Materials* **2017**, *71*, 114–121, doi:10.1016/j.jmbbm.2017.03.006.
359. Qu, C.; Hirviniemi, M.; Tiitu, V.; Jurvelin, J.S.; Töyräs, J.; Lammi, M.J. Effects of Freeze–Thaw Cycle with and without Proteolysis Inhibitors and Cryopreservant on the Biochemical and Biomechanical Properties of Articular Cartilage. *CARTILAGE* **2014**, *5*, 97–106, doi:10.1177/1947603513515998.
360. Shepherd, D.E.T.; Seedhom, B.B. A Technique for Measuring the Compressive Modulus of Articular Cartilage under Physiological Loading Rates with Preliminary Results. *Proc Inst Mech Eng H* **1997**, *211*, 155–165, doi:10.1243/0954411971534278.
361. Bonnevie, E.D.; Baro, V.J.; Wang, L.; Burris, D.L. Fluid Load Support during Localized Indentation of Cartilage with a Spherical Probe. *Journal of Biomechanics* **2012**, *45*, 1036–1041, doi:10.1016/j.jbiomech.2011.12.019.
362. Hosseini, A.; Van De Velde, S.K.; Kozanek, M.; Gill, T.J.; Grodzinsky, A.J.; Rubash, H.E.; Li, G. In-Vivo Time-Dependent Articular Cartilage Contact Behavior of the Tibiofemoral Joint. *Osteoarthritis and Cartilage* **2010**, *18*, 909–916, doi:10.1016/j.joca.2010.04.011.

363. Liu, F.; Kozanek, M.; Hosseini, A.; Van De Velde, S.K.; Gill, T.J.; Rubash, H.E.; Li, G. In Vivo Tibiofemoral Cartilage Deformation during the Stance Phase of Gait. *Journal of Biomechanics* **2010**, *43*, 658–665, doi:10.1016/j.jbiomech.2009.10.028.
364. Schad, P.; Wollenweber, M.; Thüring, J.; Schock, J.; Eschweiler, J.; Palm, G.; Radermacher, K.; Eckstein, F.; Prescher, A.; Kuhl, C.; et al. Magnetic Resonance Imaging of Human Knee Joint Functionality under Variable Compressive In-Situ Loading and Axis Alignment. *Journal of the Mechanical Behavior of Biomedical Materials* **2020**, *110*, 103890, doi:10.1016/j.jmbbm.2020.103890.
365. Mow, V.C.; Holmes, M.H.; Michael Lai, W. Fluid Transport and Mechanical Properties of Articular Cartilage: A Review. *Journal of Biomechanics* **1984**, *17*, 377–394, doi:10.1016/0021-9290(84)90031-9.
366. Knecht, S.; Vanwanseele, B.; Stüssi, E. A Review on the Mechanical Quality of Articular Cartilage – Implications for the Diagnosis of Osteoarthritis. *Clinical Biomechanics* **2006**, *21*, 999–1012, doi:10.1016/j.clinbiomech.2006.07.001.
367. Berni, M.; Fantoni, S.; Fognani, R.; Cardarelli, P.; Baruffaldi, F.; Baleani, M. Assessment of CA4+ Impact on Mechanical Properties of Articular Cartilage. *Materials* **2025**, *18*, 2943, doi:10.3390/ma18132943.
368. Bhattarai, A.; Mäkelä, J.T.A.; Pouran, B.; Kröger, H.; Weinans, H.; Grinstaff, M.W.; Töyräs, J.; Turunen, M.J. Effects of Human Articular Cartilage Constituents on Simultaneous Diffusion of Cationic and Nonionic Contrast Agents. *Journal Orthopaedic Research* **2021**, *39*, 771–779, doi:10.1002/jor.24824.
369. Maroudas, A. Transport of Solutes through Cartilage: Permeability to Large Molecules. *J Anat* **1976**, *122*, 335–347.
370. Leddy, H.A.; Guilak, F. Site-Specific Molecular Diffusion in Articular Cartilage Measured Using Fluorescence Recovery after Photobleaching. *Annals of Biomedical Engineering* **2003**, *31*, 753–760, doi:10.1114/1.1581879.
371. Travascio, F.; Valladares-Prieto, S.; Jackson, A.R. Effects of Solute Size and Tissue Composition on Molecular and Macromolecular Diffusivity in Human Knee Cartilage. *Osteoarthritis and Cartilage Open* **2020**, *2*, 100087, doi:10.1016/j.ocarto.2020.100087.
372. Bajpayee, A.G.; Scheu, M.; Grodzinsky, A.J.; Porter, R.M. A Rabbit Model Demonstrates the Influence of Cartilage Thickness on Intra-articular Drug Delivery and Retention within Cartilage. *Journal Orthopaedic Research* **2015**, *33*, 660–667, doi:10.1002/jor.22841.
373. Golini, C.; Barbieri, M.; Nagmutdinova, A.; Bortolotti, V.; Testa, C.; Brizi, L. Depth-wise Multiparametric Assessment of Articular Cartilage Layers with Single-sided NMR. *NMR in Biomedicine* **2025**, *38*, e5287, doi:10.1002/nbm.5287.
374. Roughley, P.J.; Lee, E.R. Cartilage Proteoglycans: Structure and Potential Functions. *Microscopy Res & Technique* **1994**, *28*, 385–397, doi:10.1002/jemt.1070280505.
375. Buckwalter, J.A.; Mankin, H.J.; Grodzinsky, A.J. Articular Cartilage and Osteoarthritis. *Instr Course Lect* **2005**, *54*, 465–480.
376. Fischenich, K.M.; Button, K.D.; DeCamp, C.; Haut, R.C.; Donahue, T.L.H. Comparison of Two Models of Post-traumatic Osteoarthritis; Temporal Degradation of Articular Cartilage and Menisci. *Journal Orthopaedic Research* **2017**, *35*, 486–495, doi:10.1002/jor.23275.
377. Im, G.-I. The Concept of Early Osteoarthritis and Its Significance in Regenerative Medicine. *Tissue Eng Regen Med* **2022**, *19*, 431–436, doi:10.1007/s13770-022-00436-6.
378. Emanuel, K.S.; Kellner, L.J.; Peters, M.J.M.; Haartmans, M.J.J.; Hooijmans, M.T.; Emans, P.J. The Relation between the Biochemical Composition of Knee Articular Cartilage and Quantitative MRI: A Systematic Review and Meta-Analysis. *Osteoarthritis and Cartilage* **2022**, *30*, 650–662, doi:10.1016/j.joca.2021.10.016.
379. Banjar, M.; Horiuchi, S.; Gedeon, D.N.; Yoshioka, H. Review of Quantitative Knee Articular Cartilage MR Imaging. *MRMS* **2022**, *21*, 29–40, doi:10.2463/mrms.rev.2021-0052.

380. Burghardt, A.J.; Link, T.M.; Majumdar, S. High-Resolution Computed Tomography for Clinical Imaging of Bone Microarchitecture. *Clinical Orthopaedics & Related Research* **2011**, *469*, 2179–2193, doi:10.1007/s11999-010-1766-x.
381. Li, X.; Majumdar, S. Quantitative MRI of Articular Cartilage and Its Clinical Applications. *Magnetic Resonance Imaging* **2013**, *38*, 991–1008, doi:10.1002/jmri.24313.
382. Hasebroock, K.M.; Serkova, N.J. Toxicity of MRI and CT Contrast Agents. *Expert Opinion on Drug Metabolism & Toxicology* **2009**, *5*, 403–416, doi:10.1517/17425250902873796.
383. Balcaen, T.; Vangrunderbeeck, S.; De Borggraeve, W.M.; Kerckhofs, G. Contrast-Enhancing Staining Agents for Ex Vivo Contrast-Enhanced Computed Tomography: A Review. *Tomography of Materials and Structures* **2025**, *7*, 100052, doi:10.1016/j.tmater.2025.100052.
384. Cerbone, L.A.; Mettivier, G.; Lai, Y.; Jia, X.; Boyd, S.K.; Russo, P. Absorbed and Effective Dose Estimates in HR-pQCT of the Distal Radius and Tibia: Virtual Dosimetry with a GPU-Accelerated Monte Carlo Code. *Phys. Med. Biol.* **2025**, *70*, 095005, doi:10.1088/1361-6560/adc9f6.
385. Fantoni, S.; Gabucci, I.; Cardarelli, P.; Paternò, G.; Taibi, A.; Cristofori, V.; Trapella, C.; Bazzani, A.; Assenza, M.; Zanna Bonacorsi, A.; et al. A Cationic Contrast Agent in X-Ray Imaging of Articular Cartilage: Pre-Clinical Evaluation of Diffusion and Attenuation Properties. *Diagnostics* **2022**, *12*, 2111, doi:10.3390/diagnostics12092111.
386. Berni, M.; Erani, P.; Lopomo, N.F.; Baleani, M. Optimization of In Situ Indentation Protocol to Map the Mechanical Properties of Articular Cartilage. *Materials* **2022**, *15*, 6425, doi:10.3390/ma15186425.
387. Mys, K.; Stockmans, F.; Vereecke, E.; Van Lenthe, G.H. Quantification of Bone Microstructure in the Wrist Using Cone-Beam Computed Tomography. *Bone* **2018**, *114*, 206–214, doi:10.1016/j.bone.2018.06.006.
388. Pastrama, M.-I.; Ortiz, A.C.; Zevenbergen, L.; Famaey, N.; Gsell, W.; Neu, C.P.; Himmelreich, U.; Jonkers, I. Combined Enzymatic Degradation of Proteoglycans and Collagen Significantly Alters Intratissue Strains in Articular Cartilage during Cyclic Compression. *Journal of the Mechanical Behavior of Biomedical Materials* **2019**, *98*, 383–394, doi:10.1016/j.jmbbm.2019.05.040.
389. Xia, Y.; Zheng, S.; Bidthanapally, A. Depth-dependent Profiles of Glycosaminoglycans in Articular Cartilage by μMRI and Histochemistry. *Magnetic Resonance Imaging* **2008**, *28*, 151–157, doi:10.1002/jmri.21392.
390. Mohammadi, A.; Te Moller, N.C.R.; Ebrahimi, M.; Plomp, S.; Brommer, H.; Van Weeren, P.R.; Mäkelä, J.T.A.; Töyräs, J.; Korhonen, R.K. Site- and Zone-Dependent Changes in Proteoglycan Content and Biomechanical Properties of Bluntly and Sharply Grooved Equine Articular Cartilage. *Ann Biomed Eng* **2022**, *50*, 1787–1797, doi:10.1007/s10439-022-02991-4.
391. Yin, J.-H.; Xia, Y.; Ramakrishnan, N. Depth-Dependent Anisotropy of Proteoglycan in Articular Cartilage by Fourier Transform Infrared Imaging. *Vibrational Spectroscopy* **2011**, *57*, 338–341, doi:10.1016/j.vibspec.2011.08.005.
392. Shehata, E.; Nippolainen, E.; Shaikh, R.; Ronkainen, A.-P.; Töyräs, J.; Sarin, J.K.; Afara, I.O. Raman Spectroscopy and Machine Learning Enables Estimation of Articular Cartilage Structural, Compositional, and Functional Properties. *Ann Biomed Eng* **2023**, *51*, 2301–2312, doi:10.1007/s10439-023-03271-5.
393. Kamisan, N.; Naveen, S.V.; Ahmad, R.E.; Tunku, K. Chondrocyte Density, Proteoglycan Content and Gene Expressions from Native Cartilage Are Species Specific and Not Dependent on Cartilage Thickness: A Comparative Analysis between Rat, Rabbit and Goat. *BMC Vet Res* **2013**, *9*, 62, doi:10.1186/1746-6148-9-62.
394. Linus, A.; Tanska, P.; Nippolainen, E.; Tiitu, V.; Töyras, J.; Korhonen, R.K.; Afara, I.O.; Mononen, M.E. Site-Specific Elastic and Viscoelastic Biomechanical Properties of Healthy and Osteoarthritic Human Knee Joint Articular Cartilage. *Journal of Biomechanics* **2024**, *169*, 112135, doi:10.1016/j.jbiomech.2024.112135.

395. Ebrahimi, M.; Turkiewicz, A.; Finnilä, M.A.J.; Saarakkala, S.; Englund, M.; Korhonen, R.K.; Tanska, P. Associations of Human Femoral Condyle Cartilage Structure and Composition with Viscoelastic and Constituent-Specific Material Properties at Different Stages of Osteoarthritis. *Journal of Biomechanics* **2022**, *145*, 111390, doi:10.1016/j.jbiomech.2022.111390.
396. Kumar, R.; Pierce, D.; Isaksen, V.; Davies, C.; Drogset, J.; Lilledahl, M. Comparison of Compressive Stress-Relaxation Behavior in Osteoarthritic (ICRS Graded) Human Articular Cartilage. *IJMS* **2018**, *19*, 413, doi:10.3390/ijms19020413.
397. Ateshian, G.A.; Chahine, N.O.; Basalo, I.M.; Hung, C.T. The Correspondence between Equilibrium Biphasic and Triphasic Material Properties in Mixture Models of Articular Cartilage. *Journal of Biomechanics* **2004**, *37*, 391–400, doi:10.1016/S0021-9290(03)00252-5.
398. Canal Guterl, C.; Hung, C.T.; Ateshian, G.A. Electrostatic and Non-Electrostatic Contributions of Proteoglycans to the Compressive Equilibrium Modulus of Bovine Articular Cartilage. *Journal of Biomechanics* **2010**, *43*, 1343–1350, doi:10.1016/j.jbiomech.2010.01.021.
399. June, R.K.; Neu, C.P.; Barone, J.R.; Fyhrie, D.P. Polymer Mechanics as a Model for Short-Term and Flow-Independent Cartilage Viscoelasticity. *Materials Science and Engineering: C* **2011**, *31*, 781–788, doi:10.1016/j.msec.2010.11.029.
400. Huttu, M.R.J.; Puhakka, J.; Mäkelä, J.T.A.; Takakubo, Y.; Tiitu, V.; Saarakkala, S.; Konttinen, Y.T.; Kiviranta, I.; Korhonen, R.K. Cell–Tissue Interactions in Osteoarthritic Human Hip Joint Articular Cartilage. *Connective Tissue Research* **2014**, *55*, 282–291, doi:10.3109/03008207.2014.912645.
401. Khan, B.; Nippolainen, E.; Shahini, F.; Nonappa; Popov, A.; Töyräs, J.; Afara, I.O. Relationship between Depth-Wise Refractive Index and Biomechanical Properties of Human Articular Cartilage. *J. Biomed. Opt.* **2024**, *29*, doi:10.1117/1.JBO.29.9.095003.
402. Korhonen, R.K.; Jurvelin, J.S. Compressive and Tensile Properties of Articular Cartilage in Axial Loading Are Modulated Differently by Osmotic Environment. *Medical Engineering & Physics* **2010**, *32*, 155–160, doi:10.1016/j.medengphy.2009.11.004.
403. De Gennes, P.-G. Relaxation Anomalies in Linear Polymer Melts. *Macromolecules* **2002**, *35*, 3785–3786, doi:10.1021/ma012167y.
404. Robinson, D.L.; Kersh, M.E.; Walsh, N.C.; Ackland, D.C.; De Steiger, R.N.; Pandy, M.G. Mechanical Properties of Normal and Osteoarthritic Human Articular Cartilage. *Journal of the Mechanical Behavior of Biomedical Materials* **2016**, *61*, 96–109, doi:10.1016/j.jmbbm.2016.01.015.
405. Hu, Y.J.; Yu, Y.E.; Cooper, H.J.; Shah, R.P.; Geller, J.A.; Lu, X.L.; Shane, E.; Bathon, J.; Lane, N.E.; Guo, X.E. Mechanical and Structural Properties of Articular Cartilage and Subchondral Bone in Human Osteoarthritic Knees. *Journal of Bone and Mineral Research* **2024**, *39*, 1120–1131, doi:10.1093/jbmr/zjae094.
406. De Roy, L.; Teixeira, G.Q.; Schwer, J.; Sukopp, M.; Faschingbauer, M.; Ignatius, A.; Seitz, A.M. Structure-Function of Cartilage in Osteoarthritis: An Ex-Vivo Correlation Analysis between Its Structural, Viscoelastic and Frictional Properties. *Acta Biomaterialia* **2024**, *190*, 293–302, doi:10.1016/j.actbio.2024.10.027.
407. Fugazzola, M.; Nissinen, M.T.; Jäntti, J.; Tuppurainen, J.; Plomp, S.; Te Moller, N.; Mäkelä, J.T.A.; Van Weeren, R. Composition, Architecture and Biomechanical Properties of Articular Cartilage in Differently Loaded Areas of the Equine Stifle. *Equine Veterinary Journal* **2024**, *56*, 573–585, doi:10.1111/evj.13960.
408. Goldring, S.R.; Goldring, M.B. Changes in the Osteochondral Unit during Osteoarthritis: Structure, Function and Cartilage–Bone Crosstalk. *Nat Rev Rheumatol* **2016**, *12*, 632–644, doi:10.1038/nrrheum.2016.148.
409. Fratini, M.; Bukreeva, I.; Campi, G.; Brun, F.; Tromba, G.; Modregger, P.; Bucci, D.; Battaglia, G.; Spanò, R.; Mastrogiacomo, M.; et al. Simultaneous Submicrometric 3D Imaging of the Micro-Vascular Network and the Neuronal System in a Mouse Spinal Cord. *Sci Rep* **2015**, *5*, 8514, doi:10.1038/srep08514.

410. Massimi, L.; Bukreeva, I.; Santamaria, G.; Fratini, M.; Corbelli, A.; Brun, F.; Fumagalli, S.; Maugeri, L.; Pacureanu, A.; Cloetens, P.; et al. Exploring Alzheimer's Disease Mouse Brain through X-Ray Phase Contrast Tomography: From the Cell to the Organ. *NeuroImage* **2019**, *184*, 490–495, doi:10.1016/j.neuroimage.2018.09.044.
411. Akhter, M.P.; Recker, R.R. High Resolution Imaging in Bone Tissue Research-Review. *Bone* **2021**, *143*, 115620, doi:10.1016/j.bone.2020.115620.
412. Fredenberg, E. Spectral and Dual-Energy X-Ray Imaging for Medical Applications. *Nuclear Instruments and Methods in Physics Research Section A: Accelerators, Spectrometers, Detectors and Associated Equipment* **2018**, *878*, 74–87, doi:10.1016/j.nima.2017.07.044.
413. Willemink, M.J.; Persson, M.; Pourmorteza, A.; Pelc, N.J.; Fleischmann, D. Photon-Counting CT: Technical Principles and Clinical Prospects. *Radiology* **2018**, *289*, 293–312, doi:10.1148/radiol.2018172656.
414. Hsieh, S.S.; Leng, S.; Rajendran, K.; Tao, S.; McCollough, C.H. Photon Counting CT: Clinical Applications and Future Developments. *IEEE Trans. Radiat. Plasma Med. Sci.* **2021**, *5*, 441–452, doi:10.1109/TRPMS.2020.3020212.
415. Brun, F.; Di Trapani, V.; Albers, J.; Sacco, P.; Dreossi, D.; Brombal, L.; Rigon, L.; Longo, R.; Mittone, A.; Dullin, C.; et al. Single-Shot K-Edge Subtraction x-Ray Discrete Computed Tomography with a Polychromatic Source and the Pixie-III Detector. *Phys. Med. Biol.* **2020**, *65*, 055016, doi:10.1088/1361-6560/ab7105.
416. Ballabriga, R.; Alozy, J.; Blaj, G.; Campbell, M.; Fiederle, M.; Frojdh, E.; Heijne, E.H.M.; Llopart, X.; Pichotka, M.; Procz, S.; et al. The Medipix3RX: A High Resolution, Zero Dead-Time Pixel Detector Readout Chip Allowing Spectroscopic Imaging. *J. Inst.* **2013**, *8*, C02016–C02016, doi:10.1088/1748-0221/8/02/C02016.
417. Bellazzini, R.; Brez, A.; Spandre, G.; Minuti, M.; Pinchera, M.; Delogu, P.; De Ruvo, P.L.; Vincenzi, A. PIXIE III: A Very Large Area Photon-Counting CMOS Pixel ASIC for Sharp X-Ray Spectral Imaging. *J. Inst.* **2015**, *10*, C01032–C01032, doi:10.1088/1748-0221/10/01/C01032.
418. Di Trapani, V.; Bravin, A.; Brun, F.; Dreossi, D.; Longo, R.; Mittone, A.; Rigon, L.; Delogu, P. Characterization of the Acquisition Modes Implemented in Pixirad-1/Pixie-III X-Ray Detector: Effects of Charge Sharing Correction on Spectral Resolution and Image Quality. *Nuclear Instruments and Methods in Physics Research Section A: Accelerators, Spectrometers, Detectors and Associated Equipment* **2020**, *955*, 163220, doi:10.1016/j.nima.2019.163220.
419. Brombal, L.; Donato, S.; Brun, F.; Delogu, P.; Fanti, V.; Oliva, P.; Rigon, L.; Di Trapani, V.; Longo, R.; Golosio, B. Large-Area Single-Photon-Counting CdTe Detector for Synchrotron Radiation Computed Tomography: A Dedicated Pre-Processing Procedure. *J Synchrotron Rad* **2018**, *25*, 1068–1077, doi:10.1107/S1600577518006197.
420. Hagen, C.K.; Endrizzi, M.; Towns, R.; Meganck, J.A.; Olivo, A. A Preliminary Investigation into the Use of Edge Illumination X-Ray Phase Contrast Micro-CT for Preclinical Imaging. *Mol Imaging Biol* **2020**, *22*, 539–548, doi:10.1007/s11307-019-01396-5.
421. Di Trapani, V.; Brombal, L.; Brun, F. Multi-Material Spectral Photon-Counting Micro-CT with Minimum Residual Decomposition and Self-Supervised Deep Denoising. *Opt. Express* **2022**, *30*, 42995, doi:10.1364/OE.471439.
422. Feldkamp, L.A.; Davis, L.C.; Kress, J.W. Practical Cone-Beam Algorithm. *J. Opt. Soc. Am. A* **1984**, *1*, 612, doi:10.1364/JOSAA.1.000612.
423. Biguri, A.; Dosanjh, M.; Hancock, S.; Soleimani, M. TIGRE: A MATLAB-GPU Toolbox for CBCT Image Reconstruction. *Biomed. Phys. Eng. Express* **2016**, *2*, 055010, doi:10.1088/2057-1976/2/5/055010.
424. Brombal, L.; Rigon, L.; Arfelli, F.; Menk, R.H.; Brun, F. A Geant4 Tool for Edge-Illumination X-Ray Phase-Contrast Imaging. *J. Inst.* **2022**, *17*, C01043, doi:10.1088/1748-0221/17/01/C01043.

425. Di Trapani, V.; Oliva, P.; Arfelli, F.; Brombal, L.; Menk, R.H.; Delogu, P. Development and Validation of a Simulation Tool for K-Edge Subtraction Imaging with Polychromatic Spectra and X-Ray Photon Counting Detectors. *Nuclear Instruments and Methods in Physics Research Section A: Accelerators, Spectrometers, Detectors and Associated Equipment* **2023**, *1046*, 167675, doi:10.1016/j.nima.2022.167675.
426. Heismann, B.J.; Schmidt, B.T.; Flohr, T.G. *Spectral Computed Tomography*; SPIE, 2012; ISBN 978-0-8194-9258-6.
427. Otsu, N. A Threshold Selection Method from Gray-Level Histograms. *IEEE Trans. Syst., Man, Cybern.* **1979**, *9*, 62–66, doi:10.1109/TSMC.1979.4310076.
428. Kauppinen, S.; Karhula, S.S.; Thevenot, J.; Ylitalo, T.; Rieppo, L.; Kestilä, I.; Haapea, M.; Hadjab, I.; Finnilä, M.A.; Quenneville, E.; et al. 3D Morphometric Analysis of Calcified Cartilage Properties Using Micro-Computed Tomography. *Osteoarthritis and Cartilage* **2019**, *27*, 172–180, doi:10.1016/j.joca.2018.09.009.
429. Franz, T.; Hasler, E.M.; Hagg, R.; Weiler, C.; Jakob, R.P.; Mainil-Varlet, P. In Situ Compressive Stiffness, Biochemical Composition, and Structural Integrity of Articular Cartilage of the Human Knee Joint. *Osteoarthritis and Cartilage* **2001**, *9*, 582–592, doi:10.1053/joca.2001.0418.
430. Kumar, R.; Pierce, D.; Isaksen, V.; Davies, C.; Drogset, J.; Lilledahl, M. Comparison of Compressive Stress-Relaxation Behavior in Osteoarthritic (ICRS Graded) Human Articular Cartilage. *IJMS* **2018**, *19*, 413, doi:10.3390/ijms19020413.
431. Suri, S.; Walsh, D.A. Osteochondral Alterations in Osteoarthritis. *Bone* **2012**, *51*, 204–211, doi:10.1016/j.bone.2011.10.010.
432. Davis, S.; Karali, A.; Balcaen, T.; Zekonyte, J.; Pétré, M.; Roldo, M.; Kerckhofs, G.; Blunn, G. Comparison of Two Contrast-Enhancing Staining Agents for Use in X-Ray Imaging and Digital Volume Correlation Measurements across the Cartilage-Bone Interface. *Journal of the Mechanical Behavior of Biomedical Materials* **2024**, *152*, doi:10.1016/j.jmbbm.2024.106414.
433. de Bournonville, S.; Vangrunderbeeck, S.; Ly, H.G.T.; Geeroms, C.; De Borggraeve, W.M.; Parac-Vogt, T.N.; Kerckhofs, G. Exploring Polyoxometalates as Non-Destructive Staining Agents for Contrast-Enhanced Microfocus Computed Tomography of Biological Tissues. *ACTA BIOMATERIALIA* **2020**, *105*, 253–262, doi:10.1016/j.actbio.2020.01.038.
434. Wilkins, S.W.; Gureyev, T.E.; Gao, D.; Pogany, A.; Stevenson, A.W. Phase-Contrast Imaging Using Polychromatic Hard X-Rays. *Nature* **1996**, *384*, 335–338, doi:10.1038/384335a0.
435. Snigirev, A.; Snigireva, I.; Kohn, V.; Kuznetsov, S.; Schelokov, I. On the Possibilities of X-Ray Phase Contrast Microimaging by Coherent High-Energy Synchrotron Radiation. *Review of Scientific Instruments* **1995**, *66*, 5486–5492, doi:10.1063/1.1146073.
436. Albers, J.; Svetlove, A.; Duke, E. Synchrotron X-Ray Imaging of Soft Biological Tissues – Principles, Applications and Future Prospects. *Journal of Cell Science* **2024**, *137*, jcs261953, doi:10.1242/jcs.261953.
437. Chen, H.; He, X.; Sheng, C.; Ma, Y.; Nie, H.; Xia, W.; Ying, W. Interactions between Synchrotron Radiation X-Ray and Biological Tissues - Theoretical and Clinical Significance. *Int J Physiol Pathophysiol Pharmacol* **2011**, *3*, 243–248.
438. Longo, E.; Contillo, A.; D'Amico, L.; Prašek, M.; Saccomano, G.; Sodini, N.; Dullin, C.; Dreossi, D.; Tromba, G. SYRMEP Beamline: State of the Art, Upgrades and Future Prospects. *Eur. Phys. J. Plus* **2024**, *139*, 880, doi:10.1140/epjp/s13360-024-05489-1.
439. Kerl, H.U.; Isaza, C.T.; Boll, H.; Schambach, S.J.; Nolte, I.S.; Groden, C.; Brockmann, M.A. Evaluation of a Continuous-Rotation, High-Speed Scanning Protocol for Micro-Computed Tomography: *Journal of Computer Assisted Tomography* **2011**, *35*, 517–523, doi:10.1097/RCT.0b013e31821c662b.
440. Oncan, T. Effect of Low-Dose Irradiation on Structural and Mechanical Properties of Hyaline Cartilage-like Fibrocartilage. *Acta Orthop Traumatol Turc* **2013**, *47*, 127–133, doi:10.3944/AOTT.2013.2709.

441. Lindburg, C.A.; Willey, J.S.; Dean, D. Effects of Low Dose X-Ray Irradiation on Porcine Articular Cartilage Explants. *J Orthop Res* **2013**, *31*, 1780–1785, doi:10.1002/jor.22406.
442. Rautiainen, J.; Nieminen, M.T.; Salo, E.-N.; Kokkonen, H.T.; Mangia, S.; Michaeli, S.; Gröhn, O.; Jurvelin, J.S.; Töyräs, J.; Nissi, M.J. Effect of Collagen Cross-Linking on Quantitative MRI Parameters of Articular Cartilage. *Osteoarthritis and Cartilage* **2016**, *24*, 1656–1664, doi:10.1016/j.joca.2016.04.017.
443. Hutchinson, I.D.; Olson, J.; Lindburg, C.A.; Payne, V.; Collins, B.; Smith, T.L.; Munley, M.T.; Wheeler, K.T.; Willey, J.S. Total-Body Irradiation Produces Late Degenerative Joint Damage in Rats. *International Journal of Radiation Biology* **2014**, *90*, 821–830, doi:10.3109/09553002.2014.927935.
444. McGann, M.E.; Bonitsky, C.M.; Ovaert, T.C.; Wagner, D.R. The Effect of Collagen Crosslinking on the Biphasic Poroviscoelastic Cartilage Properties Determined from a Semi-Automated Microindentation Protocol for Stress Relaxation. *Journal of the Mechanical Behavior of Biomedical Materials* **2014**, *34*, 264–272, doi:10.1016/j.jmbbm.2014.02.013.
445. Verzijl, N.; DeGroot, J.; Zaken, C.B.; Braun-Benjamin, O.; Maroudas, A.; Bank, R.A.; Mizrahi, J.; Schalkwijk, C.G.; Thorpe, S.R.; Baynes, J.W.; et al. Crosslinking by Advanced Glycation End Products Increases the Stiffness of the Collagen Network in Human Articular Cartilage: A Possible Mechanism through Which Age Is a Risk Factor for Osteoarthritis. *Arthritis & Rheumatism* **2002**, *46*, 114–123, doi:10.1002/1529-0131(200201)46:1%3C114::AID-ART10025%3E3.0.CO;2-P.
446. Kyriakidou, M.; Mavrogenis, A.F.; Kyriazis, S.; Markouizou, A.; Theophanides, T.; Anastassopoulou, J. An FT-IR Spectral Analysis of the Effects of γ-Radiation on Normal and Cancerous Cartilage. *In Vivo* **2016**, *30*, 599–604.
447. Kaplan, L.D.; Ionescu, D.; Ernsthausen, J.M.; Bradley, J.P.; Fu, F.H.; Farkas, D.L. Temperature Requirements for Altering the Morphology of Osteoarthritic and Nonarthritic Articular Cartilage: In Vitro Thermal Alteration of Articular Cartilage. *Am J Sports Med* **2004**, *32*, 688–692, doi:10.1177/0363546503258858.
448. Korhonen, R.K.; Julkunen, P.; Wilson, W.; Herzog, W. Importance of Collagen Orientation and Depth-Dependent Fixed Charge Densities of Cartilage on Mechanical Behavior of Chondrocytes. *Journal of Biomechanical Engineering* **2008**, *130*, 021003, doi:10.1115/1.2898725.
449. Yeh, M.; Luo, Z. The Structure of Proteoglycan Aggregate Determined by Atomic Force Microscopy. *Scanning* **2004**, *26*, 273–276, doi:10.1002/sca.4950260604.
450. Xia, Y.; Zheng, S.; Bidthanapally, A. Depth-dependent Profiles of Glycosaminoglycans in Articular Cartilage by μMRI and Histochemistry. *Magnetic Resonance Imaging* **2008**, *28*, 151–157, doi:10.1002/jmri.21392.
451. Appel, C.; Schmeltz, M.; Rodriguez-Fernandez, I.; Anschuetz, L.; Nielsen, L.C.; Panepucci, E.; Marijolovic, T.; Wakonig, K.; Ivanovic, A.; Bonnin, A.; et al. Fast Small-Angle X-Ray Scattering Tensor Tomography: An Outlook into Future Applications in Life Sciences. *Small Methods* **2025**, 2500162, doi:10.1002/smtd.202500162.

Acknowledgements

I have been fortunate enough to meet truly amazing people along this journey called a PhD. During my time at the Istituto Ortopedico Rizzoli, I barely realized how quickly time could pass—three years have flown by in the blink of an eye.

My deepest gratitude goes to Prof. Marco Viceconti for his academic mentorship and for giving me the opportunity to pursue my doctoral path under his supervision. I am deeply thankful to Massimiliano Baleani and Fabio Baruffaldi for their constant support and guidance throughout these three years of navigating the unknown world of the Istituto Ortopedico Rizzoli—their survival tips were truly invaluable. I am also sincerely grateful to Prof. Hanna Isaksson for welcoming me into the Biomechanics Group at Lund University and for sharing her expertise in the challenging yet fascinating field of cartilage analysis. My thanks go to Dr. Paolo Cardarelli for introducing me to the Medical Technology Lab, and to Dr. Luca Brombal for opening the door to the world of synchrotron radiation and advanced imaging techniques—I hope we'll share many more beamtimes together.

Beyond the scientific aspects, I would like to thank all the people I met during my time at the Medical Technology Lab and beyond. Though our time together may have been brief, I'm grateful to Ilenia, Alice, Daniele, Serena, and Sara – my best physicists. I also wish to thank the wonderful members of the Biomechanics Group at Lund University, who made my stay in Sweden such an enjoyable experience. Heartfelt thanks to Chiara and Giulia for the countless hugs and laughs; to Roberta, Paolo, Gigi and Marilina for their wise and caring words and their emotional support, and once again to Fabio and Max for their trust and encouragement.

Last—but certainly not least—my deepest thanks go to Matteo for his unwavering support, his help, and for sharing both the burdens and the successes. Thankfully, my adventure in the Lab is not over yet—brace yourselves!

Finally, I owe infinite gratitude to my family for their unconditional support and for always allowing me to follow my passions. If I have come this far, it is entirely thanks to you.